HARVARD UNIVERSITY
Graduate School of Arts and Sciences



DISSERTATION ACCEPTANCE CERTIFICATE

The undersigned, appointed by the

Department of Earth and Planetary Sciences

have examined a dissertation entitled

"Modeling the Impact of Human-Driven Fires on Air Quality from Regional and Global Perspectives"

presented by

Tianjia Liu

candidate for the degree of Doctor of Philosophy and hereby certify that it is worthy of acceptance.

Signature _____

Typed name: Prof. Daniel Jacob

Signature _____

Typed name: Prof. Loretta Mickley

Signature _____

Typed name: Prof. Elsie Sunderland

Signature _____

Typed name: Prof. Zhiming Kuang

Signature _____

Typed name: Prof. Kaighin McColl

Date: April 28, 2022

Modeling the Impact of Human-Driven Fires on Air Quality from Regional and Global Perspectives

A DISSERTATION PRESENTED
BY
TIANJIA LIU
TO
THE DEPARTMENT OF EARTH AND PLANETARY SCIENCES

IN PARTIAL FULFILLMENT OF THE REQUIREMENTS
FOR THE DEGREE OF
DOCTOR OF PHILOSOPHY
IN THE SUBJECT OF
EARTH AND PLANETARY SCIENCES

HARVARD UNIVERSITY
CAMBRIDGE, MASSACHUSETTS
APRIL 2022

©2022 – Tianjia Liu
all rights reserved.

Modeling the Impact of Human-Driven Fires on Air Quality from Regional and Global Perspectives

Abstract

Natural and anthropogenic fires emitted 2.2 Pg C yr^{-1} on average from 1997-2016, with widespread impacts on climate, ecosystem dynamics, air quality, and public health (van der Werf et al., 2017). In contrast to the 24% decline in global burned area over the past two decades (Andela et al., 2017), agricultural intensification and expansion have enhanced fire activity in India (Liu et al., 2019) and Indonesia (Marlier et al., 2015). In India, post-harvest crop residue burning, concentrated in the state of Punjab, severely degrades the air quality downwind in both rural and urban centers, including Delhi and the densely-populated Indo-Gangetic Plain (Kaskaoutis et al., 2014; Liu et al., 2018; Cusworth et al., 2018; Bikkina et al., 2019). In Indonesia, the combination of deforestation fires and dense network of carbon-rich peatlands spells a recipe for severe haze and elevated mortality risk during drought years (Fanin & van der Werf, 2017; Koplitz et al., 2016, 2018a). Together with daily, global monitoring of fires and vegetation from satellites, recent advances in cloud computing and geospatial analysis with the Google Earth Engine platform have accelerated the data processing and analysis pipeline by orders of magnitude (Gorelick et al., 2017). However, large uncertainty in satellite fire observations, fuel loading, small fire and cloud corrections, and emissions factors has led to substantial disagreement among global fire emissions inventories and lowered our confidence in projected health outcomes (Liu et al., 2020a). Here I use a combination of observations and models to understand factors contributing to these differences, improve current emissions estimates, and quantify spatio-temporal trends in fires in the context of human activity.

This dissertation is partitioned into two themes, focused on India (Chapter 1-3) and globally (Chapters 4-6). In north India, cascading delays in the monsoon growing season and post-monsoon agricultural burning have led to increased air quality degradation. In Chapter 1, I quantify the temporal shift in the post-monsoon fire season in the state of Punjab over 2003-2016 and discuss how a 2-week delay is connected to changes in the monsoon rice growing season, the implementation of a 2009 groundwater policy in India, and increased aerosol loading (Liu et al., 2021a). In Chapter 2, I combine survey and satellite data to build a new agricultural fire emissions

inventory, SAGE-IGP (Liu et al., 2020b). In Chapter 3, I use atmospheric transport modeling with the SAGE-IGP inventory as input to quantify the effect of the post-monsoon fire season delay on air quality in downwind cities, such as New Delhi (Liu et al., 2022).

In Chapter 4, I develop metrics to understand the spatial uncertainties and biases in global fire emissions inventories, using Indonesia as a case study (Liu et al., 2020a). In Chapter 5, I discuss how tile-based processing in satellite burned area products can lead to discontinuities in burned area mapping and impact analyses (Liu & Crowley, 2021). In Chapter 6, I search globally for regions with temporal shifts in the primary fire season; I focus on north Australia and southwest Russia as two case study regions where human decisions and interventions either directly or indirectly influenced the timing of the fire season (Liu et al., 2021b).

Contents

Title Page i

Copyright Page ii

Abstract iii

Table of Contents v

List of Figures ix

List of Tables xiii

Prior Publications and Contributing Authors xvi

Dedication xviii

Acknowledgements xix

1 Detection of delay in post-monsoon agricultural burning across Punjab, India: potential drivers and consequences for air quality 1

1.1 Abstract . . . 1
1.2 Introduction . . . 2
1.3 Data and Methods . . . 3
1.3.1 Study region . . . 3
1.3.2 Active fires and vegetation indices . . . 5
1.3.3 Statistical analysis . . . 5
1.3.3.1 Characterizing the temporal progression of agricultural fires . . . 5
1.3.3.2 Tracking crop phenology with NDVI and NBR . . . 6
1.3.4 Regional aerosol optical depth exceedances . . . 7
1.4 Results . . . 8
1.4.1 Trends in seasonal agricultural fire activity . . . 8
1.4.2 Trends in vegetation greenness from monsoon to post-monsoon . . . 10
1.4.2.1 The utility of NBR as a vegetation index . . . 10
1.4.3 Trends in post-monsoon regional aerosol optical depth . . . 12
1.5 Discussion . . . 12
1.5.1 Implications of delays in post-monsoon fire activity . . . 12
1.5.2 Potential drivers of delays in the rice-wheat rotation . . . 14
1.6 Conclusion . . . 16

2 Crop residue burning practices across north India inferred from household survey data: bridging gaps in satellite observations 17
2.1 Abstract . . . 17
2.2 Introduction . . . 18
2.3 Data and Methods . . . 20
2.3.1 Study region . . . 20
2.3.2 Household survey . . . 20
2.3.3 Satellite datasets . . . 20
2.3.4 Statistical adjustments of agricultural fire emissions using satellite and survey data . . . 22
2.3.4.1 Adjustment of FRP based on survey data and additional satellite observations . . . 23
2.3.4.2 Conversion to dry matter burned and emissions . . . 27
2.3.4.3 Constructing a spatially and temporally explicit gridded emissions inventory 30
2.3.5 Ground and satellite-based measurements of aerosols . . . 31
2.3.6 Atmospheric modeling of smoke from agricultural fires: validation using station $PM_{2.5}$ observations . . . 31
2.4 Results and Discussion . . . 32
2.4.1 Crop residue burning across the Indo-Gangetic Plain: drivers, consequences, and farmer perceptions . . . 32
2.4.2 Adjusted emissions from agricultural fires using satellite and survey data . . . 35
2.4.2.1 Limitations and uncertainties in constructing spatio-temporal explicit emissions . . . 41
2.4.3 Differences in fire activity, fuel consumption, and emissions factors assumed in inventories and the consequences for emissions estimates . . . 43
2.5 Conclusion . . . 45

3 Cascading delays in the monsoon growing season and post-monsoon fires may exacerbate poor air quality in north India 47
3.1 Abstract . . . 47
3.2 Introduction . . . 48
3.3 Data and Methods . . . 50
3.3.1 Satellite fire and surface reflectance datasets: temporal shifts in fire activity and vegetation greenness . . . 50
3.3.2 STILT modeling . . . 51
3.3.2.1 Impact of temporal shifts in fire activity on downwind smoke exposure . . 53
3.4 Results and Discussion . . . 53
3.4.1 Delays in monsoon rice growth led to delays in post-monsoon fires . . . 53
3.4.2 Sensitivity of downwind smoke exposure to timing of post-monsoon fires . . . 58
3.4.3 Contextualizing the importance of delays in the post-monsoon fire season . . . 65
3.5 Conclusion . . . 68

4 Diagnosing spatial biases and uncertainties in global fire emissions inventories: Indonesia as regional case study 70
4.1 Abstract . . . 70
4.2 Introduction . . . 71
4.2.1 Global fire emissions inventories: role in modeling studies and methodological differences . . . 71
4.2.2 Regional case study: smoke exposure from fires in Indonesia . . . 74

4.2.3 Google Earth Engine: online platform for rapid geospatial analysis . . . 75
4.3 Methods . . . 76
4.3.1 Satellite fire datasets . . . 76
4.3.2 Relative fire confidence metrics . . . 76
4.3.2.1 Bottom-up inventories: relative fire confidence scores (BA-score, AFA-score) 80
4.3.2.2 Top-down inventories: adjusted potential FRP adjustment (pFRP) . . . 81
4.3.3 Global fire emissions inventories . . . 82
4.3.4 Modeling smoke $PM_{2.5}$ from regional fire emissions . . . 82
4.4 Results . . . 83
4.4.1 Spatial patterns in relative fire confidence metrics and scores . . . 83
4.4.2 Comparison of global fire emissions inventories: speciation and emissions factors . . . 88
4.4.3 Modeling monthly smoke $PM_{2.5}$ from Indonesia fires . . . 91
4.4.4 Comparison of global fire emissions inventories: speciation and emissions factors . . . 91
4.4.4.1 2006 and 2015 severe haze events . . . 91
4.5 Discussion and Conclusion . . . 96
4.5.1 Relative fire confidence metrics: spatial patterns . . . 96
4.5.2 Regional application: validation of modeled smoke $PM_{2.5}$ across Equatorial Asia from Indonesia fires . . . 97
4.5.3 Uncertainties in global fire emissions inventories . . . 98
4.5.4 Future directions and recommendations . . . 99

5 Detection and impacts of tiling artifacts in MODIS burned area classification **101**
5.1 Abstract . . . 101
5.2 Introduction . . . 101
5.3 Methods . . . 102
5.3.1 Satellite fire datasets . . . 102
5.3.2 Identifying tiling artifacts . . . 103
5.3.2.1 Method 1: normalized difference of burned area and active fire area . . . 103
5.3.2.2 Method 2: adjacent burned pixel pairs across tile edges . . . 103

6 Global search for temporal shifts in fire activity: potential human influence on southwest Russia and north Australia fire seasons **109**
6.1 Abstract . . . 109
6.2 Introduction . . . 109
6.3 Data and Methods . . . 111
6.3.1 Satellite fire datasets . . . 111
6.3.2 Global search for temporal shifts in the primary fire season . . . 111
6.4 Results and Discussion . . . 114
6.4.1 Global temporal shifts in fire activity . . . 114
6.4.2 Case study 1: southwest Russia . . . 117
6.4.3 Case study 2: north Australia . . . 120
6.4.4 Drivers of temporal shifts . . . 123
6.5 Conclusion . . . 124

Appendix A Supplemental Material for Chapter 1 **126**
A.1 Data and Methods . . . 126
A.1.1 Active fires . . . 127

A.1.2 Vegetation indices . . . 128
A.1.3 Aerosol optical depth . . . 129
A.1.4 Population count . . . 130
A.2 India state-level agricultural fire activity . . . 130
A.3 Temporal shifts in fires and vegetation greenness in Punjab . . . 134
A.4 Vegetation indices: NBR and NDVI . . . 139
A.5 Thick haze and fog over the Indo-Gangetic Plain . . . 140
A.6 Variations in Monsoon Onset and Withdrawal . . . 141
A.7 Synthesis of the potential drivers and consequences of delays in agricultural burning associated with the double-crop cycle . . . 143

Appendix B Supplemental Material for Chapter 2 **144**
B.1 Household survey . . . 144
B.2 Characterizing fires, crop phenology, and rainfall using satellite data . . . 150
B.3 Gridded inventory for agricultural fire emissions across the Indo-Gangetic Plain . . . 152
B.3.1 Additional details on VIIRS FRP boost . . . 152
B.3.2 Additional details on cloud/haze gap-filling . . . 153
B.3.3 Additional details on the adjustment for the diurnal cycle of fire activity . . . 157
B.3.4 Hourly diurnal cycle of fire activity . . . 159
B.3.5 Uncertainty analysis . . . 161
B.4 Estimates of agricultural fire emissions based on active fires and burned area . . . 165
B.4.1 BA/AFA-based inventories . . . 167
B.4.2 FRP-based inventories . . . 167
B.4.3 Uncertainties in burned area, fuel consumption, and emissions factors . . . 168
B.5 Delays in post-monsoon fire activity in Punjab, India . . . 170

Appendix C Supplemental Material for Chapter 3 **173**
C.1 Satellite-observed temporal shifts in crop phenology and fire activity . . . 174
C.1.1 Spatial heterogeneity in groundwater usage and trends in context of temporal shifts in the monsoon growing season and post-monsoon fires . . . 176
C.2 Atmospheric Transport Modeling of Smoke $PM_{2.5}$ . . . 179
C.2.1 STILT modeling . . . 179
C.2.2 Background $PM_{2.5}$ . . . 179

Appendix D Supplemental Material for Chapter 4 **183**
D.1 Inventory-specific relative fire confidence scores . . . 184
D.2 Global fire emissions inventories: "bottom-up" and "top-down" methods . . . 186
D.2.1 Bottom-up emissions inventories: GFED and FINN . . . 186
D.2.2 Top-down emissions inventories: GFAS, QFED, and FEER . . . 187
D.3 Validation of smoke exposure in Equatorial Asia from Indonesia fires . . . 190
D.3.1 Singapore . . . 190
D.3.2 Malaysia and Indonesia . . . 193
D.4 Ancillary information on burn date uncertainty, fire diurnal cycle, and land use/ land cover . . . 199
D.5 Fire Inventories: Regional Evaluation, Comparison, and Metrics (FIRECAM) online tool . . . 201
D.6 Relative fire confidence metrics: consistency with other regional studies . . . 203
D.7 Trends in global fire emissions . . . 205
D.8 Implementation of global fire emissions inventories in GEOS-Chem . . . 206

Appendix E Supplemental Material for Chapter 5 210
E.1 The φ and ε metrics: complications and limitation 210

Appendix F Supplemental Material for Chapter 6 215
F.1 Datasets 215
F.2 Ancillary Datasets 217
F.3 Southwest Russia 218
F.4 North Australia 219
F.5 Temporal shifts in regions of interest 221
F.6 Case study 1: southwest Russia 223
F.7 Case study 2: north Australia 227

References 250

List of Figures

1.1 Cycles of fire activity and vegetation greenness in Punjab, India 4
1.2 Temporal shifts in post-monsoon fires in Punjab from 2003-2016 9
1.3 Trends in monsoon peak greenness and post-monsoon trough greenness in Punjab from 2003-2016 11
1.4 Trend in the timing of peak post-monsoon AOD over the western Indo-Gangetic Plain from 2003-2016 13

2.1 Temporal and methodological characteristics of rice residue burning across the Indo-Gangetic Plain, inferred from household survey data for the 2017-18 growing season 21
2.2 Pictorial flowchart for FRP adjustments using satellite and survey data for Punjab in the sample year 2017 24
2.3 Satellite-derived daily vegetation greenness, fire intensity, and rainfall in Punjab, Haryana, Uttar Pradesh, and Bihar from 2003-2018 32
2.4 Mechanized harvesting of rice related to crop residue burning across the Indo-Gangetic Plain inferred from household survey data 33
2.5 Post-monsoon agricultural fire emissions over the IGP from 2003-2018 36
2.6 Dry matter (DM) burned from adjusted FRP and comparison of OC+BC emissions for Punjab, India, from 2003-2018 37
2.7 Daily fire emissions and intensity in Punjab, India, and aerosols observed over Punjab and in Kanpur, India, during the 2017 post-monsoon burning period 39
2.8 Correlations of daily observed station $PM_{2.5}$ in New Delhi and modeled $PM_{2.5}$ using SAGE-IGP and five global inventories for the 2013-2018 post-monsoon burning seasons 40
2.9 Comparison of average dry matter (DM) burned derived from different combinations of bottom-up burned area and fuel consumption estimates for the 2003-2016 post-monsoon burning seasons in Punjab, India 44

3.1 Correlation of temporal shifts in post-monsoon fires and peak monsoon greenness by district in Punjab across 2003-2019 54
3.2 Correlation between the earliest rice sowing dates and timing of the peak monsoon greenness and midpoint of the post-monsoon fire season in Punjab from 2008-2019 56
3.3 Regional summary of district-level trends in phenology, fires, and groundwater levels in Punjab, India 57
3.4 Effect of temporal shifts in the post-monsoon agricultural fire season on downwind $PM_{2.5}$ in New Delhi in 2017 59
3.5 Effect on $PM_{2.5}$ in New Delhi from 2008-2018 if the post-monsoon agricultural fire season had not experienced delays relative to the 2003-2007 period 60
3.6 Effect on $PM_{2.5}$ in New Delhi from 2008-2019 if the post-monsoon agricultural fire season had not experienced delays relative to the 2003-2007 period 61

3.7 Compression of daily afternoon boundary layer heights and increase in average STILT sensitivities for New Delhi during the post-monsoon burning season . . . 63
3.8 STILT sensitivity footprints for six receptors . . . 64
3.9 $PM_{2.5}$ concentrations in six cities during the post-monsoon agricultural fire season from 2008-2019 . . . 65
3.10 Effect on $PM_{2.5}$ in six cities from 2008-2019 if the post-monsoon agricultural fire season had not experienced delays relative to the 2003-2007 period . . . 66

4.1 Metric 1 for relative fire confidence score (φ_{area}) . . . 84
4.2 Metric 2 for relative fire confidence score (φ_{cloud_haze}) . . . 85
4.3 Metric 3 for relative fire confidence score ($\varphi_{fragment}$) . . . 85
4.4 Metric 4 for relative fire confidence score ($\varphi_{topography}$) . . . 86
4.5 Metric 5 for relative fire confidence score (φ_{VIIRS_sf} . . . 86
4.6 Mean annual OC + BC emissions (Tg yr^{-1}, $\pm 1\sigma$), over 2003-2016, from five global fire emissions inventories . . . 88
4.7 Indonesia fires, smoke exposure in Singapore, and AOD in Equatorial Asia during July-October in 2006 . . . 92
4.8 Smoke $PM_{2.5}$ exposure in Singapore, from 2003-2016. . . . 93
4.9 Under-detection of 2015 Indonesia fires in MODIS active fire and burned area products relative to the 2003-2016 period. . . . 95

5.1 Pictorial depiction of the pixel-level approach to identify burned area artifacts at tile edges . . . 104
5.2 Example of the tiling artifacts in FireCCI in November in northwest India . . . 106
5.3 Average MCD64A1 and FireCCI burned area in northwest India from 2003-2019 . . . 107

6.1 Temporal shifts in the midpoint of the primary fire season over a 16-year period from 2003-2018 115
6.2 Regional temporal shifts in fire activity from 2003-2018 for two case study regions . . . 116
6.3 Winter wheat phenology, fire activity, and drought in southwest Russia . . . 118
6.4 Trends in early and late dry season fires in north Australia from 2003-2018 . . . 122

A.1 Overview of pre-monsoon and post-monsoon fire activity in India at state-level . . . 132
A.2 Trends in all-India agricultural FRP and fire emissions . . . 133
A.3 Trends in peak post-monsoon burning of in Punjab by district . . . 134
A.4 Timing of the Diwali festival and post-monsoon burning season in Punjab . . . 136
A.5 Rice production in Punjab . . . 137
A.6 Temporal compression of the duration from the onset of post-monsoon burning season to trough greenness in Punjab . . . 138
A.7 Detrended correlation between daily median NDVI and NBR, by month, in Punjab . . . 139
A.8 Example of thick haze and fog over the Indo-Gangetic Plain . . . 140
A.9 Monsoon onset and withdrawal date in Punjab from 2003-2016 . . . 142
A.10 Potential drivers and consequences of the temporal shifts in the double crop-fire cycle for Punjab 143

B.1 Drivers of rice residue burning across the Indo-Gangetic Plain inferred from household survey data for the 2017-18 growing season . . . 148
B.2 Interannual variability in the VIIRS to MODIS/Aqua FRP ratio by state . . . 152
B.3 Haze and cloud cover over Punjab, India from Oct 28-Nov 8 in 2016 and 2017 . . . 153
B.4 Satellite observable fraction in the IGP during September to December from 2003-2018, weighted by FRP . . . 154

B.5 Graphic depiction of which fires are seen by a satellite during its overpass over north India: The timing of the satellite overpass, which lasts 1-2 minutes, is denoted by the filled-in circle 157
B.6 Temporal distribution of daytime active fire detections by MODIS and VIIRS in north India from 2012-2018 158
B.7 GFEDv4s diurnal cycle of fire activity in Punjab, Haryana, UP, and Bihar 160
B.8 Relative uncertainty in satellite-derived FRP due to cloud/haze gaps in observations 162
B.9 Post-monsoon burn footprint over the Indo-Gangetic Plain 165
B.10 Delays in the post-monsoon burning season in Punjab, India from 2003-2018 171

C.1 Spatial variability in monsoon crop phenology in Punjab during the 2003-2007 period 174
C.2 Spatial variability in the midpoint of the post-monsoon fire season among Punjab districts from 2003-2019 175
C.3 Household survey locations in Punjab 177
C.4 Duration from green-up to green-down during the monsoon growing season in northwest India 178
C.5 Annual variation in STILT sensitivities from 2007-2019 with New Delhi as the receptor 179
C.6 Increase in daily background $PM_{2.5}$ in New Delhi from post-monsoon to winter, 2013-2019 . . 180
C.7 Observed and modeled $PM_{2.5}$ in New Delhi in October and December from 2015-2017 182

D.1 Relative fire confidence score for bottom-up emissions inventories 184
D.2 Adjusted potential FRP enhancement (pFRP), expressed as fractional fire energy, for top-down FRP-based emissions inventories 185
D.3 Average CHIRPS rainfall rate (mm day^{-1}) over Sumatra and Kalimantan, from 2003-2016. . . 190
D.4 Under-detection of 2015 Indonesia fires in burned area relative to the 2003-2016 period 191
D.5 Observed (red) and reconstructed (black) smoke $PM_{2.5}$ in Singapore for 2003-2016 192
D.6 PM_{10} station network (n = 59) in Malaysia overlaid on population density in 2010 194
D.7 Smoke $PM_{2.5}$ exposure in Malaysia, from 2003-2015. 197
D.8 Smoke AOD and $PM_{2.5}$ exposure in Indonesia, from 2003-2016. 198
D.9 Average burn date uncertainty (in days), over 2003-2017, for burned area estimates from the MODIS MCD64A1 burned area product. 199
D.10 Ancillary information on the diurnal cycle in fire energy and entropy of land use/land cover classification, mapped at 0.25° x 0.25° spatial resolution 200
D.11 Screenshot of the Fire Inventories: Regional Evaluation, Comparison, and Metrics (FIRE-CAM) online tool 201
D.12 The 14 basis regions defined in GFEDv4s 202

E.1 Regions with large-scale tiling artifacts 211
E.2 Example of the tiling artifacts in FireCCI in March in Myanmar 213
E.3 Example of the tiling artifacts in MCD64A1 in August in Ukraine and southwest Russia 214

F.1 Temporal shifts in the primary fire season over a 16-year period from 2003-2018 in secondary regions of interest 221
F.2 Study area in southwest Russia 224
F.3 Winter wheat in southwest Russia from 2003-2018 225
F.4 Average fire intensity per active fire detection in southwest Russia by month from 2003-2018 . . 226
F.5 Aboriginal freehold lands in north Australia 227
F.6 Savanna burning projects in north Australia 228
F.7 Trends in early and late dry season fires in north Australia from 2003-2018 230
F.8 Trends in GFEDv4s CO_2 emissions and fuel consumption in north Australia 231

F.9 Meteorology drives the inter-annual variability in burned area in north Australia during the late dry season 232

List of Tables

2.1 Parameters for estimates of agricultural fire emissions based on burned area, active fire area, and Fire Radiative Power (FRP) . . . 28

3.1 Locations of receptors / cities used in STILT simulations . . . 52
3.2 Correlations between the temporal shifts in the timing of the monsoon growing season and post-monsoon fire season . . . 55

4.1 Comprehensive comparison of the global fire emissions inventories for various methodological details and technical parameters . . . 73
4.2 Satellite-derived datasets used for the five relative fire confidence metrics . . . 77
4.3 Average annual global CO_2, CO, CH_4, organic carbon (OC), black carbon (BC) and fine particulate matter ($PM_{2.5}$) emissions (Tg yr^{-1}, $\pm 1\sigma$) by inventory, from 2003-2016. . . . 89
4.4 Average emissions factors (g species kg^{-1} dry matter) for CO_2, CO, CH_4, OC, BC and $PM_{2.5}$, weighted by fractional emissions over GFEDv4s land use and land cover (LULC). . . . 90

6.1 Regions of interest with coherent spatial signals of temporal shifts at the midpoint of the primary fire season from 2003-2018 . . . 112

A.1 Satellite-derived fire, surface reflectance, aerosol, and land cover datasets used in this study . . . 126
A.2 Temporal shifts (days yr^{-1}) in pre-monsoon and post-monsoon FRP in Punjab, from 2003-2016, with bootstrapped 95% confidence intervals . . . 135
A.3 Temporal shifts (days yr^{-1}) in fire intensity (MxD14A1), active fire counts (MCD14ML), burned area (MCD64A1), and agricultural fire dry matter (DM) emissions (GFEDv4s) in Punjab, from 2003-2016, during the post-monsoon burning season . . . 135
A.4 Trends (yr^{-1}) in fire intensity (MxD14A1), active fire counts (MCD14ML), burned area (MCD64A1), and agricultural fire dry matter emissions (GFEDv4s) in Punjab during the post-monsoon burning season over 2003-2016 . . . 135
A.5 Step difference in the timing of peak monsoon greenness and trough post-monsoon greenness from the 2003-2007 to 2008-2016 time period and linear trends in the timing and magnitude of peak monsoon and trough post-monsoon greenness in Punjab . . . 136

B.1 Questions from the 2017-18 household survey on agricultural practices across the Indo-Gangetic Plain and possible responses . . . 145
B.2 2017-18 household survey data on crop residue burning and mechanization in the IGP . . . 146
B.3 2017-18 household survey data on the reasons for and effects of crop residue burning in the IGP 147
B.4 Potential increase in post-monsoon burning, weighted by operational landholding area, across the Indo-Gangetic Plain for a hypothetical scenario in which all farmers use fully mechanical harvesting (combine harvesters) . . . 149

B.5 State-level fraction of partial and complete-field burns and fractional fire diurnal cycle, weighted by operational landholding area, derived from the 2017 household survey 149
B.6 Satellite datasets used in this study 150
B.7 Uncertainty in VIIRS FRP boost, calculated per season using the ratio of VIIRS to MODIS/Aqua FRP from 2012-2018, when applied to post-monsoon burning seasons from 2003-2011 161
B.8 Uncertainty in partial burn and mid-day fire fractions (10 a.m. to 2 p.m.) from household survey responses 163
B.9 Average emissions factors and associated uncertainty (±1 SD) for OC, BC, CO, and CO_2 for agricultural burning 164
B.10 Regional and global fire emissions inventories 166
B.11 Different fuel consumption (FC) assumptions for Punjab, India from 2003-2016 168
B.12 Range of emissions factors (g kg^{-1} DM) used for agricultural waste burning in global fire emissions inventories 168
B.13 Uncertainties in bottom-up and top-down emissions inventories and range of average post-monsoon fire emissions in Punjab, India, compared to this study, from 2003-2016 169
B.14 Temporal shifts (days yr^{-1}) in the post-monsoon burning season in Punjab, India from 2003-2018 172

C.1 Irrigation practices in Punjab, India by district from household survey data 177
C.2 Background and smoke $PM_{2.5}$ ($\mu g\ m^{-3}$) in the six receptor cities from 2015-2017. 181

D.1 Emissions factors (g species kg^{-1} dry matter) for CO_2, CO, CH_4, organic carbon (OC), black carbon (BC) and fine particulate matter ($PM_{2.5}$) used in the global fire emissions inventories . . 189
D.2 Details on PM_{10} stations in Malaysia used for validation of modeled population-weighted exposure 195
D.3 Linear trends in global fire emissions, from 2003-2016, by inventory and species 205
D.4 Differences in mean annual global GFEDv4s CO_2, CO, CH_4, OC, and BC emissions (Tg yr^{-1}, $\pm 1\sigma$) using the original and updated emissions factors. 207
D.5 Differences in original and updated emissions factors (EFs; g species kg^{-1} dry matter) for GFEDv4s 208
D.6 Differences in mean annual global CO_2, CO, CH_4, OC, and BC emissions (Tg yr^{-1}, $\pm 1\sigma$) between "out-of-box" and HEMCO FINNv1.5 208
D.7 Differences in scaling factors from CO_2 to CO, CH_4, OC, and BC emissions between "out-of-box" and HEMCO FINNv1.5 209

E.1 Regions with tiling artifacts in MCD64A1 and FireCCI according to the φ and ε metrics 212

F.1 Details on the primary satellite fire datasets used in this study 215
F.2 Details on the ancillary satellite-based and reanalysis datasets used in this study 217
F.3 Regions of interest with coherent spatial signals of a temporal shift in the midpoint of the primary fire season from 2003-2018 222
F.4 Temporal shifts in the midpoint of the primary fire season in oblasts in southwest Russia 223
F.5 Temporal shifts in the midpoint of the primary fire season in savanna burning project areas in north Australia 229

Prior Publications and Contributing Authors

Chapter 1 has previously appeared as:

> **Liu, T.**, L.J. Mickley, R. Gautam, M.K. Singh, R.S. DeFries, and M.E. Marlier (2021). Detection of delay in post-monsoon agricultural burning across Punjab, India: potential drivers and consequences for air quality. *Environ. Res. Lett.*, **16**(1), 014014. https://doi.org/10.1088/1748-9326/abcc28

Chapter 2 has previously appeared as:

> **Liu, T.**, L.J. Mickley, S. Singh, M. Jain, R.S. DeFries, and M.E. Marlier (2020). Crop residue burning practices across north India inferred from household survey data: bridging gaps in satellite observations. *Atmos. Environ. X*, **8**, 100091. https://doi.org/10.1016/j.aeaoa.2020.100091

Chapter 3 has been submitted for publication:

> **Liu, T.**, L.J. Mickley, P.N. Patel, R. Gautam, M. Jain, S. Singh, Balwinder-Singh, R.S. DeFries, and M.E. Marlier. Cascading delays in the monsoon rice growing season and post-monsoon agricultural fires likely exacerbate air pollution in north India. *Under review* at *J. Geophys. Res. Atmos.*

Chapter 4 has previously appeared as:

> **Liu, T.**, L.J. Mickley, M.E. Marlier, R.S. DeFries, M.F. Khan, M.T. Latif, and A. Karambelas (2020). Diagnosing spatial biases and uncertainties in global fire emissions inventories: Indonesia as regional case study. *Remote Sens. Environ.*, **237**, 111557. https://doi.org/10.1016/j.rse.2019.111557

Chapter 5 has previously appeared as:

> **Liu, T.** and M.A. Crowley (2021). Detection and impacts of tiling artifacts in MODIS burned area classification. *IOP SciNotes*, **2**, 014003. https://doi.org/10.1088/2633-1357/abd8e2

Chapter 6 has previously appeared as:

> **Liu, T.**, L.J. Mickley, and J.L. McCarty (2021). Global search for temporal shifts in fire activity: potential human influence on southwest Russia and north Australia fire seasons. *Environ. Res. Lett.*, **16**(4), 044023. https://doi.org/10.1088/1748-9326/abe328

To my parents, for their sacrifices and undying support that have brought me to this moment.

Acknowledgments

To all of you who have touched my life, thank you. This marks not only an end, but also the beginning of another chapter. There is yet much to strive for, much to accomplish, and much to live for — I will always cherish these memories of the past five years.

First, I would like to thank Loretta Mickley for her unwavering support, guidance and wisdom, timely feedback, openness, and unending curiosity about my research. I am grateful to Loretta for serving as my research adviser, and she has been a steadying presence throughout my Ph.D. at Harvard. I will miss our weekly meetings dearly. Thank you to Daniel Jacob for serving as my academic adviser and my thesis committee, Zhiming Kuang, Elsie Sunderland, and Kaighin McColl.

Without my research mentors during my undergraduate years, I would not be here. A huge thanks to Ruth DeFries, Miriam Marlier, Ray Schmitt, Laifang Li, Jerry McManus, Jon Nichols, Dorothy Peteet, and Alex Karambelas. Thank you to my future postdoc mentor Jim Randerson for welcoming me to UC Irvine for the next two years.

Thank you to Brendan Meade and Esther James, for making my first teaching experience fun and rewarding. Thank you to the Department of Earth and Planetary Sciences and to Sarah Colgan and Aimee Smith. Thank you to the Mittal Institute and Megan Siwek, Danielle Wallner, Kellie Nault, and Taamra Segal for organizing events for the Graduate Student Associates and helping me to share my research. Thank you to Colette Heald for organizing the 2021 Rising Stars Workshop at MIT.

I would like to thank my collaborators and co-authors, who have helped to elevated my research and graciously allowed me to contribute to theirs. Thank you to Ritesh Gautam, Meha Jain, Manoj Singh, Sukwinder Singh, Piyush Patel, Dan Cusworth, Morgan Crowley, Shannon Koplitz, Sam Myers, Budi Wardhana, Sachin Gunthe, Pengfei Liu, Xiaodan Zhou, Francesca Dominici, Md Firoz Khan, Mohd Talib Latif, Shradda Dhungel, Jessica McCarty, Alex Karambelas, Ruoyu Lan, Seb Eastham, and others. Thank you to everyone in the Atmospheric Chemistry Modeling Group. Thank you to the Google Earth Engine team, especially to Justin Braaten, Tomomi Matsuoka, and Nick Clinton. I would also like to thank Makoto Kelp, Drew Pendergrass, and Loretta Mickley for our seamless collaboration in mentoring three wonderful undergraduate students: Miah Caine, Marie Panday, and Kent Toshima.

I would like to thank the National Science Foundation (NSF) for funding support during my Ph.D. with the Graduate Research Student Fellowship (GRFP) program. I would also like to thank NOAA Climate & Global Change Fellowship for future funding support during my postdoc at UC Irvine.

The Ph.D. journey is never fun without friends to share it with. Thank you to Makoto Kelp, Nadia Colombi, Elise Penn, Jennifer Sun, Drew Pendergrass, Shannon Beattie, Haipeng Lin, Jack Bruno, Danielle Wallner, Ben Geyman, Seth Olinger, Laura Yang, Hairuo Fu, Ju Chulakadabba, Lois Tang, Yang Li, and many others. Thank you to my friends outside Harvard and academia, especially to Quinn Tran, Janaki Nakum, Bhavna Nakum, Pranavi Depur, Chris Bui, and Emily Bui. Thank you for the endless laughter and all the fun trips, game nights, and tasty meals we've shared. Additionally, thank you to Diane Lulek and the Harvard Ceramics program for providing a creative, welcoming, and relaxing space.

Last but not least, thank you to my family, and especially to my parents, for caring so deeply about my academic path and for the sacrifices they made along the way.

1

Detection of delay in post-monsoon agricultural burning across Punjab, India: potential drivers and consequences for air quality

1.1 Abstract

Since the Green Revolution in the mid-1960s, a widespread transition to a rice-wheat rotation in the Indian state of Punjab has led to steady increases in crop yield and production. After harvest of the summer monsoon rice crop, the burning of excess crop residue in Punjab from October to November allows for rapid preparation of fields for sowing of the winter wheat crop. Here we use daily satellite remote sensing data to show that the timing of peak post-monsoon fire activity in Punjab and regional aerosol optical depth (AOD) has shifted later by approximately two weeks in Punjab from 2003-2016. This shift is consistent with delays of 11-15 days in the timing of maximum greenness of the monsoon crop and smaller delays of 4-6 days in the timing of minimum greenness during the monsoon-to-winter crop transition period. The resulting compression of the harvest-to-sowing period coincides with a 42% increase in total burning and 55% increase in regional AOD. Potential drivers of these trends include agricultural intensification and a recent groundwater policy that delays sowing of the monsoon crop. The delay and amplification of burning into the late post-monsoon season suggest greater air quality degradation and public health consequences across the densely-populated Indo-Gangetic Plain.

1.2 Introduction

Rapid increases in mechanized harvesting in the Indo-Gangetic Plain (IGP) since the mid-1980s, together with steady increases in crop production, have led many farmers to burn the abundant residue left behind by this practice (Badarinath et al., 2006). Such burning is a quick, cheap, and efficient method to ready the fields for the next crop. However, the smoke from post-monsoon crop residue burning, primarily during October to November, amplifies severe haze events in the region (Kaskaoutis et al., 2014), such as that observed in early November 2016 (Cusworth et al., 2018). Of particular concern is the observed increase in aerosol loading associated with an upward trend in post-monsoon burned area and with a shift toward a later peak in post-monsoon fires in northwestern India (Thumaty et al., 2015; Jethva et al., 2018; Liu et al., 2019; Balwinder-Singh et al., 2019; Jethva et al., 2019) Here we use daily satellite remote sensing data to quantify the temporal shift toward later burning in the state of Punjab, the "breadbasket" of India. Such a shift would have implications for air quality degradation, since peak burning is more likely to coincide with meteorological conditions that are favorable in amplifying persistent haze, such as weak winds, low mixing layer heights, temperature inversions, and high relative humidity (Ojha et al., 2020).

Agricultural intensification of rice and wheat in India has led to over two-fold and three-fold increases, respectively, in crop yield since the Green Revolution in the mid-1960s. In the western IGP, the predominant rice-wheat rotation is highly productive (Kumar et al., 2015). Punjab, an agricultural state in northwestern India, contributes more than one-fifth of rice and one-third of wheat to the central grain pool in India, and thus generates large amounts of crop residue annually. Since the mid-to-late 1980s, farmers have increasingly used mechanized harvesting methods in preference to sickle-based manual harvesting in order to reduce labor costs and save time (Badarinath et al., 2006; Kumar et al., 2015). The use of combine harvesters, however, leaves behind an abundance of scattered and root-bound residue that is difficult to remove and thus often burned post-harvest to prepare for timely sowing of the next crop (Kumar et al., 2015). The burning allows for quick disposal of crop residues and shortens the harvest-to-sowing transition from the *kharif* (monsoon crop) to *rabi* (winter crop) season. A quicker transition between crops also allows for earlier sowing of wheat during post-monsoon to avoid springtime heat (Lobell et al., 2013).

However, the burning of post-monsoon rice residue can severely degrade air quality downwind of the agricultural fires over the IGP (Badarinath et al., 2006; Singh & Kaskaoutis, 2014; Kaskaoutis et al., 2014; Liu et al.,

2018; Cusworth et al., 2018; Jethva et al., 2018; Sarkar et al., 2018). In particular, smoke from rice residue burning in October and November may account for more than half the fine particulate matter ($PM_{2.5}$) concentrations in the Delhi National Capital Region (Cusworth et al., 2018), which already experiences intense urban pollution from local and other regional sources (Amann et al., 2017). A temporal shift in fire activity to later in the year could exacerbate air quality degradation since late autumn-to-winter meteorology in the IGP favors smog formation due to weak winds, frequent temperature inversions, and a shallow boundary layer (Choudhury et al., 2007; Saraf et al., 2010; Liu et al., 2018).

Observations from the Moderate Resolution Imaging Spectroradiometer (MODIS), aboard NASA's Terra and Aqua satellites, have been extensively used to investigate fire activity, crop yields, production, and phenology, and land use change detection. However, MODIS multi-day composites (8-day, 16-day) typically analyzed are insufficient to capture and resolve rapid changes in crop phenology (Zhao et al., 2009). Here we use daily active fire and surface reflectance data from MODIS to investigate trends in agricultural activity in Punjab. Specifically, we quantify the delays in post-monsoon agricultural fire activity and determine whether the seasonal cycle of monsoon to post-monsoon vegetation greenness reveals similar delays. We conclude with a discussion of the potential drivers of these interannual changes and an analysis of the consequences for regional air quality.

1.3 Data and Methods

1.3.1 Study region

The IGP is home to over 700 million people (Appendix A1.4), many of whom rely on agricultural productivity of the densely cropped belt of northern India and parts of Pakistan, Nepal, and Bangladesh for livelihood and food security. Relative to other double-cropped states in northern India, such as Haryana, Uttar Pradesh, and Bihar, Punjab has the highest rice-wheat productivity (Kumar et al., 2015) and is spatially more homogenous in terms of fire intensity (Figure 1.1a), rice-wheat yields, and topography (Azzari et al., 2017). Here we focus on Punjab during the post-monsoon rice residue burning season (defined here as September 20 to November 30), when fields are prepared for winter wheat sowing. To a lesser degree, we examine the pre-monsoon wheat residue burning season (April 1 to May 31), when fields are prepared for monsoon rice sowing (Figure 1.1b).

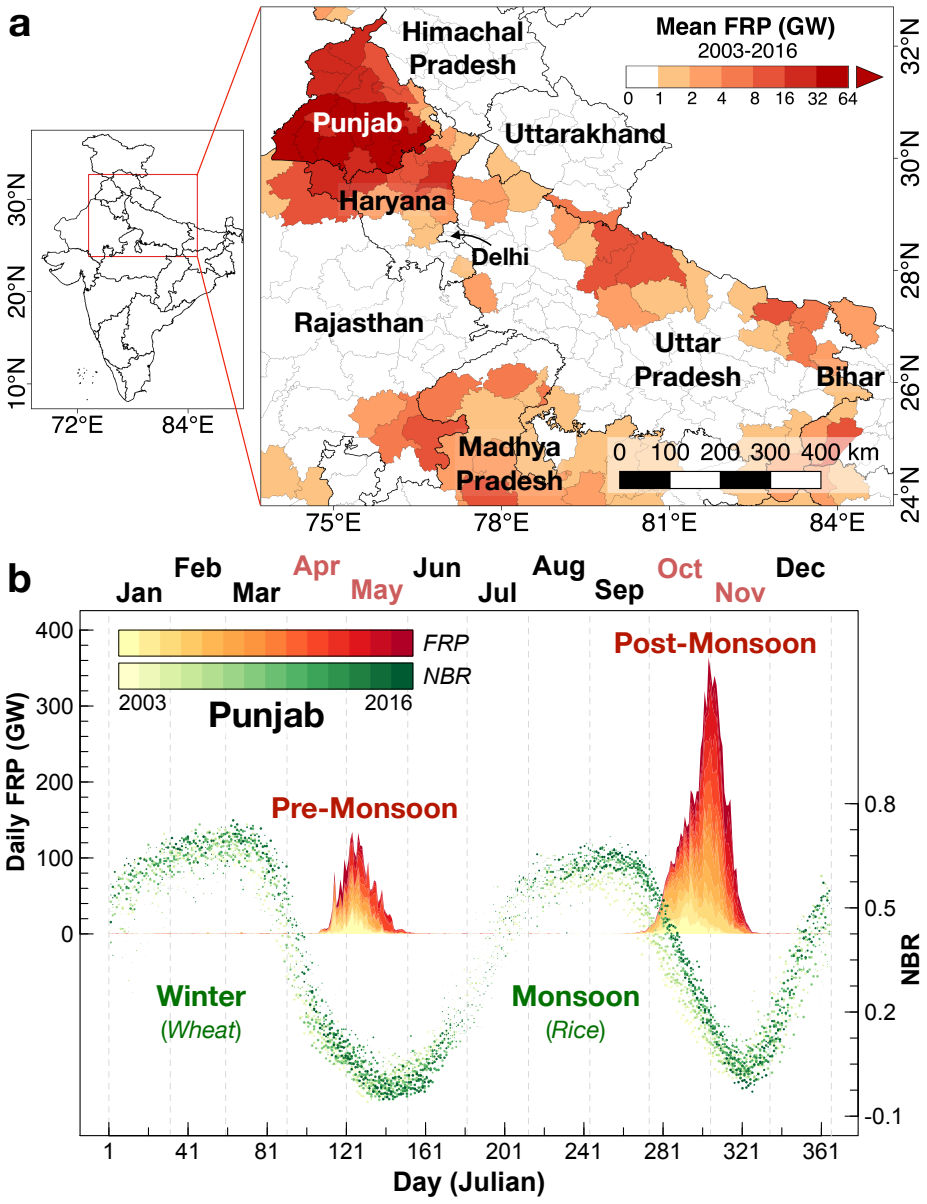


Figure 1.1: Cycles of fire activity and vegetation greenness in Punjab, India. District-level maps of (a) the Indo-Gangetic Plain (IGP) overlaid with annual agricultural MODIS Terra + Aqua Fire Radiative Power (GW), averaged over 2003-2016. Note that the increment of the color bar increases by a factor of 2. (b) Daily FRP (left axis) and median Normalized Burn Ratio (NBR; right axis) in Punjab. FRP values are stacked with earlier years on the bottom. The double-crop cycle indicated by NBR, a proxy for greenness, is predominantly a rice-wheat rotation. Pre-monsoon fires occur from April to May after the winter wheat growing season, and post-monsoon fires occur from October to November after the monsoon rice growing season.

1.3.2 Active fires and vegetation indices

For analysis of fire activity, we sum daily 1-km maximum Fire Radiative Power (FRP), a proxy for fire intensity, derived from MODIS/Terra and Aqua (MOD14A1/MYD14A1, Collection 6). We also compare FRP with MODIS-derived fire counts and burned area and MODIS-based fire emissions from the Global Fire Emissions Database, version 4 with small fires (GFEDv4s) (Table A.1). For analysis of vegetation greenness, we use daily 500-m MODIS/Terra surface reflectance (MOD09GA, Collection 6) to derive two vegetation indices, the Normalized Difference Vegetation Index (NDVI) and Normalized Burn Ratio (NBR):

$$NDVI = \frac{\rho_2 - \rho_1}{\rho_2 + \rho_1} \tag{1.1}$$

$$NBR = \frac{\rho_2 - \rho_7}{\rho_2 + \rho_7} \tag{1.2}$$

where ρ_i is the surface reflectance of MODIS band i. The wavelength range of the bands is as follows: 620-670 nm for band 1 (red), 841-876 nm for band 2 (near infrared), and 2105-2155 nm for band 7 (shortwave infrared). These active fire and surface reflectance datasets are described in more detail in Appendix A1.

1.3.3 Statistical analysis

We estimate linear trends with residuals bootstrapping. Unlike the linear regression t-test, which assumes that the residuals are normally distributed, bootstrapping preserves and resamples from the sample residuals distribution. To obtain a sample distribution, 1000 iterations are performed in which residuals are randomly sampled with replacement for each iteration and the dependent variable y re-fit using linear regression.

1.3.3.1 Characterizing the temporal progression of agricultural fires

We characterize the progression of the pre-monsoon and post-monsoon burning seasons, defined in Chapter 1.3.1, of each year in order to assess interannual temporal trends. First, let $X = \{x_t | x_1, x_2, x_3 ... x_n\}$ denote the daily time series of a fire metric, such as FRP, during a given burning season lasting n days. We define the pre-monsoon (April 1-May 31) and post-monsoon (September 20-November 30) burning seasons with broad windows in order to capture all possible seasonal fire activity. To derive the peak burning date, k_{peak}, we fit Gaussian density curves to X, thus smoothing potential noise in FRP due to inconsistencies in observing area caused by

cloud and haze cover:

$$g(t) = \gamma \cdot e^{0.5[\frac{t-u}{\sigma}]^2} \tag{1.3}$$

where $g(t)$ is the Gaussian function to be optimized, t is days of the burning season expressed as 1 to n total days, μ is the mean of t, σ is the standard deviation of t, and γ is an arbitrary scaling parameter. k_{peak} is the day t that corresponds to the maximum value of $g(t)$. We then use the optim function from the R *stats* package to minimize non-linear least squares of $g(t)$ and X and to estimate the μ, σ, and γ parameters that yield the optimal Gaussian fit. As first guesses of the three parameters for the *optim* function, we set σ to 7, γ to 1, and μ to our estimate of the midpoint of the burning season, $k_{midpoint,w}$. We estimate $k_{midpoint,w}$ using a simple weighted average approach. We weight t by x_t and take the average to obtain $k_{midpoint,w}$:

$$k_{midpoint,w} = \frac{\sum_{t=1}^{n} t \times x_t}{\sum_{t=1}^{n} x_t} \tag{1.4}$$

Following Zhang et al. (2014b), we also estimate the start, midpoint, and end of the pre-monsoon and post-monsoon burning seasons for each year. We define a sequence of partial sums, $Y = \{y_k | y_1, y_2, y_3 ... y_n\}$, in which $y_k = \sum_{t=1}^{k} x_t$. We normalize y_k by y_n, or the sum of FRP during the entire burning season. We then approximate k_β, or the first day when normalized Y has surpassed breakpoint β:

$$k_\beta = arg\,min_k\{(\frac{y_k}{y_n} - \beta) | (\frac{y_k}{y_n} - \beta) > 0\} \tag{1.5}$$

As in Zhang et al. (2014b), we define arbitrary breakpoints, β = 0.1, 0.5, and 0.9, to represent the start ($k_{\beta=0.1)}$ or k_{start}), midpoint ($k_{\beta=0.5}$ or $k_{midpoint}$), and end ($k_{\beta=0.9}$ or k_{end}), respectively, of the burning season.

1.3.3.2 Tracking crop phenology with NDVI and NBR

NDVI is widely used to characterize the cycling in vegetation growth, land cover change, and crop productivity (Yengoh et al., 2015; Justice et al., 1985). NBR, while typically used in burned area and burn severity classification (Key and Benson 2006), is analogous to NDVI, which relies on the visible red reflectance instead of the shortwave infrared (SWIR) reflectance. A major advantage of NBR is that compared to visible wavelengths, SWIR wavelengths can better discriminate between vegetation and bare soil (Chen et al., 2005; Asner & Lobell,

2000) and are less susceptible to atmospheric interference from smoke aerosols and thin clouds (Roy et al., 1999; Eva & Lambin, 1998; Avery & Berlin, 1992). Here we use NBR as a complement to NDVI to track crop phenology with variations in vegetation greenness.

We estimate the timing of crop maturation, or maximum greenness, during the monsoon growing season with both the daily median NDVI and NBR time series. Assuming that the seasonal progression in the crop cycle is similar across years, the timing of peak greenness in the growing season diagnoses the timing of the overall growing season. To estimate the timing of the maximum monsoon greenness with the noisy daily time series, we apply weighted cubic splines smoothing with bootstrapping on time steps within a defined window that straddles the day of monsoon peak greenness. Cubic splines smoothing stitches together piecewise third-order polynomial interpolation between "knots," or selected experimental points, and has been used extensively for crop phenology applications (Jain et al., 2013; Mondal et al., 2014, 2015; Jain et al., 2017). We apply weights to the NDVI and NBR time series using the daily fraction of "usable" pixels, or those uncontaminated by clouds or thick haze (hereafter referred to as usable fraction) in the study area. This weighting follows from our greater confidence in daily median NDVI and NBR on clearer days versus cloudier and/or hazier days. Prior to bootstrapping, we make initial guesses of the four local maxima and minima: monsoon and winter peak greenness and pre-monsoon and post-monsoon trough greenness. We use these initial guesses to center a window of 300 days. Using a smoothing parameter of 0.75, we smooth the vegetation index time series with weighted cubic splines within the defined window and estimate the bootstrapped mean timing of maximum NDVI or NBR for each year. We repeat this process to estimate the earliest date when fields are ready to sow the winter crop, or trough greenness, during the post-monsoon transition period.

1.3.4 Regional aerosol optical depth exceedances

To quantify enhancements in regional air quality degradation during the post-monsoon burning season, we use MODIS/Terra Deep Blue retrievals of aerosol optical depth (AOD) over Punjab, Haryana, Delhi, and western Uttar Pradesh (i.e., encompassing the aerosol source and downwind transport regions of the IGP) (Levy et al. 2013, Appendix A1.1.3). Previous studies have shown that during the post-monsoon burning season, AOD co-varies with FRP, visibility, and PM, thus indicating the level of surface air quality degradation across north India (Vadrevu et al., 2011; Kaskaoutis et al., 2014; Liu et al., 2018; Cusworth et al., 2018). In order to minimize the contribution of background AOD, we analyze regionally averaged AOD "exceedances" — that

is, the daily spatial mean of AOD increments above the mean AOD $+1\sigma$ for each pixel and season across Punjab, Haryana, Delhi, and western Uttar Pradesh. We analyze these daily mean AOD exceedances within the $k_{start}(FRP)$ and $k_{end}(FRP)$ window to isolate the effect of agricultural burning. To estimate the timing of peak AOD exceedances, or $k_{peak}(AOD)$, we apply Gaussian density curve optimization to values within this window expanded by two weeks. Such expansion ensures that the optimization is not thrown off by high AOD days isolated at the beginning or end of the season.

1.4 Results

1.4.1 Trends in seasonal agricultural fire activity

The bimodal distribution of peak agricultural fire activity in both pre-monsoon and post-monsoon periods is limited to northwestern India, primarily in Punjab, as well as northern Haryana (Figures 1.1, A.2). Generally, 80% of post-monsoon fires in Punjab are set within an approximate three-week window (23 ± 3 days) from mid-October to early November. We estimate that the timing of peak post-monsoon fire intensity has shifted later in Punjab by 1.17 days yr^{-1} (95% CI: [0.86, 1.49]), statistically significant at the 95% confidence interval (CI), indicating that the burning of rice residue has shifted later by over two weeks from 2003-2016 (Figure 1.2, Table A.2). The timing of the start, midpoint, and end of the post-monsoon fire has shifted by a similar magnitude of 13-17 days. These findings using MODIS FRP are corroborated by similar temporal and magnitude shifts in GFEDv4s fire emissions and MODIS fire counts and burned area (Table A.3). In contrast, we generally find no consistent statistically significant delays in the pre-monsoon burning season in Punjab (Table A.2).

Spatially, the post-monsoon temporal shift is larger in magnitude in districts in western Punjab than in eastern Punjab (Figure A.3). Moreover, the 14-year trends in total fire intensity for each 3-day block within this window signal a shift in the peak burning period, with decreasing FRP in mid-to-late October and increasing FRP in early November (Figure 1.2). The magnitude of peak post-monsoon fire activity, indicated by the maximum 3-day block sums of FRP, has more than doubled over the 14-year period, an increase that may be partly attributed to some homogenization in the timing of burning across districts.

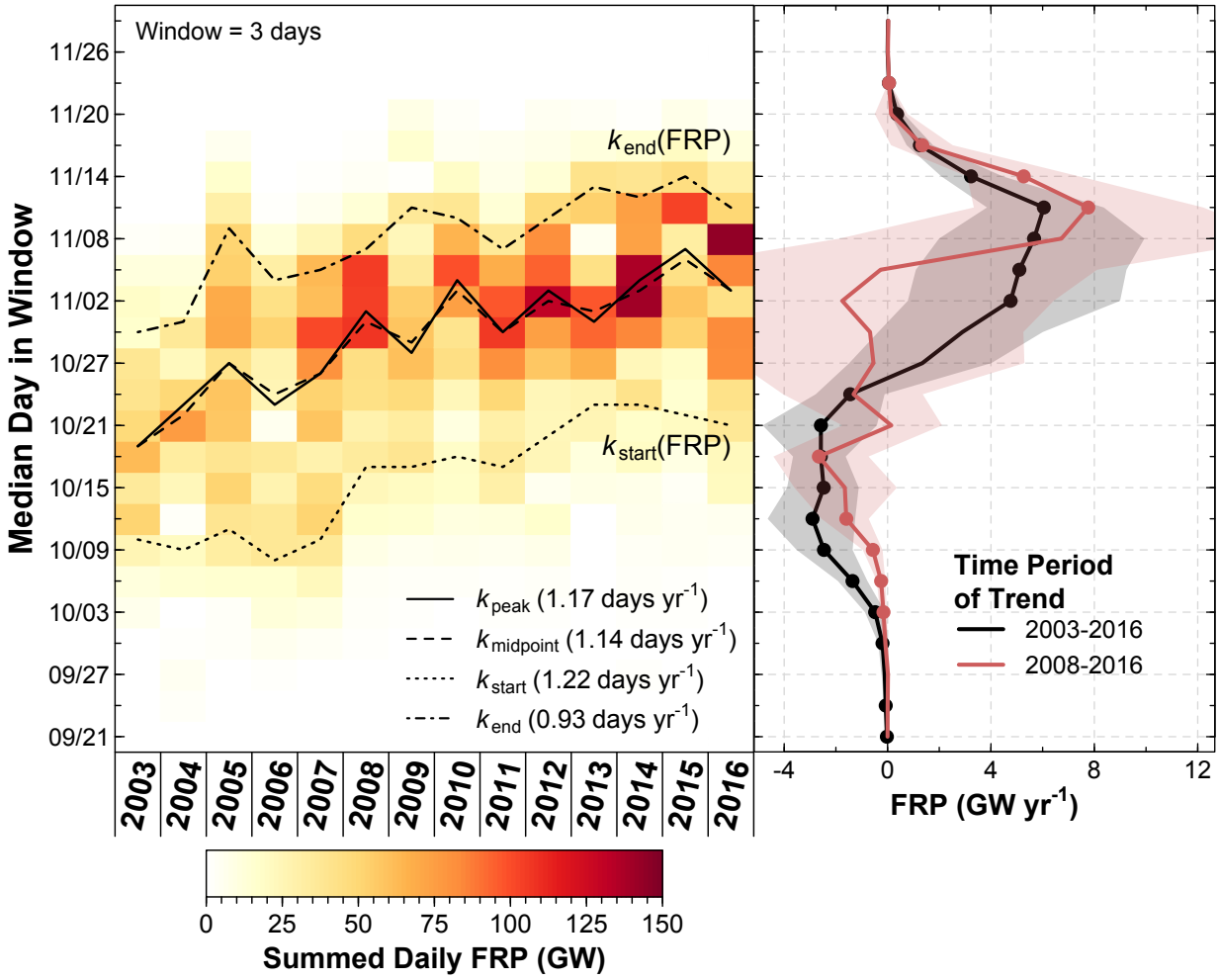


Figure 1.2: Temporal shifts in post-monsoon fires in Punjab from 2003-2016. (left) Each block represents the 3-day summed Fire Radiative Power (FRP). Dashed and solid lines represent the timing of the start, peak, midpoint, and end of the post-monsoon burning season, based on daily observations of FRP. Text inset in the left panel shows the linear trends in the $k_{start}(FRP)$, $k_{peak}(FRP)$, $k_{midpoint}(FRP)$, and $k_{end}(FRP)$; all trends shown are statistically significant at the 95% confidence level. (right) Trends in summed FRP (GW yr^{-1}) for each 3-day block window from September 20 to November 30 for the 2003-2016 (black line) and 2008-2016 time periods (red line). The shaded envelopes denote the 95% confidence interval, and dots represent statistically significant increases or decreases in 3-day block FRP.

1.4.2 Trends in vegetation greenness from monsoon to post-monsoon

We also examine whether vegetation greenness in Punjab show similar shifts during the monsoon growing season and post-monsoon harvest-to-sowing transition period. Whereas the timing of minimum NBR and NDVI occurs after near-completion of post-monsoon burning in mid-to-late November, the temporal maximum of these vegetation indices occurs near the end of the monsoon around late August or early September (Figure 1.1b), indicating crop maturation. In Punjab, the timing of maximum NDVI and NBR shows an overall delay of 11-15 days, with a large, abrupt shift of 7-9 days around 2008-09 (Figure 1.3a-b). Concurrently, there is an evident increasing trend in maximum monsoon NBR (0.06 decade^{-1}, 95% CI: [0.04, 0.08]) and NDVI (0.07 decade^{-1}, 95% CI: [0.05, 0.09]), consistent with steady increases in annual total kharif rice production in Punjab of 0.13 Tg yr^{-1} (95% CI: [0.09, 0.17]) (Figures 1.3b, A.5, Table A.5). Such increases in peak NBR and NDVI also suggest greater quantities of crop residue, which may lead to amplified fire intensity and emissions. In contrast to the shift in maximum NBR and NDVI, we find a smaller delay of 4-6 days in the timing of the minimum values of these indices during post-monsoon (Figure 1.3c-d, Table A.5), indicating that the shift in the monsoon growing season is greater than the corresponding shift in the timing of the earliest date when fields are ready for winter wheat sowing. In addition, we find that the duration from the start of the burning season to trough post-monsoon greenness has decreased by 0.71 days yr^{-1} (95% CI: [-1.02, -0.39]), providing evidence for a shortened harvest-to-sowing period (Figure A.6). Taken together, our results suggest that the temporal shifts in post-monsoon burning are likely associated with later sowing and harvesting of the monsoon crop.

1.4.2.1 The utility of NBR as a vegetation index

We have so far considered NBR and NDVI as complementary vegetation indices. Here we further demonstrate the utility of NBR for tracking crop phenology, particularly in resolving the troughs of the crop cycle. The weaker detrended correlations ($r = 0.23 \pm 0.39$) between the two vegetation indices during transition months between the kharif and rabi seasons (May, June, October, and November) compared to other months ($r = 0.88 \pm 0.12$) support the notion that NDVI more poorly resolves and tends to "flatten" the troughs of the double-crop cycle curve (Figure A.7). Moreover, the monthly distributions of detrended r(NDVI, NBR) values closely follow variations in greenness in the double-crop cycle, with greater correlation during seasons of crop growth. This pattern of correlation suggests that the performance of NDVI depends on the level of greenness in-field and

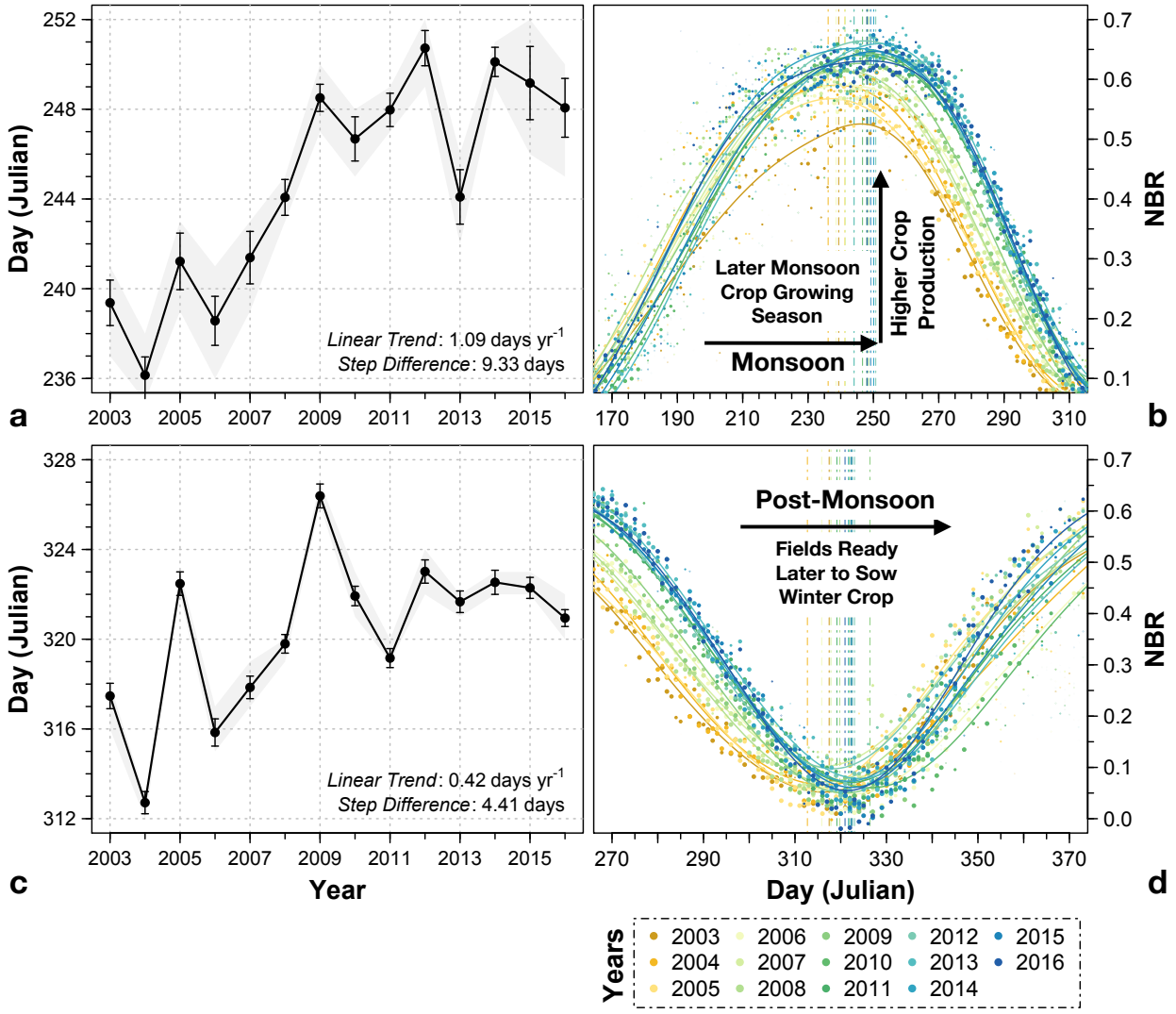


Figure 1.3: Trends in monsoon peak greenness and post-monsoon trough greenness in Punjab from 2003-2016. Bootstrapped mean maximum NBR during the (a) monsoon crop growing season and (c) post-monsoon harvest season, from 2003-2016. Error bars show one σ uncertainty, and shaded gray envelopes denote the 95% confidence interval. Text inset shows the bootstrapped linear trend in the timing of (a) maximum monsoon greenness and (c) minimum post-monsoon greenness from 2003-2016 and mean step difference between the 2003-2007 and 2008-2016 time periods. Daily median NBR during the (b) monsoon crop growing season and (d) post-monsoon harvest season, with lines showing the weighted parabola smoothing. Different colors denote different years. The bootstrapped mean day of (b) maximum monsoon greenness and (d) minimum post-monsoon greenness of each year is shown by vertical dashed-dot lines.

that NDVI values at or near-minimum greenness should be interpreted with caution. However, without further investigation, the noisiness and saturation of NDVI should not be generalized to all other vegetation indices that rely partly on visible bands, including the Enhanced Vegetation Index (EVI) and Soil-Adjusted Vegetation Index (SAVI).

1.4.3 Trends in post-monsoon regional aerosol optical depth

To quantify the consequences of the delays in post-monsoon agricultural fire activity for regional air quality, we assess AOD exceedances during the main burning period bounded by $k_{start}(FRP)$ and $k_{end}(FRP)$. Within this window, post-monsoon AOD exceedances have increased by 55% from 2003-2016, likely associated with the reported upward trend in fire intensity (Figure 1.4). Similar to the magnitude of the delay in $k_{peak}(FRP)$, the timing of the peak in AOD, $k_{peak}(AOD)$, has shifted by 0.8 days yr^{-1} (95% CI: [0.47, 1.13]), or ~11 days during the 14-year period. The delay and increase in post-monsoon agricultural fire activity appear to drive the coherent shifting pattern in heavy aerosol loading episodes (higher AOD exceedances), notably observed in early November after 2008, despite the variability in AOD impacted by meteorology and other pollution sources, such as fireworks during the Diwali festival. Diwali lasts several days, and its timing is highly variable from year to year (October-November), following the lunar calendar. On average, the absolute difference between the timing of Diwali and the peak post-monsoon burning date is 7 days, with a range of 1-20 days (Figure A.4). While Diwali fireworks, concentrated over dense population centers, can severely exacerbate urban pollution for a few days, crop residue burning contributes to widespread regional pollution for weeks (Mukherjee et al., 2020; Ojha et al., 2020).

1.5 Discussion

1.5.1 Implications of delays in post-monsoon fire activity

We find that the peak fire intensity of the post-monsoon burning season in Punjab has shifted later in time by over two weeks from 2003 to 2016, with a 42% increase in overall fire intensity. This delay is gradual, likely influenced by steady increases in crop production and mechanization, which yield higher amounts of excess crop residue. We hypothesize that a shortened harvest-to-sowing turnaround time after *kharif* rice harvests has amplified this increase by making it difficult for farmers to prepare fields for timely sowing of *rabi* wheat. The optimal

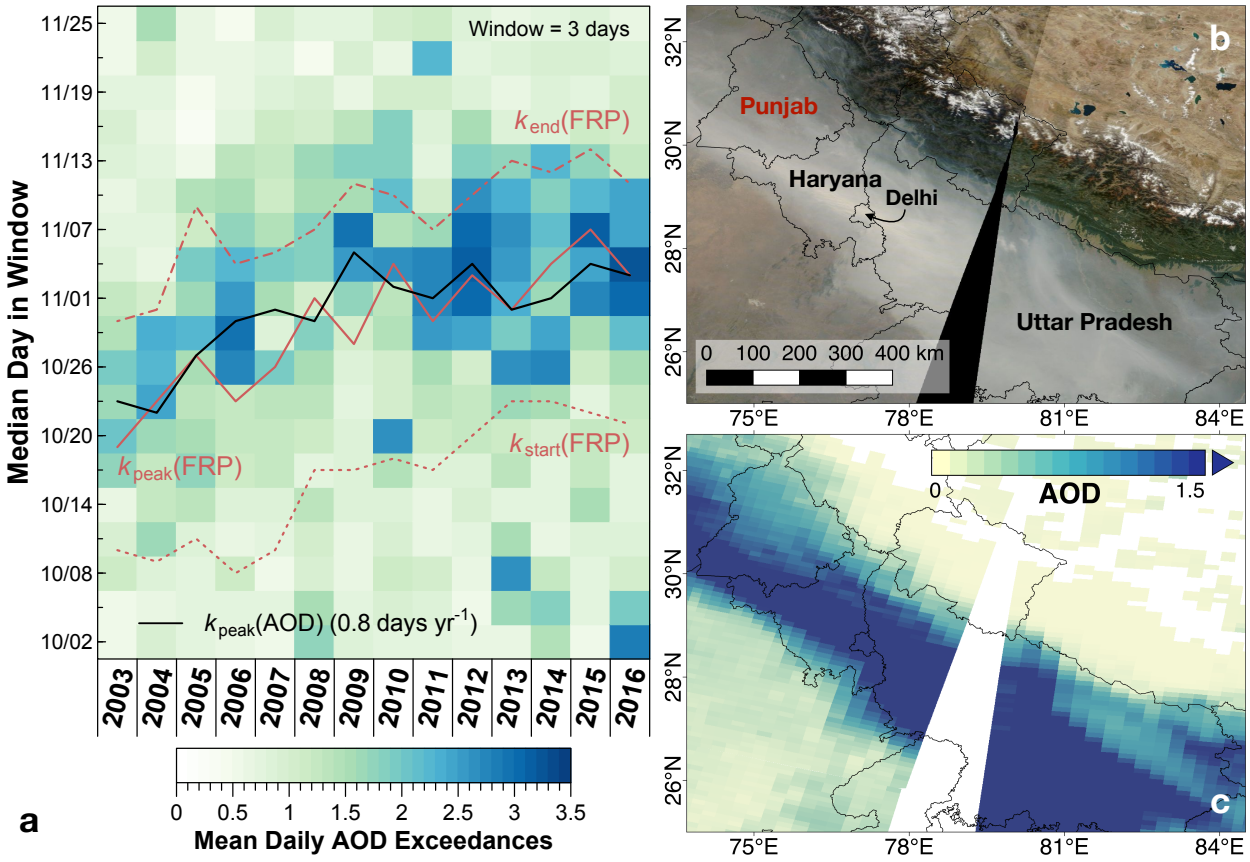


Figure 1.4: Trend in the timing of peak post-monsoon AOD over the western Indo-Gangetic Plain from 2003-2016. (a) Each block represents the 3-day average of regional aerosol optical depth (AOD) exceedances from the MODIS/Terra Deep Blue retrieval algorithm over Punjab, Haryana, Delhi, and western Uttar Pradesh. Here exceedances are defined as the spatially averaged AOD increments above the mean AOD + 1σ for each season and pixel. The black line shows the timing of peak daily AOD exceedances. The red lines represent the timing of the start, peak, and end of the post-monsoon burning season, based on daily FRP (same as in Figure 1.2). The text inset shows the linear trend in the $k_{peak}(AOD)$, statistically significant at the 95% confidence level. Example of thick haze over the western IGP on November 6, 2016, as observed by MODIS/Terra, shown as (b) true color (NASA/Worldview; https://worldview.earthdata.nasa.gov/) and (c) Deep Blue AOD at 550 nm from the MOD04_L2 product.

time to sow wheat in Punjab is late October to early November (Balwinder-Singh et al., 2016; Liu et al., 2019), yet co-occurring post-monsoon fires indicate that fields are often not ready at this time, particularly in recent years. Since fire is a quick and cheap method to remove the leftover residue generated by combine harvesters, farmers may have even greater incentive to burn crop residue, especially if harvests are delayed past the optimal date to sow wheat. Consistent with this hypothesis, we find that high fire intensity days preferentially occur during the latter half of the fire season, when the optimal window for sowing is shrinking. As post-monsoon fires increase in response to mechanization and pressures to sow on time, the burning season gradually trends later, further compressing the harvest-to-sowing window and increasing fire intensity rates. As a result, winter wheat sow dates across the region will likely homogenize, collapsing around a small optimal window to mitigate crop losses from increasing temperatures from February to March (Lobell et al., 2012).

Additionally, we estimate a 55% increase in regional AOD exceedances and ~11-day delay in the timing of peak AOD within the post-monsoon burning period from 2003-2016. Delays in the post-monsoon burning season also suggest that high fire activity periods may increasingly coincide with late-autumn/winter meteorological conditions that favor severe fog/smog and haze events across the IGP (Dey, 2018). Dense fog formation peaks in winter (December to January) over the IGP (Dey, 2018; Gautam & Singh, 2018; Ghude et al., 2017), but in recent years there appears to be an increasing tendency in dense fog episodes observed earlier in November, coinciding with the buildup of intense smoke associated with crop residue burning activity (Figure A.8). Further analysis of the long-term trends in meteorological conditions that are conducive to fog, such as western disturbances (Gautam et al., 2007), is prerequisite to assessing possible feedbacks between meteorology and smoke from late October to November. Aside from increasing exposure to high regional PM concentrations both locally and in urban centers downwind, crop residue burning depletes soil moisture and decreases roadside visibility (Kumar et al., 2015; Badarinath et al., 2006; Sidhu et al., 2015; Sinha et al., 2015). In spite of bans, such burning continues to persist and gain traction (Tallis et al., 2017). New technology that simultaneously reuses crop residue as mulch cover and incorporates seeds into the bare soil has been tested as an alternative to slash-and-burn methods of managing crop residue (Sidhu et al., 2015; Tallis et al., 2017; Shyamsundar et al., 2019).

1.5.2 Potential drivers of delays in the rice-wheat rotation

Delays in the post-monsoon burning season are consistent with such shifts in the timing of monsoon peak greenness (11-15 days) and post-monsoon trough greenness (4-6 days), though the latter is of lesser magnitude. Unlike

the steady shifts seen in post-monsoon burning, an abrupt delay of roughly one week occurring around 2008-09 dominates the overall delay in the timing of monsoon peak greenness, with relatively little change thereafter. Abrupt delays of similar magnitude are also apparent in the timing of the start of the post-monsoon burning season. Here we consider whether policy changes implemented around this time may have contributed toward these abrupt shifts. In 2009, in order to counteract severe groundwater depletion driven by low monsoon rainfall and widespread agricultural intensification, the Government of Punjab enacted the "Preservation of Sub-Soil Water Act" (ordinance in 2008), which prohibits sowing rice nurseries before May 10 and transplanting the resulting rice seedlings to flooded paddies before June 10 (Ramanathan et al., 2005; Asoka et al., 2017; Singh, 2009; Tripathi et al., 2016). The Act delays the onset of water-intensive agricultural practices that would otherwise coincide with warm temperatures and high pre-monsoon evapotranspiration rates, which lead to excessive usage of the groundwater supply from tube wells and other reservoirs (Humphreys et al., 2010).

Another policy that could be related to the shift is the 2008 all-India implementation of the Mahatma Gandhi National Rural Employment Guarantee Act (MGNREGA), a measure that provides a social security net to rural workers (Reddy et al., 2014) and may have decreased the seasonal migration of workers to Punjab and led to labor shortages there (Singh, 2009). Such shortages may have delayed the sowing of rice and incentivized use of combine harvesters, which may in turn explain the increase in crop residue burning. However, the already widespread transition to mechanized harvesting in Punjab, with diminishing dependence on manual labor, suggests that MGNREGA may have had a smaller impact on the timing of harvest and burning. Finally, variations in the timing of monsoon onset and withdrawal may be partly responsible for the interannual variability in these observed shifts, such as the early monsoon onset and rice maturation in 2013, but do not appear to drive the overall one-week delay in peak monsoon greenness from the 2003-2007 to 2008-2016 time periods (Figure A.9). It is important to note that here we do not establish direct causality with the groundwater policy, MGNREGA, or monsoon rainfall variability, but suggest a relationship that needs to be further explored in the field. Figure A.10 summarizes the potential drivers and implications of the delay in and amplification of post-monsoon fire activity associated with double-crop cycle. Although this study focuses on Punjab, similar temporal shifts may have also occurred in adjoining states, such as Haryana, that experienced both severe groundwater depletion and increases in rice production and post-monsoon fire activity (Asoka et al., 2017; Jethva et al., 2019; Balwinder-Singh et al., 2019).

1.6 Conclusion

In summary, we show robust, statistically significant temporal shifts of over two weeks in the timing of peak fire activity during the post-monsoon burning period in Punjab over a 14-year period from 2003-2016, and smaller delays of 11-15 days in monsoon peak greenness and 4-6 days in post-monsoon trough greenness. We estimate the timing of peak FRP and regional AOD exceedances by optimizing the Gaussian mean and the start, mid-point, and end of the burning season by using the partial sums of FRP. We further demonstrate the viability and applicability of using daily MODIS surface reflectance to characterize crop cycles and the utility of NBR as a useful complement to NDVI for quantifying these vegetation changes. We hypothesize that while the gradual delays in the post-monsoon burning season are likely linked to agricultural intensification and increasing mechanization, the abrupt delay of one week around 2008-09 seen in the monsoon crop growing season appears to coincide with the state-wide groundwater policy. The unintended consequences of these temporal shifts in the double-crop cycle may be severe. First, a shortened harvest-to-sowing period may further encourage farmers to burn crop residues in order to sow winter wheat on time. Second, the timing of peak crop residue burning may increasingly coincide with winter meteorology that favors severe smog events downwind across the IGP, where we diagnose a 55% increase in AOD exceedances, defined as the increment of AOD above the mean $+1\sigma$, over 2003-2016. For Punjab, alternative technology that combines the co-benefits of incorporating wheat seeds with rice residue and eliminating the need to burn residue, as well as switching to less water-intensive and stubble-producing crops, may alleviate the double bind of having to conserve groundwater while reducing public health exposure to smoke from post-monsoon fires.

2

Crop residue burning practices across north India inferred from household survey data: bridging gaps in satellite observations

2.1 Abstract

In north India, agricultural burning adversely affects local and regional air quality during the post-monsoon season (October to November), when the prevailing meteorology is favorable for smog and haze formation. Quantifying the contribution of smoke to air pollution in this region, however, is challenging. While the Moderate Resolution Imaging Spectroradiometer (MODIS), aboard NASA's Terra and Aqua satellites, provides a nearly 20-year record of global fire activity, the sensor cannot adequately capture small, short-lasting agricultural fires due to its moderate spatial resolution (500 m to 1 km) and limited overpasses (twice daily for each satellite), as well as the hazy conditions that typically obscure the north India land surface at this time of year. Moreover, current global fire emissions inventories based on MODIS observations can differ by up to an order of magnitude in this region. Here we incorporate household survey data to bridge gaps in MODIS observations and improve estimates of fire emissions over the states of Punjab, Haryana, Uttar Pradesh, and Bihar during the 2003-2018 post-monsoon burning seasons. We develop a novel method that adjusts MODIS Fire Radiative Power (FRP) for: (1) small fires detected by the Visible Infrared Imaging Radiometer Suite (VIIRS) at 375-m spatial resolution, (2) cloud/haze gaps in satellite observations, (3) partial-field burning practices, and (4) the diurnal cycle of fire activity. Adjusting FRP for the fire diurnal cycle yields the largest boost to emissions due to the short lifetime of the fires (~1/2 hour) and the brief windows of satellite detection. Using adjusted FRP, we estimate on average

10.4 ± 3 Tg dry matter (DM) burned each year, yielding emissions of 65 ± 18 Gg organic carbon (OC), 5.6 ± 1.6 Gg black carbon (BC), 791 ± 225 Gg CO, and 14.9 ± 4.2 Tg CO_2. On average, our OC+BC emissions are 3.4 times (min: 0.6, max: 6.6) the estimates from five widely used global fire emissions inventories. Our estimate for Punjab, which contributes more than two-thirds of emissions in the region, is consistent with our bottom-up validation, which uses burn rates from the household survey and government crop production statistics in 2016 and 2017. We spatially disaggregate the state-level emissions to construct a gridded inventory at daily, 0.25° x 0.25° resolution over north India from 2003-2018. The inventory, SAGE-IGP (Survey Constraints on FRP-based Agricultural Fire Emissions in the Indo-Gangetic Plain), improves modeling assessments of air quality impacts from agricultural burning, thus supporting effective policy development.

2.2 Introduction

Agricultural fires are an important seasonal source of outdoor emissions that degrade air quality in north India (Cusworth et al., 2018; Liu et al., 2018; Vadrevu et al., 2011). The gases and aerosols released by open fires not only degrade regional air quality and increase risk to acute respiratory infection and other lung and cardiac diseases (Bikkina et al., 2019; Chakrabarti et al., 2019), but may also damage crops due to elevated surface ozone exposure (Burney & Ramanathan, 2014; Ghude et al., 2016; Sinha et al., 2015). Despite the health and environmental hazards of emissions from these fires, standard estimates can differ by an order of magnitude (Liu et al., 2019), depending on the species and year. Here we diagnose the key reasons for the differences among existing emission inventories and provide an improved inventory constrained by on-the-ground survey data and additional satellite observations.

The practice of agricultural burning in north India gained traction with the rise of combine harvester use in the mid-to-late 1980s (Badarinath et al., 2006; Liu et al., 2019). Mechanical harvesting generates abundant root-bound and loose crop residues that are difficult to manage manually, and steady increases in crop production have added to the volume of excess residues. For many farmers, burning is a convenient, cost-effective method to remove crop residues and quickly transition between the monsoon (*kharif*) and winter (*rabi*) crops; observations of active fires and burned area shows increases of ~40-142% from 2003-2016 in the western Indo-Gangetic Plain (IGP) (Liu et al., 2019, 2021a). Both satellites and ground-based monitors have detected enhanced aerosol loading downwind of smoke plumes from agricultural fires across north India in recent years (Badarinath et al., 2009; Jethva et al., 2018; Kaskaoutis et al., 2014; Liu et al., 2018; Sarkar et al., 2018). Recent bans and intervention ef-

forts, such as Happy Seeder technology, aim to reduce post-monsoon fires (Shyamsundar et al., 2019; Sidhu et al., 2015; Tallis et al., 2017).

Much of the focus in the literature so far has been on agricultural fires in Punjab and Haryana, two northern states that account for over 90% of post-monsoon fire intensity in India (Liu et al., 2021a; Sarkar et al., 2018; Vadrevu et al., 2013). Less is known about burning practices elsewhere in north India, such as Uttar Pradesh (UP) and Bihar, where many farmers also follow a rice-wheat rotation (Singh et al., 2011). This study examines crop residue burning practices in four states: Punjab, Haryana, UP, and Bihar. One difficulty in monitoring agricultural fires in this region is the coarse spatio-temporal resolution of satellite measurements (Liu et al., 2019). The small size and duration of the fires, as well as increasing haziness from the smoke itself, also complicate interpretation of satellite observations (Cusworth et al., 2018; Liu et al., 2019; Thumaty et al., 2015). These challenges may lead to gross underestimation of fire emissions driving atmospheric models (Cusworth et al., 2018; Dekker et al., 2019; Lasko et al., 2017). To date, models have relied on global fire emissions inventories due to the lack of inventories specific to India, but these emissions estimates, including those for aerosols, in the global inventories can differ by an order of magnitude (Liu et al., 2019). Here we use survey data to help constrain satellite-based estimates by filling observational gaps.

In this study, we use on-the-ground survey data to help constrain satellite-based estimates and provide greater clarity on the magnitude of fire emissions and their impact on air quality downwind. We also seek to better understand the drivers, consequences, and farmer perceptions of crop residue burning across north India. We develop a FRP-based approach incorporating satellite and household survey data to adjust state-level MODIS FRP for small fires from VIIRS, cloud/haze gaps in satellite observations, partial-field burns, and the diurnal cycle in fire activity. We validate our FRP-based estimates using survey burn rates, government statistics on crop production, and fuel-related factors from the literature. Finally, we spatially disaggregate total dry matter (DM) burned to construct a daily, gridded 0.25° x 0.25° emissions inventory for Punjab, Haryana, UP, and Bihar from 2003-2018. Our regional inventory, SAGE-IGP, can be used to update agricultural emissions in north India in existing global inventories for use in atmospheric modeling studies, thus bolstering confidence in assessments of the burden of smoke from agricultural fires on air quality metrics downwind.

2.3 Data and Methods

2.3.1 Study region

Many agricultural regions across the Indian IGP are double-cropped with a rice-wheat rotation, which is critical to the food security and livelihood of over 400 million inhabitants across north India (Kumar et al., 2015). In this study, we focus on four states in north India: Punjab, Haryana, UP, and Bihar (Figure 2.1a). Punjab and Haryana, the western IGP states and "breadbasket" of India, have rice yields ~1.5 times those of UP and Bihar (Palanisami et al., 2019).

2.3.2 Household survey

In a household survey in 2017, we asked over 2000 farmers in the four target states about agricultural practices pertaining to rice harvests and rice residue burning for the 2016-17 growing season. For each village, we used a stratified purposive sampling technique to select a subset of 20 households that represent the village-level distribution of landholding sizes and social classes (Palinkas et al., 2015). We hired two survey teams to conduct the surveys on a mobile-based application in Hindi (Haryana, UP, and Bihar) and Punjabi (Punjab). In particular, we asked farmers about the method of harvesting rice (mechanical or manual) and subsequent burning of rice residues (Table B.1). In 2018, we repeated the survey with 90% of the same participants for the 2017-18 growing season and expanded our list of questions to determine the farmers' primary reasons for crop residue burning, as well as details on their burning practices: (1) start year of burning, (2) method of burning (complete or partial burn of field), (3) time of day for burning, (4) wait time (in days) from harvest to burning, and (5) reasons for burning. More details about the household survey are provided in Appendix B.1.

2.3.3 Satellite datasets

We use the MODIS Collection 6 gridded products for active fires (MOD14A1/MYD14A1, 1 km), surface reflectance (MOD09GA/MYD09GA, 500 m), and land cover (MCD12Q1, 500 m), all available from the Google Earth Engine platform (Gorelick et al., 2017), to derive daily fire intensity and surface reflectance in agricultural regions across the IGP (Table B.6) (Andela et al., 2019; Giglio et al., 2009, 2018; Sulla-Menashe et al., 2019). We also use the higher spatial resolution active fire product (VNP14IMGML, 375m) from the Visible Infrared Imag-

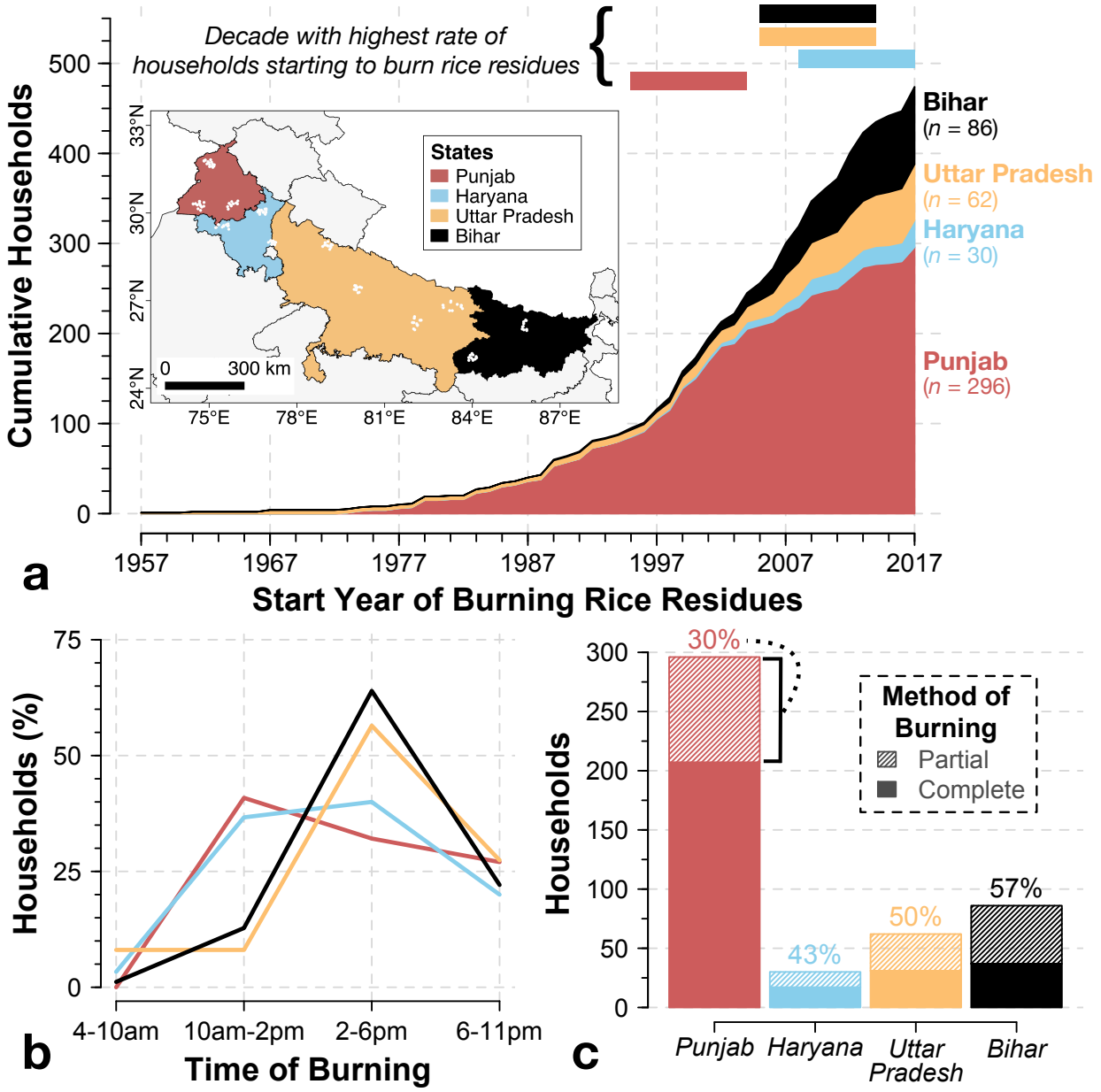


Figure 2.1: Temporal and methodological characteristics of rice residue burning across the Indo-Gangetic Plain, inferred from household survey data for the 2017-18 growing season: (a) Cumulative distribution of number of households burning rice residues, ordered by start year of burning with stacked contours representing contributions of four different states. The colored bars at top denote the 10-yr period for each state with the highest rate of households starting to burn rice residues. White dots in inset panel show the locations of surveyed households that harvested rice in the four states (Punjab, Haryana, Uttar Pradesh, and Bihar). (b) Diurnal cycle of rice residue burning from early morning to late night, color coded by state. (c) Method of burning rice residues, separated into complete and partial burning of fields. Percentages represent the fraction of households that use partial burning.

ing Radiometer Suite (VIIRS), aboard the Suomi Near-Polar Orbiting Partnership (S-NPP) and available from 2012 (Schroeder et al., 2014). Our workflow relies on the cloud-computing platform, Google Earth Engine, and the datasets available in its public data catalog (Gorelick et al., 2017).

As our fire metric, we rely on the daily maximum Fire Radiative Power (FRP), a proxy for fire intensity. The Fire Radiative Energy (FRE), or the time integral of FRP, scales linearly to dry matter burned (Wooster et al., 2005).

Following Zhang et al. (2014b) and Liu et al. (2021a), we estimate the start, midpoint, and end of the cumulative FRP during each post-monsoon burning season from 2003-2018:

$$\begin{aligned} k_\beta &= arg\ min_k\{(\tfrac{\hat{y}_k}{\hat{y}_n} - \beta)|(\tfrac{\hat{y}_k}{\hat{y}_n} - \beta) > 0\} \\ &\{k = k \in N\,|\,1 \leq k \leq n\} \end{aligned} \tag{2.1}$$

where $\hat{y}_k$ is the sigmoid-smoothed partial sums of the sequence of daily FRP over day 1 to k, n is the total number of days in the burning season, and k_β is the first day by when $\hat{y}_k$, normalized by the seasonal sum of FRP $\hat{y}_n$, has surpassed breakpoint β. We take β = 0.1, 0.5, and 0.9 to represent the start, midpoint, and end, respectively, of the burning season. Unlike Liu et al. (2021a), here we test the effect of sigmoid smoothing on estimating k_β and its trends (Zhang et al., 2014b). Zhang et al. (2014b) found that the sigmoidal function well represents the cumulative biomass consumed by fire. For sigmoid smoothing, we use the nonlinear squares *nls* function in the R stats package to fit a sigmoidal curve to the partial sums of FRP:

$$\hat{y}_k = 1/[1 + e^{a+bt}] \tag{2.2}$$

where a and b are shape parameters to be optimized and t is a sequence from 1 to n representing days in the burning season.

2.3.4 Statistical adjustments of agricultural fire emissions using satellite and survey data

Liu et al. (2019) found that MODIS cannot capture > 75% of small, short-lasting fires in Punjab and Haryana. While that study developed a hybrid MODIS-Landsat algorithm (ModL2T) to improve the spatial allocation of burned area (BA) and BA-based fire emissions, the low temporal resolution of Landsat (every 16 days) and the

possible conflation of harvested area and burned area suggests that FRP-based algorithms may enable fire emissions estimates at finer temporal resolution and with lower commission errors (Vadrevu & Lasko, 2018). Here we first derive daily state-level post-monsoon fire emissions from 2003-2018 for Punjab, Haryana, UP, and Bihar from MODIS FRP (Chapter 2.3.4.1-2.3.4.2). Then, we disaggregate the state-level emissions to a gridded, 0.25° x 0.25° inventory (Chapter 2.3.4.3). We estimate emissions by state first rather than by grid cell to limit inconsistencies between neighboring grid cells and for computational efficiency. A reconstruction of long-term fire activity from 2003-2018 is valuable for assessments of air quality trends and to compare our regional inventory with global fire inventories, which generally start from 2003 at daily scale.

2.3.4.1 Adjustment of FRP based on survey data and additional satellite observations

Using both satellite and household survey data, we adjust the MODIS FRP to account for small fires, cloud/haze gaps, partial burning, and limited satellite overpasses. For each state and year, we derive an adjusted daily FRP timeseries over a 4-month period, September to December. This extended study period for post-monsoon fires allows us to accommodate the different timing of each state's fire season and to ensure stability in smoothing FRP timeseries. Figure 2.2 shows the graphical depiction of each step detailed below.

1. **MODIS observations of FRP.** We first sum daily MODIS Terra and Aqua FRP during each post-monsoon burning season and over each state. This step assumes that the agricultural fires in this region are short-lived (~ 1/2 hour), following Thumaty et al. (2015), and that the instruments detect different fires at the overpass times, Terra at 10:30 a.m. and Aqua at 1:30 p.m. at the equator. Here we use the maximum FRP from the MOD/MYD14A1 gridded active fire product and apply an agricultural mask derived from MCD12Q1 to ensure that only cropland fires are considered and conservatively exclude FRP in intermixed land covers. We adjust Terra and Aqua FRP separately for Steps 2-3 but sum the adjusted Terra and Aqua FRP at the end of Step 3.

2. **Use of VIIRS observations for small fires.** Next, we incorporate the FRP observations from VIIRS, which at 375 m has a finer spatial resolution than the MODIS products (1 km) and so can more accurately capture fine-scale fire activity than MODIS. To account for these missing small fires, we diagnose those VIIRS active fires that do not intersect with MODIS/Aqua active fires within a 1-km buffer and then add VIIRS FRP of these fires to MODIS/Aqua FRP. We use only MODIS/Aqua FRP because VIIRS does not observe active fires during the Terra overpass. Because VIIRS observations are available only from 2012, we derive the incremental VIIRS

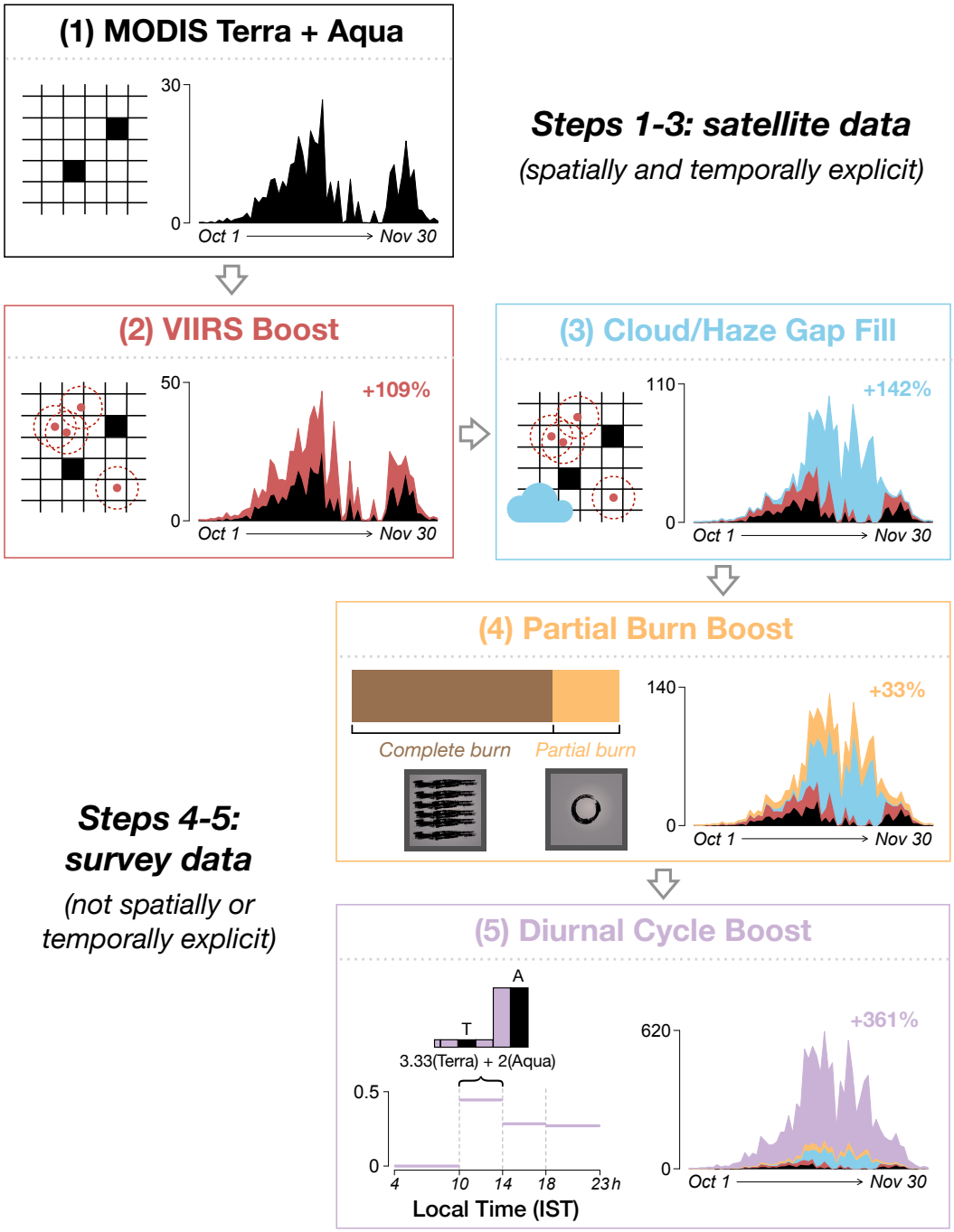


Figure 2.2: Pictorial flowchart for FRP adjustments using satellite and survey data for Punjab in the sample year 2017: The units for the daily FRP timeseries is GW. Percentages denote the FRP increase relative to the previous step. Checkerboards in Steps 1-3 denote a 1-km grid with MODIS FRP observations in black, VIIRS hotspots with a 1-km buffer in red, and clouds/haze cover in blue. Squares in Step 4 show the difference between complete versus partial burns, where black striations depict burning within the field. In Step 5, the plot on the left shows the diurnal cycle of fire activity, with horizontal lines showing the survey fractions (same as Figure 2.1b but weighted by landholding area) and vertical bars depicting our adjustment of mid-day satellite FRP. Detailed methods for each step are described in Chapter 2.3.4.1.

boost for 2003-2011 for the entire state by taking the average ratio of additional VIIRS FRP and MODIS/Aqua FRP over 2012-2018 and then scaling up the MODIS/Aqua FRP over the earlier years by that ratio. Assuming that the fraction of FRP missed by MODIS but detected by VIIRS is the same during the Terra and Aqua overpasses, we also boost MODIS/Terra FRP uniformly by the same ratio from 2003-2018 to account for missed small fires during the morning overpass.

3. **Filling in gaps of observed FRP due to clouds and haze.** The evolution of fire activity over the burning season as detected by MODIS is not smoothly varying but is instead characterized by dips or gaps in regional total FRP. Cusworth et al. (2018) suggest that this large day-to-day variability in active fire detections in north India is due in large part to clouds, haze, and/or smoke, occasionally obscuring the fire activity on the ground (Figure B.3). While MODIS and VIIRS routinely detect fires through thin haze by using thermal infrared bands (Giglio et al., 2016), the persistent, dense haze during peak fire days in north India can decrease brightness temperature over a broad region, thus interfering with detection of thermal signatures of small fires. Generally, agricultural fires are short-lasting, but temporally and spatially aggregating the fires in Punjab and Haryana reveals a Gaussian-like distribution (Jethva et al., 2019; Liu et al., 2021a). Taken together, many agricultural fires act like a large, long-lasting fire, and so we can track the influence of cloudy/hazy days as deviations from the expected Gaussian curve. To test this hypothesis, we check whether these dips or gaps in the summed FRP timeseries for each state correspond with MODIS observations of surface reflectance (MOD/MYD09GA) in the red visible band, ρ_1. As noted above, surface reflectance in this band is sensitive to clouds (Xiang et al., 2013) and so would be expected to anticorrelate with the area visible to satellites during the burning season. We extend this assumption to thick haze, which can be misclassified as cloud in this region and also obscure active fires from satellite detection (Cusworth et al., 2018). We then take advantage of ρ_1 measurements to gauge the extent to which clouds or haze interferes with fire detection, and we iteratively fill in the cloud/haze gaps in the statewide data for each fire season. Additional details on cloud/haze gap-filling procedure is described in Appendix B.3.2.

4. **Boosting FRP with survey data on partial field burning.** The survey data reveal that in the four states, 30-57% of farmers piled the loose crop residue in the center of the field before setting the residue on fire, resulting in partial burning of the field. Taking the practice into account has importance in constructing fire emission inventories for three reasons. First, the FRP from partial burns, which consume small, discrete areas, are much less likely to be observed from space than the FRP from fires that completely burn a field (Liu et al., 2019). Second, only loose residues are set on fire in partial burns, yielding less DM burned than in complete burns (Kumar

et al., 2015). Third, observations suggest that the emissions factor for $PM_{2.5}$ in partial burns, with respect to the mass of rice residue burned, is on average ∼1.92 times that for complete burns due to the incomplete, smoldering combustion of wetter residues (Lasko & Vadrevu, 2018).

To overcome these challenges, we assume as an upper bound that all partial fires have been missed by satellite detection (Liu et al., 2019). For each state, we boost the daily FRP by the partial-burn fraction derived from survey data and normalized by operational landholding area. To account for the lower mass of DM burned in partial burns, we also apply a scaling factor to the partial-burn FRP, since FRP is linearly proportional to DM burned (Wooster et al., 2005). Here we scale partial-burn FRP by 0.75, or the approximate fraction of total crop residues that are piled in the center of the field and burned. This factor assumes a rice plant height of ∼101 cm, of which 20-22 cm are left standing after harvest (Mahajan et al., 2009). Our resulting estimates of FRP from partial fires are then distributed uniformly in time across each burning season.

5. **Adjustment to take into account the diurnal cycle of fire activity.** The two satellites associated with MODIS each have one daytime overpass per day – Terra at 10:30 a.m. and Aqua at ∼1:30 p.m. local time at the equator. Typically, Aqua detects over five times as many fires as Terra in northwest India during the post-monsoon (Liu et al., 2019). These overpass times can miss the peak burning times of individual agricultural fires, which are small and short-lived, each lasting only about half an hour (Thumaty et al., 2015). Here we adjust the satellite-derived FRP to reflect those fires unseen by satellites. While GFEDv4s provides 3-hourly diurnal fractions of fire activity, they are extrapolated to other regions using geostationary observations over North and South America, aggregated by broad land cover types (Mu et al., 2011; van der Werf et al., 2017). We thus take advantage of the survey data to adjust the FRP captured by MODIS to reflect the diurnal variation of agricultural fire activity specific to north India. The survey responses are separated into four time periods: early morning (4-10 a.m.), mid-day (10 a.m.-2 p.m.), evening (2-6 p.m.), and late night (6-11 p.m.). For example, the survey data reveal that 8-41% of IGP farmers typically set fires between 10 a.m.-2 p.m., depending on the state. Additionally, the Terra and Aqua/S-NPP daytime overpasses only partly overlap with the mid-day burning window, assuming that all fires last half an hour. Accounting for variance in when satellites see each fire and how long each fire burns, we estimate that satellite-derived FRP captures just 45 minutes of fire activity per satellite over this 4-hr mid-day time interval (Figure B.5). The temporal distribution of active fire counts, binned at 15-minute intervals, for Terra and Aqua show that Terra peaks at ∼11:15 a.m. while Aqua peaks at ∼1:45 p.m. (Figure B.6). We extrapolate Terra FRP from 10:00 a.m. to 12:30 p.m., and Aqua FRP from 12:30-2 p.m. to match the survey's

4-hr mid-day window. Based on the fire duration and transition from Terra to Aqua at 12:30 p.m., we multiply Terra and Aqua FRP by a scaling factor of 3.33 and 2, respectively. We further adjust daily total FRP by assuming that all fires outside the mid-day window are undetected and by adding FRP increments according to the temporal distribution implied by the survey data. We weight these increments by the operational landholding area with reported burning in each time window.

As a post-processing step, we remove anomalous FRP spikes that often occur outside the burning season and are likely contaminated by false satellite detections. An anomalous day is tagged if its FRP exceeds three times the maximum FRP in a 2-day buffer window (5 days in total) and is above the 25th percentile of daily FRP from September-December of that year.

To account for agricultural fires that extend eastward from Haryana into the state of Rajasthan along the Ghaggar-Hakra River, we also include Ganganagar and Hanumangarh, two districts in north Rajasthan. We follow the same methods as described above but use survey data for Haryana for Steps 4-5.

2.3.4.2 Conversion to dry matter burned and emissions

For the final step in constructing our improved fire inventory, SAGE-IGP, we follow Kaiser et al. (2012) to convert FRP in each grid cell to dry matter burned and then to emissions for various chemical species, as is done in constructing the Global Fire Assimilation System (GFAS) emissions inventory:

$$E_i = FRE \times \alpha \times EF_i \tag{2.3}$$

where E_i is the emissions of species i (g species), FRE is the fire radiative energy (MJ), or the time integral of FRP, α is a conversion factor dependent on land use/land cover (kg DM MJ^{-1}) that yields DM burned, and E_i is the emissions factor for species i (g species kg^{-1} DM). To convert FRP to FRE, we multiply the adjusted daily FRP by the lifetime of the agricultural fires, which we assume to be 30 minutes, or 1.8×10^4 s day^{-1}, in this region (Thumaty et al., 2015). Following Kaiser et al. (2014) and Liu et al. (2015), we use a conversion factor α for agricultural fires of 0.41 kg MJ^{-1}.

To validate the DM burned derived from adjusted FRP, we focus on Punjab, which accounts for > 85% of MODIS-observed FRP during the post-monsoon in the study region. We use a bottom-up method, following Aalde et al. (2006), that involves burn rates from the household survey and government crop production esti-

Table 2.1: Parameters for estimates of agricultural fire emissions based on burned area, active fire area, and Fire Radiative Power (FRP).

Parameter	Description	Value	Units	Source
FRE	Fire Radiative Energy	*varies*	MJ	Derived from MODIS FRP
α	Conversion factor from FRE to dry matter burned	0.41	kg MJ^{-1}	Kaiser et al. (2014)
f_{burned}	Fraction of rice residues burned	*varies*	unitless	Derived from survey data
CP	Crop production (*rice*)	*varies*	kg	Indiastat
A	Area cultivated (*rice*)	*varies*	m^2	Indiastat
RC	Residue-to-crop ratio (*rice*)	1.4-1.8	unitless	Bouwman et al. (2000); Ravindranath et al. (2005); Jain et al. (2014)
f_{DM}	Mass fraction of dry matter burned from total rice production	0.82-0.88	unitless	Bouwman et al. (2000); Jain et al. (2014)
f_{CC}	Combustion completeness	0.89 (CB), 0.67 (PB)	unitless	Lasko & Vadrevu (2018)
EF	Emissions factor	e.g. 4.9 (OC), 0.42 (BC)	g species kg^{-1} DM	Andreae (2019)
	PB to CB ratio for aerosol-based emissions factors	1.92	unitless	Lasko & Vadrevu (2018)

CB = complete-field burn, PB = partial-field burn

mates from the Indiastat data portal (Indiastat.com), and crop-specific parameters from literature for 2016 and 2017:

$$E_i = f_{burned} \times CP \times RC \times f_{DM} \times f_{CC} \times EF_i \tag{2.4}$$

where f_{burned} is the fraction burned, CP is crop production in kg (in this case, of *kharif* rice), RC is residue-to-crop ratio, f_{CC} is combustion completeness, and f_{DM} is the mass fraction of DM burned of total from crop production (Table 2.1). Here, fuel loading (FL) is the product of CP, RC, and f_{DM} over the cultivated area (A) in units of g m^{-2}; fuel consumption (FC) is the product of fuel loading and f_{CC}:

$$FL = \frac{CP \times RC \times f_{DM}}{A} \tag{2.5}$$

$$FC = FL \times f_{CC} \tag{2.6}$$

Following the FRP-based method for estimating adjusted DM burned, here we also adjust the DM for partial burns using survey data.

As we will see, our top-down estimates of fuel load agree well with bottom-up validation for the 2016 and 2017 post-monsoon burning seasons (Chapter 2.4.2). We then extend these bottom-up estimates to 2003-2018 by first calculating the ratio of survey burn rates to the satellite-derived, adjusted FRP for 2016-17 and then applying this ratio to all years in the satellite FRP record.

Finally, application of emissions factors allows us to quantify emissions of black carbon (BC) and primary organic carbon (OC), as well as of CO_2 and CO, from the agricultural fires. We focus on these four species for the following reasons: OC and BC as components of particulate matter, CO_2 as a greenhouse gas, and CO as a primary pollutant from combustion. However, we note that DM burned, provided in our SAGE-IGP inventory, can be converted to any chemical species provided that a corresponding emissions factor is available. Here we use the compilation from Andreae (2019) to be consistent with fire emissions broadly designated as "agricultural"in standard global inventories, but we note differences in emissions factors that are region-specific and derived from rice residue burning in Appendix B.3.4. For OC and BC from partial field burns, we additionally scale DM by a factor of 1.92 to account for the higher PM2.5 emissions factor in these fires relative to complete-field burns (Lasko & Vadrevu, 2018), as described in Chapter 2.3.4.1. We compare the resulting statewide emissions estimates with five global inventories: (1) Global Fire Emissions Database (GFEDv4s) (van der Werf et al., 2017), (2) Fire Inventory from NCAR (FINNv1.5) (Wiedinmyer et al., 2011), (3) Global Fire Assimilation Sys-

tem (GFASv1.2) (Kaiser et al., 2012), (4) Quick Fire Emissions Dataset (QFEDv2.5r1) (Darmenov & da Silva, 2013), and (5) Fire Energetics and Emissions Research (FEERv1.0-G1.2) (Ichoku & Ellison, 2014). Each of these inventories relies on a different combination of observations, algorithms, and assumptions. For example, GFEDv4s and FINNv1.5 are primarily derived from burned area (BA) and active fire area (AFA), while GFASv1.2, QFEDv2.5r1, and FEERv1.0-G1.2 are FRP-based. More details about these inventories are given in Appendix B.4.1-B.4.2.

2.3.4.3 Constructing a spatially and temporally explicit gridded emissions inventory

The steps described so far yield total seasonal emissions for each state for 2003-2018. We next disaggregate the state-level DM emissions to daily, 0.25° x 0.25° spatial resolution to create a gridded inventory, SAGE-IGP. We start with total state-level emissions rather than the finer gridded resolution to limit noise, ensure convergence in our cloud/haze gap-filling step, and aggregate survey responses from sparsely located households.

First, we allocate the seasonal DM emissions spatially according to the fraction of MODIS Terra + Aqua unadjusted FRP in each grid cell for the season. Second, we approximate the evolution of fire activity over the season in each grid cell as Gaussian, using the dates of three breakpoints, or k_β, where $\beta = 0.1, 0.5$, and 0.9 (defined in Chapter 2.3.3):

$$g(t) = e^{0.5[\frac{(t-k_{\beta=0.5})}{(k_{\beta=0.9}-k_{\beta=0.1})/2.5)}]^2} \tag{2.7}$$

where g is the value of the Gaussian on day t. Because the day of peak burning varies spatially within the state, we cannot simply impose uniform daily variability across the state using our daily DM emissions. For each grid cell, the corresponding Gaussian distribution, whose maximum value is 1, is multiplied by the spatially-allocated DM emissions from Step 1. Finally, we iteratively nudge the gridded DM emissions until convergence such that (1) the daily total of our gridded inventory matches the state-level adjusted DM emissions, and (2) the spatial allocation of our gridded inventory matches that of the MODIS Terra + Aqua unadjusted FRP on a seasonal basis. One caveat is that this step assumes all grid cells within each state are equally obscured by clouds and/or thick haze. However, this is a reasonable assumption given that cloud cover and thick haze generally affect large areas across the state (Figure B.3). With our gridded inventory, we also provide an ancillary dataset of gridded

hourly fractions of fire activity, based on household survey data (Appendix B.3.3).

2.3.5 Ground and satellite-based measurements of aerosols

We use ground and satellite-based measurements of aerosols to check whether we improve the temporal distribution of fire emissions over current global inventories. We focus on October-November 2017, when a hazy/cloudy period lasted for almost 3 weeks during the post-monsoon fire season. The Aerosol Robotic Network (AERONET) site in Kanpur, India (80.23°E, 26.51°N) provides a long record of ground-based aerosol optical depth (AOD) measurements (from 2001-present), which have been used to infer the properties and transport of smoke aerosols emitted from post-monsoon agricultural fires across the IGP (Kaskaoutis et al., 2014). As an ancillary dataset, we use the Aerosol Index (AI) from the Ozone Measuring Instrument (OMI) aboard the Aura satellite, gridded to a spatial resolution of 1° x 1°. The OMI AI reliably indicates enhancements in absorbing aerosols, such as those in soot and smoke, using radiances at the 354 and 388-nm ultraviolet wavelengths (Kaskaoutis et al., 2014; Torres et al., 2007). We spatially average daily AI over Punjab but exclude those days with only one observation across the state.

2.3.6 Atmospheric modeling of smoke from agricultural fires: validation using station $PM_{2.5}$ observations

We assess the utility of our regional inventory, SAGE-IGP, compared to the five global inventories, in the context of atmospheric modeling (Table B.10). Following Cusworth et al. (2018), we use the Stochastic Time-Inverted Lagrangian Transport (STILT) model, version 2, to generate gridded maps of the sensitivity of air quality in New Delhi to upwind fire emissions in October-November from 2013-2018 (Fasoli et al., 2018). We drive STILT with meteorology from the Global Data Assimilation System (GDAS; https://www.ready.noaa.gov/archives.php), available at 0.5° x 0.5° spatial resolution, to simulate the 5-day back trajectories of an ensemble of 500 air parcels. The resulting STILT sensitivity footprints, in units of ppm/[μmol/(m^2s)], are then multiplied by the emissions of primary $PM_{2.5}$ from each fire inventory, including SAGE-IGP, to obtain the modeled smoke $PM_{2.5}$ for New Delhi. Here we define primary $PM_{2.5}$ as the sum of OC and BC, following Koplitz et al. (2016) and Cusworth et al. (2018). For each inventory and year, we then calculate the correlation between daily-averaged modeled $PM_{2.5}$ and $PM_{2.5}$ observed at the U.S. Embassy in New Delhi (https://in.usembassy.gov/embassy-consulates/new-delhi/air-quality-data/). Cusworth et al. (2018)

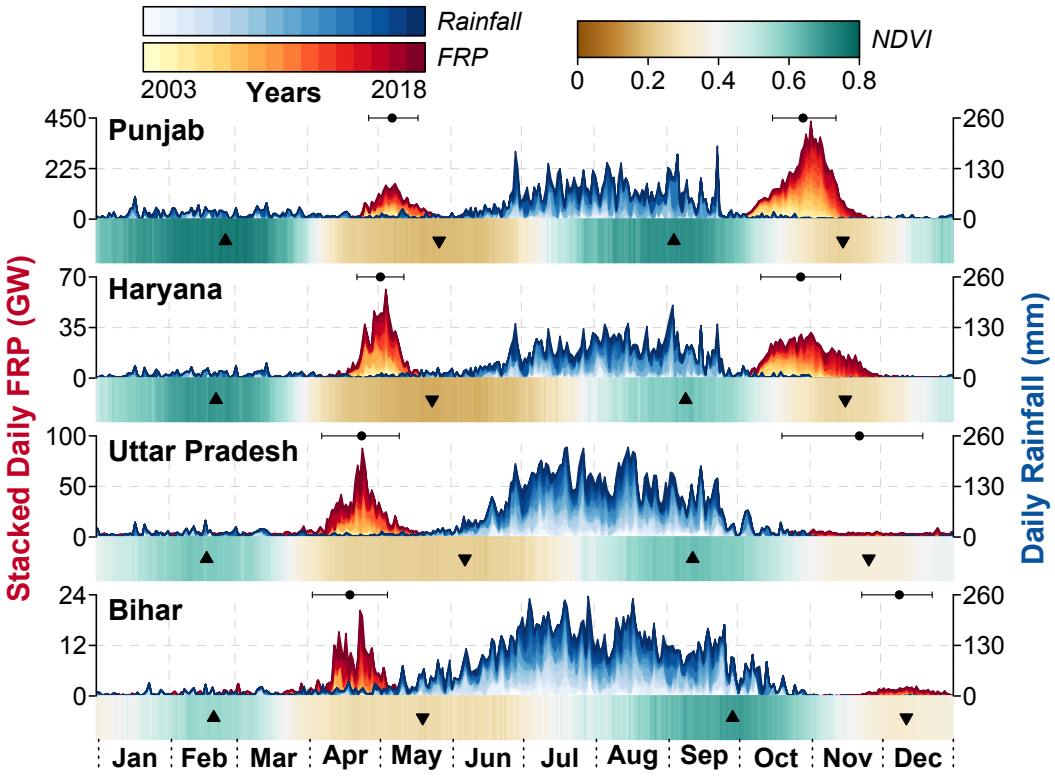


Figure 2.3: Satellite-derived daily vegetation greenness, fire intensity, and rainfall in Punjab, Haryana, Uttar Pradesh, and Bihar from 2003-2018: The Normalized Difference Vegetation Index (NDVI), a proxy for vegetation greenness, and Fire Radiative Power (FRP), a proxy for fire intensity (note the differing y-axis scales), are derived from MODIS over agricultural regions. FRP and rainfall are stacked by year, while NDVI is shown as the weighted average across all years, with weights based on the usable fraction, or fraction of agricultural area that is cloud and haze-free on that day in each year. Horizontal segmented bars above each subplot denote the approximate midpoint (black dot) and start and end (whiskers) of the pre-monsoon (March-May) and post-monsoon (Oct-Dec) burning seasons in each state. Upward triangles denote the timing of maximum monsoon and winter greenness; conversely, downward triangles denote the timing of minimum pre-monsoon and post-monsoon greenness.

previously found that the $PM_{2.5}$ observations at the U.S. Embassy are well correlated with average citywide measurements from the Indian Central Pollution Control Board (CPCB) during the post-monsoon burning period.

2.4 Results and Discussion

2.4.1 Crop residue burning across the Indo-Gangetic Plain: drivers, consequences, and farmer perceptions

Figure 2.3 shows the average temporal evolution of fire activity, crop phenology, and rainfall in Punjab, Haryana, UP, and Bihar derived from satellite data. The total post-monsoon fire intensity in Punjab is on average one to two orders of magnitude higher than that in Haryana, UP, and Bihar. Punjab is a highly productive state with

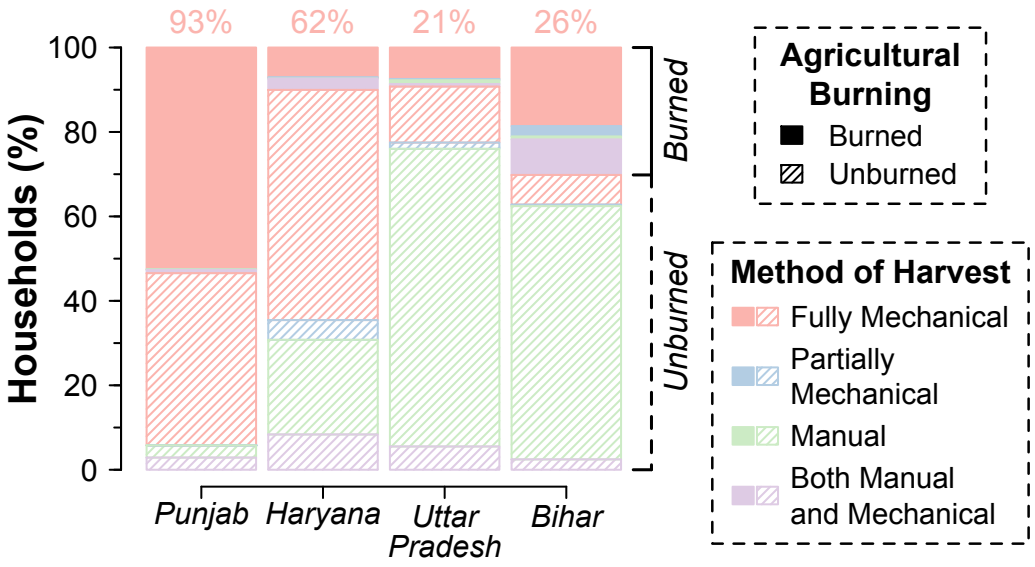


Figure 2.4: Mechanized harvesting of rice related to crop residue burning across the Indo-Gangetic Plain inferred from household survey data: The percentage of households that burned and did not burn rice residues, separated by the method of harvest, for the 2017-18 growing season. Percentages above bars denote the fraction of households using fully mechanical methods (combine harvesters) to harvest *kharif* rice.

larger fields and higher use of combine harvesters, thereby yielding more excess residues that need to be managed. As revealed by the upward triangles in the NDVI time series, maximum winter greenness in the western IGP is greater than that in the eastern IGP, with Haryana at 0.7 and Punjab at 0.76 versus Bihar at 0.56 and UP at 0.6; this confirms the gap in winter crop productivity between these two regions (Jain et al., 2017). Maximum monsoon greenness is more homogenous across all states (0.61-0.71). In the western IGP, the summer monsoon follows the pre-monsoon fire season from March to May and precedes the post-monsoon fire season from October to December. In the eastern IGP, the pre-monsoon fire season follows the earlier monsoon onset and thus starts in mid-March rather than mid-to-late April. As the monsoon continues through October, the post-monsoon fire season occurs later and extends to December.

Traditionally, farmers across the IGP have harvested rice in the post-monsoon season manually. By 2017, 61% of households in surveyed in Bihar and 71% in UP still followed this practice, while 62% in Haryana and 93% in Punjab had transitioned to fully mechanized harvesting, namely using combine harvesters (Figure 2.4). The large amounts of loose and intact residues generated from combine harvesters are difficult to clear manually and thus often burned (Tallis et al., 2017). Based on 474 responses, we find that IGP farmers started to burn rice residues as early as 1957, with the most rapid growth occurring after the mid-1990s (Figure 2.1a). The 10-yr period with the highest rate of households adopting the practice of crop residue burning took place more than a decade earlier

in Punjab (mid-1990s to early 2000s) than in Haryana, Bihar, and UP (mid-2000s to 2010s).

As crop production increased and mechanization continued spreading across eastern IGP, burn rates also increased. In 2017, over a quarter of surveyed farmers burned crop residue after rice harvests, with post-monsoon fire activity concentrated in Punjab: 53% of farmers in Punjab burned rice residue, compared to 9-30% in Haryana, Bihar, and UP (Figure 2.4). At the household level, the year-to-year persistence in burning varies: in 2016, higher percentages of farmers in Punjab (82%), Haryana (20%), and UP (14%) burned rice residue compared to 2017, while a lower percentage of farmers in Bihar (18%) burned. However, the 2016-2017 decline in the burn rate in Punjab is less pronounced (71% vs. 89%) when weighted by operational landholding area, suggesting that farmers with larger fields continued to burn residues in 2017. In any case, the recent decline in burning may reflect intentional underreporting, given the recent government bans on agricultural fires.

We find that the time of burning varies spatially: peak burning occurs roughly evenly between mid-day (10 a.m.-2 p.m.) and evening (2-6 p.m.) in Punjab and Haryana but mainly in the evening in UP and Bihar (Figure 2.1b). Liu et al. (2019) found that the method of burning also varies spatially: crop residues are primarily managed by complete-field burning in Punjab and northern Haryana and more commonly by partial-field burning in central and southern Haryana. This conclusion is supported by the increasing fraction of partial burning from western to eastern IGP (30% in Punjab to 57% in Bihar) (Figure 2.1c). Consistent with Kim Oanh et al. (2011), we find that the type of burning is associated with the method of harvest, with 68% of fields with complete burns – and conversely, only 19% of those with partial burns – were harvested fully mechanically in the IGP.

Relative to Punjab, the more recent adoption of crop residue burning at the household-level in Haryana, Bihar, and UP, along with the current low rate of burning (12-46%) among survey households in these states, suggests high potential growth in agricultural fire activity (Figure 2.1a, Table B.4). For example, assuming a future scenario in which all households across the IGP harvest rice mechanically, the rate of crop residue burning in terms of landholding area would increase by just 2-27% in Punjab and Haryana, compared to 2016-2017, but by 67-207% in UP and Bihar (Table B.4). These values assume that the proportion of burned versus unburned fields relying on mechanized harvesting remains constant in each state.

Nearly 90% of farmers surveyed across the IGP believe that rice residue burning impacts the air quality of nearby cities (Table B.3). Nevertheless, for farmers, the positive effects of burning, namely saving time and cost in rice residue management, ultimately outweigh the potential negative effects, including what the farmers fear could be damages to soil health and lower crop yield. We find that 56-92% farmers burn rice residue to overcome

the short turnaround time to prepare the land to sow the next crop (Figure B.1a). Nearly three quarters of households wait 10 or fewer days after rice harvests to burn the crop residue, underscoring the quick transition from the *kharif* to *rabi* crops (Figure B.1b). Other factors that play a role in the decision to burn crop residue include the unsuitability of the rice residue as cattle feed (42-76% of farmers), difficulty in cutting and managing the residue (61-80%), absence of technology to manage the residue (29-64%), and lack of incentive from the government to not burn, especially in Punjab, where 81% of surveyed farmers cite this factor (Figure B.1a). In addition to circumventing the short transition period between crops, 80% of farmers say that burning saves cost in cutting and managing rice residue (Table B.3). On the other hand, more farmers (39-44%) believe that crop residue burning negatively impacts soil health, in terms of crop yield, fertilizer usage, and soil color and texture. Only 7-29% of farmers think that fire improves soil health in these ways.

2.4.2 Adjusted emissions from agricultural fires using satellite and survey data

Figure 2.2 shows an example of daily timeseries of MODIS FRP adjusted for small fires, cloud/haze gaps in satellite observations, partial-field burning, and the fire diurnal cycle for Punjab for the 2017 post-monsoon season. The VIIRS small fires boost increases MODIS FRP on clear-sky days and overall by 109%, while the cloud/haze gap-fill further increases the overall MODIS + VIIRS FRP by 142%, with the greatest adjustment during cloudy/hazy periods, such as from October 30 to November 17. The household survey data implies that partial field burning adds 33% more FRP. Accounting for the fire diurnal cycle results in a further 361% boost in FRP, by far the most uncertain of the adjustments. This boost is due to the large number of short-lasting fires inferred from the survey data that occur outside the satellite overpass times, leading to "missing," or unobserved fire activity in this region. Our FRP estimates are not sensitive to the assumption that fires last just half an hour, because any change in our fire duration assumption affects both the diurnal cycle adjustment and the FRP to FRE conversion. For example, if we assume instead that fires last an hour, the factor to account for fires seen outside the satellite overpasses during mid-day survey period would be halved, and the FRP to FRE conversion factor would double, thereby yielding no net change in our estimate of DM burned.

Using the adjusted FRP, we estimate on average 10.4 ± 3 Tg DM burned each year, or 65 ± 18 Gg OC, 5.6 ± 1.6 Gg BC, 791 ± 225 Gg CO, and 14.9 ± 4.2 Tg CO_2, in the IGP per post-monsoon burning season from 2003-2018 (Figure 2.5a-b). Punjab comprises 70% of total DM burned and 67% of aerosol emissions. Importantly, for Punjab, our FRP-based estimates of DM burned calculated from adjusted FRP in 2016-2017 are consistent

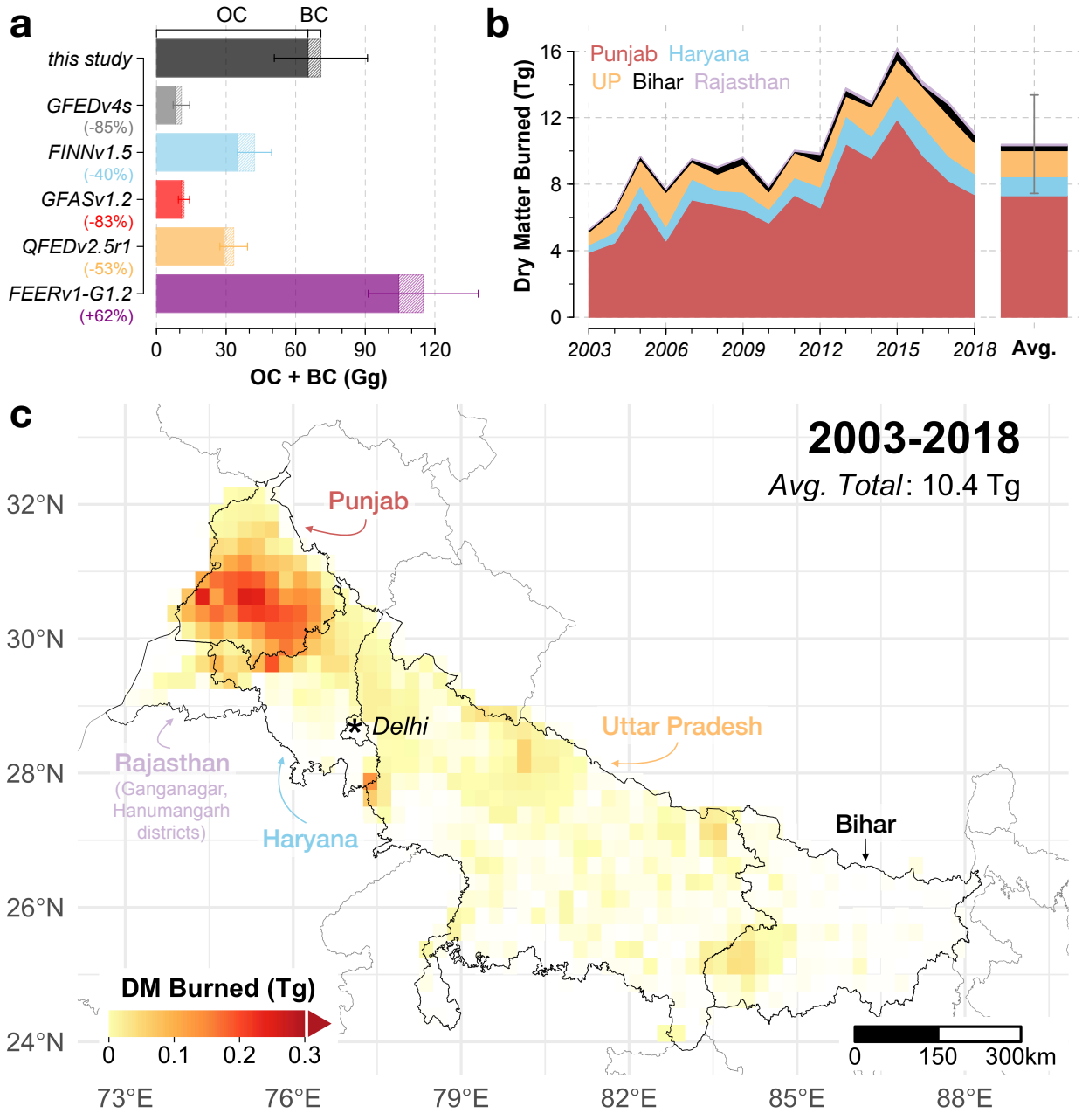


Figure 2.5: Post-monsoon agricultural fire emissions over the IGP from 2003-2018: (a) Comparison of average OC+BC emissions ($\pm 1\sigma$) from this study (SAGE-IGP) with five global fire emissions inventories. On the y-axis, percentages denote the difference in OC+BC emissions from each inventory relative to this study. (b) Time series of annual dry matter (DM) burned, and average DM burned from 2003-2018, with stacked contours showing contributions by state. Vertical bars denote $\pm 1\sigma$ for the total DM burned across all years. (c) Average state-level DM burned in Punjab, Haryana, Uttar Pradesh, and Bihar, disaggregated to 0.25° x 0.25° spatial resolution using the top-down adjusted FRP approach from this study. DM burned is also estimated for two Rajasthan districts, Ganganagar and Hanumangarh, which border Punjab and Haryana. Inset shows the average total DM burned from 2003-2018.

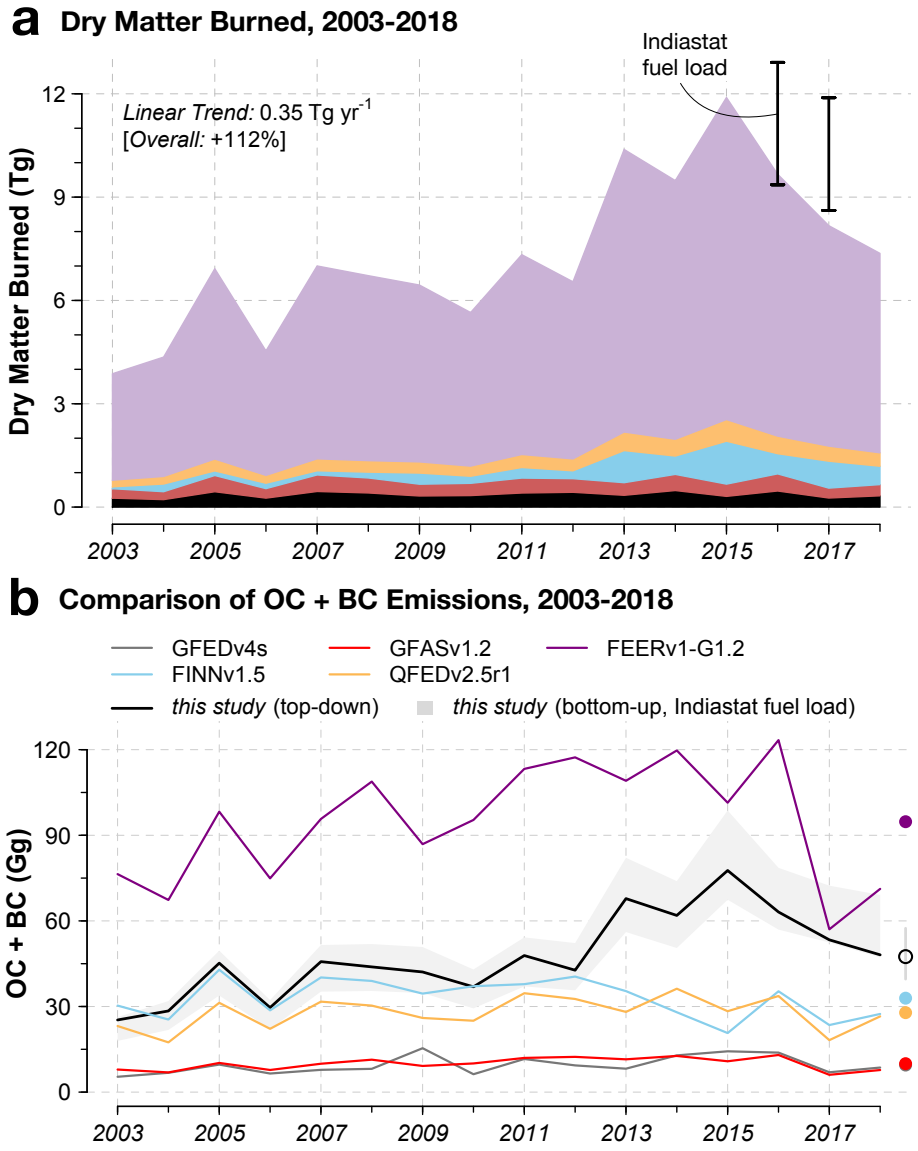


Figure 2.6: Dry matter (DM) burned from adjusted FRP and comparison of OC+BC emissions for Punjab, India, from 2003-2018: (a) Post-monsoon DM burned (Tg), derived using an FRP-based approach with both satellite and survey data. Stacked colored contours represent the FRP adjustments illustrated in Figure 2.2. Black bars denote the range of post-monsoon DM burned derived using a bottom-up approach with Indiastat crop statistics and household survey data for 2016 and 2017. (b) Comparison of post-monsoon OC+BC emissions from this study and five global fire emissions inventories. Dots on the right show average OC+BC emissions for this study and all inventories. The gray envelope for this study's bottom-up estimate denotes ranges in the residue-to-crop ratio and fraction of DM burned tuned to 2016-17 survey burn rates (see Table 2.1), and the grey bar at right shows the average across years.

with our bottom-up estimates based on burn rates from the household survey and Indiastat-derived fuel loadings (Figure 2.6a), lending confidence to our method. Overall, we find that DM burned increased by 112% from 2003 to 2018. In contrast, without adjustment, the apparent 16% increase in MODIS Terra + Aqua FRP is not statistically significant ($p = 0.45$). The discrepancy in trends arises because as fire intensity increases, haze cover also likely increases and obscures fires to a greater extent. Our cloud/haze gap-fill compensates for the ~36% decline in the satellite observable fraction (Figure B.4b), contributing on average four times the FRP boost in later years (2013-2018) as in previous years (2003-2012).

Figure 2.6b compares the 2003-2018 timeseries of OC+BC emissions from this study to five global fire emissions inventories during the post-monsoon season. The average seasonal OC+BC emissions can differ by > 90 Gg between the minimum (GFASv1.2, GFEDv4s) and maximum (FEERv1.0-G1.2) values. Our estimates are closest in magnitude to FINNv1.5, higher than GFEDv4s, GFASv1.2, and QFEDv2.5r1 but lower than FEERv1.0-G1.2. These differences with other inventories are discussed below. As we shall see, the close match with FINNv1.5 is fortuitous, with FINNv1.5 underestimating burned area and overestimating fuel consumption. To further examine the utility of our adjusted FRP approach, we compare our daily DM burned with different global inventories in the context of aerosol loading in Punjab from October-November 2017 (Figure 2.7). In 2017, an almost 3-week cloudy/hazy period persisted from October 30 to November 17, with minimal fire activity detected during the second and third weeks of November. Using a model combined with satellite data, Dekker et al. (2019) suggested that residential and commercial combustion was the most important driver of extreme pollution over the IGP from November 11-19, 2017. However, we argue that agricultural fire activity during this period is grossly underestimated and likely also a key emissions source. Our reasoning is as follows. First, three global inventories — GFASv1.2 (used in Dekker et al. (2019)), FINNv1.5, and QFEDv2.5r1 — all show a hiatus in fire activity bounded by two local maxima in fire activity (Figure 2.7a-b). This hiatus coincides with the cloudy/hazy period and low satellite observable fraction (mostly < 0.7) during the Aqua overpass time, or when most post-monsoon fires occur (Figure 2.7b) (Vadrevu et al., 2011). Second, the variations in aerosol loading during this time period closely follow the Gaussian-like temporal evolution expected of post-monsoon fires (Figure 2.7c) (Kaskaoutis et al., 2014; Liu et al., 2021a). Finally, large enhancements in both daily AOD (> 1) at Kanpur and mean OMI AI (> 1.5) over Punjab throughout the cloudy/hazy period suggest that fire activity continued during this time although obscured from satellite detection.

Figure 2.8 shows the correlations of observed $PM_{2.5}$ in New Delhi and modeled smoke $PM_{2.5}$ using our in-

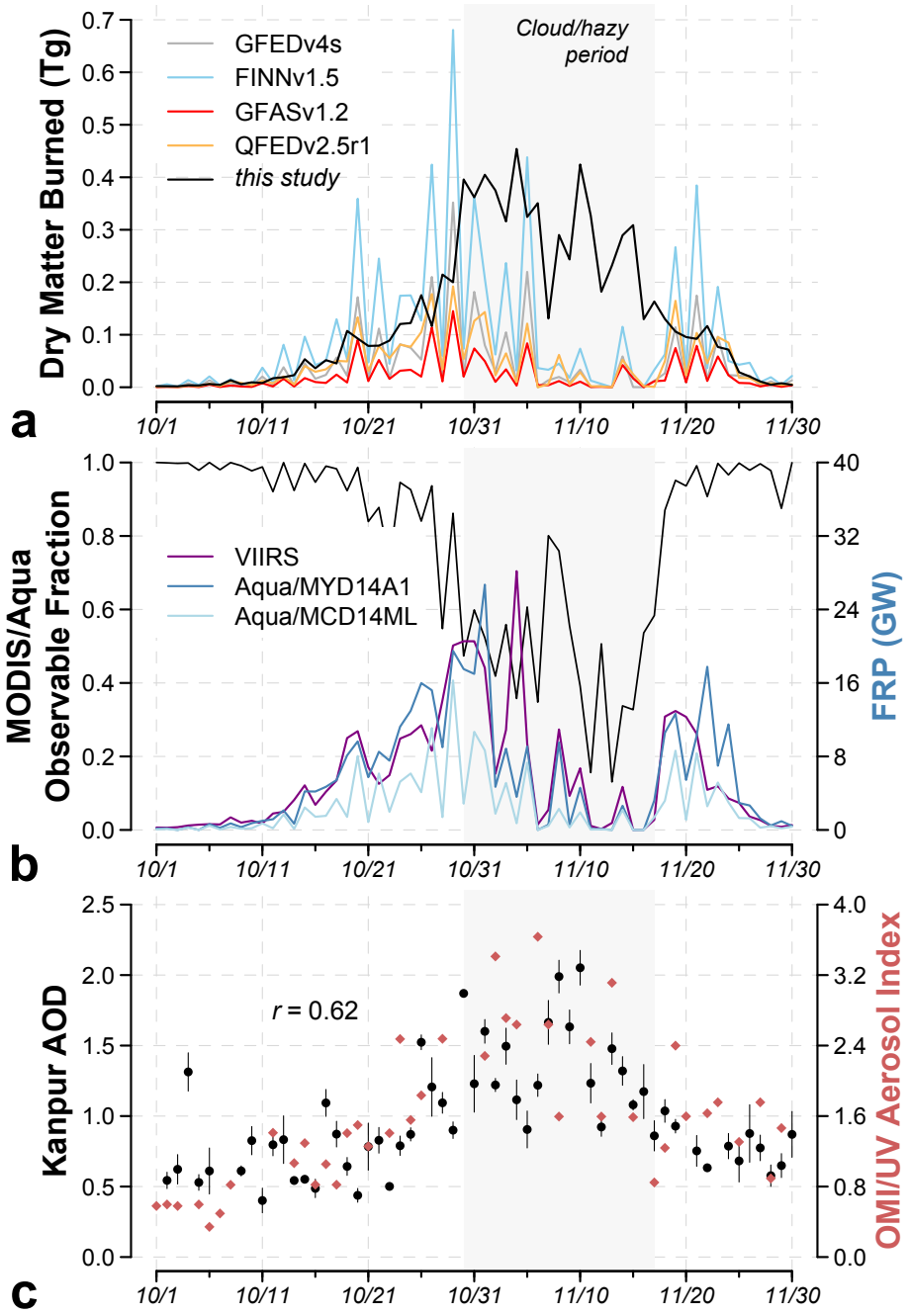


Figure 2.7: Daily fire emissions and intensity in Punjab, India, and aerosols observed over Punjab and in Kanpur, India, during the 2017 post-monsoon burning period: (a) DM burned from this study and three fire emissions inventories: GFASv1.2, QFEDv2.5r1, and FINNv1.5. (Note: GFEDv4s DM burned estimates for 2017 is preliminary.) (b) Fire intensity as measured by FRP from MODIS/Aqua (MYD14A1 gridded maximum FRP and MCD14ML FRP from individual active fire hotpots) and from VIIRS (VNP14IMGML), overlaid with the MODIS/Aqua "observable fraction" f_o, or the degree to which MODIS/Aqua can "see" active fires. The cloudy/hazy period from October 30 to November 17 is highlighted in light gray. (c) Daily mean AOD ($\pm 1\sigma$) at 500 nm from the AERONET site in Kanpur (black) and OMI/UV Aerosol Index (AI, red) over Punjab. The correlation r between the AOD and AI timeseries is shown inset.

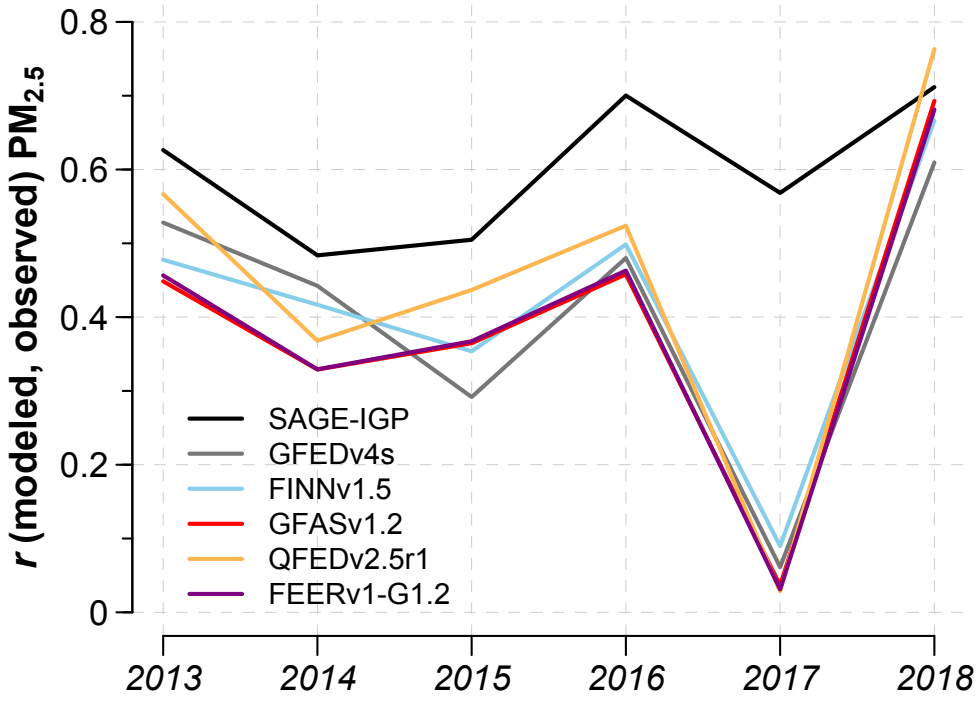


Figure 2.8: Correlations of daily observed station $PM_{2.5}$ in New Delhi and modeled $PM_{2.5}$ using SAGE-IGP and five global inventories for the 2013-2018 post-monsoon burning seasons: Observed and modeled $PM_{2.5}$ are averaged across 3-hour intervals to compare at the daily scale from October to November. The black line refers to the SAGE-IGP regional inventory (this study) and colored lines to five global inventories: GFEDv4s, FINNv1.5, GFASv1.2, QFEDv2.5r1, and FEERv1.0-G1.2. Observations are from the $PM_{2.5}$ monitor at the U.S. Embassy.

ventory, SAGE-IGP, and the five global inventories from 2013-2018. Of particular importance is our finding that modeled $PM_{2.5}$ using SAGE-IGP emissions is moderately correlated with observed $PM_{2.5}$ in 2017 ($r = 0.57$) but not correlated when the global inventories are applied ($r < 0.1$). With regard to the 2013-2018 time period, the higher correlation achieved using SAGE-IGP (mean $r = 0.6$) over the global inventories ($r = 0.39$ to 0.45) demonstrates the utility of our regional inventory for atmospheric modeling studies.

Our study demonstrates that more rigorous correction is needed during persistent cloudy/hazy conditions than is carried out by the current cloud correction algorithms used in some inventories, such as GFASv1.2 and QFEDv2.5r1 (Darmenov & da Silva, 2013; Kaiser et al., 2012). Our method iteratively gap-fills this hiatus in observed FRP in 2017, resulting in daily DM burned that follows a Gaussian-like distribution similar to that in other years, and more closely matches the bottom-up approach based on the household survey burn rates and Indiastat rice production (Figure 2.7a) (Liu et al., 2021a). However, the 5-31% underestimate of DM burned in 2017 using our FRP-based approach compared to the bottom-up method suggests that our cloud/haze gap-fill adjustments to MODIS FRP may still be somewhat conservative (Figure 2.6). In particular, our cloud/haze gap-fill method requires some peak fire days to be well-observed to provide an upper bound for the adjustment. In 2017, however, weeks-long thick haze persisted through the expected peak fire days, leading to severe underestimates of fire activity (Figure B.3).

2.4.2.1 Limitations and uncertainties in constructing spatio-temporal explicit emissions

Figure 2.5c shows average total DM burned from 2003-2018 over the IGP from our gridded 0.25° x 0.25° inventory. While our adjusted FRP approach leads to a more realistic seasonal, state-level budget for DM emissions than current global inventories, we note several limitations. First, the disaggregated emissions inventory contains statistical noise from the iterative cloud/haze gap-fill adjustments as well as from our application of a Gaussian temporal distribution of emissions within each grid cell. Further analysis using AOD observations with back trajectory modeling could help constrain the daily variability in fire emissions. Second, the household survey sample sizes for Haryana, UP, and Bihar are only 10-29% of that for Punjab, leading to uncertainty in the implications of the survey for these states (Figure 2.1). We are relatively confident in the partial burn fractions and the fire diurnal cycle that we derived from survey data. However, the burn rate used for validation is more uncertain, given that recent bans on agricultural burning may have led to underreporting by the farmers. We also do not know if the

partial-field burn fraction or diurnal cycle changed over time. To our knowledge, the household survey provides the best available ground-level data we have access to on agricultural burning in north India. Third, the adjusted FRP assumes a uniform fire diurnal cycle across each state throughout the time period, as well as a uniform spatial and temporal distribution of partial-field burning. More detailed on-the-ground data may help constrain the spatio-temporal variability in these two parameters. Fourth, as with current global fire emissions inventories, we lack information to provide detailed uncertainty estimates for our gridded emissions. Thus far, only the emissions factors for different species allow for a detailed uncertainty analysis based on standard deviations from the laboratory and field studies compiled by Andreae (2019) and Lasko & Vadrevu (2018).

In our adjusted FRP approach, the fraction of cloud/haze gap-fill FRP to satellite-observed FRP can be taken as the relative uncertainty of satellite-derived FRP from year to year (Figure B.7). This uncertainty anti-correlates with the satellite observable fraction (Figure B.4b). A further 5-9% uncertainty stems from the static VIIRS FRP boost factor applied to years from 2003-2011, when no VIIRS observations are available (Table B.7). For the survey-based components, we use a bootstrap hold-out method to estimate 10-18% uncertainty in partial burn fractions and 14-42% in the diurnal cycle boost for the four states (Table B.8). A more detailed discussion of the uncertainties associated with each step is provided in Appendix B.3.4.

In future versions of SAGE-IGP, several technical improvements can be made to the adjusted FRP method with regard to input satellite products. First, taking into account the slight day-to-day variability in satellite overpass times may increase the accuracy of the VIIRS boost and diurnal cycle adjustment. Currently, we assume that the Aqua and S-NPP overpasses are perfectly aligned for the VIIRS FRP boost, but the offset between the two overpasses varies from a few seconds to 50 minutes (Li et al., 2018). Second, the VIIRS and MODIS FRP merging can be fine-tuned by correcting for biases in FRP due to atmospheric absorption and solar zenith angle (Dickinson et al., 2016). Li et al. (2018) found nearly a 1:1 ratio between daytime MODIS and VIIRS FRP in Asia, though this correlation may vary with fire intensity, location, timing, and land cover. When available in Google Earth Engine, the VNP14A1 gridded active fire product can replace the VIIRS VNP14IMGML active fire geolocation product currently used in our workflow to better complement the MODIS MxD14A1 gridded products. Both the MODIS and VIIRS "A1" products are in sinusoidal projection, and together their use avoids resampling errors introduced by using the VNP14IMGML product, which is unprojected. Finally, explicit calculations of the detection limits of MODIS and VIIRS in view of both the small fire size and observing conditions are needed to refine the cloud-haze gap fill.

2.4.3 Differences in fire activity, fuel consumption, and emissions factors assumed in inventories and the consequences for emissions estimates

Global fire emissions inventories ingest different combinations of MODIS burned area and active fire products. For example, GFEDv4s, a bottom-up inventory, relies primarily on the MCD64A1 burned area product with the MCD14ML active fire product for its small fire boost, while GFASv1.2, QFEDv2.5r1, and FEERv1.0-G1.2 use FRP from the MOD/MYD14 active fire products (Liu et al., 2020a). In Figure B.9, we compare the spatial patterns of burned area (MCD64A1) and active fire pixels (MxD14A1) stacked by year, in which for each pixel any occurrence of burning for a given post-monsoon season is assigned a value of 1. The stacked values for MCD64A1 are more spatially uneven than MxD14A1 and tend to cluster, which may reflect classification bias in this product caused by the conflation of harvest and burning. This conflation becomes especially problematic as rice production increases (Jethva et al., 2019; Liu et al., 2021a), because the greater drawdown in satellite-observed greenness after rice maturation may artificially inflate total burned area.

In contrast, MxD14 can capture smaller, fragmented burns but may miss fires occurring outside overpass times and result in inconsistent detection from year to year. In constructing GFAS, Kaiser et al. (2012) surmised that FRP observed during the MODIS overpasses is representative of daily fire activity. While this is a reasonable assumption for large wildfires, the short duration of fires in north India makes this approach problematic. Some top-down inventories, such as GFASv1.2, also rely in part on bottom-up inventories, such as GFEDv4s, to linearly scale FRP to DM (Kaiser et al., 2012). Consequently, biases in bottom-up estimates of DM burned can propagate to top-down inventories.

Here we discuss differences in the bottom-up approach used in GFEDv4s versus FINNv1.5. Calculating DM burned mainly depends on two variables: burned area and fuel consumption, which is the mass of biomass burned per unit area. We next explore how the range in these two components in different datasets affects estimates of DM burned and the resulting aerosol emissions for the 2003-2016 time period. We consider (1) burned area estimates from GFEDv4s, FINNv1.5, and ModL2T (Liu et al., 2019); (2) fuel consumption estimates from GFEDv4s, FINNv1.5, and Indiastat (Table B.11); and (3) emissions factors used by GFEDv4s, FINNv1.0, GFASv1.0, and QFEDv2.4 (Table B.12) (van der Werf et al., 2017; Wiedinmyer et al., 2011; Kaiser et al., 2012; Darmenov & da Silva, 2013), and from Andreae (2019). We find that the DM burned calculated using our best estimates of burned area (ModL2T) and fuel consumption (Indiastat) is consistent with the adjusted FRP ap-

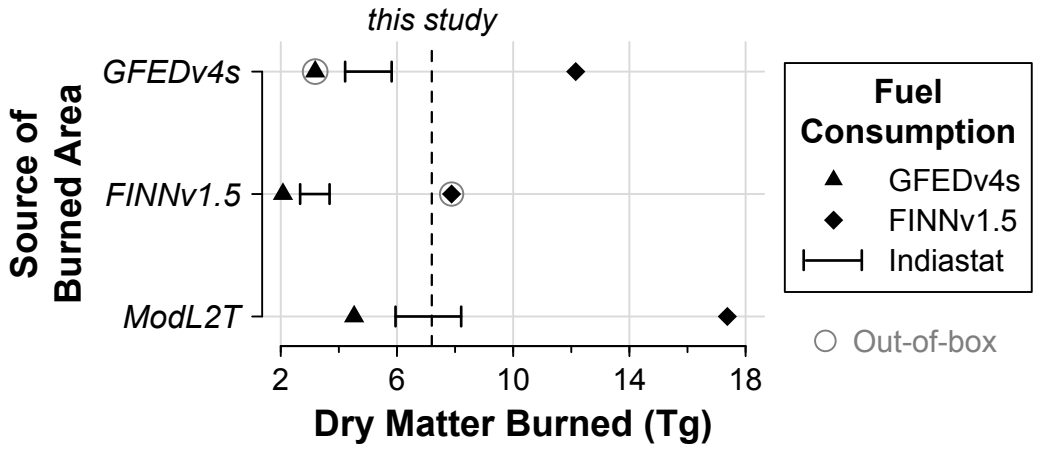


Figure 2.9: Comparison of average dry matter (DM) burned derived from different combinations of bottom-up burned area and fuel consumption estimates for the 2003-2016 post-monsoon burning seasons in Punjab, India: Three sources of burned area (GFEDv4s, FINNv1.5, and ModL2T (Liu et al., 2019)) and four fuel consumption estimates (GFEDv4s, FINNv1.5, Indiastat) provide a range of DM estimates (Tg). The out-of-box DM averages from GFEDv4s and FINNv1.5 are circled. The average DM estimated from the top-down approach developed in this study is shown as the vertical dashed line.

proach of this study (7.2 Tg) (Figure 2.9). This indicates that ModL2T burned area has utility for deriving agricultural fire emissions, but only when paired with reasonable fuel consumption estimates. The average out-of-box GFEDv4s DM burned (3.2 Tg) is 56% lower than this study, while that of FINNv1.5 (7.9 Tg) is comparable. However, the FINNv1.5 fuel consumption is more than twice that estimated from Indiastat (Table B.11), compensating for its 37-55% lower burned area compared to other estimates. If we apply FINNv1.5 fuel consumption to GFEDv4s and ModL2T burned area, the resulting DM burned is ~2-3 times as high as this study's FRP-based estimates (Figure 2.9).

We also calculate the percent contribution of burned area, fuel consumption, and emissions factors to the range in OC, BC, CO, and CO_2 agricultural fire emissions. We find that fuel consumption is the most uncertain component (54-66%), followed by burned area (24-29%) and emissions factors (5-22%) (Table B.13). We also diagnose a 16-27% decline ($p < 0.05$) in GFEDv4s and FINNv1.5 fuel consumption from 2003-2016 (Table B.11), while that based on Indiastat is relatively constant (+3%, $p = 0.3$). Here we focus on the fuel load component of fuel consumption (see Equation 2.6) since combustion completeness is not readily observable using satellite data. In Indiastat, the increase in rice production implies a higher fuel load, but the concurrent increase in rice area cancels out this effect. The discrepancy between the two satellite products and Indiastat can be explained by assumptions in GFEDv4s and FINNv1.5 regarding vegetated fraction and fuel load. First, both global inventories use satellite-derived sub-pixel-level vegetated fraction to scale fire pixels such that only the vegetated fraction of

each pixel counts toward the total burned area. Overall, these vegetated fractions increased by 9% ($p < 0.05$) in Punjab from 2003-2016, consistent with the increase in rice area reported by Indiastat. Second, we would also expect to see a positive trend in fuel load in FINNv1.5 and GFEDv4s due to the increase in rice production. However, FINNv1.5 assumes a constant fuel load for each region and land cover type (Wiedinmyer et al., 2011), while GFEDv4s models carbon fluxes to calculate fire emissions at monthly time steps, using climatological fuel loads (van der Werf et al., 2010). The shift in peak burning from October to November in Punjab (Figure B.10) means that a higher fraction of post-monsoon burned area in GFEDv4s is multiplied by the lower fuel consumption historically characteristic of this state in November.

Taken together, fuel consumption and the fire diurnal cycle represent two important sources of uncertainty in agricultural fire emissions in global inventories. The new inventory, SAGE-IGP, addresses these uncertainties with the bottom-up validation and use of household survey responses. While the survey constraints in this study cannot be applied globally due to the expense of conducting such surveys, our work suggests that global inventories should consider satellite-derived or government statistics of crop production, yield, and area to improve fuel load estimates. Geostationary satellite fire observations can also be useful to constrain the diurnal cycle of fire activity, where such data are available. Despite limitations and uncertainties, our SAGE-IGP inventory is a substantial improvement compared to existing global inventories and regional estimates. While global inventories tend to place more emphasis on large wildfires, regional estimates of agricultural fire emissions are often temporally or spatially limited due to global generalizations. Here we rely on both satellite and on-the-ground household survey data to improve FRP estimates. Based on our detailed adjusted FRP approach, our SAGE-IGP inventory provides daily, gridded emissions estimates in north India over a 16-year period from 2003-2018.

2.5 Conclusion

In summary, we combine household survey results with satellite observations to revise estimates of post-monsoon agricultural fire emissions across north India from 2003-2018. To do so, we develop an approach based on MODIS FRP, adjusted for small fires from VIIRS, cloud/haze gaps in satellite observations, partial-field burns, and the diurnal cycle of fire activity. Regionally, we estimate an average of 10.4 ± 3 Tg DM burned each year, yielding emissions of 65 ± 18 Gg OC, 5.6 ± 1.6 Gg BC, 791 ± 225 Gg CO, and 14.9 ± 4.2 Tg CO_2. Our estimates of DM burned for Punjab, which contributes more than two-thirds of emissions, closely match the bottom-up validation estimates using state-level government statistics and survey burn rates from 2016 and 2017.

Importantly, our cloud/haze gap-filling method leads to an 84% increase in DM burned in Punjab from 2003-2018; without this adjustment, the trend in MODIS FRP is only 16% and not statistically significant. Here we constrain the fire diurnal cycle and fuel consumption, two components that contribute most to bias and disagreement across this region among standard global fire emissions inventories used in atmospheric studies. Our results suggest that additional information from household surveys and crop statistics can help constrain these two components. We construct a daily, 0.25° x 0.25° emissions inventory over the IGP by disaggregating state-level DM burned. As we show, our emissions inventory, SAGE-IGP, may be used in atmospheric transport models to improve estimates of smoke exposure downwind and evaluate the associated public health burden and climate impacts. The likely expansion of crop residue burning among smallholder farms in north India, where satellites poorly capture fire activity, makes regional, survey-constrained inventories such as ours especially valuable for improving emissions estimates.

3

Cascading delays in the monsoon growing season and post-monsoon fires may exacerbate poor air quality in north India

3.1 Abstract

Over the past two decades, smoke aerosols from crop residue burning have increasingly degraded post-monsoon (October-November) air quality in north India. We use satellite data and atmospheric modeling to investigate whether cascading delays in monsoon rice growth and post-monsoon fires over 2003-2019 have exacerbated the already poor urban air quality downwind of the fires. Beginning in 2008, a government effort to combat groundwater depletion in Punjab mandated rice sowing until closer to the arrival of monsoon rains. We find evidence of district-level delays in the timing of both monsoon rice growth and post-monsoon fires, which vary from 1-4 weeks with largely an east-west gradient. These delays are correlated spatially (r = 0.51 to 0.77), with northern and western districts in Punjab, which rely less on groundwater for irrigation, tending to have the greatest delays. Had the delays in fire activity not occurred, we estimate that cities downwind and near the fire source, such as New Delhi, Bathinda, and Jind, would have consistently seen 11-21% less smoke-related fine particulate matter ($PM_{2.5}$) during 2008-2019, depending on that year's meteorology. This net benefit of earlier post-monsoon burning could have been even larger given that (1) a longer rice-to-wheat transition could incentivize farmers to find alternatives to burning crop residues; and (2) background $PM_{2.5}$ is less abundant earlier in the season, decreasing the likelihood of extreme pollution episodes. Strategies aiming to mitigate air pollution while conserving groundwater may be more effective by promoting an earlier monsoon growing season in districts with less

groundwater depletion.

3.2 Introduction

In India, the northwestern states of Punjab and Haryana, the so-called "breadbasket," are a major rice and wheat-producing region. Many farmers burn crop residues to quickly and cheaply clear fields when transitioning between the monsoon and winter crops in a primarily rice-wheat rotation (Liu et al., 2020b; Vadrevu et al., 2011). Agricultural intensification, mechanization, and labor shortages helped sustain and spread the practice of post-harvest crop residue burning in spite of government bans (Jethva et al., 2019; Liu et al., 2019; Shyamsundar et al., 2019). Most of the agriculture is dependent on groundwater-based irrigation, and overconsumption has led to unsustainable decline in the water table decline at a rate of -2 cm yr^{-1} in north India from 2002-2013 (Asoka et al., 2017). In response, the Punjab and Haryana governments enacted legislation in 2008-09 to delay monsoon rice sowing closer to the monsoon onset (Rodell et al., 2018; Singh, 2009) to conserve ground water by minimizing the need for irrigation. Moreover, the earliest paddy sowing date, mandated as June 10 in Punjab in 2008, has not remained static, shifting to June 15 in 2014, June 20 in 2018, and finally to June 13 in 2019 (The Indian Express, 2019). Delays in rice sowing shorten the post-monsoon turnaround between monsoon rice harvests and winter wheat sowing, further elevating fire as an attractive option for rice residue management (Balwinder-Singh et al., 2019; Jethva et al., 2019; Liu et al., 2021a). Previous observational and modeling studies show that post-monsoon fires from October to November degrade regional air quality downwind and can exacerbate urban air pollution to hazardous levels (Cusworth et al., 2018; Jethva et al., 2018; Kaskaoutis et al., 2014; Liu et al., 2018; Ojha et al., 2020; Patel et al., 2021). A key question is whether the ~2-week delay in post-monsoon fires from 2003-2018 may have worsened air pollution, regardless of any trends in anthropogenic emissions levels (Liu et al., 2021a). Peak fire activity shifts from late October to early November, when meteorological conditions (i.e., cooler temperatures, weak winds) are more conducive to trapping haze within the shallow boundary layer (Gautam et al., 2021; Liu et al., 2018, 2021a; Ojha et al., 2020; Sembhi et al., 2020).

Here we use satellite observations and atmospheric modeling to directly link shifts in the monsoon growing season and post-monsoon fire season to increases in air pollution. Previous studies have thus far established a coincident delay in the timing of peak monsoon greenness and post-monsoon fire activity in northwest India at the region or state level (Balwinder-Singh et al., 2019; Jethva et al., 2019; Liu et al., 2021a). If these trends are associated with one another, we should see evidence that: (1) the temporal shifts of peak monsoon greenness

are positively correlated with those of post-monsoon fires at the district level; and (2) the timing of the monsoon growing season and post-monsoon fires is positively correlated with the policy-mandated planting dates post-2008. Liu et al. (2021a) found that the magnitude of the delay in the post-monsoon fire activity from 2003-2016 across Punjab exhibited a longitudinal gradient, with greater delays in western districts (>1.5 days yr^{-1}) and smaller delays in eastern districts (<1 day yr^{-1}), and we thus expect a similar pattern in the timing of peak monsoon greenness, as well as other breakpoints in the monsoon growing season (e.g., green-up, senescence). The observed trends in satellite-derived aerosol loading are consistent with both the delay and increased magnitude in post-monsoon fires (Jethva et al., 2019; Liu et al., 2021a), which suggests negative air quality impacts downwind due to these cascading delays, as Kant et al. (2022) found. We thus expect further air quality degradation if fires occur even later, but better air quality with no delays in the fire season. Kant et al. (2022), however, did not isolate the effects of the fire season delays from increases in fire activity. Sembhi et al. (2020) found that enhancements in air pollution due to the observed delay in post-monsoon fires from 2016-2018 are in fact minimal in cities across the IGP but highly sensitive to year-to-year meteorological variability. Sembhi et al. (2020) designed three scenarios to evaluate air quality impacts from temporal shifts in the post-monsoon fires in their modeling approach, in which the input fire emissions were (a) kept as is (baseline), (b) shifted 10 days earlier, and (c) shifted 10 days later.

In this study, our goals are two-fold. First, we present satellite-based evidence that links the delays in rice growing season and post-monsoon fires at the district level in Punjab. Second, we use a receptor-oriented Lagrangian plume model to simulate the effect of these delays on downwind air quality at six cities. More specifically, we undertake a more systematic modeling approach than that utilized by Sembhi et al. (2020) by applying fire emissions, artificially shifted 0-21 days forward and backward in time, to the receptor sensitivities generated under a large set of meteorological conditions (2007-2019). By testing the model with many different combinations of fire season start times and meteorological conditions, we can distinguish the effects of timing versus meteorology on the response of air quality downwind.

3.3 Data and Methods

3.3.1 Satellite fire and surface reflectance datasets: temporal shifts in fire activity and vegetation greenness

The Moderate Resolution Imaging Spectroradiometer (MODIS) aboard the Terra and Aqua satellites provide two decades of daily observations of fires and surface reflectance. As a measure of fire intensity, we use maximum Fire Radiative Power (FRP) from the MODIS/Terra and Aqua gridded active fire datasets, MOD14A1 and MYD14A1, at 1-km spatial resolution (Giglio et al., 2016). The Collection 6 MODIS active fire detection algorithm uses a series of contextual tests to identify active fire pixels, or pixels with enhanced thermal infrared signatures relative to the background at the time of the satellite overpass.

As indicators of crop phenology, we derive the Normalized Difference Vegetation Index (NDVI) and Normalized Burn Ratio (NBR) from the 500-m MODIS/Terra MOD09GA surface reflectance at the red (0.65 μm), near-infrared (0.86 μm), and shortwave infrared (2.13 μmm) wavelengths (Vermote et al., 2015). Time series of MODIS-derived vegetation indices have been used extensively to track crop phenology and quantify crop yields in India and globally (Jain et al., 2013; Liu et al., 2021a; Lobell et al., 2013; Sakamoto et al., 2005). NDVI and NBR are analogous indices, but NBR's dependence on the shortwave infrared rather than red band make it less susceptible to noise during the summer monsoon, when cloud cover is high (Liu et al., 2021a).

Following Liu et al. (2021a), we calculate the day of (1) the midpoint of the post-monsoon fire season and (2) maximum greenness during the monsoon growing season for each district in Punjab and Haryana from 2003-2019. First, we estimate the midpoint of the fire season as the weighted average of the sequence of Julian days, with each day's FRP as the weight. Second, we use cubic splines to smooth the yearly timeseries of NBR or NDVI. We make an initial guess of the day of maximum monsoon greenness as the second of two local maxima of the year; these two maxima represent the timing of winter wheat and monsoon rice maturity. We define a 300-day window around this initial guess to perform the final spline smoothing. We use the 500-m MODIS global land cover product, MCD12Q1, with the University of Maryland (UMD) scheme to retain only agricultural pixels for analysis (Sulla-Menashe et al., 2019). For NBR and NDVI, we further mask out areas with zero active fire observations from 2003-2019 during the post-monsoon period (here defined as September to November). We then assess the spatial correlation between the temporal shifts in the midpoint date of the post-monsoon burning season and peak monsoon greenness for districts in Punjab. Our analysis includes 19 districts, where we

observe at least one temporal shift that is statistically significant at $p < 0.05$. To further examine spatial patterns in the monsoon crop phenology at the MODIS pixel resolution (500 m), we use the MCD12Q2 annual land cover dynamics product, which relies on the Enhanced Vegetation Index (EVI) to estimate the key dates in crop cycles, such as green-up, peak, maturity, and senescence (Gray et al., 2019).

Finally, we evaluate how the temporal shifts in the monsoon growing season and post-monsoon burning relate to irrigation practices. We obtained well data from the India Water Resources Information System (India-WRIS, https://indiawris.gov.in/wris/, last accessed: January 1, 2021). We use the district average groundwater levels in Punjab from 2003-2019. Over 300 wells are monitored in Punjab as of 2019. To estimate the district-level percentage of area irrigated by groundwater relative to canal, we use India census data from the Directorate of Economics and Statistics, Department of Agriculture and Cooperation, Ministry of Agriculture (Dacnet: https://aps.dac.gov.in/LUS/Index.htm).

3.3.2 STILT modeling

We use the Stochastic Time-Inverted Lagrangian Transport (STILT) model (https://uataq.github.io/stilt/) to quantify the air quality impacts due to temporal shifts in the post-monsoon fire season (Fasoli et al., 2018). STILT uses meteorology-driven particle dispersion to generate influence footprints, which can then be convolved with surface emissions to calculate the concentration of chemical species at a given receptor. STILT is based on NOAA's Hybrid Single-Particle Lagrangian Integrated Trajectory (HYSPLIT) model, which uses meteorological fields to track the trajectories of theoretical particles either backward or forward in time (Stein et al., 2015). STILT takes one step further and uses Gaussian weighting to calculate the sensitivity of emissions in each grid cell to the receptor at each time step based on an ensemble of many particles' trajectories, each slightly different due to the stochastic fluctuations applied to simulate turbulent motions in the atmosphere (Fasoli et al., 2018). Compared to forward models like WRF-Chem or GEOS-Chem, STILT provides a computationally efficient approach to test the influence of multiple emissions scenarios, which in this case differ by timing of peak burning (Cusworth et al., 2018).

We drive STILT, version 2, with daily meteorology from the Global Data Assimilation System (GDAS) at 0.5° x 0.5° spatial resolution from 2007-2018 and the Global Forecast System (GFS) at 0.25° x 0.25° spatial resolution in 2019. Following Cusworth et al. (2018) and Liu et al. (2018), for each model run, we send 500 air particles backward in time for 120 hours (5 days), starting from a height of 5 m above ground at the receptor. For our re-

Table 3.1: Locations of receptors / cities used in STILT simulations.

Receptor / City	**State / Province**	**Country**	**Coordinates** (longitude, latitude)	**Population**[1] (in millions)
New Delhi	Delhi	India	77.1°E, 28.7°N	17 (union territory), 26 (metro)
Kanpur	Uttar Pradesh	India	80.33°E, 26.45°N	2.9
Lahore	Punjab	Pakistan	74.36°E, 31.52°N	11
Ludhiana	Punjab	India	75.86°E, 30.9°N	1.6
Bathinda	Punjab	India	74.95°E, 30.21°N	0.3
Jind	Haryana	India	76.3°E, 29.33°N	0.2

[1] The population of Indian cities are from India's 2011 census, while that of Lahore, Pakistan is from Pakistan's 2017 census

gion and time of interest, 500 is a reasonable number of particles for our STILT simulations, since the prevailing meteorology (i.e., slow winds, stable boundary layer, and flat terrain) leads to relatively low variation in the trajectories of different particles. The model domain is defined as 60-90°E and 20-40°N. Cusworth et al. (2018) started each model simulation at 12 p.m. local time to represent the daily smoke $PM_{2.5}$ from agricultural fires. Here we calculate the hourly $PM_{2.5}$ every 3 hours from 0 to 21 h local time from October 1 to November 30 of each year to better account for the diurnal variability in station $PM_{2.5}$ observations.

We generate STILT footprints for six receptor cities across the IGP: New Delhi, Kanpur, Lahore, Ludhiana, Bathinda, and Jind (Table 3.1). These six receptors vary in terms of their population, as well as location and proximity relative to the fire source, and are likely representative of pollution impacts in surrounding areas. To obtain the smoke $PM_{2.5}$ exposure at the receptor, we multiply the sensitivity footprints with fire emissions rates and integrate across all hourly timesteps. For agricultural fire emissions, we use the SAGE-IGP regional inventory (Liu et al., 2020b). SAGE-IGP relies on both satellite observations and household survey data to adjust MODIS FRP for small fires detected by VIIRS, cloud/haze gaps in observations, partial-field burns, and the diurnal cycle of fire activity. When validated against ground-based observations of $PM_{2.5}$ in New Delhi and aerosol loading in Kanpur, STILT simulations with SAGE-IGP perform better than those with global fire emissions inventories (Liu et al., 2020b).

3.3.2.1 Impact of temporal shifts in fire activity on downwind smoke exposure

Peak burning during the 2008-2019 fire seasons on average takes place 1-2 weeks later than during 2003-2007. To estimate the impact of the delayed post-monsoon fire season on downwind smoke exposure, we artificially shift the temporal distribution of each fire season from 2008-2019 by magnitudes ranging from 21 days earlier to 21 days later in 1-day intervals, keeping the total emissions level constant. For this more intensive calculation, we use the footprint sensitivities only for 12 pm local time, following Cusworth et al. (2018). Based on a sensitivity test for New Delhi, our results using 12 pm as the start time of the STILT simulations are likely conservative in terms of the impact on $PM_{2.5}$ but as we will see, consistent with results starting at other hours of the day. By calculating STILT footprints using meteorological conditions from 2007-2019, we can gauge the sensitivity of $PM_{2.5}$ at the receptor to a range of possible meteorological conditions. For each iteration and combination of the temporally shifted fire season and associated meteorology, we estimate the maximum $PM_{2.5}$ from a 21-day rolling mean from September 15 to December 15. In total, we test 43 iterations for each year from 2008-2019, and then apply 13 years of meteorology from 2007-2019, for 559 iterations total for each year's fire emissions at each receptor. We calculate the 21-day rolling mean as our metric to capture the $PM_{2.5}$ relevant to post-monsoon fire activity, 80% of which occur within an approximate 3-week period (Liu et al., 2021a). Specifically, we focus on the impact to smoke $PM_{2.5}$ if the fire seasons had not been delayed such that peak burning hypothetically matched either (1) the average date from 2003-2007 or (2) the earliest peak date among 2003-2007. For each year, we fit a Gaussian curve to the daily FRP timeseries to determine the peak burning date of the post-monsoon burning season (Liu et al., 2020b, 2021a).

3.4 Results and Discussion

3.4.1 Delays in monsoon rice growth led to delays in post-monsoon fires

Across Punjab, we observe a longitudinal gradient in the temporal shifts in both the peak monsoon greenness and midpoint of the post-monsoon burning season, two central metrics discussed in Liu et al. (2021a) (Figure 3.1a-b). Western districts experienced more than two-fold greater temporal shifts than eastern districts. The spatial correlation of $r = 0.71$ ($p < 0.05$) in the district-level shifts of the two metrics suggest that delays in the monsoon growing season may drive those in the post-monsoon burning season (Figure 3.1c). In sensitivity tests, we find that this correlation is consistent ($r = 0.51$ to 0.77, $p < 0.05$) across various breakpoints during the post-

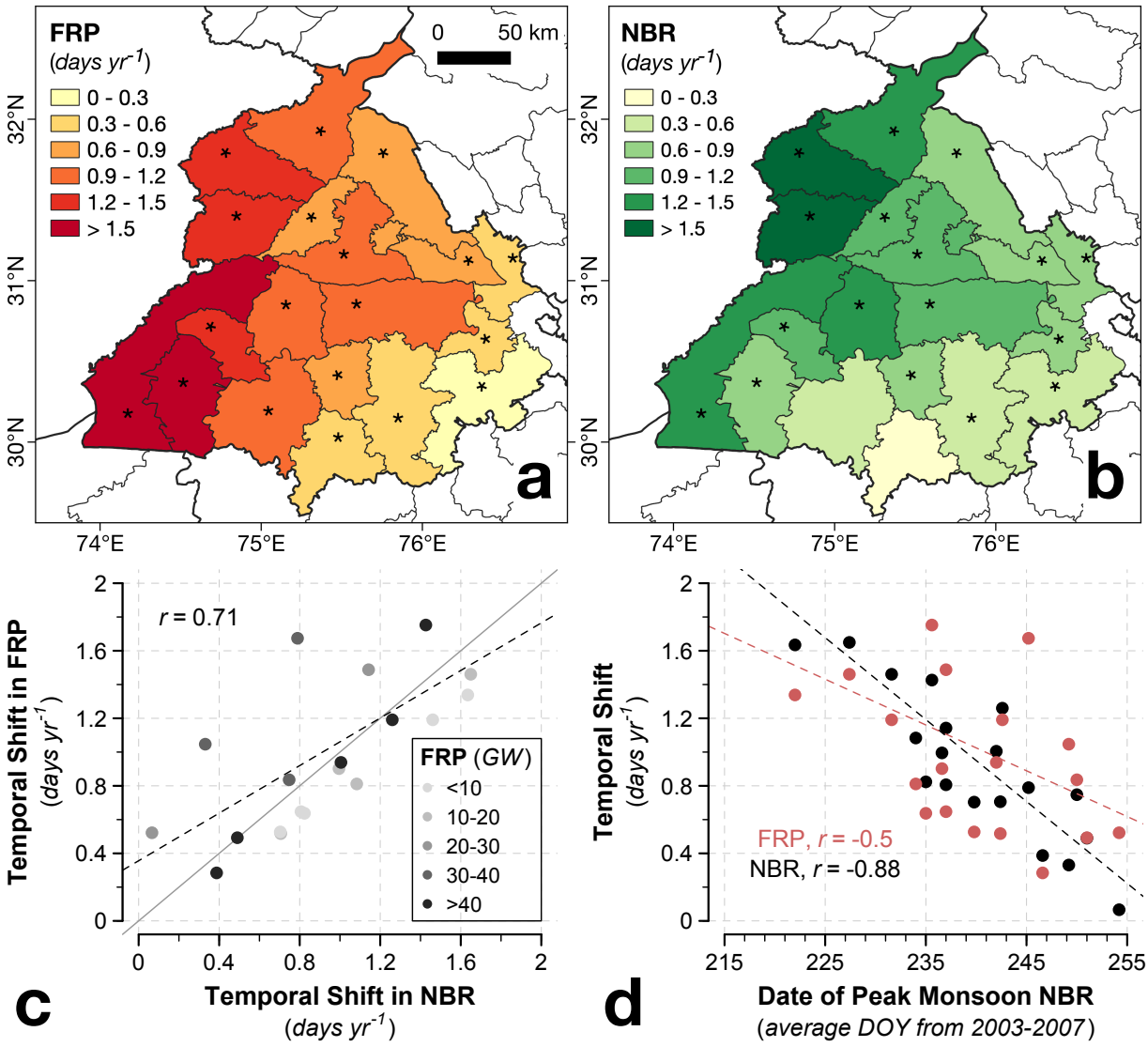


Figure 3.1: Correlation of temporal shifts in post-monsoon fires and peak monsoon greenness by district in Punjab across 2003-2019. We use Fire Radiative Power (FRP) to calculate the midpoint of the post-monsoon fire season and maximum monsoon greenness, indicated by the proxy Normalized Burn Ratio (NBR), to represent the timing of rice maturity. Maps of the district-level temporal shift in (a) FPR and (b) NBR are presented for 19 districts in Punjab. Stars indicate that temporal shift (days yr^{-1}) in FRP or NBR is statistically significant ($p < 0.05$) for that district. Districts without statistically significant temporal shifts in both FRP and NBR are omitted from this analysis. (c) Spatial correlation of the temporal shifts in FRP and NBR in districts shown in (a) and (b). The color of the dots denotes the mean post-monsoon FRP. The solid gray line depicts the 1:1 line. (d) Correlation of the average day of year at peak monsoon NBR from 2003-2007 and the temporal shifts in NBR and FRP. The correlation coefficients, weighted by the agricultural area of each district, are shown inset.

Table 3.2: Correlations between the temporal shifts in the timing of the monsoon growing season and post-monsoon fire season. The correlation coefficient r is calculated for the 19 Punjab districts with statistically significant ($p < 0.05$) temporal shifts in the midpoint of the fire season (using the weighted mean method) and/or peak monsoon greenness (NBR), such as shown in Figures 3.1 and 3.2. All correlations are statistically significant at $p < 0.05$.

		Post-Monsoon Fire Season (FRP)			
		Midpoint (weighted mean)	Midpoint (β=0.5)	Start (β=0.1)	End (β=0.9)
Monsoon Rice Growing Season	*MOD09GA*				
	Peak (NBR)	0.71	0.74	0.66	0.63
	Peak (NDVI)	0.72	0.74	0.66	0.65
	MCD12Q2 (EVI)				
	Green-up	0.73	0.75	0.57	0.71
	Maturity	0.67	0.71	0.58	0.64
	Peak	0.65	0.7	0.58	0.61
	Senescence	0.73	0.77	0.68	0.67
	Dormancy	0.56	0.61	0.51	0.52

monsoon fire season (start, midpoint, and end) and monsoon growing season (green-up, peak, maturity, senescence, and dormancy), derived from multiple greenness indices (NBR, NDVI, and EVI) (Table 3.2). Here we focus on Punjab, but we also find temporal shifts in some districts in Haryana and northern Rajasthan, though the linkage between the delays is less clear in those districts. This may arise from greater spatial intra-district heterogeneity in cropping patterns and use of fire for clearing crop residues.

Further, the average day of peak monsoon greenness from 2003-2007 is negatively correlated with the temporal shifts in post-monsoon fires (r = -0.5, $p < 0.05$) and monsoon greenness (r = -0.88, $p < 0.05$), which indicates that those districts that initially sowed rice the earliest also experienced the greatest cascading delays from paddy sowing to post-monsoon burning within the 2003-2019 period (Figure 3.1d, C.1). The net effect is the closer alignment of the timing of the midpoint of the post-monsoon fire season across districts in later years, as shown by the 53% ($p < 0.05$) overall decrease in the standard deviation of the spatial distribution of the midpoint (Figure C.2). Thus, a higher biomass load is burned within a shorter time window.

One proposed driver of these delays is Punjab's implementation of the Preservation of Subsoil Water Act, 2009, a policy that sets the earliest date by which farmers can sow paddy, which changed from June 10 in 2008 to June 15 in 2014, June 20 in 2018, and June 13 in 2019 (The Indian Express, 2019). From 2008 onward, we find a strong correlation ($p < 0.05$) between changes in the policy-mandated paddy sowing date and satellite-derived timing of the monsoon growing season (r = 0.77) and post-monsoon fires (r = 0.81) (Figure 3.2). This

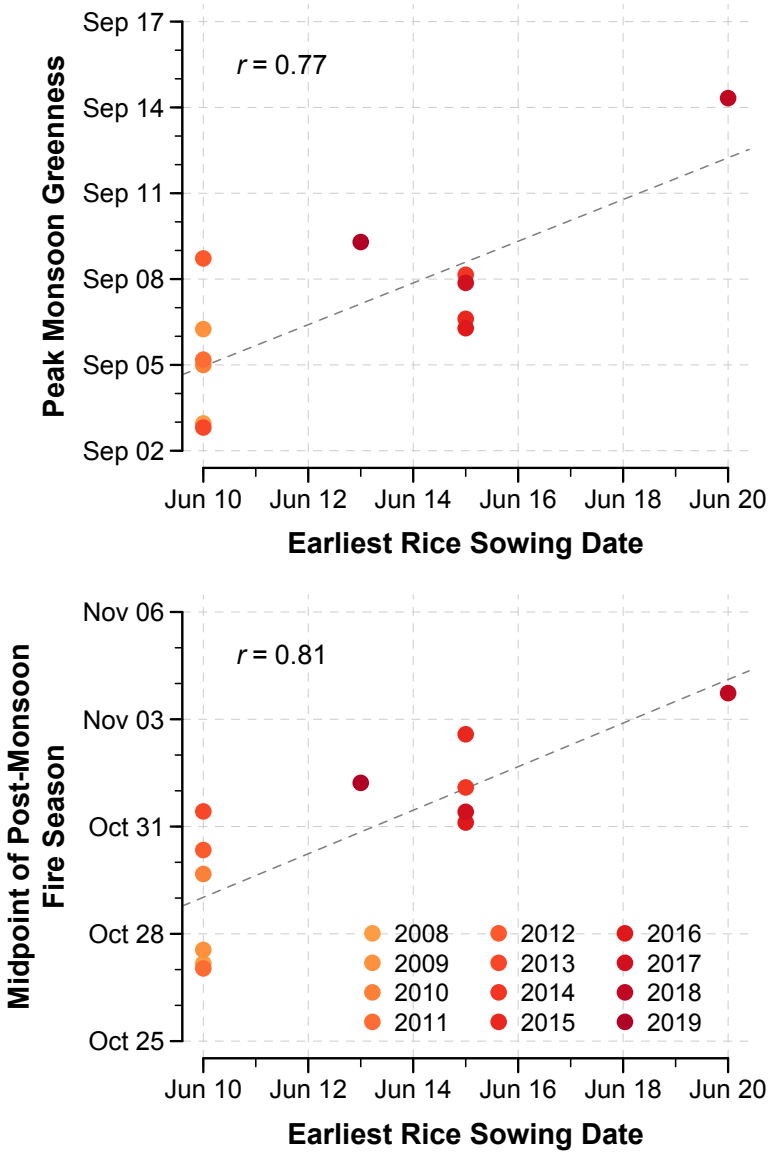


Figure 3.2: Correlation between the earliest rice sowing dates and timing of the peak monsoon greenness and midpoint of the post-monsoon fire season in Punjab from 2008-2019: The earliest rice paddy sowing dates mandated by the Punjab Preservation of Sub-Soil Water Act are shown with respect to the satellite-derived (a) peak monsoon greenness and (b) midpoint of the post-monsoon fire season. Dates for the peak monsoon greenness and midpoint of the post-monsoon fire season are averaged across the districts in Punjab shown in Figure 3.1, weighted by the districts' agricultural area. The color of the dots corresponds to the year. The correlation coefficients are shown inset and are statistically significant at $p < 0.05$.

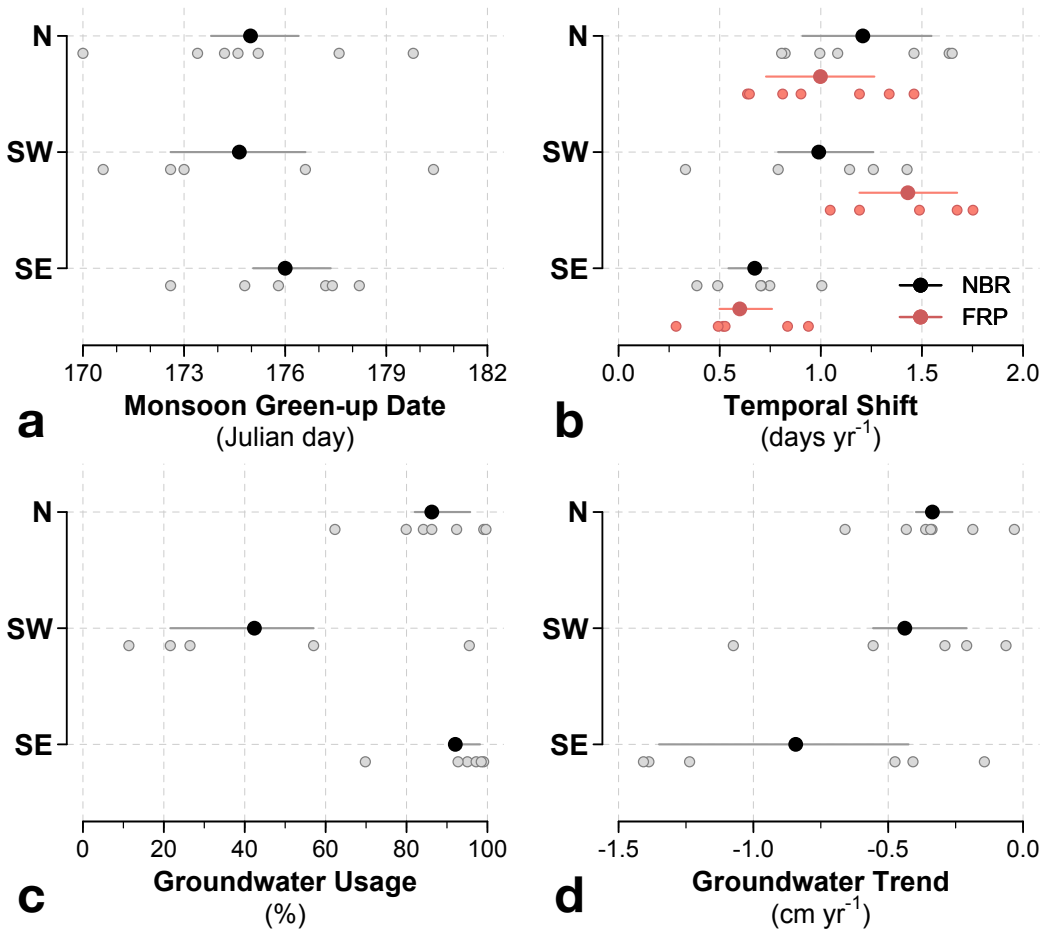


Figure 3.3: Regional summary of district-level trends in phenology, fires, and groundwater levels in Punjab, India: (a) monsoon green-up date from 2003-2007, (b) temporal shifts in the timing of the peak monsoon greenness (i.e., maximum NBR) and midpoint of the post-monsoon fire season (i.e., weighted average using FRP) from 2003-2019, denoted by black and red, respectively, (c) groundwater usage as a percentage of total area irrigated by wells and canals, and (d) groundwater level trends from 2008-2019. Here Punjab is split into three regions: north (N), southwest (SW), and southeast (SE). Solid dots represent the average across districts in that region, and lines represent the 25th to 75th percentile range. Light gray dots represent values for individual districts.

correlation suggests that farmers generally adhered to the groundwater policy. While the sample size is small, we see that the anomaly in the late 2018 growing season and subsequent fires, followed by the 2019 return to the median are consistent with changes in the mandated paddy sowing dates.

In addition to the spatial heterogeneity in the temporal shifts in the monsoon growing season and post-monsoon fires, we also find spatial variation in groundwater usage and trends (Figure 3.3). For simplicity, we divide Punjab into three regional clusters (north, southwest, and southeast) to illustrate these spatial differences. Observations show that districts in southeast — relative to those districts in the north and southwest — initially sowed paddy the latest (Figure 3.3a) and experienced the smallest temporal shifts (Figure 3.3b) but counterintuitively had the highest groundwater usage (Figure 3.3c) and most severe groundwater depletion after the policy

implementation (Figure 3.3d). Two potential scenarios may explain these observations: (1) the groundwater policy was effective — i.e., districts that needed to drastically shift rice sowing dates to align with that mandated by the policy, indicated by large temporal shifts, subsequently experienced the least severe groundwater depletion; or (2) the policy was inefficient — i.e., districts least affected by the policy, indicated by small temporal shifts, continued to suffer from severe groundwater depletion. If the groundwater policy broadly stemmed falling groundwater levels but failed to target districts that are most in need, it is possible that the policy was both effective and inefficient. Further observational data, such as survey data with large sample sizes, are needed to robustly link the groundwater policy and its intended effect at the district level to changes in irrigation water management practices. Confounding factors include variation in the type of rice grown (i.e., basmati versus coarse grain), soil texture, and recent shifts in the crops planted (e.g., cotton to rice).

3.4.2 Sensitivity of downwind smoke exposure to timing of post-monsoon fires

We first focus on the effects of temporal shifts of burning on downwind smoke exposure in New Delhi, the most populous megacity in India. As STILT footprints show, air quality in New Delhi is sensitive to fires in Punjab and Haryana due to prevailing northwesterly winds that are consistent year after year (Figure C.5). Figure 3.4 shows an example of the ratio of modeled smoke $PM_{2.5}$ in Delhi for the 2017 post-monsoon fire season that is hypothetically shifted forward and backward in time relative to the observed fire season in daily increments. Generally, smoke $PM_{2.5}$ decreases as the fire season shifts earlier and increases as the fire season shifts later.

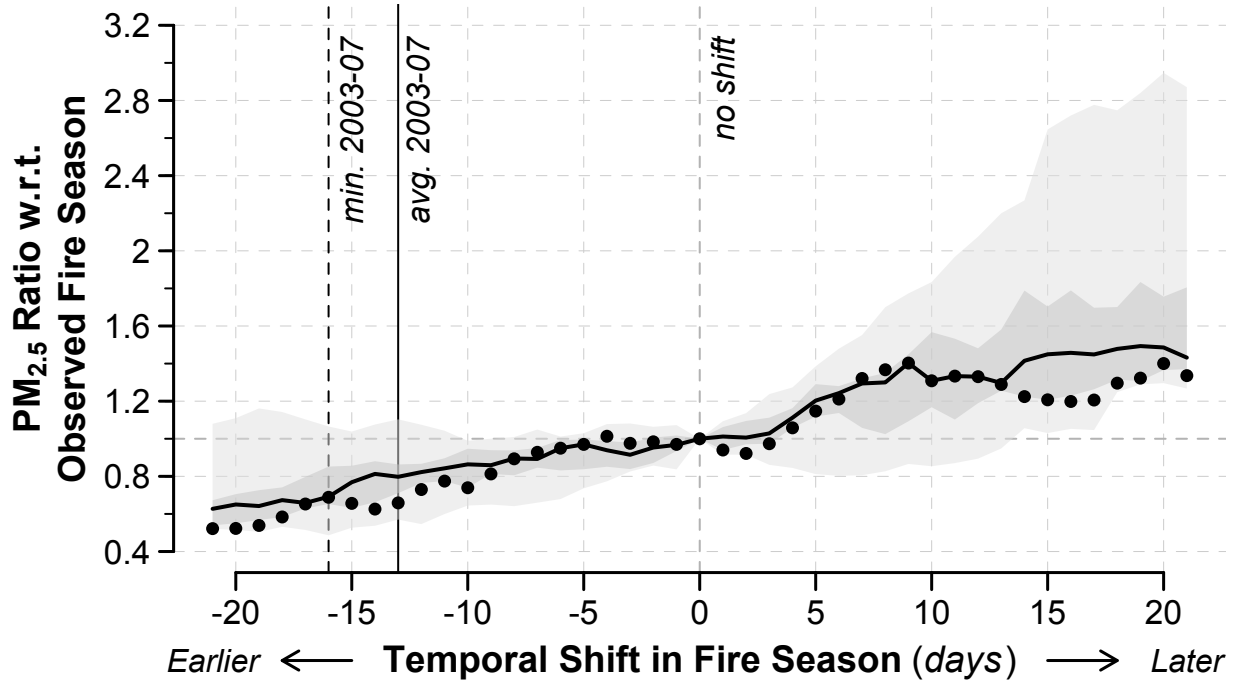


Figure 3.4: Effect of temporal shifts in the post-monsoon agricultural fire season on downwind $PM_{2.5}$ in New Delhi in 2017. The response of seasonal maximum $PM_{2.5}$ concentrations is shown for hypothetical shifts in the fire season from 21 days earlier to 21 days later, for 2017 fire emissions and a range of meteorological scenarios. For each scenario, we calculate the maximum smoke $PM_{2.5}$ in New Delhi from a 21-day rolling mean from October 1 to November 30 for a hypothetical shift in the fire season relative to the one observed. The median ratio derived from varying STILT footprint sensitivities by meteorology from 2007-2019 is shown as the solid curve. The dark gray envelope shows the 25th-75th percentiles in ratios, and the light gray envelope shows the 5th-95th percentiles. Dots indicate the relative smoke $PM_{2.5}$ using only 2017 meteorology. The vertical black lines show the change in $PM_{2.5}$ if the 2017 post-monsoon fire season is shifted earlier to two baselines: (1) average from 2003-2007 (solid) and (2) earliest peak date among 2003-2007 (dashed).

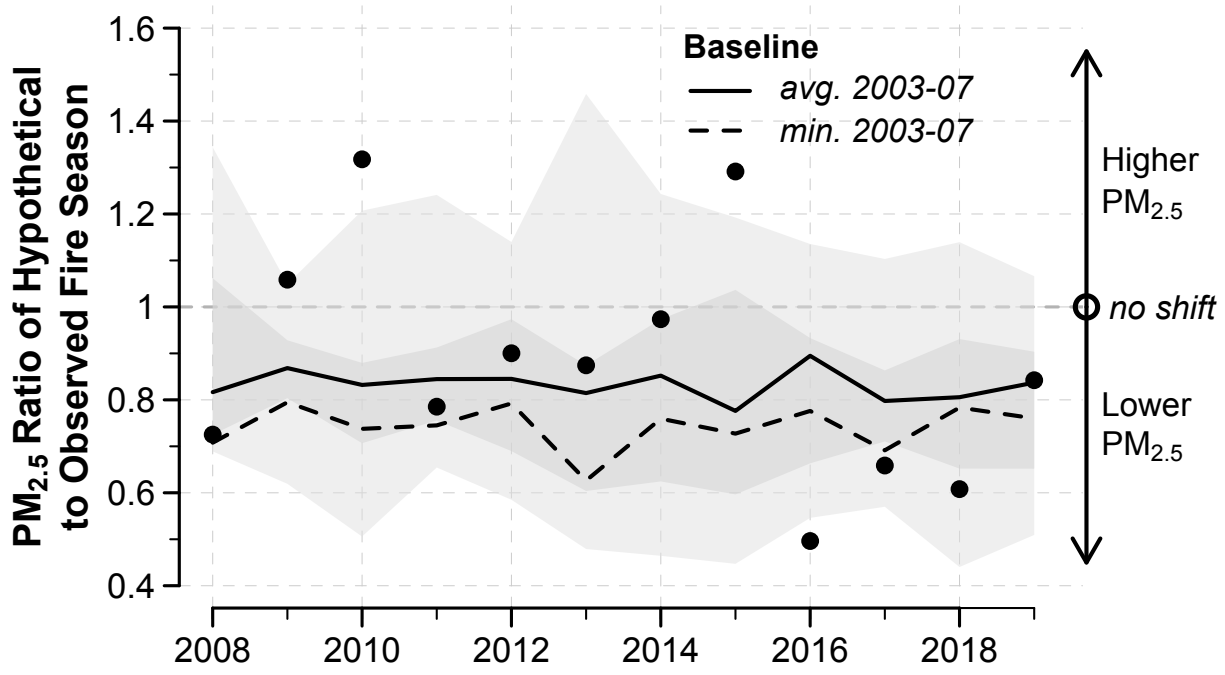


Figure 3.5: Effect on $PM_{2.5}$ in New Delhi from 2008-2018 if the post-monsoon agricultural fire season had not experienced delays relative to the 2003-2007 period. The response of seasonal $PM_{2.5}$ concentrations is shown for two different hypothetical shifts in the fire season for a range of meteorological scenarios. For each year, that season's fire emissions are shifted earlier by the number of days between the peak burning day of each fire season and that of two baselines: (1) average from 2003-2007 (solid line) and (2) earliest during 2003-2007 (dashed line). Smoke $PM_{2.5}$ in New Delhi is calculated as the maximum of 21-day rolling means from October 1 to November 30 for a hypothetical fire season that is shifted earlier relative to one that was observed. The medians derived from varying STILT footprint sensitivities from 2007-2019 are shown as the solid and dashed lines. Dots indicate the smoke $PM_{2.5}$ estimated with the meteorology and fire emissions of the given year relative to that for a hypothetical fire season aligned with the 2003-2007 average peak timing. Shaded envelopes denote the 25th-75th percentile range in relative smoke $PM_{2.5}$ (dark gray) and the 5th-95th percentile range (light gray), again using fire emissions of the given year and the 2003-2007 peak timing, but meteorology in all available years from 2008-2019.

If the 2008-2019 post-monsoon burning seasons had not been delayed and occurred earlier by 1-2 weeks on par with the average timing of peak fires observed in 2003-2007, the maximum 21-day mean $PM_{2.5}$ in New Delhi would on average be reduced by 12% (min: -50%, max: +32%) (Figure 3.5). This result is consistent across various start hours of the day for the STILT simulations, with our choice of 12 pm likely leading to conservative estimates (Figure 3.6). The range of this response to the temporal shift in burning indicates that year-to-year meteorology drives substantial variability in downwind $PM_{2.5}$. Nonetheless, in nine of the 12 years from 2008-2019, Delhi would have experienced lower $PM_{2.5}$ in the absence of the shift toward later peak burning (Figure 3.5). Next, we apply a range of meteorology-driven footprint sensitivities (2007-2019) to each year's fire emissions. We find that the median $PM_{2.5}$ would be reduced by 17% (11-22%), compared with the business-as-usual scenario of delayed burning. If we further shift fire emissions by another 4 days earlier such that peak burning matches

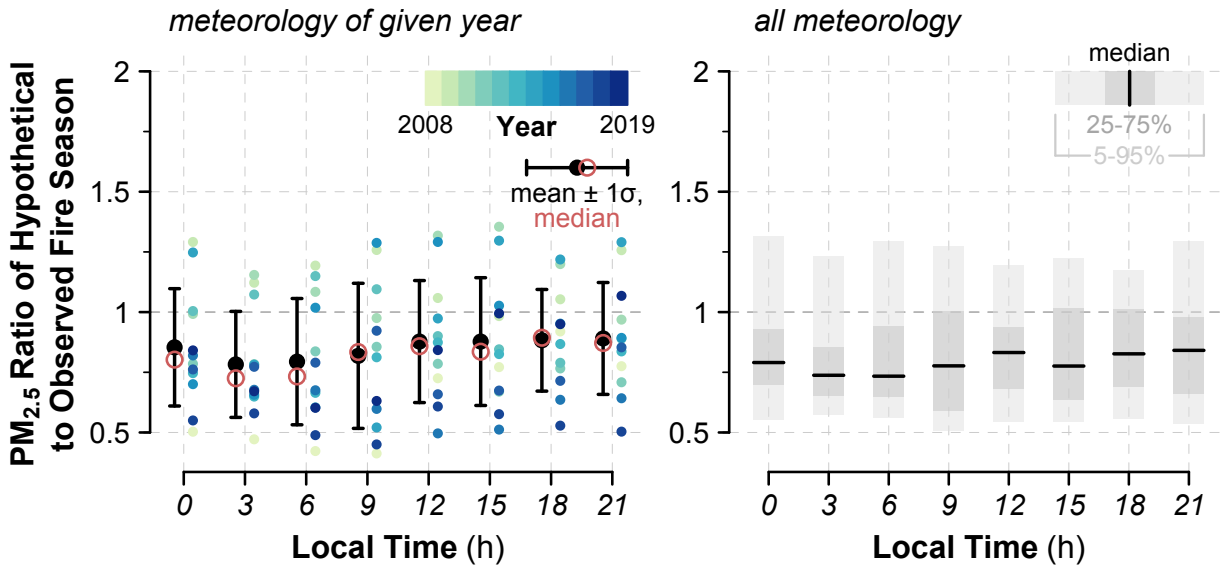


Figure 3.6: Effect on $PM_{2.5}$ in New Delhi from 2008-2019 if the post-monsoon agricultural fire season had not experienced delays relative to the 2003-2007 period: Fire emissions are shifted earlier by the number of days between the peak burning day of each fire season and that of the 2003-2007 average. Unlike Figure 3.5, here the STILT-simulated $PM_{2.5}$ ratio is shown for eight different local hours of the day: 0, 3, 6, 9, 12, 15, 18, and 21 h. (Left panel) Maximum smoke $PM_{2.5}$ from a 21-day rolling mean from October 1 to November 30 for a hypothetical fire season that is shifted earlier relative to one that was observed. For each hour, the $PM_{2.5}$ ratio is shown as the median (red circles), mean ± 1σ (black dots and bars), and for individual years (colored dots). (Right panel) The fire emissions of each year are applied to STILT sensitivities for all years from 2007-2019 to show a range of possible meteorological conditions. The $PM_{2.5}$ ratio is averaged across meteorological years by quantiles. The horizontal bars show the median for each hour; the dark gray envelopes show the 25th-75th percentile range, and the light gray envelopes show the 5th-95th percentile range.

that of the earliest peak date from 2003-2007, the decrease in median $PM_{2.5}$ would be ~1.5 times as high at 26% (20-37%). Conversely, if the post-monsoon fire season continues to shift later, we find that the $PM_{2.5}$ burden in downwind areas will likely increase further under our 13-year range of meteorological conditions.

Figure 3.7 illustrates why delays in the post-monsoon fire season — without any consideration of increases in fire activity — can lead to increased $PM_{2.5}$ in New Delhi. Afternoon mixing layer heights in New Delhi decrease from ~1900 m in October to ~1200 m by mid-November, pointing to weak ventilation conditions that favor aerosol buildup near the surface (Figure 3.7a). Simultaneously, the spatial average of STILT sensitivity for New Delhi, weighted by fire emissions, steadily rises during this period, suggesting that air quality in New Delhi is increasingly susceptible to degradation from regional fires with time (Figure 3.7b). Due to the delays in the fire season, peak fires occur when New Delhi is 41% more sensitive to regional fires in 2008-2019 than in 2003-2007. As the post-monsoon transitions to winter, weak winds, cooler temperatures, and a shallow boundary layer may also drive a steady increase in background $PM_{2.5}$, which would further reduce air quality (Appendix C.2.2, Figure C.6). Further analysis is needed to dissect how different meteorological parameters (i.e., winds, boundary layer dynamics, diurnal variability, and temperature inversion) contribute to air quality degradation.

Next, we examine how air quality responds to delays in fire activity in five other cities across the IGP: Kanpur, Lahore, Ludhiana, Bathinda, and Jind (Table 3.2; Figure 3.8). These six cities represent a diverse sample of receptors that range in proximity and direction relative to the fire-dominant regions. This is evident in the range in 21-day average smoke $PM_{2.5}$ of 15-173 $\mu g\ m^{-3}$ experienced at each receptor (Figure 3.9, Table C.2). Figure 3.8 shows the spatial pattern of each city's mean STILT sensitivity, weighted by the daily smoke $PM_{2.5}$ at the receptor. We find that if post-monsoon fires had not been delayed during 2008-2019, receptors that are downwind and close to the fire source (i.e., Bathinda, Jind, and New Delhi) — and with the highest 21-day average smoke $PM_{2.5}$ – consistently see decreases in smoke $PM_{2.5}$ of 11-21% on average (Figure 3.10, Table C.2). In contrast, the effect of the fire season delays on smoke $PM_{2.5}$ is highly variable from year to year in Kanpur, Lahore, and Ludhiana, where smoke $PM_{2.5}$ is more sensitive to changes in meteorology. Specifically, Lahore and Ludhiana are often upwind of the fires due to prevailing northwesterly winds (Liu et al., 2018; Patel et al., 2021), while Kanpur is the farthest receptor from the fire source.

Our modeling design has some limitations. For our hypothetical simulations of smoke $PM_{2.5}$ where fire emissions are shifted backward in time, we assume that fire emissions shift uniformly across all grid cells. In reality, as seen in our satellite-based analysis, western districts in northwest India experienced greater delays in post-

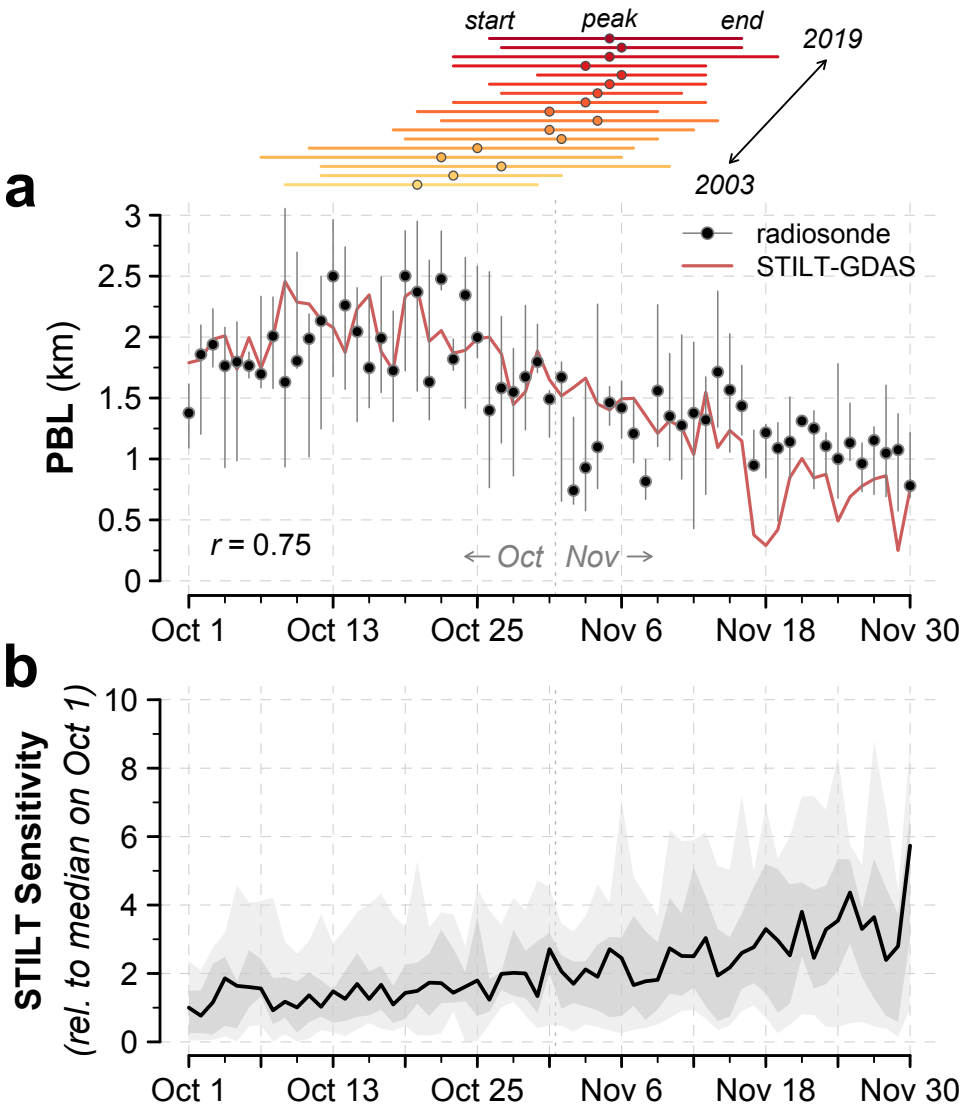


Figure 3.7: Compression of daily afternoon boundary layer heights and increase in average STILT sensitivities for New Delhi during the post-monsoon burning season: (a) The median PBL heights from radiosonde data (black dots) and from STILT with GDAS meteorology (red line) at 5:30 pm local time from 2003-2019. Gray segments depict the 25th-75th percentiles of the radiosonde data, and the correlation coefficient between radiosonde and STILT-GDAS PBL is shown inset. Segments at the top show the timing of the start, peak, and end of the post-monsoon burning season in Punjab and Haryana from 2003-2019, with warmer colors indicating later years. (b) Daily average STILT sensitivity footprints for New Delhi are weighted by the average 2003-2019 post-monsoon SAGE-IGP dry matter emissions. The STILT sensitivities are shown as normalized values relative to the mean STILT sensitivity on October 1. The black line indicates normalized median STILT sensitivity across 2007-2019, while the dark gray envelope denotes the 25th-75th percentiles, and the light gray envelope shows the 5th-95th percentiles.

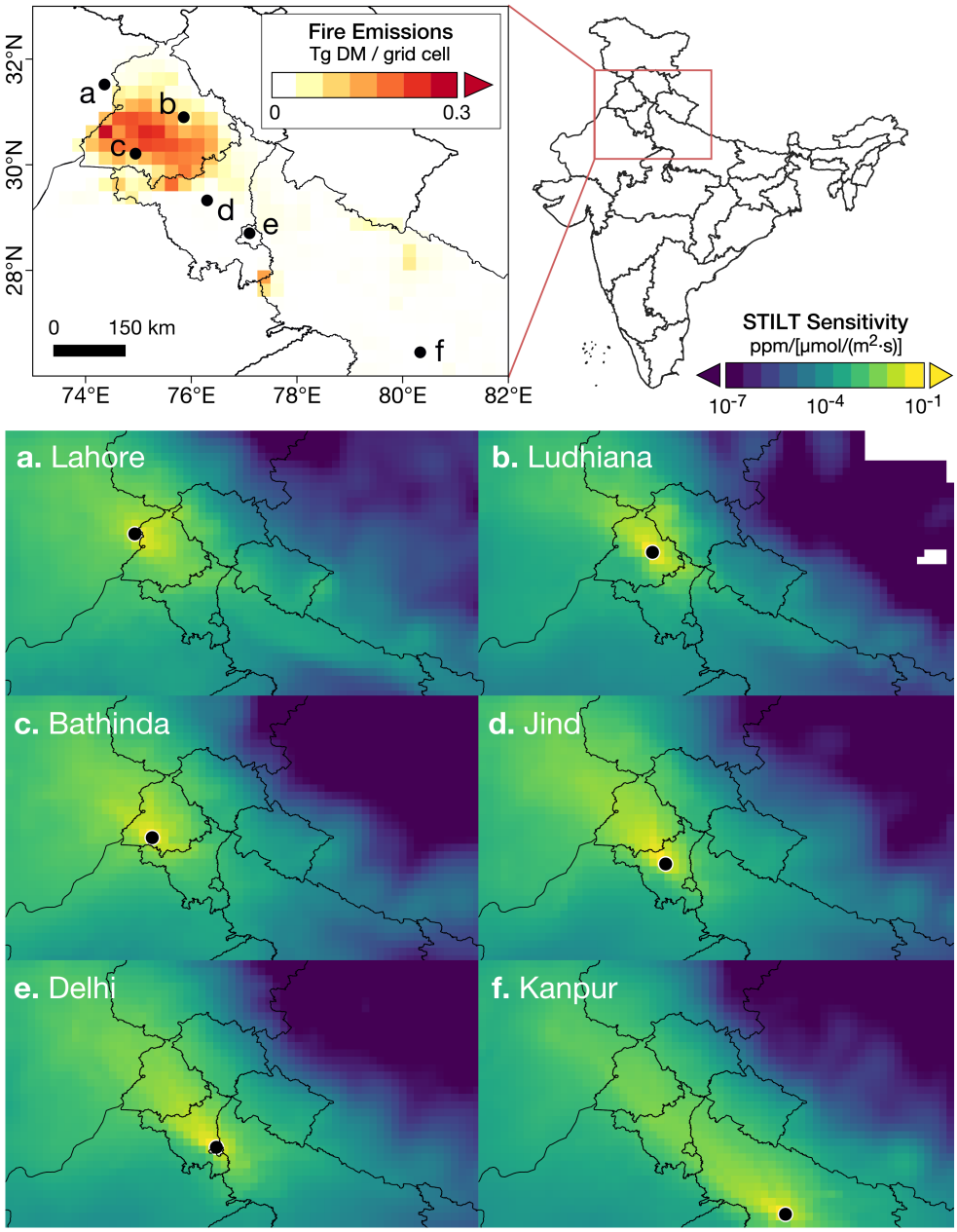


Figure 3.8: STILT sensitivity footprints for six receptors: (Top panel) Location of the six selected STILT receptors, overlaid on SAGE-IGP post-monsoon dry matter burned, averaged across 2008-2019: (a) Lahore, (b) Ludhiana, (c) Bathinda, (d) Jind, (e) New Delhi, and (f) Kanpur. (Bottom panels) STILT sensitivities are averaged first from Oct 1 to Nov 30 of each year, weighted by the smoke $PM_{2.5}$ at the receptor, and then across 2008-2019. Note that the color bar increments for the STILT sensitivities are logarithmic.

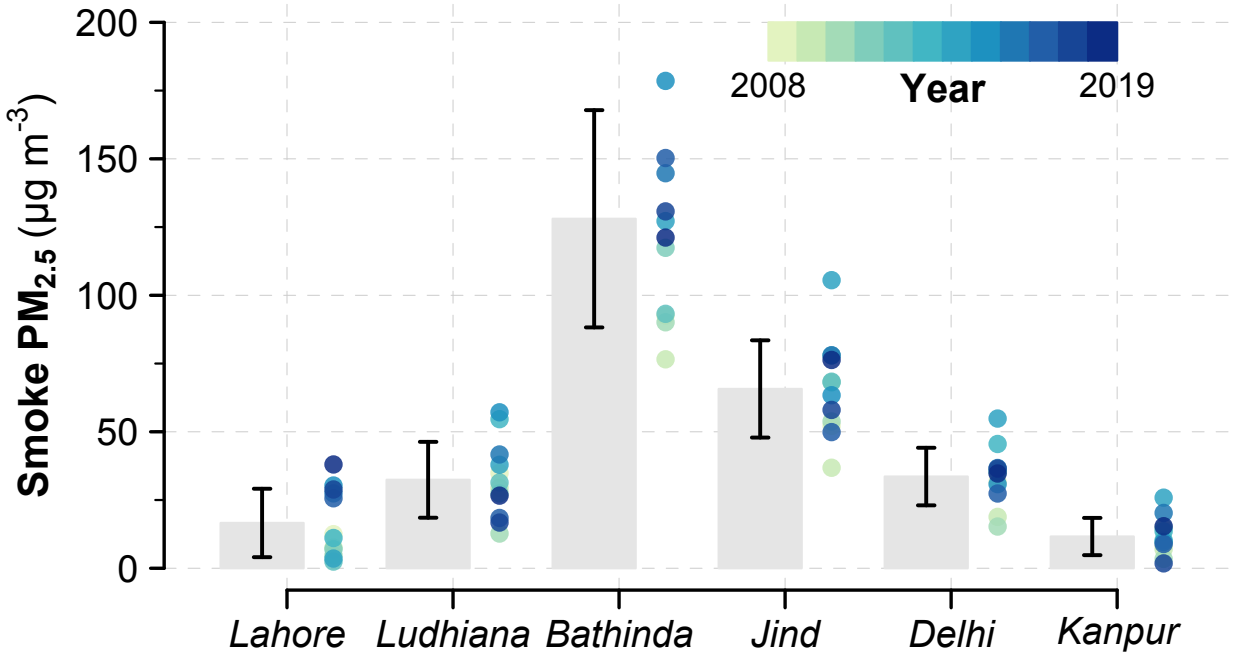


Figure 3.9: $PM_{2.5}$ concentrations in six cities during the post-monsoon agricultural fire season from 2008-2019: Maximum smoke $PM_{2.5}$ from a 21-day rolling mean from October 1 to November 30. Bars depict the average from 2008-2019, and segments denote ±1σ. Dots denote the maximum 21-day rolling mean $PM_{2.5}$ in each year, with lighter colors representing earlier years and darker colors, later years. Here the years of the fire emissions and meteorology match, and no additional meteorological conditions are considered.

monsoon fire activity than eastern districts (Figure 3.1a). While our atmospheric modeling approach simplifies this heterogeneity of the observed delays, the consistent decreases in smoke $PM_{2.5}$ as fire emissions gradually shift earlier in 1-day intervals — and increases in smoke $PM_{2.5}$ with further delays — lend confidence to our results (Figure 3.4). The magnitude of fire emissions is also not well-constrained, as satellites may miss fires with low thermal anomalies and those that occur outside the overpass times and during periods with thick haze and smog (Liu et al., 2021a). However, this study focuses on relative changes in $PM_{2.5}$, for which the magnitude of fire emissions is less important. Finally, while we show that there are associations between the groundwater policy, delays in monsoon season sowing date, and delays in burning at the end of the monsoon season, it is possible that other factors, such as changes in crop type or variety, may explain some of these associations. Future work should examine the causal relationship between these variables using large scale survey data and/or causal inference methods.

3.4.3 Contextualizing the importance of delays in the post-monsoon fire season

Sembhi et al. (2020) suggest that the impact of the delay in the post-monsoon fire season on regional air quality

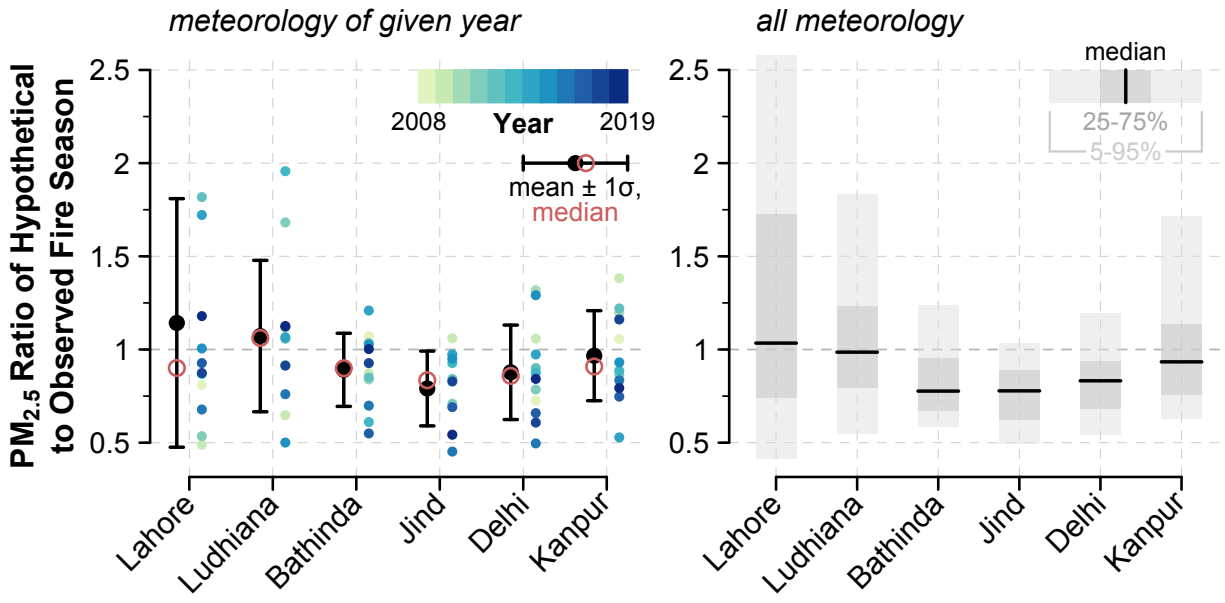


Figure 3.10: Effect on $PM_{2.5}$ in six cities from 2008-2019 if the post-monsoon agricultural fire season had not experienced delays relative to the 2003-2007 period: Fire emissions are shifted earlier by the number of days between the peak burning day of each fire season and that of the 2003-2007 average. (Left panel) Maximum smoke $PM_{2.5}$ from a 21-day rolling mean from October 1 to November 30 for a hypothetical fire season that is shifted earlier relative to one that was observed. For each city, the $PM_{2.5}$ ratio is shown as the median across all years (red circles), mean ± 1σ (black dots and bars), and for individual years (colored dots). Cities are arranged from east to west along the x-axis. (Right panel) Same as left panel, except the fire emissions of each year are applied to STILT sensitivities for all years from 2007-2019 to show the impact of a range of possible meteorological conditions. The $PM_{2.5}$ ratio is averaged across meteorological years by quantiles. The horizontal bars show the median; the dark gray envelopes show the 25th-75th percentile range, and the light gray envelopes show the 5th-95th percentile range.

may be small relative to that of the increase in fire activity or meteorological variability. Under a larger range of meteorological conditions, our results generally show a consistent decrease in smoke $PM_{2.5}$ had the fire season been earlier; the $PM_{2.5}$ decreases are robust in Jind, Bathinda, and New Delhi, three downwind receptors that experience high 21-day mean smoke $PM_{2.5}$ of 44-173 $\mu g\ m^{-3}$. Additionally, two contextual factors may enhance the importance of the delay to regional air pollution mitigation strategies: (1) the linkage between the increase and delay in fire activity and (2) the superposition of high smoke $PM_{2.5}$ on increased background $PM_{2.5}$ with potential aerosol-radiation feedbacks. Gautam et al. (2021) and Pan et al. (2015) previously underscored the role of secondary aerosol formation in the context of heavy aerosol pollution in northern India. We describe these factors in greater detail below.

First, the increase and delay in fires are intrinsically linked — that is, the cascading delays in the rice growing season and post-monsoon burning compress the harvest-to-sowing window, driving further use of fire as farmers attempt to efficiently clear their fields of crop residues (Liu et al., 2020b). Consequently, fire activity is particularly intense later in the fire season in early to mid-November (Liu et al., 2021a), when thick haze and smog can obscure fires from satellite detection and lead to underestimates in fire emissions (Cusworth et al., 2018; Liu et al., 2020b). Several factors — including the delay in the fire season, increasing use of combine harvesters, and increasing crop production — likely all drive the overall increase in fire activity (Jethva et al., 2019; Liu et al., 2021a). It is difficult to disentangle the influence of each factor, as farmers often cite multiple, inter-connected reasons for burning rice residues, including saving time and cost, overcoming the short harvest-to-sowing transition window, labor shortages, and lacking technology and incentives to manage the residues (Bhuvaneshwari et al., 2019; Liu et al., 2020b).

Second, background $PM_{2.5}$ from primarily anthropogenic pollution sources increases from post-monsoon to winter, at least in part because of meteorological conditions favoring pollution buildup. For example, we find that the background $PM_{2.5}$ steadily increased by 1.06-1.66 $\mu g\ m^{-3}$ per day in New Delhi from October to December, though this apparent increase may not be captured by standard atmospheric modeling frameworks (Figures C.6-7; Appendix C.2.2). Superposing smoke $PM_{2.5}$ on higher background $PM_{2.5}$ later in the burning season increases the risk of extremely polluted days (>250 $\mu g\ m^{-3}$), when wide-reaching emergency measures are taken to protect public health and safety, such as by cancelling flights, halting construction, and closing schools (The Guardian, 2017; The Times of India, 2017). As experienced in early-to-mid November in 2017, the buildup of smoke aerosols in northwest India can lead to both large spikes in $PM_{2.5}$ concentrations

and regional smog that persists into the early afternoon, a phenomenon typically observed in winter (Gautam et al., 2007, 2021; Ghude et al., 2017; Liu et al., 2021a). Due to the heterogeneity in the post-monsoon fire season delay across districts, the timing of burning across all districts is now more closely aligned, increasing regional smoke concentrations on peak burning days. Thus, models such as that in Sembhi et al. (2020) may not have captured the full impact of the delayed fire season on downwind $PM_{2.5}$. In addition, the positive feedback of aerosol-radiation interactions, by strengthening temperature inversions and increasing boundary layer stability, may have further enhanced $PM_{2.5}$ concentrations, as has been previously examined over China (Gao et al., 2015; Miao et al., 2019; Qiu et al., 2017; Wang et al., 2018a,b). For north India, Gautam et al. (2021) used satellite, ground-based, and reanalysis data to show that a decadal trend in aerosol-induced warming potentially strengthened lower tropospheric stability and increased smog-heavy, low visibility days. Due to computational cost, many atmospheric modeling studies do not account for two-way aerosol interactions with meteorology (Li et al., 2017c; Petäjä et al., 2016). Secondary aerosol formation, an important driver of severe haze episodes (Li et al., 2017c) — particularly from fires (Palm et al., 2020) — is also not well-constrained in models and in modeled representations of smoke loading which has been previously underscored in multi-model analyses focusing on north India (Pan et al., 2015).

3.5 Conclusion

In summary, we present evidence that delays in the monsoon rice growing season are strongly associated with similar delays in the post-monsoon burning season, resulting in a cascading effect that further degrades downwind air quality. Along with weak northwesterly winds during the post-monsoon, this is driven by the lower boundary layer and cooler surface air temperatures typically observed in November. We find that in the absence of the delay in biomass burning during 2008-2019, cities that are both downwind and near the fire source — New Delhi, Bathinda, and Jind — would have consistently seen 11-21% less smoke $PM_{2.5}$ than occurred if the same fires happened earlier in the season. Some of the range of uncertainty arises from the influence of plausible meteorological conditions, i.e., variability in wind patterns and boundary layer heights that influence the sensitivity of the receptor to smoke; for example, in New Delhi, we find that $PM_{2.5}$ would have on average been reduced by 12% from 2008-2019, but the year-to-year range varies from -50% to +32%. However, despite variable meteorology, nine of the 12 years examined would have experienced lower $PM_{2.5}$ with had there been no delays in burning. While we show that the delays alone have led to increased $PM_{2.5}$ in downwind areas, the later fire sea-

son also drives further fire activity, thus compounding the net negative impact on $PM_{2.5}$. Our work suggests that allowing earlier sowing dates, particularly in districts in Punjab where delays in post-monsoon fire season have occurred with less groundwater depletion, could improve air quality in north India while conserving groundwater.

4

Diagnosing spatial biases and uncertainties in global fire emissions inventories: Indonesia as regional case study

4.1 Abstract

Models of atmospheric composition rely on fire emissions inventories to reconstruct and project impacts of biomass burning on air quality, public health, climate, ecosystem dynamics, and land-atmosphere exchanges. Many such global inventories use satellite measurements of active fires and/or burned area from the Moderate Resolution Imaging Spectroradiometer (MODIS). However, differences across inventories in the interpretation of satellite imagery, the emissions factors assumed for different components of smoke, and the adjustments made for small and obscured fires can result in large regional differences in fire emissions estimates across inventories. Using Google Earth Engine, we leverage 15 years (2003-2017) of MODIS observations and 6 years (2012-2017) of observations from the higher spatial resolution Visible Imaging Infrared Radiometer Suite (VIIRS) sensor to develop metrics to quantify five major sources of spatial bias or uncertainty in the inventories: (1) primary reliance on active fires versus burned area, (2) cloud/haze burden on the ability of satellites to "see" fires, (3) fragmentation of burned area, (4) roughness in topography, and (5) small fires, which are challenging to detect. Based on all these uncertainties, we devise comprehensive "relative fire confidence scores," mapped globally at 0.25° x 0.25° spatial resolution over 2003-2017.

We then focus on fire activity in Indonesia as a case study to analyze how the choice of a fire emissions inventory affects model estimates of smoke-induced health impacts across Equatorial Asia. We use the adjoint of

the GEOS-Chem chemical transport model and apply emissions of particulate organic carbon and black carbon (OC+BC smoke) from five global inventories: Global Fire Emissions Database (GFEDv4s), Fire Inventory from NCAR (FINNv1.5), Global Fire Assimilation System (GFASv1.2), Quick Fire Emissions Dataset (QFEDv2.5r1), and Fire Energetics and Emissions Research (FEERv1.0-G1.2). We find that modeled monthly smoke $PM_{2.5}$ in Singapore from 2003-2016 correlates with observed smoke $PM_{2.5}$, with r ranging from 0.64-0.84 depending on the inventory. However, during the burning season (July to October) of high fire intensity years (e.g., 2006 and 2015), the magnitude of mean Jul-Oct modeled smoke $PM_{2.5}$ can differ across inventories by more than 20 $\mu g\ m^{-3}$ (> 500%). Using the relative fire confidence metrics, we deduce that uncertainties in this region arise primarily from the small, fragmented fire landscape and very poor satellite observing conditions due to clouds and thick haze at this time of year. Indeed, we find that modeled smoke $PM_{2.5}$ using GFASv1.2, which adjusts for fires obscured by clouds and thick haze and accounts for peatland emissions, is most consistent with observations in Singapore, as well as in Malaysia and Indonesia. Finally, we develop an online app called FIRE-CAM for end-users of global fire emissions inventories. The app diagnoses differences in emissions among the five inventories and gauges the relative uncertainty associated with satellite-observed fires on a regional basis.

4.2 Introduction

4.2.1 Global fire emissions inventories: role in modeling studies and methodological differences

Models of atmospheric composition depend on global fire emissions inventories to reconstruct and project the impacts of biomass burning on air quality (Cusworth et al., 2018), public health (Crippa et al., 2016; Koplitz et al., 2016), climate (Rogers et al., 2015; Tosca et al., 2013), ecosystem dynamics (Yi et al., 2014), and land-atmosphere exchanges (Prentice et al., 2011). Many regional and global modeling studies consider only one global fire emissions inventory as input primarily to limit computational cost (Crippa et al., 2016; Kim et al., 2015; Koplitz et al., 2016; Maasakkers et al., 2016; Marlier et al., 2019). End-users may simply choose an inventory based on spatio-temporal resolution, near-real-time availability, or keep the default inventory imposed in some chemical transport models (CTM). However, disagreements in the magnitude and temporal variability of emissions among inventories can significantly impact model estimates of variables relevant to air quality (Cusworth et al., 2018), public health (Koplitz et al., 2018b), or the budgets of atmospheric species (Heymann et al.,

2017; Li et al., 2019; Shi et al., 2015; Zhang et al., 2014b). Thus, it is important to understand the underlying causes for differences in both the magnitude and spatio-temporal variability of fire emissions in order to better inform fire prediction (Chen et al., 2017), land management decisions (Marlier et al., 2019), and other applications. While previous studies have identified regional discrepancies among various global fire emissions inventories (Li et al., 2019; Shi et al., 2015), here we also construct metrics to diagnose such discrepancies, and we present the online app FIRECAM to allow end-users to rapidly compare inventories across the globe and view the metrics.

Five global fire emissions inventories are widely used in modeling studies: (1) Global Fire Emissions Database (GFED) (van der Werf et al., 2017), (2) Fire Inventory from NCAR (FINN) (Wiedinmyer et al., 2011), (3) Global Fire Assimilation System (GFAS) (Kaiser et al., 2012), (4) Quick Fire Emissions Dataset (QFED) (Darmenov & da Silva, 2013), and (5) Fire Energetics and Emissions Research (FEER) (Ichoku & Ellison, 2014) (Table 4.1). Estimates of fire emissions generally follow the "bottom-up" (e.g. GFED, FINN) or "top-down" approach (e.g. QFED, GFAS, FEER). In this study, we broadly define "bottom-up" as burned area-based and "top-down" as fire energy-based. The bottom-up burned area approach in GFED and FINN is based on MODIS burned area (MCD64A1) and/or active fire (MOD14, MYD14) products. It is important to note that even the bottom-up approach relies on active fire data: GFED has essentially become a hybrid product that ingests active fire locations for its small fire boost (Randerson et al., 2012), and the MCD64A1 algorithm itself is coupled with active fire data (Giglio et al., 2009). Fuel loadings, combustion completeness, and emissions factors, which are dependent on region and land use and land cover (LULC), are then used to convert burned area to fire emissions. Fuel loadings are derived from biogeochemical models (Hoelzemann et al., 2004; van der Werf et al., 2010), and combustion completeness is estimated as a function of soil moisture (van der Werf et al., 2017) or tree cover (Wiedinmyer et al., 2011). Emissions factors are compiled from lab experiments and vary by LULC (Akagi et al., 2011; Andreae & Merlet, 2001). The top-down approach in QFED, GFAS, and FEER uses fire energy from MODIS-derived fire radiative power (FRP), which is remotely sensed at top-of-atmosphere. Fire radiative energy (FRE), or the temporal integral of FRP, approximately linearly scales with the mass of dry matter (DM) consumed as fuel due to combustion (Wooster et al., 2005). Besides correcting for fires obscured by clouds in the top-down approach, GFAS, QFED, and FEER also use MODIS aerosol optical depth (AOD) to determine scaling factors for emissions of organic carbon (OC), black carbon (BC), and particulate matter less than 2.5 μm in diameter ($PM_{2.5}$), which includes OC and BC (Darmenov & da Silva, 2013; Ichoku & Ellison, 2014; Kaiser et al., 2012).

Table 4.1: Comprehensive comparison of the global fire emissions inventories for various methodological details and technical parameters. Broadly, we define "bottom-up" as burned area-based and "top-down" as fire energy-based inventories.

Inventory	GFEDv4s	FINNv1.5	GFASv1.2	QFEDv2.5r1	FEERv1.0-G1.2
	"Bottom-up"		*"Top-down"*		
Primary satellite fire input	MCD64A1 C5.1 burned area (500 m)	MCD14DL C5 active fire area (1 km)	MOD14/MYD14 C5/C6 FRP (1 km)	MOD14/MYD14 C6 FRP (1 km)	GFASv1.2 FRP (0.1°)
Spatio-temporal resolution	0.25°, monthly (daily fraction)	1 km, daily	0.1°, daily	0.1°, daily (0.25° x 0.375°, NRT)	0.1°, daily
Temporal range	1997-2018*	2002- (NRT)	2003- (NRT)	2000- (NRT)	2003- (NRT)
Statistical boosts	Small fires boost	x	Cloud gap adjustment		
Conversion to dry matter (DM) emissions	CASA biogeochemical model (van der Werf et al., 2010)	Hoelzemann et al. (2004)	GFAS FRP-GFEDv3 DM conversion factors by LULC	QFED FRP-GFEDv2 DM global calibration	x
Smoke AOD constraints for aerosol emissions	x	x	Recommends 3.4 global scaling	Applies global scaling constants for OC, BC, $PM_{2.5}$ separately	Uses FRP-smoke AOD relationships to derive regional TPM emissions
Primary land use/ land cover (LULC)	MCD12Q1 (UMD), annual (500 m)	MCD12Q1 (IGBP), 2005 (500 m)	GFEDv3 dominant fire-prone LULC (0.5°)	IGBP-INPE (1 km)	MODIS IGBP dominant fire-prone LULC, 2004 (1°)
Peatland maps	Olson et al. (2001)	x	Same as GFED3 Heil et al. (2010)	x	x
Partitioning of emissions by LULC	yes	yes	x	yes	x
Emissions factors	Akagi et al. (2011) + updates from M.O. Andreae in 2013	Akagi et al. (2011), Andreae & Merlet (2001)	Andreae and Merlet (2001) + updates from literature	Andreae and Merlet (2001)	Andreae and Merlet (2001) + updates from M.O. Andreae in 2014
Speciation	41 species	27 species	42 species	17 species	30 species
Ancillary products	boosted BA, diurnal cycle, NPP	x	cloud-gap adjusted FRP density, plume top/ smoke injection altitude	cloud-gap adjusted FRP density by LULC	x
References	van der Werf et al. (2017)	Wiedinmyer et al. (2011)	Kaiser et al. (2012)	Darmenov and da Silva (2013)	Ichoku and Ellison (2014)

NRT = near real time; CASA = Carnegie Ames Stanford Approach; UMD = University of Maryland; IGBP = International Biosphere-Geosphere Program; INPE = Instituto Nacional De Pesquisas Espaciais (Brazil's National Space Institute); NPP = Net Primary Production; *2017-2018 are beta version releases

To understand the causes for differences in fire emissions estimates, we first devise five "relative fire confidence metrics" based on major methodological differences between the five global inventories and factors that can affect satellite observing conditions: (1) type of input satellite fire dataset (i.e., burned area versus active fires), (2) cloud/haze obscuration of land surface, (3) burn extent and fragmentation, (4) variance in topography, and (5) additional small fires from VIIRS. We combine the five relative fire confidence metrics to map the relative fire confidence score for bottom-up emissions inventories primarily based on burned area (e.g. GFED) or active fire area (e.g. FINN). For top-down inventories, we estimate an FRP-based score to estimate the potential FRP enhancement from small fires below the MODIS detection limit, large fires not well-captured by the MODIS active fire product, and fires obscured by clouds and thick haze.

4.2.2 Regional case study: smoke exposure from fires in Indonesia

We then focus on Indonesia as a regional case study, as Indonesia can contribute a substantial fraction of annual global fire emissions. By some estimates, fires in Equatorial Asia, which mostly occur in Indonesia, account for 8% of carbon emissions from global fire activity on average, but as much as over a third during high fire intensity years (van der Werf et al., 2017). From incomplete combustion, fires release greenhouse gases and aerosols, including $PM_{2.5}$, and such emissions can trigger haze events, impacting visibility, air quality, climate, ecosystem services, and human health (Harrison et al., 2009; Page et al., 2009). Three main factors exacerbate haze episodes over Equatorial Asia: (1) synoptic meteorology, (2) fire-driven deforestation and agricultural management, and (3) carbon-rich peatlands in Indonesia (Marlier et al., 2019). First, during years with a strong El Niño and positive Indian Ocean Dipole phase, such as 2006 and 2015, suppression of convection over Indonesia leads to drought conditions (Crippa et al., 2016; Fernandes et al., 2017; Koplitz et al., 2016). Chen et al. (2017) found that a temporal cascade of pan-tropical fires, including large fires in Indonesia, is driven by the El Niño Southern Oscillation (ENSO) and changes in precipitation and terrestrial water storage. Second, smallholder farms and industrial concessions (oil palm, pulpwood, and rubber) are typically managed by fire to clear residues; forests are also cleared for agriculture and new plantations via burning (Dennis et al., 2005; Hoscilo et al., 2011; Marlier et al., 2015). Third, if the water table is low, peat fires can burrow underground and become extremely difficult to extinguish. Such fires can smolder for days to weeks, releasing substantial amounts of smoke into the atmosphere (Gras & Jensen, 1999; Hayasaka et al., 2014; Rein et al., 2008; van der Werf et al., 2008). Although fires occur every year in Indonesia (Koplitz et al., 2016), the combination of these three natural and human-induced

factors leads to especially severe haze over Equatorial Asia, such as in 1997, 2006, and 2015.

The high concentrations of $PM_{2.5}$ generated by fires in Equatorial Asia pose adverse health risks, leading to increased premature mortality. For example, Koplitz et al. (2016), Crippa et al. (2016), and Marlier et al. (2019) estimate 75,600-100,300 long-term premature adult deaths from cardiovascular and respiratory disease in Equatorial Asia due to the 2015 severe haze event. However, each of these studies differ in methodology, and specifically, in the global fire emissions inventory used: GFASv1.0 in Koplitz et al. (2016), FINNv2.0 in Crippa et al. (2016), and GFEDv4s in Marlier et al. (2019). In this study, we diagnose the impact of using different emissions inventories on estimates of population-weighted smoke exposures for Singapore, Indonesia, and Malaysia, following Koplitz et al. (2016) and Marlier et al. (2019).

4.2.3 Google Earth Engine: online platform for rapid geospatial analysis

In this study, we leverage Google Earth Engine (GEE; `https://earthengine.google.com`), an online platform for rapid geospatial analysis (Gorelick et al., 2017). Recently, GEE has been used in studies that require ease of access to satellite datasets and high computational power, such as for mapping crop yields (Azzari et al., 2017; Azzari & Lobell, 2017), trends in land use change (Kennedy et al., 2018), travel distance to cities (Weiss et al., 2018), and smoke exposure from fires (Marlier et al., 2019). Some of these studies also incorporate GEE's user interface capabilities, including Earth Engine Apps (`https://www.earthengine.app`) into online apps. Our use of GEE is two-fold: (1) to apply the relative fire confidence metrics at the global scale and (2) to use Earth Engine Apps to build the FIRECAM online tool.

The main objective of this study is to identify the methodological differences between five global fire emissions inventories and for end-users, show how these differences may lead to biases in results. To do so, we first use GEE to develop five relative fire confidence metrics to quantify some of the uncertainties. Next, we isolate the impact of using different inventories to estimate smoke exposure in Equatorial Asia from fires in Indonesia. Finally, we develop an online tool to help end-users to rapidly gauge the regional differences in emissions estimates and reduce potential biases in model results.

4.3 Methods

In this study, we use GEE to access and analyze satellite-derived datasets, many of which are already included in the GEE public data catalog. GEE couples a multi-petabyte-scale data catalog with cloud computing to make rapid geospatial analysis possible at scale (Gorelick et al., 2017). Use of GEE is thus critical to this study in order to apply the relative fire confidence metrics at a global scale and build the FIRECAM online tool.

4.3.1 Satellite fire datasets

We primarily use the Collection 6 (C6) satellite fire datasets from the MODIS sensors aboard the Terra and Aqua satellites, which have daily overpasses at ~10:30 am/pm and ~1:30 am/pm local time, respectively. These datasets are used in the construction of the five global fire emissions inventories considered here and publicly available from the NASA Earthdata catalog (`https://earthdata.nasa.gov/`). We analyze 15 years (2003-2017) of data from Collection 6 MCD64A1 burned area at monthly, 500-m spatial resolution (Giglio et al., 2009, 2018), MOD/MYD14A1 FRP and fire mask at daily, 1-km resolution (Giglio et al., 2003, 2016), and MCD14ML active fire geolocations also at daily, 1-km resolution. We hereafter refer to the Level-3 gridded active fire products MOD14A1 (Terra) and MYD14A1 (Aqua) collectively as MxD14A1 and Level-2 swath products as MxD14. We also use Collection 1 VNP14IMGML active fire geolocations, available since 2012, from the VIIRS sensor aboard the Suomi National Polar-orbiting Partnership (S-NPP) satellite. VNP14IMGML is analogous to MCD14ML, but provides data at higher spatial resolution (375 m) and only during the Aqua overpass times (Schroeder & Giglio, 2018).

4.3.2 Relative fire confidence metrics

We devise five simple fire confidence metrics (φ) to assess the overall spatial variability and relative bias in global fire emissions inventories at 0.25° x 0.25° spatial resolution and aggregated across 15 years (2003-2017) from monthly timesteps, as described below. Table 4.2 describes the satellite-derived datasets used. Then, as an example to end-users, we integrate the five metrics into more comprehensive "scores" to independently evaluate the spatial variability in uncertainty for bottom-up and top-down inventories. That is, we identify regions where each inventory may capture fire emissions either well or poorly, based on the five metrics.

(1) **Spatial discrepancy between burned area and active fire area (φ_{area})**: We classify two main types of

Table 4.2: Satellite-derived datasets used for the five relative fire confidence metrics, which are described in Chapter 4.3.2.

Dataset	Description	Resolution	Satellite	Sensor	GEE ID
MCD64A1	Burned Area	Monthly, 500 m	Terra/Aqua	MODIS	MODIS/006/MCD64A1
MOD14A1	Active Fires	Daily, 1 km	Terra		MODIS/006/MOD14A1
MYD14A1			Aqua		MODIS/006/MYD14A1
MOD09GA	Surface Reflectance	Daily, 500 m	Terra		MODIS/006/MOD09GA
MYD09GA			Aqua		MODIS/006/MYD09GA
MCD12Q1	Land Cover	Yearly, 500 m	Terra/Aqua		MODIS/006/MCD12Q1
MCD14ML	Active Fire Geolocations	Daily, 1 km	Terra/Aqua		projects/GlobalFires/MCD14ML
VNP14IMGML		Daily, 375 m	S-NPP	VIIRS	projects/GlobalFires/VNP14IMGML
GMTED2010	Terrain Elevation	2010 only, 7.5 arc sec	NGA's SRTM Digital Terrain Elevation Data		USGS/GMTED2010

NGA = National Geospatial-Intelligence Agency

bottom-up emissions inventories, based on the observations used to derive these inventories. For example, both GFED and FINN estimate burned area, but GFED uses the MCD64A1 burned area product, and FINN relies on MCD14ML active fire geolocations. MODIS burned area is typically classified based on the difference in the surface reflectance, or Normalized Burn Ratio (NBR), of pre-burn and post-burn images, while MODIS active fires are detected as "hotspots," or thermal anomalies, each of which can be associated with areal extent to estimate burned area. To avoid confusion, we refer to burned area derived from MCD64A1 as $BA_{MCD64A1}$ or burned area (BA; as in GFED) and that from MxD14A1 as $BA_{MxD14A1}$ or "active fire area" (AFA; as in FINN). In contrast to the high threshold for the MCD64A1 burned area product, which reliably classifies burn scars > 1.2 km^2 (Giglio et al., 2006), the MxD14A1 active fire product can detect cool, smoldering fires more consistently and fires as small as 100 m^2 under clear-sky conditions (Giglio et al., 2003). However, burned area products may better capture short-lasting fires (sub-daily) and fires obscured by thick haze or clouds, since the burned area pre-burn versus post-burn algorithm is not limited by satellite overpass times (Giglio et al., 2009). The persistence of burn scars enables satellites to detect fires after clouds and haze have dissipated. To gauge the relative areal discrepancy of $BA_{MCD64A1}$ and $BA_{MxD14A1}$, we first aggregate $BA_{MCD64A1}$ to the 1-km spatial resolution of $BA_{MxD14A1}$. We then estimate total $BA_{MCD64A1}$ outside $BA_{MxD14A1}$ (BA_{β}) and $BA_{MxD14A1}$ outside $BA_{MCD64A1}$ (BA_{α}), over 2003-2017, and calculate the normalized difference index of BA_{β} and BA_{α} at 0.25° x 0.25° spatial

resolution:

$$\varphi_{area} = \frac{\sum BA_{\beta} - \sum BA_{\alpha}}{\sum BA_{\beta} + \sum BA_{\alpha}} \tag{4.1}$$

where

$$BA_{\beta} = BA_{MCD64A1} - (BA_{MCD64A1} \cap BA_{MxD14A1}) \tag{4.2}$$

$$BA_{\alpha} = BA_{MxD14A1} - (BA_{MCD64A1} \cap BA_{MxD14A1}) \tag{4.3}$$

The range of the normalized difference index (-1 to +1) for the BA-AFA discrepancy indicates whether grid cells are either dominated by burned area (> 0) or active fire area (< 0). If either burned area or active fire area dominates (near -1 or +1), the datasets will not agree, and uncertainty is high. If the index is ~0, the discrepancies between the datasets are minimal, wherein $BA_{\beta} \approx BA_{\alpha}$; in this case, however, the magnitude of BA_{β} and BA_{α} can vary while yielding similar index values.

(2) **Cloud/haze effect on the ability of satellites to "see" fires (φ_{cloud_haze})**: Persistent cloud coverage and thick haze limit the opportunities for satellites to detect active fires or retrieve usable scenes for burned area classification. This metric diagnoses the fractional monthly cloud/haze burden at 500-m spatial resolution, weighted by FRP, but does not distinguish between smoke and cloud or varying cloud thickness and opacity. We use FRP rather than burned area since FRP is linearly related to DM emissions and more readily captures small fires (Wooster et al., 2005). We use the Collection 6 MODIS daily surface reflectance products MxD09GA and follow the algorithm proposed by Xiang et al. (2013) in each pixel, with "pixel" defined as one satellite observation in the native MODIS sinusoidal projection:

$$\varphi_{cloud\_haze} = \frac{\rho_1 - \rho_7}{\rho_1 + \rho_7} > 0 \text{ or } \rho_1 > 0.3 \tag{4.4}$$

where φ_{cloud_haze} refers to pixels designated as cloudy/hazy, ρ_1 indicates the MODIS surface reflectance in the 620-670 nm band (Red) and ρ_7, the 2105-2155 nm band (SWIR-2). Cloudy and hazy pixels tend to be saturated in the visible bands relative to SWIR bands (Xiang et al., 2013). Pixels are classified as cloudy/hazy if either of the two criteria in Equation 4.4 is met. We consider only those pixels with one or more active fire or burned area observations over the 2003-2017 timeframe to exclude misclassification of cloud/haze in snow, ice, and desert

regions. After averaging the fraction of clouds and haze across 0.25° x 0.25° grid cells, we weight the monthly fractional cloud/haze burden by FRP aggregated by month and satellite, over 2003-2017, to place more emphasis on the observing conditions during the months and hours of the diurnal cycle when fires are more likely to occur.

Like Xiang et al. (2013), MODIS also diagnoses clouds and haze but at coarser, 1-km resolution, which can result in overestimates of the cloud/haze fraction since clear pixels are mixed with cloudy or mixed cloudy pixels. However, the MODIS algorithm is better able than Xiang et al. (2013) to separate clouds or haze from bright surfaces such as snow/ice, desert, and built-up areas. We therefore use the FRP-weighted cloud/haze fraction derived from the MODIS algorithm to identify grid cells that may be misclassified as clouds due to the underlying bright surfaces. We assume that those pixels that MODIS characterizes as "cloudy" or having "mixed" clouds, cloud shadow, or high aerosol content are pixels obscured by cloud or haze. Then, for these grid cells, we check whether the FRP-weighted cloud/haze fraction derived from the Xiang et al. (2013) algorithm is positive. If yes, we use the FRP-weighted cloud/haze fraction from the MODIS algorithm for our metric.

(3) **Fragmentation and size of contiguous burned area ($\varphi_{fragment}$)**: Burned area products can better capture large, contiguous fires than small, fragmented fires due to the greater difference in NBR from pre-fire to post-fire and the persistence of burn scars on the land surface. On croplands, the small drop in NBR due to small fires can be conflated with harvest or masked by timely sowing of the next crop or by regrowth (Hall et al., 2016; Liu et al., 2019). In contrast, active fire products can generally detect such small, fragmented fires more accurately, so long as they occur during the satellite overpasses and are not obscured by clouds or haze. Dense clusters of small fires within a pixel can also increase the detection probability by enhancing the thermal anomaly or the NBR difference relative to background. For this metric, we estimate the total burned area and number of burn scar fragments over 2003-2017, using the average burned area per contiguous burn scar patch as a proxy for burn scar size and fragmentation. The *connectedComponents* function in GEE allows us to estimate the number of contiguous burn patches on a monthly basis at 500-m spatial resolution (Gorelick et al., 2017). To determine the connectivity of burn scars, we apply a circle kernel with a radius of 1 pixel; this assumes a "half neighbors" scheme, in which each pixel has 4 neighbors, and only pixels that share an edge are merged. One limitation of connectedComponents is that the algorithm limits the maximum number of pixels per patch at 256 pixels and identifies larger patches as background. We account for this limitation by increasing the total number of burn scar fragments in a grid cell by one if the MCD64A1 burned area is larger than the size of the patch derived by connectedComponents. Additionally, the 0.25° x 0.25° grid used to extract the contiguous burn scars sets an

upper bound on burned area per patch for those large fires extending across multiple grid cells. Values > 2 km^2 per burn fragment indicate large, contiguous fires, while small values represent small, fragmented fires.

(4) **Roughness in topography ($\varphi_{topography}$)**: Rough terrain, or large variances in local elevation, can inhibit active fire detection or burned area classification by introducing shadows, leading to insufficient background control pixels and artificial variations in surface reflectance (Fornacca et al., 2017). We estimate the neighborhood variance of terrain elevation as an indication of rough terrain. We use the U.S. Geological Survey (USGS) Global Multi-resolution Terrain Elevation Data 2010 (GMTED2010) at 7.5 arc seconds (~250 m) spatial resolution, derived primarily from the Shuttle Radar Topography Mission (SRTM) Digital Terrain Elevation Data from the National Geospatial-Intelligence Agency (NGA). For each pixel, we estimate the neighborhood variance using a square kernel with a radius of 2 pixels. We then mask out water bodies using the 250-m MODIS/Terra land/water mask (MOD44W C6) and upscale the topography variance to 0.25° x 0.25° spatial resolution by calculating the mean. Values close to 0 indicate flat topography, while values > 1000 m^2 indicate rough, mountainous terrain. One limitation of this simple metric is that it does not account for terrain curvature, whose calculation is not yet supported by GEE.

(5) **Additional small fires detected by VIIRS (φ_{VIIRS_sf})**: VIIRS aboard S-NPP detects active fires at 375-m (I-bands) and 750-m (M-bands) spatial resolution in comparison to the 1-km spatial resolution of MODIS active fire detections (Schroeder & Giglio, 2018). The difference in spatial resolution suggests that VIIRS can detect smaller and cooler fires than MODIS. However, global fire emissions inventories have historically depended on MODIS since VIIRS is available only since 2012, or over a decade less than MODIS. While these additional small fires may comprise only a small portion of the global carbon budget, they can be important local point sources that contribute to regional air pollution. We approximate additional FRP observed by VIIRS at 375-m spatial resolution as the fractional FRP of VIIRS fires outside MODIS active fire and burned area pixels during the time period when the two satellite records overlap (2012-2017). Values range from 0 (no additional VIIRS FRP outside MODIS burn extent) to 1 (only VIIRS FRP).

4.3.2.1 Bottom-up inventories: relative fire confidence scores (BA-score, AFA-score)

Taken together, the five metrics described above capture the primary reliance on MODIS burned area (e.g., GFED) versus active fire (e.g., FINN) products as the base input satellite-derived fire dataset in a bottom-up

approach and difficulty in the satellite detection of fires due to cloud/haze obscuration and limited spatial and temporal resolution. Using these five metrics, we estimate a relative fire confidence score for the two bottom-up emissions inventories, which are based on either burned area (as in GFED) or active fire area (as in FINN). For each metric and each grid cell, we assign an initial integer confidence score ranging from 0 to 10, with 10 as highest confidence score, based on the decile distribution of all grid cells. Grid cells with only MODIS active fire, only MODIS burned area, or only VIIRS active fire observations are assigned the lowest confidence score of 0. We then average the scores from the fire confidence metrics in each grid cell and adjust the scale by setting the median score for the final relative fire confidence score for that grid cell to 0. This score represents the relative degree to which we can be confident in fire emissions for these inventories. We associate low cloud/haze burden, low variance in elevation, and low fraction of additional VIIRS fires with high confidence. To assess inventories based on burned area (e.g., GFED), we calculate a "BA-score," in which high burned area outside active fire area (metric 1) and low burn fragmentation (metric 3) denote high confidence. For inventories based on active fires (e.g., FINN), we calculate an "AFA-score," in which we reverse the scales for metrics 1 and 3 and place more relative confidence in grid cells dominated by active fire area over burned area and fragmented burn landscapes.

4.3.2.2 Top-down inventories: adjusted potential FRP adjustment (pFRP)

Top-down FRP-based inventories often include statistical cloud-gap adjustment and/or smoke AOD constraints, making them difficult to directly compare against the bottom-up inventories. Cloud-gap adjustments correct for fires blocked from satellite detection due to clouds or thick haze. These adjustments rely on data assimilation of previous observations and assumptions regarding fire persistence (Darmenov & da Silva, 2013; Kaiser et al., 2012). As an additional top-down constraint, fire emissions are scaled to match smoke-aerosol emissions derived from AOD observations (Ichoku & Ellison, 2014). We thus devise a separate score, the adjusted potential FRP enhancement (pFRP), or "FRP-score," to assess the three top-down inventories (GFAS, QFED, FEER). The pFRP score diagnoses additional fire energy, unaccounted for by the MODIS active fires product but indicated by large burn scars from the MODIS burned area product or very small fires from the 375-m VIIRS active fires product. We first estimate the potential FRP enhancement as the sum of (1) fractional FRP inside MCD64A1 burned area extent but outside active fire area, over 2003-2017, and (2) fractional VIIRS FRP outside the combined extent of both MODIS burned area and active fire area, or metric 5, over 2012-2017. To obtain the adjusted potential FRP enhancement, we then multiply the potential FRP enhancement by the complement of the

cloud/haze obscuration fraction, or metric 2. High pFRP values suggest low confidence in top-down inventories under clear-sky conditions.

4.3.3 Global fire emissions inventories

To convert burned area or FRP into emissions, fire emission inventories rely on estimates and assumptions regarding an array of variables as land cover type, fuel load, or emissions factors. Here we summarize these estimates and assumptions across five inventories (GFEDv4s, FINNv1.5, GFASv1.2, QFEDv2.5r1, and FEERv1.0-G1.2) over 2003-2016 and at both global and regional scale (Table 4.1). The versions of the inventories considered here are current as of 2018. We then compare the resulting emissions of carbon dioxide (CO_2), carbon monoxide (CO), methane (CH_4), OC, BC, and $PM_{2.5}$ emissions from five global fire emissions inventories. Each inventory is described in more detail in Appendix D.2.

4.3.4 Modeling smoke $PM_{2.5}$ from regional fire emissions

Following Kim et al. (2015) and Koplitz et al. (2016), we use the adjoint of the GEOS-Chem CTM to estimate the influence of upwind fires on smoke exposure at population-weighted receptors. We define smoke $PM_{2.5}$ as the enhancement in $PM_{2.5}$ due to fire activity. As used here, the GEOS-Chem adjoint maps the sensitivities of smoke $PM_{2.5}$ at particular receptors to fire emissions in grid cells across a source region, creating a footprint of such sensitivities. These footprints depend on the transport pathways from the source to the receptor and vary with meteorology. By multiplying these sensitivities by the different fire emissions inventories, we can easily compare estimates of monthly smoke $PM_{2.5}$ exposure in Indonesia, Singapore, and Malaysia, from 2003-2016. We thus apply monthly adjoint sensitivities, which span a range of meteorology from 2005-2009, to the sum of OC and BC emissions, the main components of smoke $PM_{2.5}$. Due to the high computational cost of the GEOS-Chem adjoint, we match existing 2005-2009 sensitivities to each emissions year from 2003-2016 by determining the closest meteorological year in terms of rainfall (Kim et al., 2015; Koplitz et al., 2016). To do so, we use daily rainfall rates from Climate Hazards Group Infrared Precipitation with Station Data (CHIRPS) (Funk et al., 2015), averaged temporally over the fire season and spatially over Sumatra and Kalimantan, Indonesia (Figure D.3). CHIRPS is a daily, 0.05° x 0.05° dataset that integrates both observational and satellite data to provide quasi-global rainfall data since 1981. As in Fernandes et al. (2017) and Marlier et al. (2019), we define the fire season in Indonesia as July to October.

Following Marlier et al. (2019), we further validate modeled smoke $PM_{2.5}$ with ground observations in Singapore. We first extend the daily $PM_{2.5}$ observations, available from 2014-2016, from the Singapore National Environment Agency (NEA) to 2010 by converting Pollution Standards Index (PSI) observations to $PM_{2.5}$. As used by the Singapore NEA, PSI is an air quality index that incorporates concentrations of six pollutants: CO, sulfur dioxide (SO_2), nitrogen dioxide (NO_2), ozone (O_3), PM_10, and $PM_2.5$ (https://www.haze.gov.sg/). To further extend the record back to 2003, we train a multi-variate regression model of monthly mean NEA $PM_{2.5}$ observations using visibility, air temperature, wind speed, and rainfall observations from the Singapore Changi airport, available from NOAA Global Summary of the Day (GSOD). The model yields an adjusted R^2 with observations of 0.94 (Figure D.5). We then reconstruct monthly $PM_{2.5}$ for 2003-2016 and subtract the background $PM_{2.5}$, or the median $PM_{2.5}$ (13.77 $\mu g\ m^{-3}$) during non-fire season months (January to June and November to December), to obtain smoke $PM_{2.5}$ for our validation. Validation for Malaysia and Indonesia is described in Appendix D.3.2.

4.4 Results

4.4.1 Spatial patterns in relative fire confidence metrics and scores

Overall, the five relative fire confidence metrics broadly differentiate: (1) large, continuous versus small, fragmented landscapes, (2) cloudy/hazy versus clear satellite observing conditions during the fire season, and (3) flat versus mountainous or rugged terrain. First, the map of BA-AFA discrepancies (metric 1) reveals the regions where the burned area BA_β and active fire area extent BA_α disagree. Regions dominated by high burned area outside the active fire area extent ($BA_\beta \gg BA_\alpha$) include the western Australia shrublands, sub-Saharan Africa savannas, and Kazakhstan and eastern Mongolia grasslands. Regions dominated by active fire area outside burned area extent ($BA_\beta \ll BA_\alpha$) are more widespread and primarily cover agricultural and/or mountainous areas (Figure 4.1). Additionally, this metric highlights artificial discontinuities in the MODIS burned area product, most prominently north of the Black Sea, likely due to separate data processing for each MODIS tile (Giglio et al., 2018). Second, the FRP-weighted cloud/haze fraction (metric 2) shows that tropical and boreal forest regions, as well as eastern China, are conducive to poor satellite observing conditions due to cloud or haze during the fire season, with index values greater than 0.5 (Figure 4.2). These areas with persistent cloud/haze burden are consistent with independent estimates of high mean cloud frequency (Wilson & Jetz, 2016) and are also co-located with high

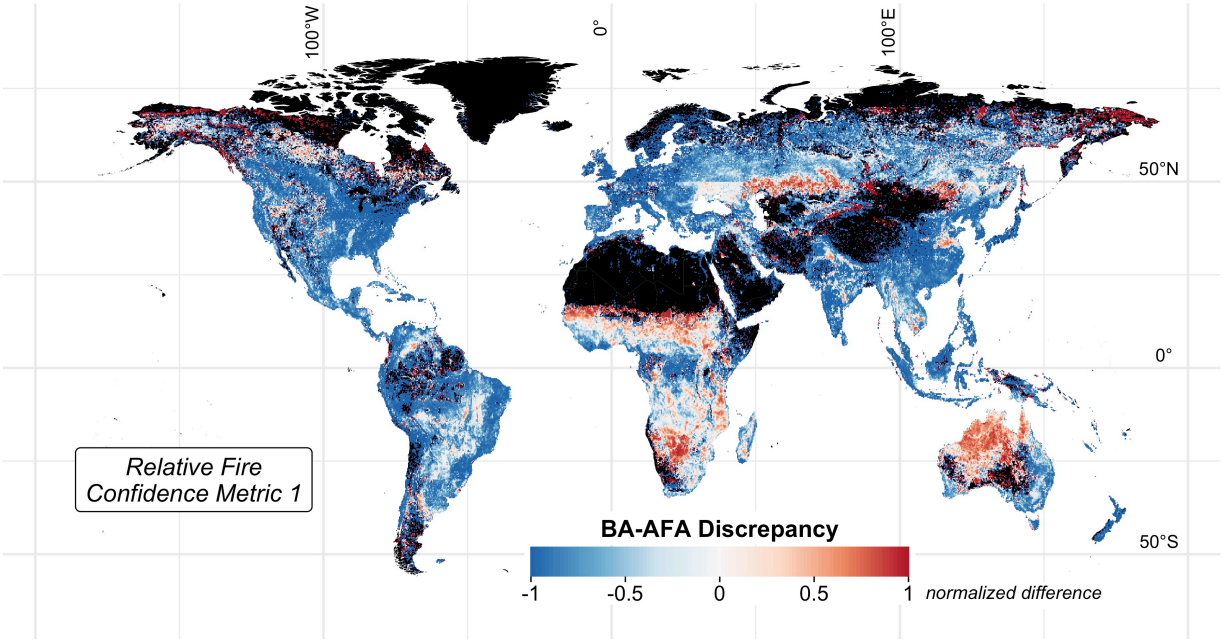


Figure 4.1: Metric 1 for relative fire confidence score (φ_{area}): discrepancy between MCD64A1 burned area (BA) and MxD14A1 active fire area (AFA) based on the normalized difference of BA outside AFA and AFA outside BA. Values are averaged over 2003-2017 and mapped at 0.25° x 0.25° spatial resolution. High values (darker red) indicate relatively more confidence in BA than AFA, and low values (darker blue) the opposite.

MODIS burn date uncertainty, indicating that many retrieved satellite scenes are unusable (Figure D.9). Third, the pattern of burn size and fragmentation (metric 3) is similar to that of the BA-AFA discrepancy: areas with large, contiguous fires are better captured by burned area, while areas with small, fragmented fires are better represented by active fire detections (Figure 4.3). Our method for burn size/fragmentation yields spatial patterns consistent with fire size from the Global Fire Atlas, a catalog that characterizes over 13 million individual fires detected by MODIS (Andela et al., 2019). Fourth, topographical variance (metric 4) differentiates mountainous or rugged terrain, such as in western U.S. and southeast Asia, versus flat terrain, such as in northern India and western Australia (Figure 4.4). Fifth, the map of VIIRS fires outside the MODIS burn extent (metric 5) reveals locations dominated by small fires that are not well-detected by a coarser resolution sensor like MODIS (Figure 4.5). In total, 38% of total VIIRS FRP does not overlap with the MODIS burn extent, revealing the importance of very small fires.

Taken together, the five metrics compose the relative fire confidence scores for bottom-up emissions inventories primarily derived from either burned area (BA-score; Figure D.1a), such as GFEDv4s, or active fire area (AFA-score; Figure D.1b), such as FINNv1.5. While the mapped BA-score and AFA-score mostly track the pat-

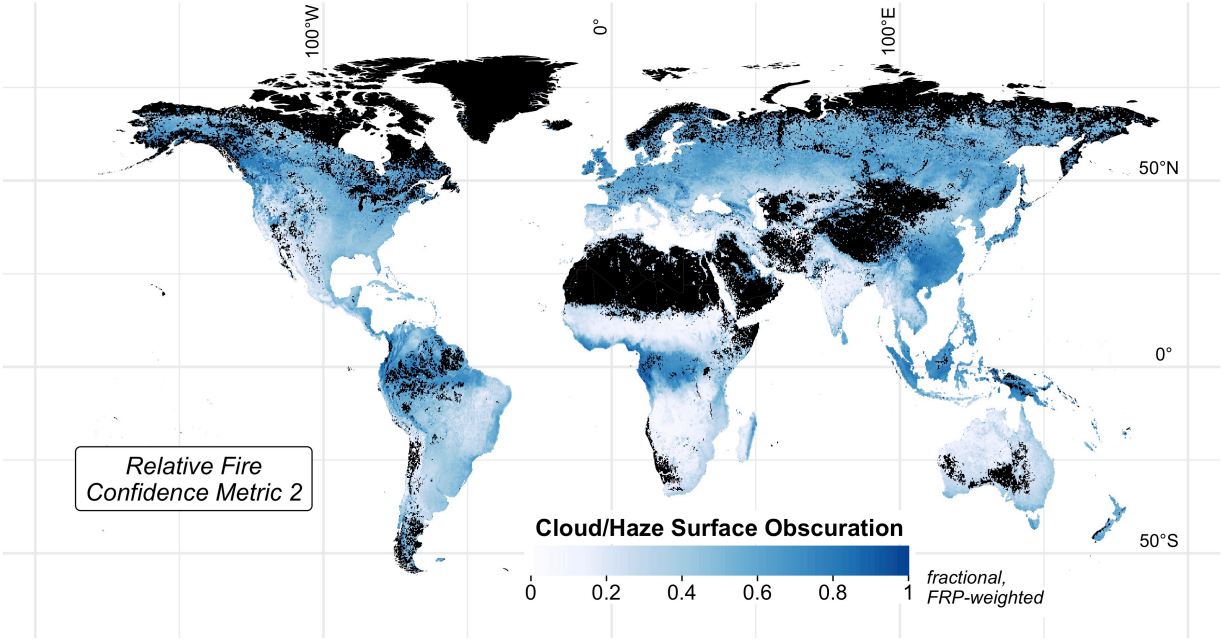


Figure 4.2: Metric 2 for relative fire confidence score (φ_{cloud_haze}): Cloud/haze fraction based on MxD09GA surface reflectance and weighted by FRP. Values are averaged 2003-2017 and mapped at 0.25° x 0.25° spatial resolution. High FRP-weighted cloud/haze fraction indicates fewer opportunities for satellite observation of the land surface during the fire season.

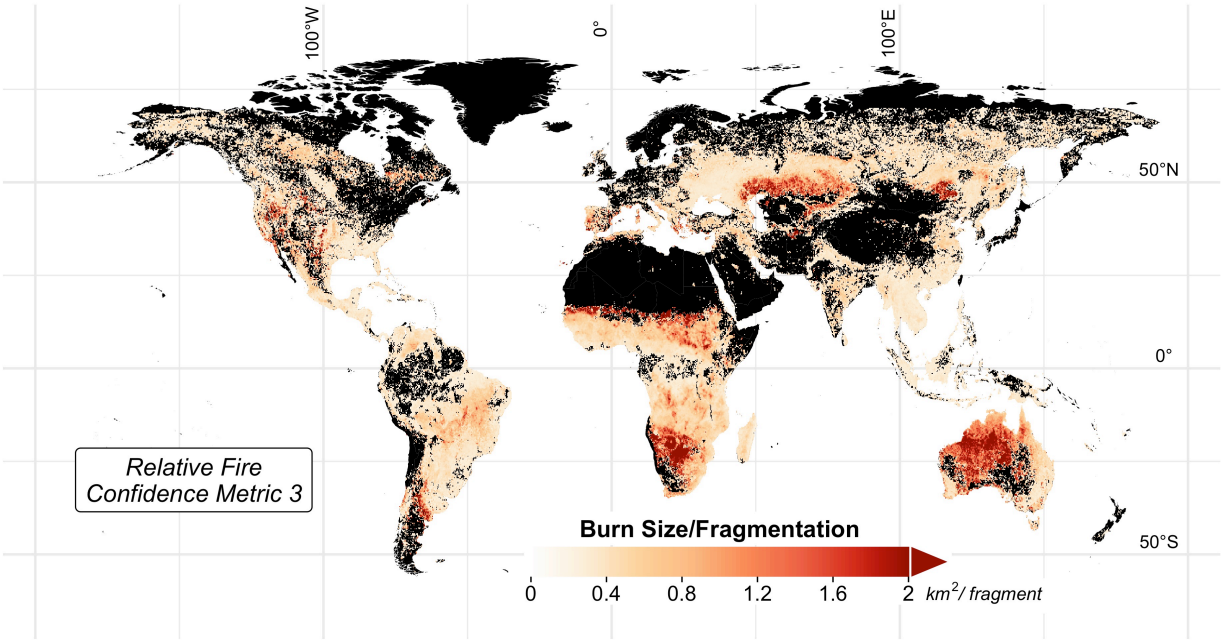


Figure 4.3: Metric 3 for relative fire confidence score ($\varphi_{fragment}$): average burned area (km^2) per "fragment," or contiguous patch of burned area, averaged over 2003-2017 and mapped at at 0.25° x 0.25° spatial resolution. High values indicate dominance of large, contiguous fires; low values denote dominance of small, fragmented fires.

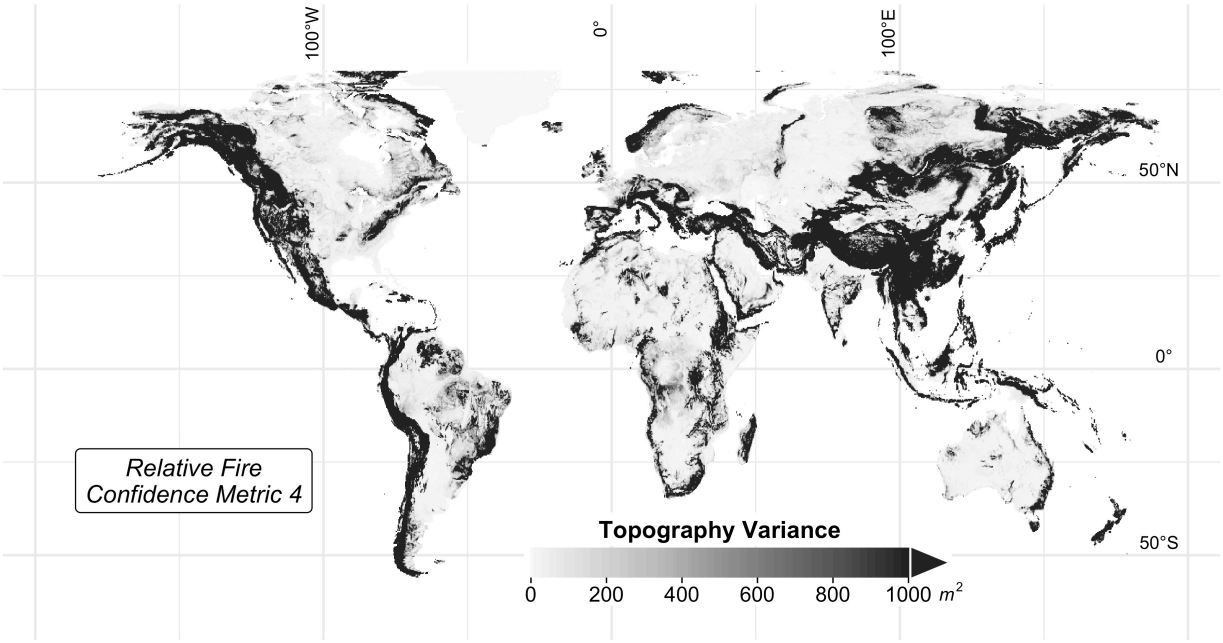


Figure 4.4: Metric 4 for relative fire confidence score ($\varphi_{topography}$): roughness in topography, expressed as variance in elevation (m^2), averaged over 2003-2017 and mapped at 0.25° x 0.25° spatial resolution. High values in topography variance indicate steep gradients in elevation, or mountainous terrain, whereas low values indicate relatively flat terrain.

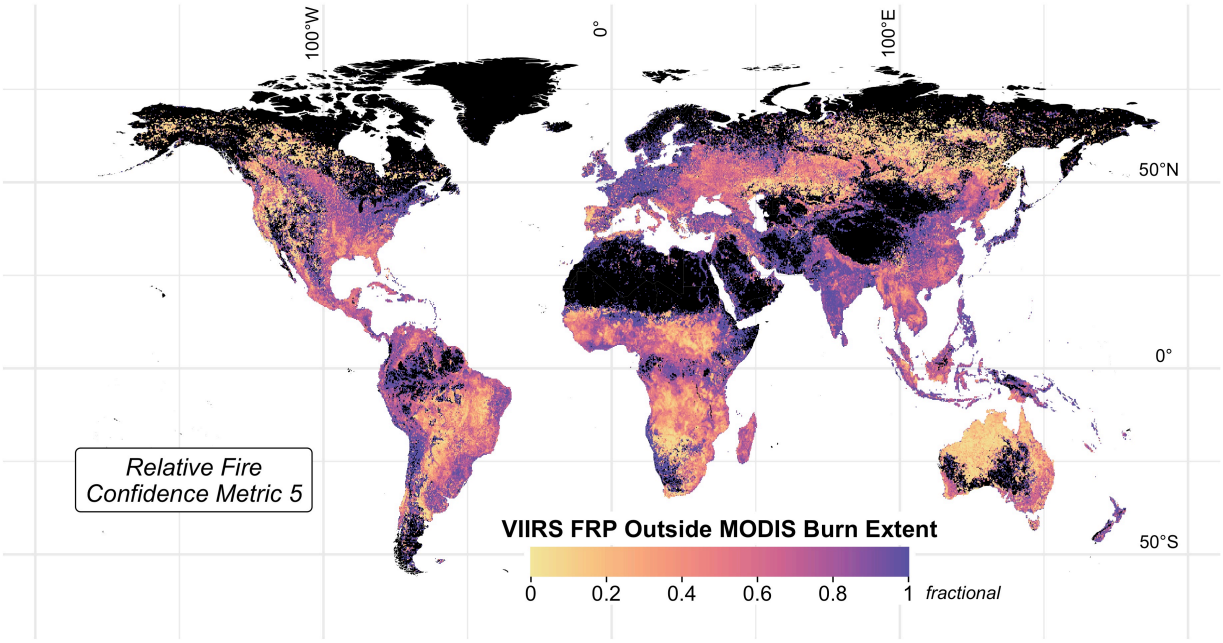


Figure 4.5: Metric 5 for relative fire confidence score ($\varphi_{VIIRS_{sf}}$): additional fires detected by VIIRS. Values are the areal fraction of VIIRS FRP occurring outside MODIS burned area and active fire pixel area, averaged over 2003-2017 and mapped at 0.25° x 0.25° spatial resolution. A value of 0 indicates that all VIIRS active fires overlap MODIS active fires, and a value of 1 indicates the presence of VIIRS active fires but no MODIS burned area or active fire observations.

terns of the large, contiguous fires versus small, fragmented fires, some areas exhibit low relative confidence (e.g., croplands in eastern China, tropical forests in the Democratic Republic of Congo) or high relative confidence (e.g., tropical forests in central-southern Amazon, savannas in Botswana and Namibia) for both scores due to the effects of cloud/haze cover and/or topographical variance. Some caveats apply here. While we take the BA-score to apply to GFEDv4s, this inventory also boosts burned area using active fire counts to account for small fires. Additionally, for AFA-score, we assume an active fire area of 1 km^2 for all fires, while FINNv1.5 uses 0.75 km^2 for savanna and grassland fires and further scales the active fire area for all fires by the fractional vegetation cover of a given 1-km pixel (Wiedinmyer et al., 2011). Both GFEDv4s and FINNv1.5 rely on outdated MODIS products: GFEDv4s on MCD64A1 C5.1 burned area and FINNv1.5 on MCD14DL C5 active fires; however, for all our metrics, we use updated satellite products from MODIS C6 (MCD64A1 and MxD14A1). Despite our simplified approach and use of different versions of the satellite fire products, the normalized difference between GFEDv4s burned area and FINNv1.5 active fire area is spatially well-correlated with the BA-AFA discrepancy ($r = 0.59, p < 0.01$), or metric 1. We also find that the normalized difference between GFEDv4s and FINNv1.5 emissions for all six species is also moderately correlated with the BA-AFA discrepancy ($r = 0.53$-$0.57, p < 0.01$), confirming that the difference between GFEDv4s and FINNv1.5 emissions is related to the satellite fire input dataset used.

The pFRP metric assesses top-down FRP-based emissions inventories (GFAS, QFED, and FEER; Figure D.2). In total, we estimate 24% and 38% potential FRP enhancement from large fires (using MODIS BA) and very small fires (using VIIRS FRP), respectively, from 2003-2017. Put another way, the FRP-based inventories may be missing nearly two-thirds of fires under clear-sky conditions. Regions with low pFRP, and thus high uncertainty, include India and sub-Saharan Africa. In these regions, the low pFRP implies that either the satellite overpasses are missing a large number of short-lived or fast-spreading fires or the fires are too small to detect at coarse resolution. For example, the satellite overpasses at 10:30 am and 1:30 pm likely underestimate fire energy in the sub-tropics, where fire activity generally peak in the late afternoon (Giglio, 2007). Regions characterized by high cloud/haze cover during the fire season, such as tropical and boreal forests, have low pFRP due to our assumption that the cloud-gap corrections in these inventories successfully capture the fires obscured by clouds/haze.

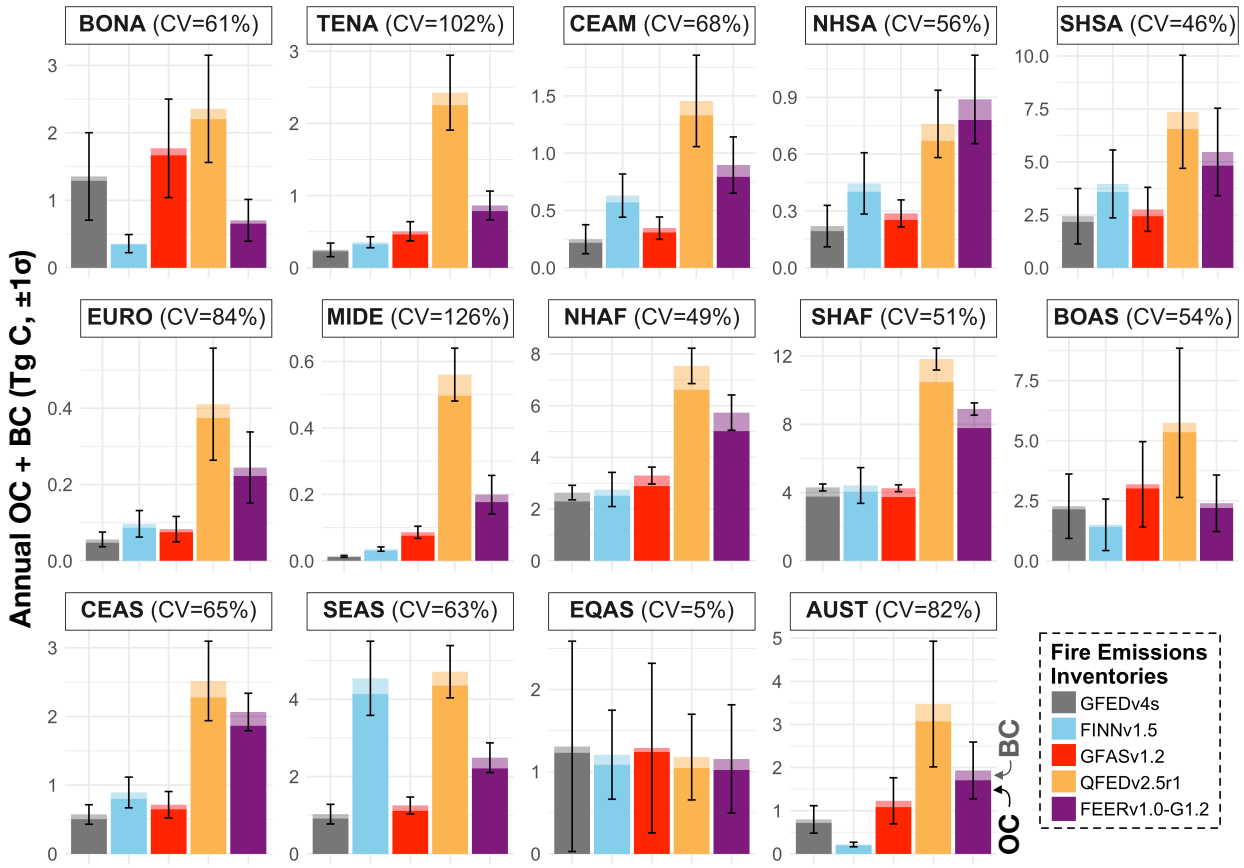


Figure 4.6: Mean annual OC + BC emissions (Tg yr^{-1}, $\pm 1\sigma$), over 2003-2016, from five global fire emissions inventories (GFEDv4s, FINNv1.5, GFASv1.2, QFEDv2.5r1, and FEERv1.0-G1.2) for the 14 GFEDv4s basis regions (Figure D.12). Acronyms for the 14 basis regions are given in Figure D.12. The fraction of OC emissions is denoted by darker shades, and that of BC emissions by lighter shades. Vertical bars show one standard deviation of the means over time. The coefficient of variation across inventories (CV, %) is shown for each region.

4.4.2 Comparison of global fire emissions inventories: speciation and emissions factors

We find inconsistencies in the speciation of the overall emissions budget for CO_2, CO, CH_4, OC, BC, and $PM_{2.5}$ across the five global fire emissions inventories. For example, QFEDv2.5r1 and FEERv1.0-G1.2 estimate ~2-3 times as much OC, BC, and $PM_{2.5}$ emissions than the other inventories, with QFEDv2.5r1 higher than FEERv1.0-G1.2 (Table 4.3). Mean annual OC + BC emissions, from 2003-2016, among inventories differ by 5-126% in coefficient of variation (CV; Figure 4.6). In regions with a high CV, such as temperate North America (102%) and the Middle East (126%), QFEDv2.5r1 OC+BC emissions are much higher than those from other inventories. These discrepancies shed light on the impact of the different algorithms that convert burned area or fire energy into aerosol emissions. For example, QFED and FEER apply top-down constraints on aerosol emis-

Table 4.3: Average annual global CO_2, CO, CH_4, organic carbon (OC), black carbon (BC) and fine particulate matter ($PM_{2.5}$) emissions (Tg yr^{-1}, $\pm 1\sigma$) by inventory, from 2003-2016. The percent difference in emissions relative to GFEDv4s is in brackets. For each species, the inventory with the highest emissions is denoted in bold font. The coefficient of variation (CV; %) indicates the spread of values, normalized by the mean, across the five inventories.

Species	Mean Annual Global Emissions (Tg)					CV (%)
	GFEDv4s	*FINNv1.5*	*GFASv1.2*	*QFEDv2.5r1*	*FEERv1.0-G1.2*	
CO_2	6986 (595) --	6362 (1025) [-9%]	7083 (604) [+1%]	7449 (665) [+7%]	**13205 (1044)** **[+89%]**	34
CO	336 (39) --	334 (54) [-1%]	366 (43) [+9%]	348 (31) [+4%]	**609 (52)** **[+81%]**	30
CH_4	15 (3) --	16 (3) [+8%]	20 (3) [+35%]	15 (1) [+2%]	**30 (3)** **[+103%]**	33
OC	16 (2) --	20 (3) [+26%]	19 (2) [+21%]	**47 (5)** **[+199%]**	30 (3) [+91%]	48
BC	1.8 (0.2) --	1.9 (0.3) [+8%]	2.1 (0.2) [+15%]	**5.3 (0.5)** **[+196%]**	3.9 (0.3) [+119%]	52
$PM_{2.5}$	35 (3) --	35 (6) [+2%]	31 (3) [-11%]	**74 (7)** **[+112%]**	51 (4) [+47%]	39

sions to match smoke AOD, while such adjustments are absent in GFED, FINN, and GFAS. FEER uses smoke AOD to directly calculate TPM, which is then broken down into aerosol species, while QFED enhances aerosol emissions with a constant global scaling factor for each LULC (Darmenov & da Silva, 2013; Ichoku & Ellison, 2014). This global, rather than regional, AOD-based scaling in QFED may explain the large CV in the Middle East and North America. Indeed, using MODIS/Aqua AOD, Darmenov & da Silva (2013) find significant variation in these scaling factors across each LULC — e.g., from 2-3 in tropical forest, 3-5 in extratropical forests, and 1-3 in grasslands and savannas.

To better understand the discrepancies across inventory emissions, we examine the emissions factors used in GFEDv4s and in earlier versions of FINN, GFAS, and QFED: FINNv1.0, GFASv1.0, and QFEDv2.4. We assume that emissions factors for the current versions of these three inventories do not deviate significantly from those in previous versions (Darmenov & da Silva, 2013; Ichoku & Ellison, 2014; Wiedinmyer et al., 2011). First, we assess the impact of LULC classification on emissions factors by deriving a globally averaged emissions factor for each emitted species in each inventory, weighted by the total DM emissions for each LULC. To isolate the differences in LULC classification among inventories, we use the GFEDv4s DM emissions partitioned by

Table 4.4: Average emissions factors (g species kg^{-1} dry matter) for CO_2, CO, CH_4, OC, BC and $PM_{2.5}$, weighted by fractional emissions over GFEDv4s land use and land cover (LULC). The coefficient of variation (CV; %) gives the variation, normalized by the mean, across inventories by species.

Species	Mean Emissions Factors (g species kg^{-1} dry matter), Weighted by GFEDv4s LULC				CV (%)
	GFEDv4s	*FINNv1.0*	*GFASv1.0*	*QFEDv2.4*	
CO_2	1648	1660	1611	1601	1.75
CO	95	87	91	84	5.45
CH_4	6.67	4.43	7.1	4.2	26.7
OC	5.73	6.43	5.77	6.09	5.38
BC	0.47	0.46	0.49	0.53	6.67
$PM_{2.5}$	9.65	12.46	8.29	8.29	20.3

LULC for the weighting. Since FINN subdivides the GFED4s savanna, grasslands, and shrublands LULC into two smaller LULC, we derive weights for these LULC using FINNv1.5 emissions. We find that the coefficients of variation in emission factors across the four inventories are relatively small for CO_2, CO, OC, and BC (1.75-6.67%), compared to those for CH_4 and $PM_{2.5}$ (20.3-26.7%; Table 4.4). On average, GFEDv4s and GFAS, which consider peatlands as a separate LULC, have about 60% higher weighted mean emissions factors for CH_4 than FINN and QFED. This discrepancy arises because the peat emissions factor (20.8 g CH_4 kg^{-1} DM) is ~2.5-14 times as high as CH_4 emissions factors for other LULC (Table D.1), and only GFEDv4s and GFAS consider peatlands separately. In contrast to Li et al. (2019) , we do not consider that FEERv1.0-G1.2 accounts for peatlands (Table 4.1), since FEER only uses the "permanent wetland" classification from the MODIS land cover product, which misses much of the peatland cover in Indonesia compared to the Olson et al. (2001) dataset used by GFED (van der Werf et al., 2017) and GFAS (Heil et al., 2010; Kaiser et al., 2012). The high CH_4, as well as CO, emissions factors for peat fires can be attributed to incomplete combustion from smoldering fires, which are common in boreal and tropical peatlands (Kasischke & Bruhwiler, 2002; Stockwell et al., 2016). Additionally, the $PM_{2.5}$ emissions factors used in FINN for woody savanna/shrubland and savanna/grassland (8.3-15.4 g $PM_{2.5}$ kg^{-1} DM) are 16-214% higher than those used in GFEDv4s, GFAS, QFED (4.9-7.17 g $PM_{2.5}$ kg^{-1} DM) for the broader savanna, grassland, and shrubland LULC, which may explain the high $PM_{2.5}$ weighted mean emissions factor for FINN (Table D.1).

4.4.3 Modeling monthly smoke $PM_{2.5}$ from Indonesia fires

4.4.4 Comparison of global fire emissions inventories: speciation and emissions factors

We use monthly GEOS-Chem adjoint sensitivities, from 2005-2009, with the five global fire emissions inventories to model smoke $PM_{2.5}$ in Singapore, Malaysia, and Indonesia from 2003-2016, focusing on the impact of upwind Indonesian fires (Figure 4.7-4.8, D.7-D.8). According to GFEDv4s, peat fires contributed almost half of total OC+BC emissions in Indonesia from 1997-2016. Modeled monthly mean smoke $PM_{2.5}$ is moderately to strongly correlated with observations (r = 0.64 to 0.84, $p < 0.01$), with GFASv1.2 smoke $PM_{2.5}$ most closely matching the temporal variability of observed $PM_{2.5}$ enhancement from smoke (Figure 4.8a). We find similarly strong correlations for population-weighted smoke PM_{10} in Malaysia (r = 0.54 to 0.89, $p < 0.01$) and satellite AOD in Indonesia (r = 0.63 to 0.93, $p < 0.01$; Figures D.7-D.8). While the correlation of modeled and observed smoke $PM_{2.5}$ in Singapore is consistent across inventories, the magnitude of modeled smoke $PM_{2.5}$ can differ by more than 20 μg m^{-3} for the Jul-Oct average during extreme smoke episodes, such as in 2006 and 2015 (Figure 4.8b). For example, the models yield mean Jul-Oct smoke $PM_{2.5}$ concentrations in 2006 that differ from observed smoke by -64% to +70%. For the 2006, 2009, and 2015 high fire intensity years, modeled Jul-Oct smoke $PM_{2.5}$ using GFASv1.2 yields the smallest mean absolute error relative to the observations (16%), compared to such errors from the other four inventories (39-66%).

4.4.4.1 2006 and 2015 severe haze events

Koplitz et al. (2016) used GFASv1.0 and the GEOS-Chem adjoint to investigate the public health effects of smoke from Indonesian fires in 2006 and 2015. These authors estimated over 150% higher premature mortality over Equatorial Asia in 2015 (100,300 excess deaths) than in 2006 (37,600 excess deaths). This suggests higher exposure to smoke and more prolonged fire activity, as well as drier El Niño conditions, in 2015 compared to 2006. In this study, we first compare relative changes in modeled Jul-Oct mean smoke exposure in Singapore between the 2006 and 2015 fire seasons. In addition, the strong negative exponential relationship between rainfall and metrics of fire activity (e.g., active fire count, burned area) in Indonesia is well-established (Fernandes et al., 2017; van der Werf et al., 2017). However, Eck et al. (2019) suggest that thick smoke may obscure fires from satellite detection. To determine whether fire activity in Equatorial Asia is under-detected in 2015 due to haze, we first

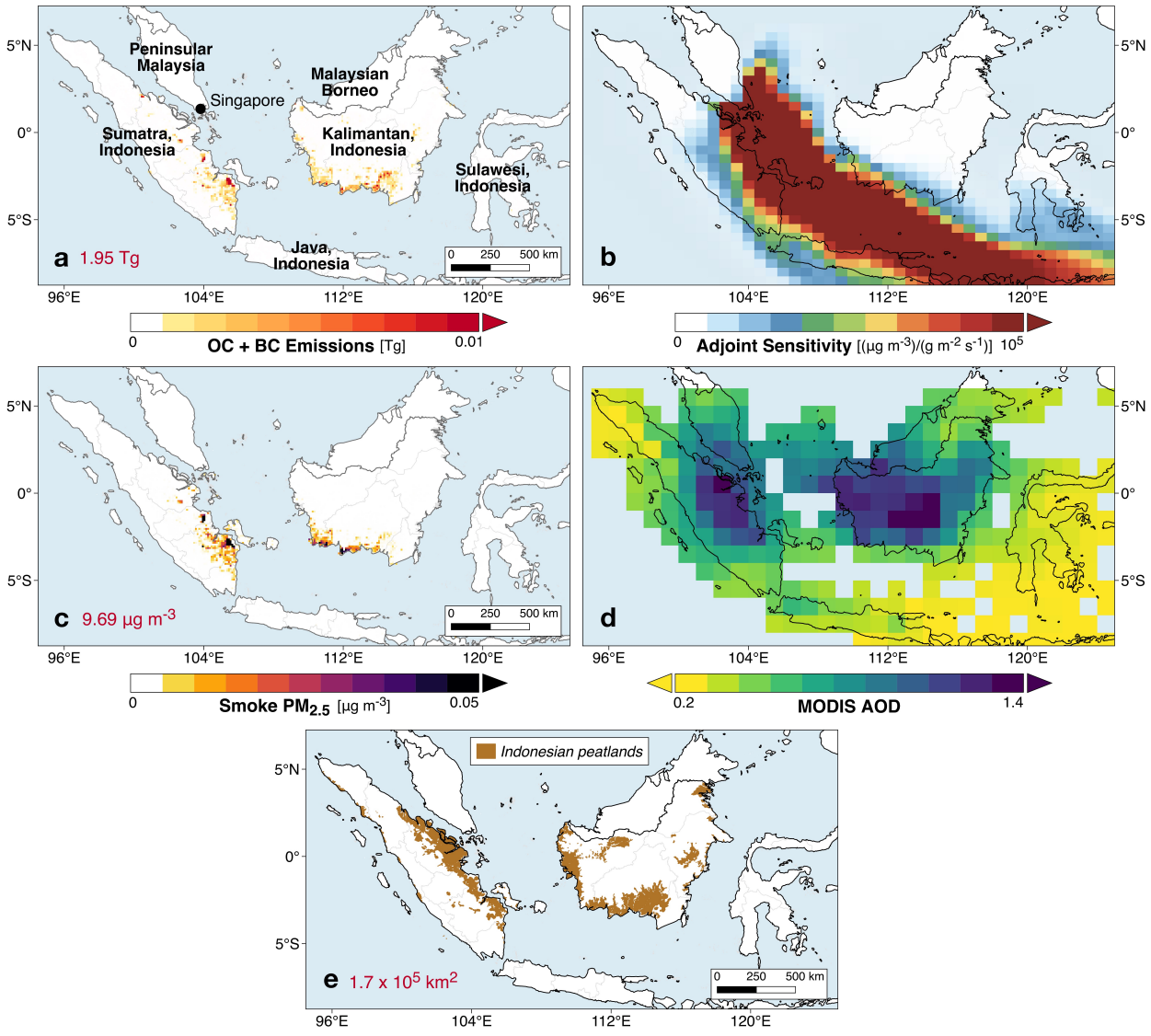


Figure 4.7: Indonesia fires, smoke exposure in Singapore, and AOD in Equatorial Asia during July-October in 2006. (a) Total organic carbon (OC) and black carbon (BC) emissions from GFASv1.2. Sum of OC+BC fire emissions over Indonesia is shown inset. (b) Sensitivity of mean July-October smoke concentrations in Singapore to the location of fire emissions, calculated by the GEOS-Chem adjoint. (c) Contribution of smoke $PM_{2.5}$ in Singapore from fires in individual grid cells over Indonesia, modeled using GFASv1.2 fire emissions. Average, calculated smoke $PM_{2.5}$ exposure in Singapore, which is the sum of these contributions, is shown inset. (d) Average MODIS Terra and Aqua aerosol optical depth (AOD) in Equatorial Asia. (e) Distribution of peatlands in Sumatra and Kalimantan, Indonesia. The approximate total peatland area in these regions is shown inset.

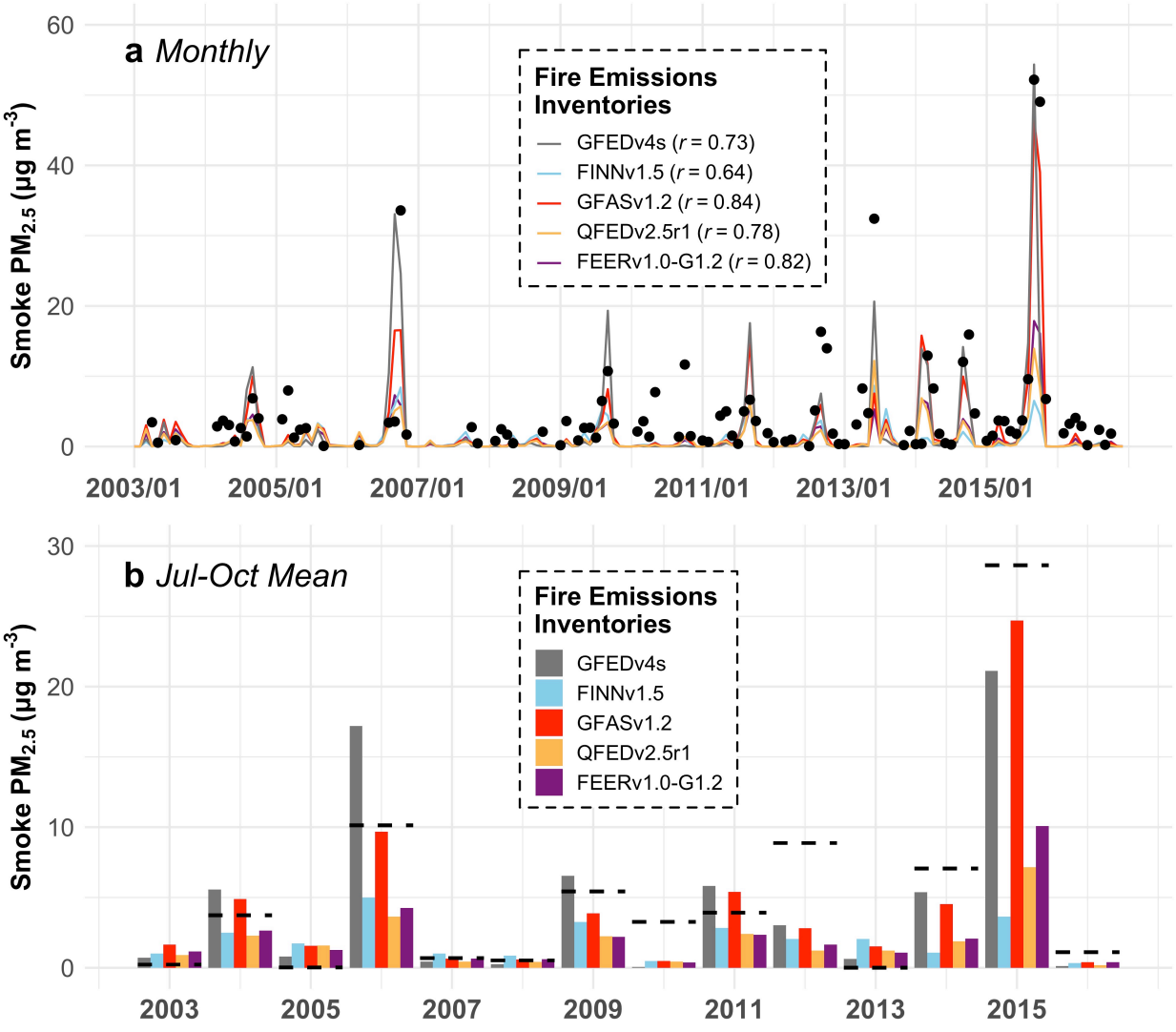


Figure 4.8: Smoke $PM_{2.5}$ exposure in Singapore, from 2003-2016. (a) Timeseries of monthly mean observed (black dots) and modeled (colored lines) smoke $PM_{2.5}$ concentrations. Observed smoke $PM_{2.5}$ is reconstructed from meteorological observations from the Singapore Changi Airport; only non-zero monthly smoke $PM_{2.5}$ observations are shown. Modeled values are from the GEOS-Chem adjoint using different global fire emissions inventories: GFEDv4s, FINNv1.5, GFASv1.2, QFEDv2.5r1, and FEERv1.0-G1.2. Correlations between observed and modeled smoke $PM_{2.5}$ are shown inset for each inventory and are statistically significant ($p < 0.01$). (b) Jul-Oct mean smoke $PM_{2.5}$ by inventory, with observed smoke $PM_{2.5}$ indicated by dashed horizontal lines.

model the linear relationship between rainfall and fire activity, as well as with satellite AOD, in the log-log space for the 2003-2016 period. We use Jul-Oct rainfall rates from CHIRPS and MxD08_M3 AOD. As measures of seasonal mean fire activity, we use the MxD14A1 active fire mask, MxD14A1 FRP, and MCD64A1 burned area, averaged over the Indonesian provinces of Sumatra and Kalimantan, where most fires are concentrated. We then predict 2015 fires in the context of the log-log linear regression of rainfall and fires, modeled excluding 2015 observations. If fires are under-detected due to haze in 2015, then active fire counts, FRP, and burned area should deviate negatively from the modeled log-log rainfall-fire relationships, compared to AOD, which should not deviate significantly.

Several phenomena indicate a more severe haze episode in 2015 than in 2006. The Niño 3.4 index, which is a proxy for ENSO and based on anomalies in tropical Pacific sea surface temperatures, suggests a stronger El Niño in 2015 than in 2006 (Koplitz et al., 2016). In addition, lower rainfall rates (-29%) and higher AOD (+31-34%) over Sumatra and Kalimantan in 2015 suggest drier and hazier conditions over these fire-prone regions, relative to 2006. In contrast, minimal increases in active fire count (+6%) and FRP (+10%) in 2015 relative to the long-term MODIS record, and even decreases in burned area (-35%) suggest that increased haziness in 2015 may have obscured many fires, making satellite detection of fires challenging. During the Indonesia fire season (Jul-Oct), satellite-observed smoke AOD and indicators of fire activity strongly correlate with rainfall in log-log space over 2003-2016 when 2015 is excluded (r = -0.87 to -0.98, $p < 0.01$; Figure 4.9). Given these relationships with rainfall, the 2015 fire activity appears severely underestimated, with active fire 60% less than expected, burned area 93% less, and FRP 62% less. In contrast, AOD in 2015 does not deviate significantly (-12%) from the modeled log-log relationship with rainfall.

The observed AOD and FRP in 2015 are within the 95% prediction interval for these variables, but both burned area and active fire counts are outside this interval. We now examine how these potential underestimates in 2015 fire activity may have affected the fire emissions inventories. We find that GFEDv4s, which includes a small fires boost, and FINNv1.5, which uses active fires to estimate burned area, less severely underestimate (63-76%) burned area in 2015 than the MODIS burned area product (Figure D.4). Inventories that make cloud-gap adjustments for obscured fires are better able to discern the more severe haze event in 2015 and match the observed enhancement of 183% in smoke $PM_{2.5}$ in Singapore: GFASv1.2 shows a 155% increase in smoke $PM_{2.5}$ relative to 2006, and QFEDv2.5r1 and FEERv1.0-G1.2 yield increases of 96-137% (Figure 4.8b). In contrast, GFEDv4s and FINNv1.5 do not capture the enhanced smoke $PM_{2.5}$ in Singapore in 2015. Over-

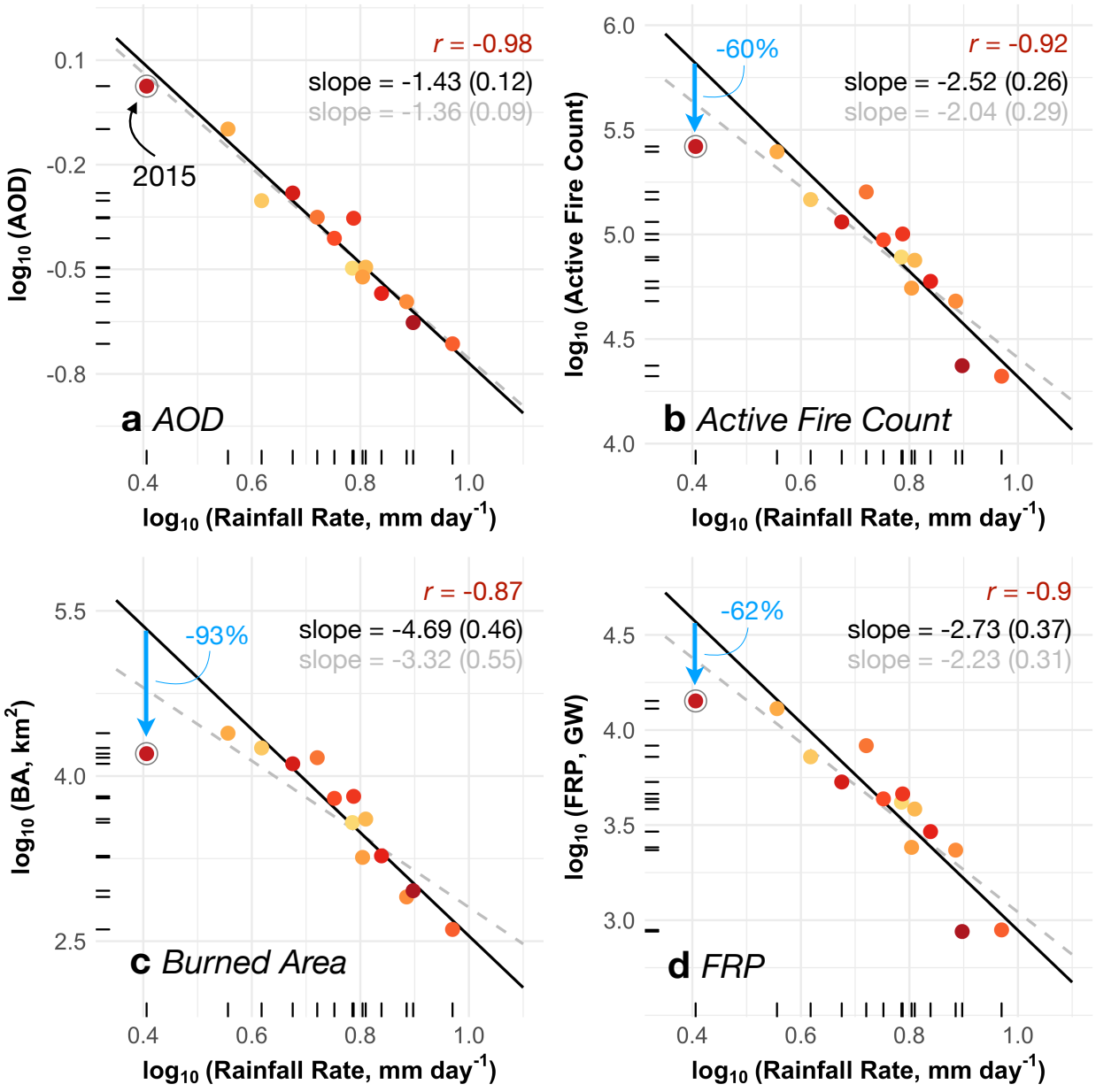


Figure 4.9: Under-detection of 2015 Indonesia fires in MODIS active fire and burned area products relative to the 2003-2016 period. CHIRPS rainfall rates (mm day^{-1}) are plotted against MODIS (a) aerosol optical depth, (b) active fire count, (c) burned area (km^2), and (d) FRP (GW) in log-log space. All variables are averaged temporally over July-October and spatially over Sumatra and Kalimantan, Indonesia. Colors denote different years from 2003-2016, with later years depicted by redder shades; values for 2015 are circled. Inset shows the correlation (r, $p < 0.01$), slope of the linear regression (gray dashed line), and slope with 2015 removed (black line) for each pair of observations. Standard errors for the slopes are shown in parentheses. There is no statistically significant linear trend in any variable over time. Blue arrows in (b), (c), and (d) show that observed fires are lower than expected based on prediction from the linear regression of rainfall and fires that excludes 2015 observations. Percent underestimate of each fire variable based on these predictions is shown in blue.

all, GFASv1.2 most accurately captures both the magnitude and temporal variability of observed smoke $PM_{2.5}$, while FINNv1.5 consistently underestimates smoke $PM_{2.5}$ in high fire intensity years and most poorly captures the temporal variability of observed smoke $PM_{2.5}$.

4.5 Discussion and Conclusion

4.5.1 Relative fire confidence metrics: spatial patterns

The goal of this study has been to quantify and interpret differences across five bottom-up and top-down global fire emission inventories. While it is difficult to directly compare bottom-up and top-down inventories, end-users may use the relative confidence indicated by the BA-score, AFA-score, and FRP-score (pFRP) to select a "best" inventory if limited by computing resources. Nevertheless, these simple scores represent just one way for end-users to evaluate the metrics together; end-users, for example, may choose to assess the five relative fire confidence metrics individually. One important limitation is that the relative fire confidence metrics are time-averaged and therefore do not fully account for interannual or seasonal variability in fire activity. However, in constructing these metrics, we have placed greater weight on high fire intensity years and the dominant fire-prone months in order for end-users to diagnose the overall spatial biases among inventories. Another caveat is that we do not investigate in as much detail the spatial differences in inventory-specific LULC, which affect the fuel consumption and emissions factors imposed.

We first find that two fire landscapes — large and cohesive versus small and fragmented — account for broad differences in the bottom-up fire emissions inventories, GFED and FINN. GFED, which relies primarily on observed burned area, better captures emissions from large, cohesive fires, while FINN, which depends on observed active fires, better captures emissions from small, fragmented fires. Second, the presence of thick cloud/haze during peak fire activity makes satellite fire detection more difficult in equatorial regions, boreal regions, and eastern China. Third, fires located in mountainous regions are also challenging to detect, especially by moderate-resolution sensors, such as MODIS (500 m or 1 km) or VIIRS (375 m or 750 m). For top-down fire emissions inventories (e.g., GFAS, QFED, and FEER), we calculate a pFRP score, which indicates potential underestimates in FRP under clear-sky conditions. We find high pFRP scores suggest that areas dominated by fast-spreading, large fires or short-lived, small fires under clear-sky conditions are not well-captured by MODIS due to limited overpasses or moderate spatial resolution.

4.5.2 Regional application: validation of modeled smoke $PM_{2.5}$ across Equatorial Asia from Indonesia fires

Here we discuss the application of the relative fire confidence metrics for Indonesia fires. (Additional examples for the contiguous United States and northwestern India are discussed in Appendix D.6.) We do not explicitly consider the influence of spatial resolution in applying these fire emissions datasets. We focused on regional scale, so this influence is likely diluted. However, we acknowledge that spatial resolution may be important at local scale.

We can first deduce that fire-prone regions in Indonesia generally follow the small, fragmented fire landscape pattern (metrics 1, 3, and 5) and that high cloud cover and/or haze (metric 2) may impede observation during the fire season. While metric 4 shows rough terrain in parts of Indonesia (e.g., western Sumatra, Java, and northern Kalimantan), most fires occur on flat terrain. However, smoldering peat fires even on flat land may also be difficult to detect.

First, we find that thick haze in very high fire intensity years, such as 2015, likely leads to lower-than-expected fire activity derived from satellite observations. The AFA-score suggests high relative confidence for FINN, in contrast to the low relative confidence by BA-score for GFED; pFRP shows low potential FRP enhancement over Indonesia, primarily because of the presence of thick clouds or haze. Our results suggest that the 93% burned area underestimate in Indonesia arises primarily due to thick haze, an effect greater than the effect of such haze on active fire count (-60%) or FRP (-62%). For Singapore, as well as for Malaysia and Indonesia, we find that top-down inventories yield modeled smoke $PM_{2.5}$ concentrations that are more consistent with observed $PM_{2.5}$ than bottom-up inventories, with r = 0.78-0.84 for top-down versus r = 0.64-0.73 for bottom-up inventories. This result is likely due to the cloud-gap adjustments in the top-down inventories.

Second, only GFAS and GFED consider peatlands as a separate LULC, while in other inventories, peatlands may be classified as savanna, tropical forest, or cropland. These discrepancies have implications for emissions since the carbon-rich peatlands are associated with high fuel load (van der Werf et al., 2010). While the moderate to strong correlation of observed and modeled smoke $PM_{2.5}$ is consistent across inventories, the magnitude of mean Jul-Oct smoke $PM_{2.5}$ in the high fire intensity years of 2006 and 2015 can vary by more than 20 $\mu g\, m^{-3}$, with GFEDv4s and GFASv1.2 best capturing the magnitude of observed smoke $PM_{2.5}$ and yielding higher smoke $PM_{2.5}$ than the other three inventories. Additionally, estimated ratios of peat OC/BC emissions factors ratios are

~150 compared to just 3-39 for other LULC types, thereby affecting the composition of smoke $PM_{2.5}$. Indeed, GFEDv4s and GFASv1.2 show 78-380% higher Jul-Oct OC/BC ratios over Sumatra and Kalimantan during 2003-2016 than the other three inventories. In summary, GFASv1.2, which adjusts for cloud gaps in satellite observations of fires and considers peatlands as a separate LULC class, performs best in terms of modeling smoke $PM_{2.5}$ that is consistent with observations in both temporal variability and magnitude.

4.5.3 Uncertainties in global fire emissions inventories

The uncertainties in global fire emissions inventories influence estimates of emissions budgets, the spatio-temporal variability of fires, and fire trends, with different inventories leading to different conclusions (Appendix D.7). Here we discuss the main sources of uncertainty in inventories: small fires, cloud gap adjustments, aerosol emissions enhancements, and emissions factors and LULC classification. Sole reliance on burned area from MCD64A1 may capture large, contiguous fires well but not the spatial allocation of small fires in fragmented burn landscapes. This is demonstrated by the moderate spatial correlation ($r = 0.36$, $p < 0.01$) between the BA-AFA discrepancy (metric 1) and burn size/fragmentation (metric 3). Additional VIIRS FRP detected outside the MODIS active fire extent (metric 5) also implies low confidence in areas dominated by small fires. As an example of low confidence in small fires, we find that many grid cells in GFEDv4s would not have any emissions without the small fires boost. Approximately one-fourth of grid cells with nonzero GFEDv4s fire emissions from 2003-2016 persistently show 100% spatial coverage by small fires, and the small fire boost alone contributes all the emissions in 57% of GFEDv4s grid cells, on average. Zhang et al. (2018) recommended that grid cells with only small fire contribution, or no MCD64A1 burned area input, be treated with caution. For example, these authors found that GFEDv4s significantly overestimates DM fuel consumption and emissions for areas with infrequent but small fires in eastern China during summer months. Under such conditions, when no burned area is detected, the scaling parameters applied to the total active fire count are not specific to individual grid cells and instead are averaged across regions, seasons, and land cover types (van der Werf et al., 2017).

On the other hand, because MODIS retrieves thermal anomalies only during satellite overpass times, use of MCD14ML active fires in the bottom-up inventories, as well as MxD14 FRP in the top-down inventories, may lead to underestimates of burned area and fire energy from large, contiguous fires. In addition, the FINN emissions inventory may overrepresent small fire emissions due to the assumption that at least 75% of the nominal pixel area is burned (Wiedinmyer et al., 2011). The active fire product also has coarser resolution and a lower de-

tection threshold compared to the burned area product. Using FRP may address this overestimate since small fires are cooler and exhibit lower FRP. Nonetheless, the dependence of the top-down inventories on GFED to convert FRP to DM burned may lead to underestimates of small fire emissions, as seen in the case of agricultural fire emissions in northwestern India (Cusworth et al., 2018).

The cloud/haze fraction (metric 2) indicates that regions with persistent cloud cover or thick haze during the fire season, such as boreal and tropical regions, degrade the quality of satellite observations of fire activity. By adjusting for cloud gaps and scaling with observed AOD, the top-down inventories — GFASv1.2, QFEDv2.5r1 and FEERv1.0-G1.2 — may be better able to match observations than the bottom-up inventories in these regions (Koplitz et al., 2018a). However, the scaling factor of 3.4 recommended by Kaiser et al. (2012) for GFAS aerosol emissions, as well as the simple global QFED scaling by LULC, may bias regional smoke exposure estimates (Koplitz et al., 2016) due to spatial variations in AOD scaling (Darmenov & da Silva, 2013; Ichoku & Ellison, 2014). We thus recommend comparison of aerosol emissions from QFEDv2.5r1 to FEERv1.0-G1.2, which directly estimates TPM using smoke AOD by region. Further, QFED calibrates the coefficient β relating FRP to DM globally, while GFAS uses LULC-specific β coefficients, which vary from 0.13 to 5.87 kg DM MJ^{-1} FRP (Kaiser et al., 2012). We also show that certain species, such as CH_4, are greatly affected by LULC classification within the inventories, and in particular, by the treatment of peatland emissions. In our case study of Indonesian fires, GFEDv4s and GFASv1.2, both of which account for peatlands, yield much higher smoke $PM_{2.5}$ more in line with observations than the other three inventories. Finally, coarse-resolution LULC maps (0.5°-1°), which are used in GFASv1.2 and FEERv1.0-G1.2, may also bias emissions due to differences in fuel loadings in regions with more heterogenous LULC, such as in Southeast Asia (Figure D.10b).

4.5.4 Future directions and recommendations

Integration of both burned area and active fire products into fire emission inventories may reduce underestimation of fires in small and fragmented or large and contiguous fire regions, respectively. Similar to the hybrid approach of using active fires for the small fire boost in GFEDv4s, incorporation of burned area in FINN could retroactively improve emissions estimates for large fires. For the top-down inventories of GFAS, QFED, and FEER, use of burned area as a secondary input satellite fire dataset may yield emissions more closely matched with observations compared to the current dependence on assumptions of fire persistence across cloud gaps and satellite overpasses. Standardization of emissions factors, in particular in the partitioning of LULC, could help

reduce inconsistencies between inventories. In particular, the peatland maps used, if any, are incomplete and could be improved using more comprehensive global peatland datasets, such as PEATMAP (Xu et al., 2018). We also expect that the updated MODIS MCD12Q1 land cover dataset from C5 to C6 will lead to some differences between current and future emissions estimates (Sulla-Menashe et al., 2019). Further, access to high spatial resolution surface reflectance datasets from Landsat (30 m, every 16 days) and Sentinel-2 (20 m, every 5 days) in the GEE data catalog makes feasible both ground truth validation and improvement of burned area estimates and LULC classifications (Casu et al., 2017). Recent studies have shown overall improvement in accuracy and small burn scar detection using Landsat and Sentinel, but low revisit times may limit this improvement in areas with high cloudiness and rapid land use change (Crowley et al., 2019b; Goodwin & Collett, 2014; Hawbaker et al., 2017; Roteta et al., 2019)

For end-users, we recommend use of multiple bottom-up and top-down inventories, if possible. Further, end-users should be aware that outdated emissions estimates can persist in models, leading to biases and errors in model results (Appendix D.8). We present here an online tool, "Fire Inventories: Regional Evaluation, Comparison, and Metrics" (FIRECAM; `https://globalfires.earthengine.app/view/firecam`), that allows users to compare regional monthly and yearly emissions, from 2003-2016, from the five global inventories for six species (CO, CO_2, CH_4, OC, BC, and $PM_{2.5}$) and to interpret the regional differences between fire emissions by using the five relative fire confidence metrics (Figure D.11, Appendix D.5). FIRECAM will be updated regularly in the foreseeable future as new versions of the inventories and underlying datasets become available. We identify three key factors that should influence the end-user's inventory selection and can also significantly affect the results of modeling studies: input satellite fire dataset, statistical adjustments, and LULC classification and emissions factors. For example, in our case study on Indonesian fires, we find that the cloud-gap adjustment and representation of peatland emissions are two important factors that distinguish different inventories in the regional validation of smoke $PM_{2.5}$; both factors are included in the GFAS inventory. FIRECAM allows users to rapidly assess such differences in regional fire emissions.

5

Detection and impacts of tiling artifacts in MODIS burned area classification

5.1 Abstract

Since 2000, observations from the Moderate Resolution Imaging Spectroradiometer (MODIS) instrument, aboard the Terra and Aqua satellites, have been used to monitor global burned area and its trends. The FireCCI and MCD64A1 products classify burned area using algorithms that detect change in surface reflectance and separately process each ~10° x 10° MODIS tile. We find that artifacts arise in both products from this tiling procedure. In particular, we find severe tiling artifacts in FireCCI, version 5.1 (FireCCI51) in northwest India and Pakistan, where the classified burned area is disjointed at the latitudinal boundary of two tiles that largely separates the Indian states of Punjab and Haryana. In contrast, this tiling effect is less noticeable in MCD64A1, Collection 6 (C6). As a result, while the average 2003-2019 October-November burned area in Haryana is of similar magnitude across the two products, that for Punjab is 13,381 km^2 for MCD64A1 and just 1,486 km^2 for FireCCI. We find moderate tiling artifacts in Southeast Asia and Eastern Europe. Our results highlight that additional processing is needed to ensure the continuity of burned area classification in FireCCI and MCD64A1, as well as other products relying on tile-dependent algorithms.

5.2 Introduction

Accurate mapping of global burned area is necessary for informing fire management strategies and understanding the role of fire in land cover and land-use change, aerosol and greenhouse gas emissions, air pollution and public health, climate-chemistry interactions, and ecosystem dynamics (Johnston et al., 2012; Andela et al., 2017;

van der Werf et al., 2017). Burned area algorithms rely on change detection in near-infrared (NIR) and shortwave infrared (SWIR) surface reflectance in pre-fire and post-fire composites (Giglio et al., 2018; Lizundia-Loiola et al., 2020; Hawbaker et al., 2017). To reduce the high computational expense in data processing, burned area algorithms are often applied to individual tiles (e.g. MODIS) or scenes (e.g. Landsat). However, this approach may introduce data artifacts at the tile boundaries, visually evident after the tile-dependent burned area maps are mosaicked together (Humber et al., 2019; Lizundia-Loiola et al., 2020; Liu et al., 2020a).

With the advent of Google Earth Engine, a cloud computing platform for geospatial analysis with a petabyte-scale public data catalog, end-users have immediate access and capability to analyze widely used global datasets, including many derived from MODIS (Gorelick et al., 2017). As more end-users include high-level satellite products in analyses, this ease in data access demands better communication of caveats in their use to avoid erroneous assumptions or biased results (Humber et al., 2019). To ameliorate such biases, it may be tenable to use a hybrid approach with multiple satellite products for regional fire studies (Crowley et al., 2019b,a; Liu et al., 2019).

As planetary-scale studies have increased, the use of tiling, or splitting data processing into arbitrary geographical chunks, has become necessary to efficiently manage large geospatial datasets and limited computational resources (Giglio et al., 2018; Lizundia-Loiola et al., 2020). In this study, we identify and analyze the tiling artifacts in two MODIS-derived global burned area products: MCD64A1 and FireCCI. We develop methods to pinpoint tiling artifacts at both upscaled and pixel-level spatial resolutions. Then, we quantify the impacts of severe tiling artifacts on burned area analyses in affected regions, such as northwest India.

5.3 Methods

5.3.1 Satellite fire datasets

MCD64A1 C6 is the current version of NASA's gridded, Level-3 MODIS burned area product at 500-m spatial resolution (Giglio et al., 2018). MCD64A1 uses 1-km MODIS active fire hotspots to select training pixels and define thresholds to classify burned area with pre-fire and post-fire composites. MCD64A1 uses a burn-sensitive index calculated from MODIS surface reflectance in the NIR (1.24 μm) and SWIR (2.13 μm) bands.

FireCCI51 is the 250-m MODIS burned area product from the European Space Agency for its Climate Change Initiative (CCI) (Chuvieco et al., 2018; Lizundia-Loiola et al., 2020). FireCCI uses a two-phase "seed" and "growing" method, where the spatial patterns of initial high confidence "seed" burn pixels are modified in

the "growing" phase. Like MCD64A1, FireCCI uses MODIS active fires as input. Because SWIR is only available only at 500-m resolution, FireCCI primarily relies on the 250-m NIR band at 0.86 μm.

MOD14A1 and MYD14A1 C6 are the gridded, Level-3 active fire products derived from MODIS observations of 1-km thermal anomalies (Giglio et al., 2016, 2018). In contrast to tile-dependent burned area algorithm, the active fire algorithm uses Level-1B MODIS brightness temperatures, which are on unprojected swath, and defines classification thresholds using a moving window centered on the sample location.

5.3.2 Identifying tiling artifacts

5.3.2.1 Method 1: normalized difference of burned area and active fire area

Liu et al. (2020a) introduced a metric to quantify the relative discrepancy between MODIS burned area and active fire products, inadvertently revealing large-scale tiling artifacts in MCD64A1. This metric relies on the normalized difference of monthly burned area and MOD/MYD14A1 active fire area on a grid with an upscaled spatial resolution of 0.25° x 0.25°. We further simplify the metric φ as follows:

$$\varphi_{i,j} = \frac{BA_{i,j} - AFA_{i,j}}{BA_{i,j} + AFA_{i,j}} \tag{5.1}$$

where BA is burned area and AFA is "active fire area," or the area of active fire pixels, in each grid cell located at longitude i and latitude j. A value of $\varphi \sim$ -1 indicates dominance of AFA over BA, while $\varphi \sim 1$ suggests the opposite. However, the exact value of φ is less important than its relative value, because we visually examine spatial patterns in φ — that is, abrupt changes in φ across different tiles — to search for regions with large-scale tiling artifacts.

5.3.2.2 Method 2: adjacent burned pixel pairs across tile edges

Additionally, we develop a method to detect classification discontinuities across tile edges at the native spatial resolution. Figure 5.1 shows a schematic detailing our approach. First, we segment MODIS tile polygons into lines that represent the north-south or east-west edge of two tiles, which we generalize here as Tile 1 ($T1$), and Tile 2 ($T2$). We then apply a buffer around the tile edge equal to the nominal scale of the burned area product (FireCCI: ~250-m, MCD64A1: ~500-m) and isolate burned pixels adjacent to the tile edge. Next, we convert the burned pixels into centroids. We use gBA to denote burned pixel centroids adjacent to the shared $T1$-$T2$ tile

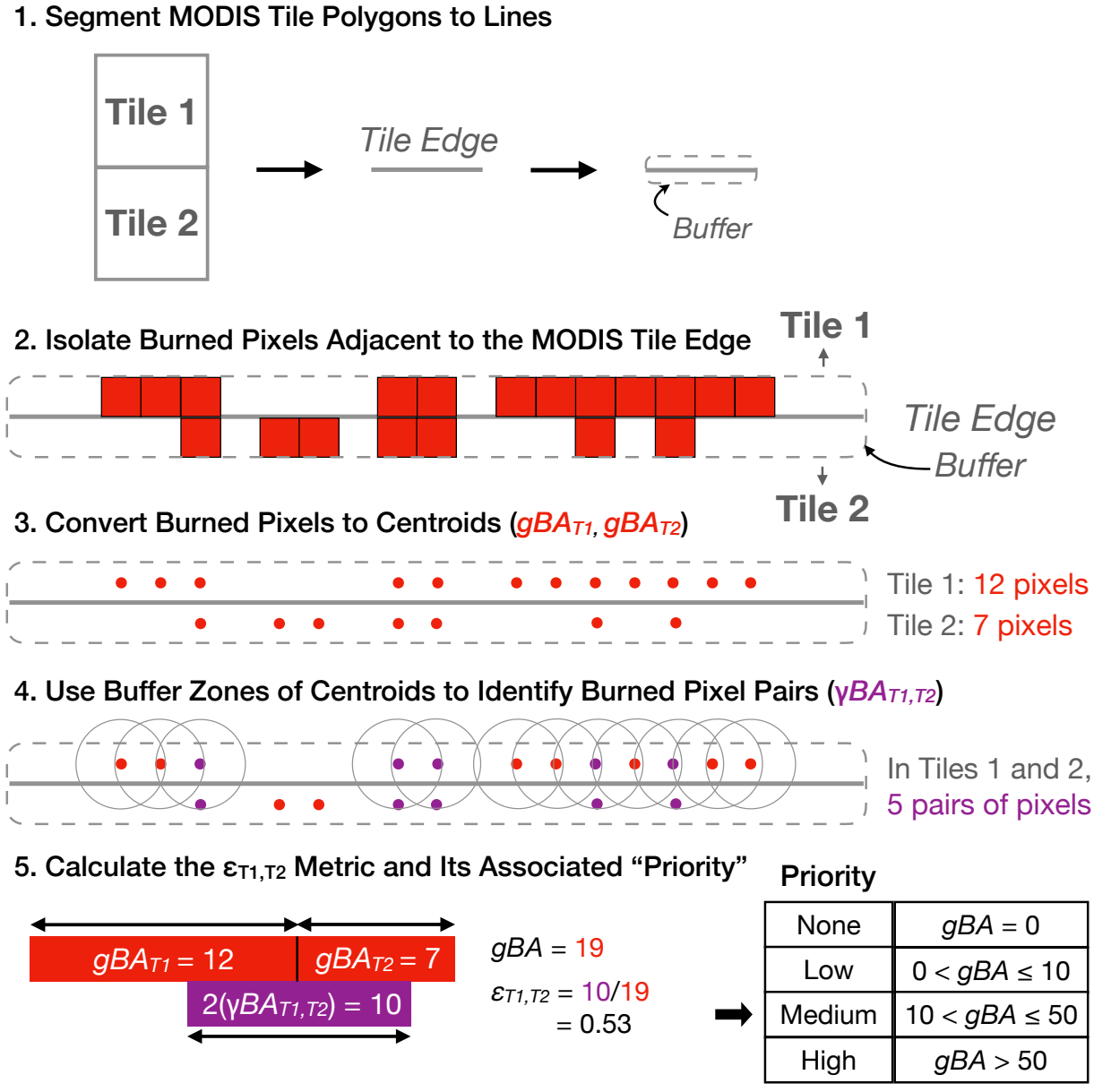


Figure 5.1: Pictorial depiction of the pixel-level approach to identify burned area artifacts at tile edges, as described in Section 5.3.2.1.

edge. Finally, we search for $T2$ centroids located within $T1$ buffer zones and use $\gamma BA_{T1,T2}$ to denote pixel pairs where the two pixels are directly adjacent to each other across the tile edge.

For each month and tile edge, we assign "priority" classes based on gBA: none ($gBA = 0$), low ($0 < gBA \leq 10$), medium ($10 < gBA \leq 50$), and high ($gBA > 50$). Specifically, we place higher priority on tile edge artifacts where many burned pixels are potentially affected. To account for the coarser spatial scale of MCD64A1, we scale gBA by 2. For low to high priority cases, we define the fraction of adjacent pixels, $\varepsilon_{T1,T2}$, as an indicator of classification continuity across tile edges:

$$\varepsilon_{T1,T2} = \frac{2(\gamma BAT1,T2)}{gBA_{T1}+gBA_{T2}} \tag{5.2}$$

Low ε (~ 0) indicates high likelihood of tile edge effects. Additional details on the φ and ε metrics, including limitations, are contained in Appendix E.1.

3. Results and Discussion By visually inspecting φ, we find large-scale tiling artifacts in MCD64A1 and FireCCI51 in three regions: R1, northwest India and Pakistan (tiles h24v05 and h24v06); R2, Myanmar and Thailand (h26v06, h27v06, h26v07, and h27v07); and R3, Ukraine and southwest Russia (h19v03, h20v03, h19v04, and h20v04) (Figure E.1). MCD64A1 contains tiling artifacts in R1 (April-May) and R3 (March-April), and FireCCI in all three regions (R1: May, October-November; R2: January-April; R3: April).

We find the most severe tiling artifacts in FireCCI in northwest India (R1) in October-November (Figure 5.2). While FireCCI and MCD64A1 largely agree in Haryana (h24v06), FireCCI is almost entirely absent in Punjab (h24v05). The sharp discontinuity in φ across the h24v05-h24v06 tile edge highlights this discrepancy; while $\varphi \sim 0$ for MCD64A1 in h24v05, $\varphi \sim$ -1 for FireCCI, indicating here the dominance of AFA over BA. At the pixel scale, the ε metric confirms tile edge artifacts in FireCCI: on average, $\varepsilon = 0$ for FireCCI and $\varepsilon = 0.5$ for MCD64A1 (Table E.1). As a result, in Punjab, MCD64A1 averages ~ 9 times the burned area (13,381 km^2) of FireCCI (1,486 km^2) during the post-monsoon (October-November). In contrast, total post-monsoon burned area in Haryana is of similar magnitude (MCD64A1: 2,361 km^2, FireCCI: 2,717 km^2). FireCCI erroneously suggests that the burned area distribution in h24v05 is unimodal and not bimodal like in h24v06 (Figure 5.3). Though not as severe as FireCCI, MCD64A1 exhibits moderate tiling effects in earlier years (e.g. 2003-2004) (Figure 5.2b-c). In the pre-monsoon (April-May), when fire activity is lower than in the post-monsoon, the φ and ε metrics indicate tiling artifacts in both MCD64A1 and FireCCI (Table E.1).

Moderate tiling artifacts are present in FireCCI in Myanmar (R2) in January-April and in both MCD64A1

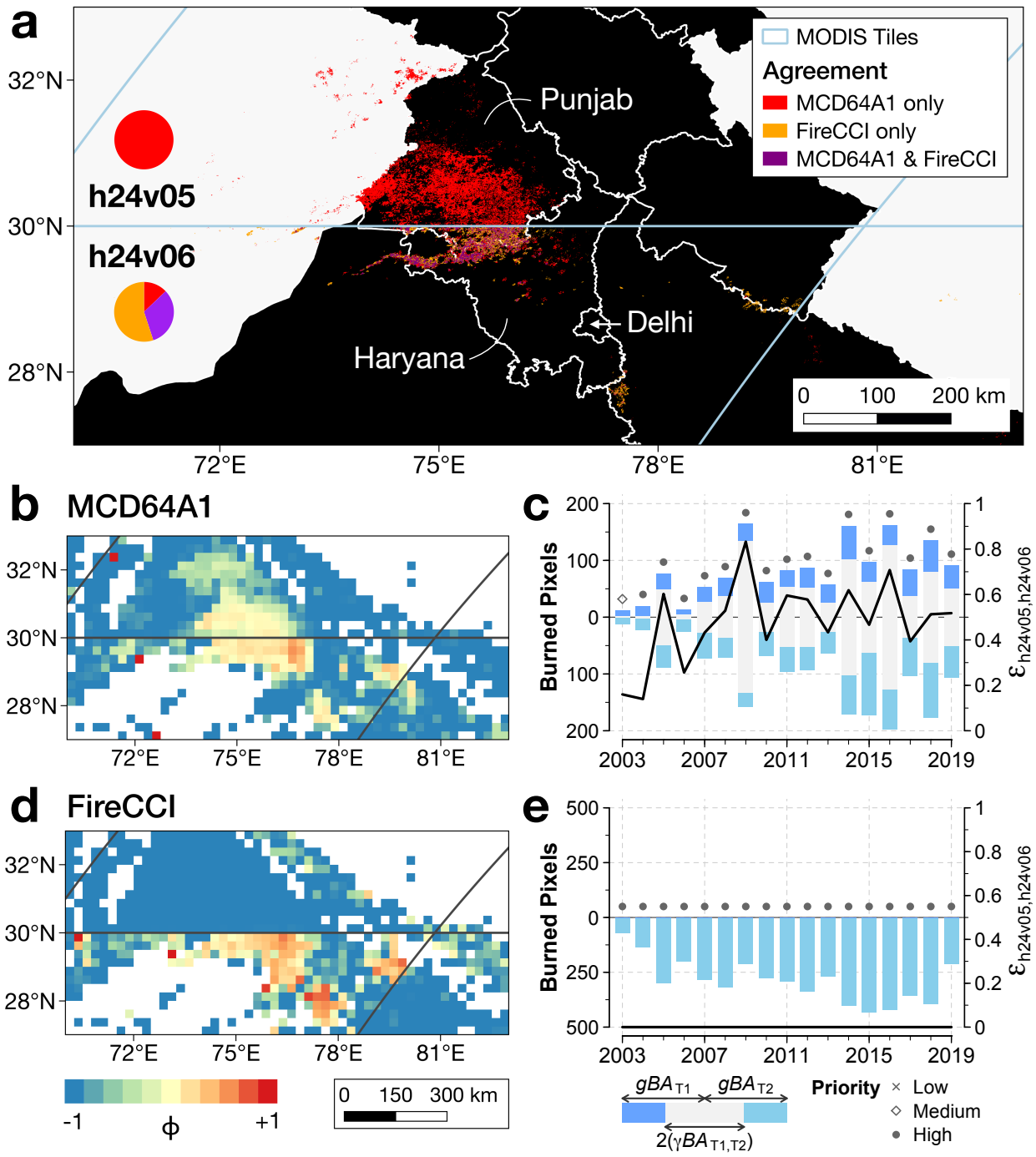


Figure 5.2: Example of the tiling artifacts in FireCCI in November in northwest India. (a) Agreement between FireCCI and MCD64A1 in 2018 in the MODIS tiles h24v05 and h24v06. Pie charts denote the per-tile proportion of burned area derived from MCD64A1 only (red), FireCCI only (orange), and both products (purple). (b) φ metric, which identifies discrepancies between for MCD64A1 burned area and MOD/MYD14A1 active fire area, aggregated over 2003-2019. (c) Right axis: ε metric for the h24v05 (T1) and h24v06 (T2) tiles (black lines), indicating the fraction of matching pixels along the tile edge from 2003-2019. A value of 0 indicates that burned area is discontinuous across the tile edge. Left axis: bars show the number of burned pixels adjacent to the tile edge with priority classes denoted by gray symbols above the bars. Pixels in adjacent pixel pairs are denoted in gray, and others are denoted in blue (T1: dark blue, T2: light blue). (d-e) Same as (b-c) but for FireCCI burned area. Close to the tile boundary, FireCCI reports burned pixels only in h24v06.

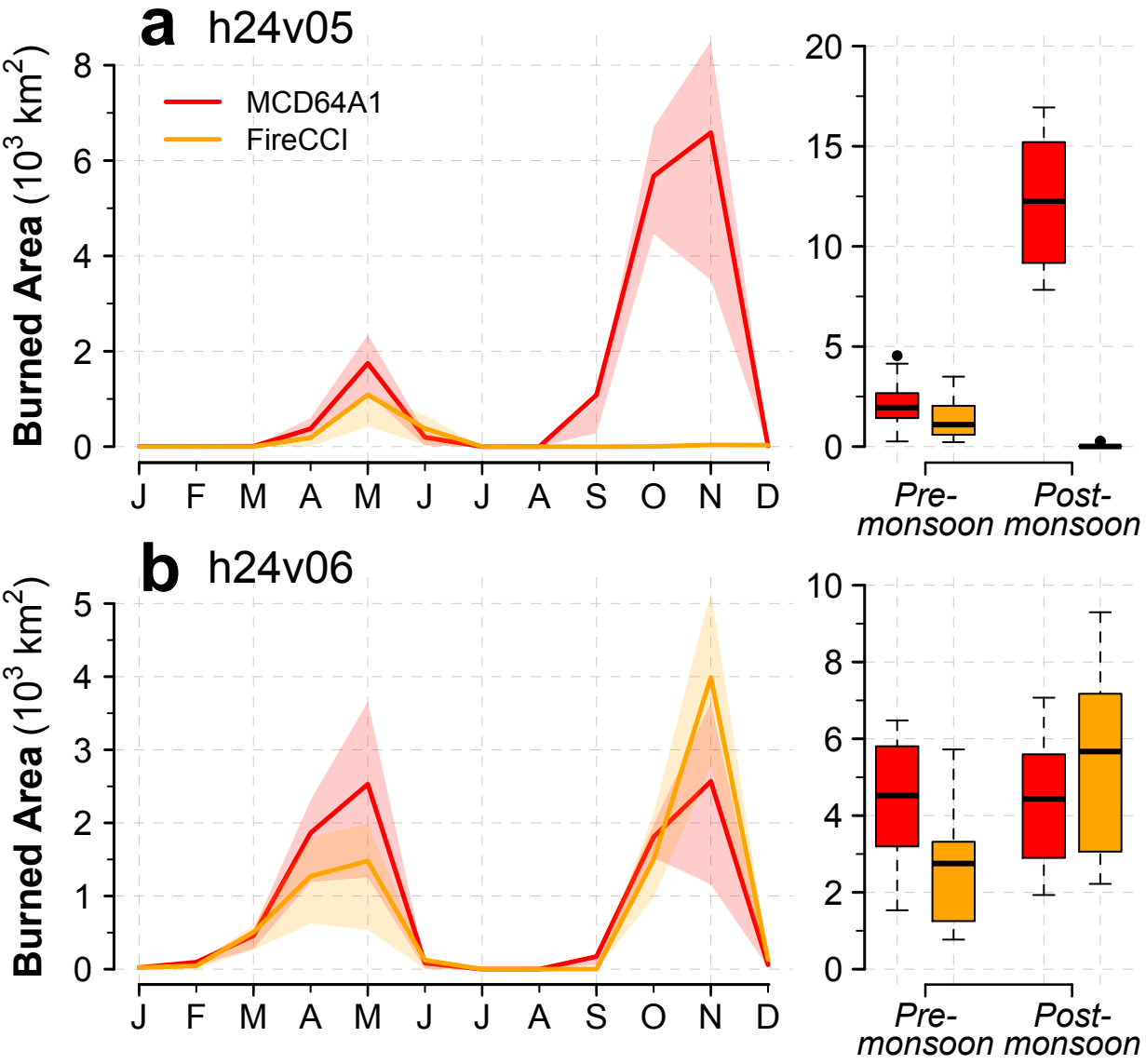


Figure 5.3: Average MCD64A1 and FireCCI burned area in northwest India from 2003-2019. Burned area in northwest India within the MODIS tiles (a) h24v05 and (b) h24v06 are shown as (left) monthly time series and (right) pre-monsoon (April-May) and post-monsoon (October-November) totals. In the left panels, lines show the mean from 2003-2019, while the envelopes denote the 25th-75th percentiles.

and FireCCI in Ukraine and southwest Russia (R3) in March-April and July-October (Table E.1, Figures E.2-E.3). In R3, the φ and ε metrics do not always agree, indicating that the artifacts are more subtle. Specifically, gradients in φ across tiles may not be clear, and there may not be enough observations at the tile edge to confidently interpret ε. We recommend using the φ and ε metrics to guide further visual inspection of the burned area products at monthly and native spatial resolution.

In summary, we propose two simple metrics to identify tiling artifacts in FireCCI and MCD64A1. As we show for northwest India, tiling artifacts can introduce large errors in burned area analyses. End-users can generate and use these metrics to compare biases in burned area datasets and identify the most appropriate data source for their region and burned area analysis. Our results suggest that additional processing in tile-based burned area products is necessary to ensure data quality in terms of spatial continuity, either through future algorithm updates or further post-processing by end-users.

6

Global search for temporal shifts in fire activity: potential human influence on southwest Russia and north Australia fire seasons

6.1 Abstract

Decadal trends in fire activity can reveal important human and climate-driven influences across a multitude of landscapes from croplands to savannas. We use 16 years of daily satellite observations from 2003-2018 to search globally for stationary temporal shifts in fire activity during the primary burning season. We focus on southwest Russia and north Australia as case study regions; both regions experienced nearly 40-day shifts over a 16-year period but in opposite directions. In southwest Russia, a major wheat-growing region, we trace the delay in post-harvest fires to several potential drivers: modernization in the agricultural system and recent droughts, followed by government restrictions on wheat exports. In north Australia, prescribed burns in the early dry season are a key practice in Aboriginal fire management of savannas, and the increasing trend of such fires has limited the size and extent of fast-spreading late dry season fires, thereby shifting overall fire activity earlier. In both regions, human action, through controlling fire ignition and extent, is an important driver of the temporal shifts in fire activity with climate as both a harbinger and an amplifier of human-induced changes.

6.2 Introduction

Two decades of daily satellite data from NASA's Moderate Resolution Imaging Spectroradiometer (MODIS) have made analysis of long-term trends in global fire activity possible at daily to monthly scale (Andela et al.,

2017). While climate variability is a dominant control on fire activity, humans play an important role in modulating fire behavior through ignition, fire suppression and management, and land use change (Andela & van der Werf, 2014; Andela et al., 2017; Chen et al., 2017; Pechony & Shindell, 2010; Riley et al., 2019; Bowman et al., 2020). Andela et al. (2017) mainly attribute the 24% decline in global burned area from 1998-2015 to human activity, through expansion in populated areas, croplands, and livestock, rather than variability in precipitation or temperature. Understanding trends in fire activity can (1) shed light on the consequences of changes in local land management practices and agricultural systems and (2) lead to efforts to mitigate fire-related impacts on air quality, public health, ecosystem services, and the carbon budget (Koplitz et al., 2016; Johnston et al., 2012; Liu et al., 2016; Zhang et al., 2014a; Bowman et al., 2020).

While most studies to date have investigated global trends in the magnitude of fire activity (Andela et al., 2017), here we focus on regional shifts in the timing of peak fire activity. Regions with large, sustained temporal shifts over a multi-year period may reveal human influence on fire regimes through management or land use. In forest management, controlled burning of fuel-abundant areas in advance of the fire season peak can reduce the number and size of large fires (Fernandes & Botelho, 2003). An earlier fire season suggests better managed forests with fewer large and destructive fires, while a later fire season would indicate the opposite. In croplands, recent work using satellite fire data identified a primarily human-driven delay in rice residue burning in north India, where a ~2-week delay in the post-monsoon fire season (October-November) from 2003-2018 can be partially attributed to a 2009 groundwater policy that delayed rice planting dates closer to the summer monsoon onset (Liu et al., 2021a; Jethva et al., 2019; Balwinder-Singh et al., 2019). The policy, which arose from an effort to combat the severe groundwater decline (Singh, 2009; Tripathi et al., 2016), unleashed a cascade of effects that delayed the rice growing season and subsequent burning of rice residues, potentially with unintentional consequences for air quality (Liu et al., 2021a; Jethva et al., 2019; Balwinder-Singh et al., 2019). This is because burning later in the year coincides with meteorological conditions that favor the accumulation of pollutants — i.e., weak ventilation from temperature inversions, stagnant winds, and low mixing layer heights (Ojha et al., 2020).

To fully understand the potential of temporal shifts in the fire season to signal human imprints and influence regional air quality and human health, we must first identify such regions. In this study, we search globally and uncover additional regions with notable temporal shifts in fire activity from 2003-2018. We further investigate two case study regions, southwest Russia and north Australia, where we observe particularly large temporal shifts of nearly 40 days during the primary fire season in opposite directions — later in Russia and earlier in Australia.

Finally, we probe and discuss possible human — and to a lesser extent, climatic — influences on temporal shifts in the two case study regions, and briefly, on a global scale.

6.3 Data and Methods

6.3.1 Satellite fire datasets

As two measures of fire activity, we use the Level 3 MODIS Collection 6 burned area (MCD64A1) and active fire (MOD14A1/MYD14A1) products (Table F.1). MCD64A1 is available in monthly timesteps from 2000-present at 500-m spatial resolution Giglio et al. (2018). We disaggregate MCD64A1 burned area to daily timesteps according to the Julian burn date. The MOD14A1 and MYD14A1 gridded active fire products are available daily at 1-km spatial resolution for the Terra (10:30 am/pm) and Aqua (1:30 am/pm) satellite overpasses, respectively Giglio et al. (2016). For each day, we combine MOD14A1 and MYD14A1 active fires (hereafter referred to as MxD14A1) into a binary fire mask (0 = no fire, 1 = fire), a custom product for this analysis that is different than the MCD14ML global monthly fire location product Giglio et al. (2016). To reduce noise at the pixel level, we sum daily MCD64A1 burned area and MxD14A1 active fire area on a 0.25° x 0.25° grid. More details about the satellite fire datasets are provided in Appendix F.1.

6.3.2 Global search for temporal shifts in the primary fire season

As an initial search for temporal shifts, we focus on a 16-year time period from 2003-2018 but include observations in 2002 if the primary fire season for a particular grid cell extends from December to January of the following year. In brief, our approach, following Liu et al. (2020b, 2021a), is to track the changes in the midpoint of the primary fire season, $k_{midpoint}$, defined as the mean of days t, weighted by daily burned area (BA_t):

$$k_{midpoint} = \frac{\sum_{t=1}^{n}(t \times BA_t)}{\sum_{t=1}^{n} BA_t} \tag{6.1}$$

For each grid cell, we define the primary fire season as a 7-month time window centered on the month with the highest burned area but exclude those months with < 1% annual burned area; we use $t = 1, 2, 3...n$ to represent days of the fire season. For each grid cell, we take the slope of a simple linear regression of the yearly $k_{midpoint}$ timeseries as the magnitude of the temporal shift in the fire season, in days per year. In this initial step, we define a lax threshold of $p < 0.1$ as statistically significant to more easily identify clusters of grid cells with temporal shifts

Table 6.1: Regions of interest with coherent spatial signals of temporal shifts at the midpoint of the primary fire season from 2003-2018. All trends are statistically significant at $p < 0.1$.

Code	Region	Provinces / States	**Fire Season** [start to end, Julian days]	**Temporal Shift** [days yr^{-1}; total 16-yr shift]
		1. Agricultural fires		
1a	NW India	Punjab, Haryana, Rajasthan [north of 29°N, east of 73.5°E]	250 to 340	+1.24 (20 days)
1b*	SW Russia	Krasnodar, Adygea, Rostov, Stavropol	140 to 330	+2.41 (39 days)
1c	S Russia	Omsk, Novosibirsk, Altai, Kemerovo, Khakassia, Krasnoyarsk, Tomsk, Irkutsk [south of 57.5°N]	70 to 150	-1.36 (22 days)
1d	Thailand	*all*	300 to 130	+0.64 (10 days)
		2. Savanna, grassland, and shrubland fires		
2a*	N Australia	Northern Territory, Queensland [north of 14.75°S]	90 to 365	-2.41 (39 days)
2b	C Madagascar	Anosy, Ihorombe, Haute Matsiatra, Amoron'i Mania, Vakinankaratra, Itasy, Bongolava, Analamanga, Betsiboka	100 to 365	-1.99 (32 days)
2c	Zimbabwe	*all*	110 to 350	+0.81 (13 days)
2d	N Brazil	Pará [south of 5.5°S]	190 to 300	+0.61 (10 days)

and define regions of interest (ROIs). We further exclude grid cells with < 5 years of nonzero annual burned area to focus on stationary temporal shifts.

Because of this focus on areas where fires recur on an annual basis at similar intensity, potential ROIs consist primarily of cropland and savanna, grassland, and shrubland areas rather than forested areas. We use the MODIS MCD12Q1 land cover product with the University of Maryland (UMD) classification to assign the primary land cover for each ROI (Sulla-Menashe et al., 2019). We further investigate two ROIs as our case studies: southwest Russia and north Australia (Figure 6.1, Table 6.1), where the temporal shifts in the primary fire season are particularly large (>1 month from 2003-2018) and spatially cohesive. For each ROI, we refine the start and end dates of the primary fire season based on the time series of daily regional BA stacked by Julian day from 2003-2018. As described above, our initial global search to identify ROIs uses a generalized 7-month window centered on the

month with the highest burned area.

Additionally, the very different geographical context of these two ROIs — croplands in southwest Russia and savannas in north Australia — allows us to juxtapose the potential land cover and region-specific mechanisms that led to the temporal shifts. Fires in both regions are heavily impacted by human activity, either through agricultural practices or fire management. For case study 1, we define southwest Russia as Krasnodar Krai, Republic of Adygea, Rostov Oblast, and Stavropol Krai, which are major wheat-growing areas located in the North Caucasus and Southern Federal Districts to the east of the Black Sea (Figure F.2a). This region, with its fertile black soils and favorable climate, produces over half of Russia's winter wheat, with ∼25% higher yields than the all-Russia average (ROSSTAT, 2020b; Schierhorn et al., 2014). For case study 2, we define north Australia as areas north of 14.75°S in the Top End of Northern Territory and Cape York in Queensland. We focus on Arnhem Land, a biodiverse region in the eastern half of the Top End, has a majority Aboriginal population, large expanse of protected lands, and a network of Aboriginal ranger groups (Price et al., 2012; Russell-Smith et al., 2019; Ansell et al., 2020) (Figure F.5a).

For our two case study regions, southwest Russia and north Australia, we use two methods to estimate $k_{midpoint}$: (1) weighted mean (as described in Section 6.3.1) and (2) sigmoid-smoothed partial sums (Zhang et al., 2014b; Liu et al., 2020b, 2021a). Both methods have been used to characterize the temporal progression of the fire season; moreover, the two methods show minimal differences in the derived temporal shifts in the fire season (Liu et al., 2020b). In method 2, $k_{midpoint}$ is defined as the first day by which 50% of total fire activity as indicated by burned area has occurred. To reduce the sensitivity of this method to large spikes in fires, we apply sigmoid smoothing to the partial sums before calculating $k_{midpoint}$. Hereafter, we abbreviate $k_{midpoint}$ from method 1 as $k_{midpoint,\omega}$ and that from method 2 as $k_{midpoint,\rho}$. We find that applying sigmoid smoothing in method 2 increases agreement between$k_{midpoint,\omega}$ and $k_{midpoint,\rho}$. While method 1 is computationally efficient for our initial global search, method 2 allows us to more accurately characterize the start and end of the fire season, k_{start} and k_{end}, for fire seasons with asymmetrical temporal distributions. We define $k_{,}tart$ and k_{end} as the day by which 10% and 90%, respectively, of total burned area for that season has accumulated. In method 2, k can generalized as k_{β}, where β represents various breakpoints in the fire season:

$$k_\beta = arg\,min_k\{(\frac{\hat{y}_k}{\hat{y}_n} - \beta)|(\frac{\hat{y}_k}{\hat{y}_n} - \beta) > 0\}, \text{where}$$
$$\{k = k \in N \,|\, 1 \leq k \leq n\} \tag{6.2}$$

where $\hat{y}_k$ is the sigmoid-smoothed partial sums of the sequence of daily burned area over day 1 to k, n is the total number of days in the primary fire season, and k_β is the first day by when $\hat{y}_k$, normalized by the sum of burned area $\hat{y}_n$ during the fire season, has surpassed breakpoint β. As in the global search, we use a simple linear regression to assess the trends in $k_{midpoint}$ (β=0.5), k_{start} (β=0.1), and k_{end} (β=0.9). Here for our case study regions, we define $p < 0.05$ as statistically significant.

Ancillary datasets and methods used to provide context on the potential links between fires, human activity, and meteorology are described in Appendix F.2. Here we focus on human influences on fire activity rather than meteorological changes, as land management practices and policies are often documented and occur on a much finer spatial scale, i.e., within designated areas or bounded by administrative borders.

6.4 Results and Discussion

6.4.1 Global temporal shifts in fire activity

We detect temporal shifts in 22% of global burned area using MCD64A1 and 25% using MxD14A1 active fire area at a statistical significance threshold of $p < 0.1$ (Figure 6.1). However, we note that some grid cells with temporal shifts are spatially fragmented or opposite in sign relative to their neighbors. This "speckle" may be characteristic of a mismatched grid cell size for analysis where it is incompatible with the process being observed (i.e., non-stationary) or statistical noise. Instead, we focus on large clusters of grid cells with similar magnitudes and the same sign in temporal shifts, so that when burned area is aggregated over the defined ROI, the overall temporal shift is likely statistically significant as well. In Figure 6.1, we highlight select ROIs with coherent temporal shifts for croplands (northwest India, southwest Russia, south Russia, and Thailand) and for savannas, grasslands, and shrublands (north Australia, central Madagascar, Zimbabwe, and north Brazil). However, other clusters may be present, such as within the African Sahel, where the spatial patterns of temporal shifts are complex.

In the following sections, we delve into the two case study regions, southwest Russia (Section 6.4.2) and north Australia (Section 6.4.3), which see large temporal shifts of 2.41 days yr^{-1}, or a total of 39 days from 2003-2018

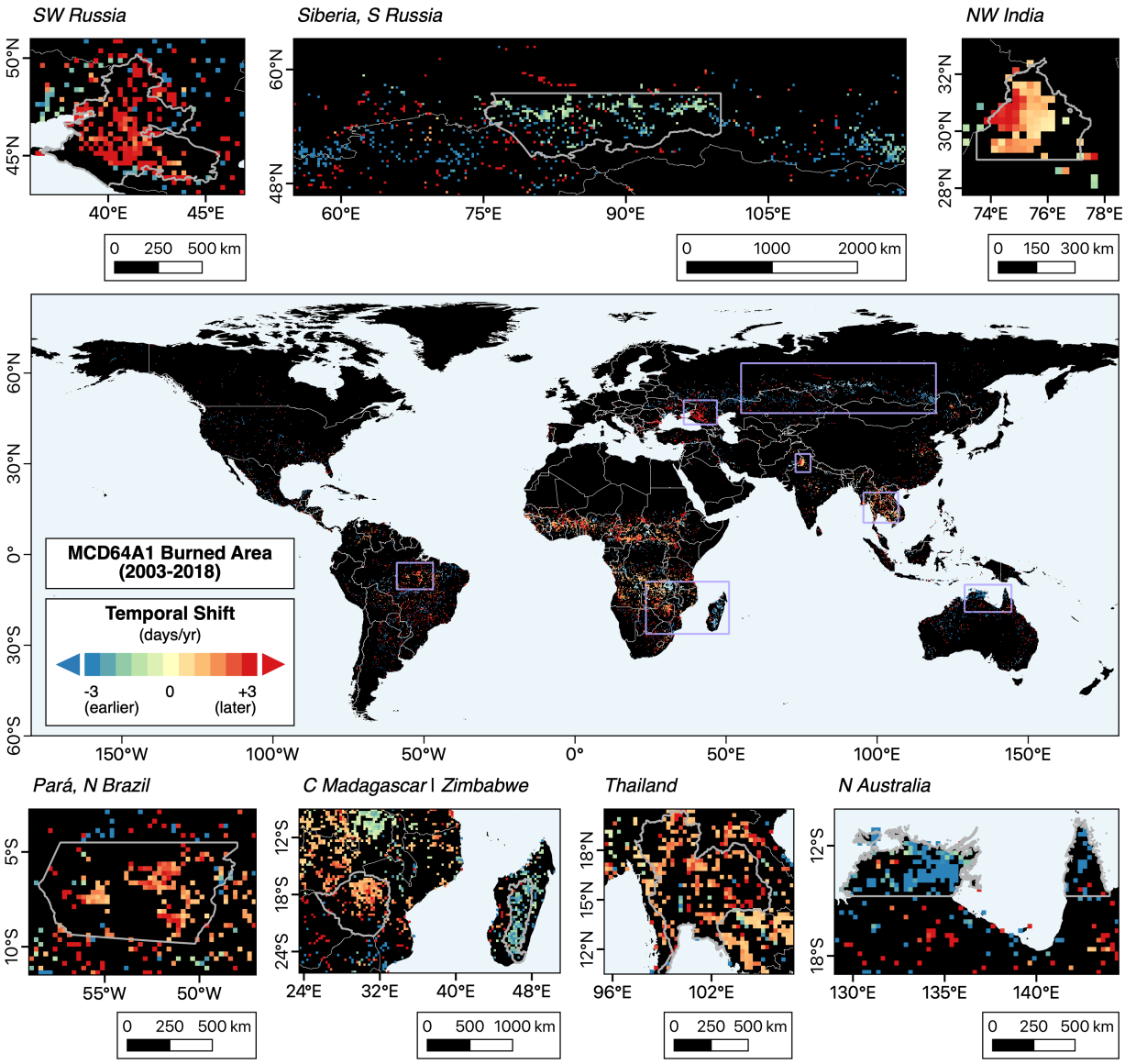


Figure 6.1: Temporal shifts in the midpoint of the primary fire season over a 16-year period from 2003-2018: The central panel shows regions of interest (outlined in purple), where coherent spatial signals in temporal shifts of MODIS MCD64A1 burned area (days yr^{-1}) are observed; smaller panels show zoomed-in maps with these regions outlined in gray. Only those grid cells with statistically significant trends ($p < 0.1$) are colored. Warm colors indicate fires occurring later over time, while cool colors represent fires occurring earlier over time.

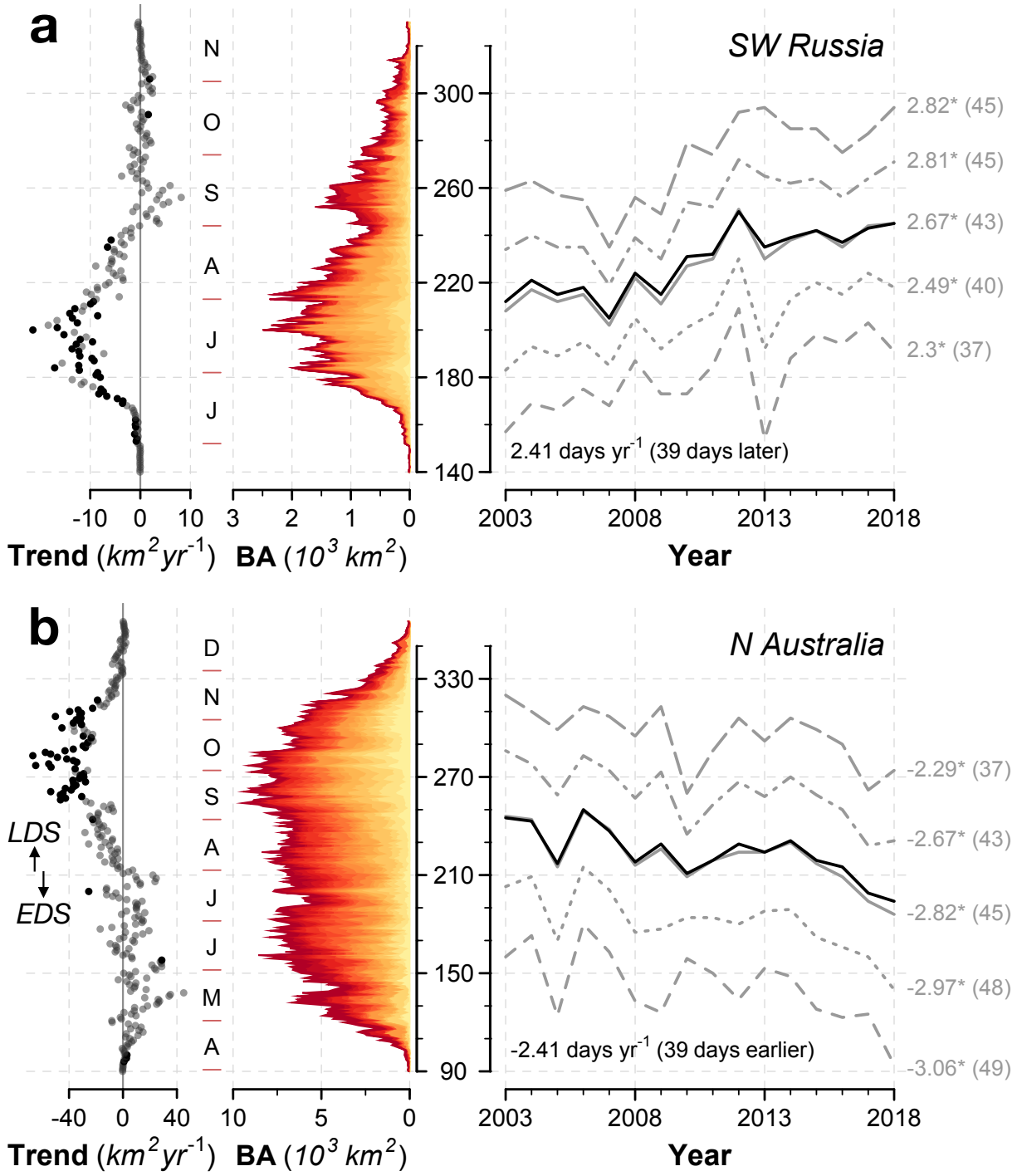


Figure 6.2: Regional temporal shifts in fire activity from 2003-2018 for two case study regions: Temporal shifts in MCD64A1 burned area for (a) southwest Russia and (b) north Australia. Left panels: Trend in burned area by Julian day. Solid dots denote statistically significant trends at $p < 0.05$. Middle panels: Stacked burned area by day from 2003-2018. Redder colors denote later years. Right panels: Estimated breakpoints (e.g., start, end, midpoint) in primary fire season. Inset shows the temporal shift at the midpoint of the fire season using the weighted mean method (black line) and the total 16-year shift. Inset right shows the temporal shift for each breakpoint using the partial sums method (gray lines), and asterisks denote statistical significance at $p < 0.05$.

(Table 6.1, Figure 6.2). In the other ROIs, not discussed in detail here, we observe temporal shifts of 1.36 days yr^{-1} (22 days earlier) in south Siberia, Russia, 0.64 days yr^{-1} (10 days later) in Thailand, 1.99 days yr^{-1} (32 days earlier) in central Madagascar highlands, 0.81 days yr^{-1} (13 days later) in Zimbabwe, and 0.61 days yr^{-1} (10 days later) in the state of Pará, Brazil (Table 6.1, Figure F.1). We conclude with a discussion of the drivers of temporal shifts in fire activity (Section 6.4.4).

6.4.2 Case study 1: southwest Russia

The primary fire season in southwest Russia croplands extends from summer to autumn, mainly from late June to October, after the winter wheat harvests (Hall et al., 2016; Korontzi et al., 2006) (Figure 6.3a-b). We estimate that the midpoint of the fire season has shifted later by 2.41 days yr^{-1}, or 39 days from 2003 to 2018 (Table 6.1, Figure 6.2a, Figure F.2). This shift is consistent across breakpoints in the fire season, varying from 2.3 to 2.82 days yr^{-1}, and driven largely by a 95% decrease in fires from June to July and a 41% increase in September.

Here the example of northwest India described above can inform our case study on southwest Russia, as both involve water-stressed agricultural systems. In northwest India, state government policies delayed rice sowing to alleviate heavy groundwater usage prior to the monsoon onset; in turn, post-monsoon rice harvests and subsequent burning of rice residues shifted later. For southwest Russia, we discuss two potential drivers of the delay in fire activity: (1) improved management, investment, and productivity in the agricultural sector and (2) groundwater depletion and drought, followed by federal government policies, such as wheat export restrictions and bans. First, since the early 2000s, the region has experienced the rise of "agroholdings," a new type of agricultural enterprise that acquires corporate farms and efficiently manages end-to-end production, processing, and distribution (Rada et al., 2017). Rada et al. (2017) attributes the high productivity in southwest Russia to these agroholdings, as well as to the favorable climate and soils and proximity to Black Sea ports. Puzzlingly, the 132% increase in winter wheat production in the region, and by extension the volume of crop residues, coincides with a 77% decrease in burned area since 2005 (Figure F.3). This is opposite of the trend in northwest India, where the rise in rice production and adoption of mechanization (i.e., use of combine harvesters) led to an increase in rice residue burning (Liu et al., 2019; Shyamsundar et al., 2019). This discrepancy between the regions may exist for two reasons. First, wheat residue is more suitable for livestock feed than rice residue, which has high silica content, so there may be greater utility for residue in southwest Russia than in north India (Sidhu et al., 2015). Second, modernized agriculture systems in southwest Russia may have driven changes in crop residue management, wherein

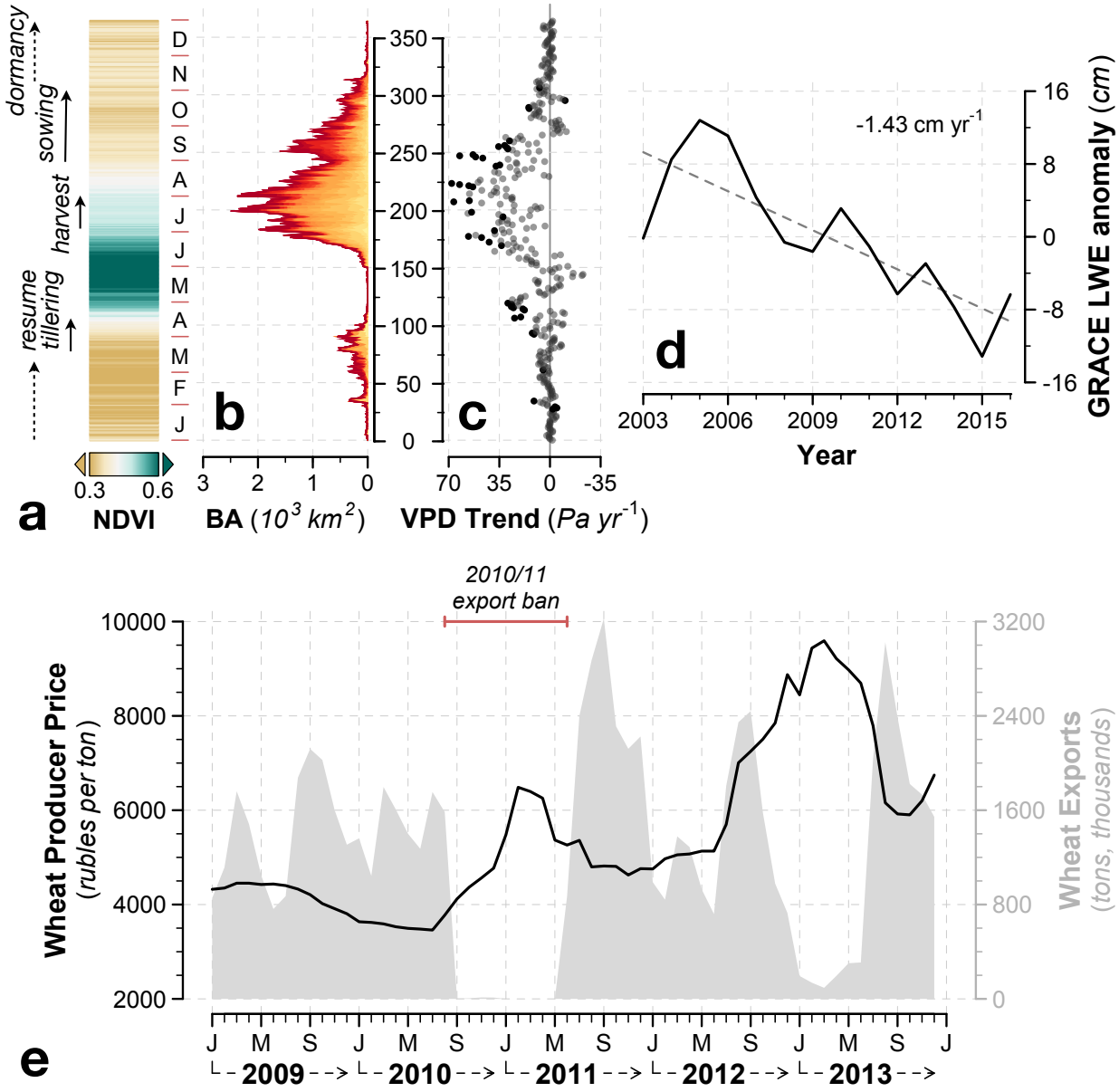


Figure 6.3: Winter wheat phenology, fire activity, and drought in southwest Russia: (a) Average 2003-2018 winter wheat phenology from MODIS-derived NDVI, with crop stages from the U.S. Department of Agriculture (https://ipad.fas.usda.gov/rssiws/al/crop_calendar/rs.aspx). (b) Aggregate burned area by day of year (same as Figure 2a but expanded to include the entire year). (c) Linear trend in ERA5 vapor pressure deficit (VPD) by day of year. Black dots denote statistical significance at $p < 0.05$. (d) Linear trend in annual GRACE freshwater storage availability, or the anomaly in equivalent liquid water thickness (LWE), from 2003-2016. Wheat producer prices and export statistics in Russia from 2009-2013: (e) Wheat producer price (black line) and export quantity (gray shading) (ROSSTAT, 2020a,b). The duration of the 2010/11 export ban is denoted as the red horizontal bar.

farmers use fire less to remove wheat residues immediately post-harvest (around July) and more to clear residual waste on fields just prior to sowing (around September) (Figures 6.2a, 6.3a-b). In contrast, the short turnaround period (on the order of weeks) between crops in the rice-wheat rotation of northwest India (Vadrevu et al., 2011), means that Indian farmers depend on fire to rapidly clear their fields (Liu et al., 2020b) (Figure 6.3a). Consistent with this hypothesis, the average fire intensity per active fire detection peaks in July and decreases by 41% by September (Figure F.4).

In addition, Rostov farmers surveyed by the U.S. Department of Agriculture (USDA) claim that only small enterprises still burn to reduce risk of soil-based diseases affecting crop growth (Hall et al., 2016). Greater alternative uses for wheat residue, as mentioned above, and the availability of direct seeding or no-till technology may explain the declining use of fire as a primary tool for crop residue management. For example, Krasnodar farmers typically embed loose wheat residues into soil as a fertilizer and to prevent soil degradation (Sidorenko et al., 2017). Additionally, wheat residues may be baled for livestock feed, in view of the resurgence in the livestock sector in the 2000s due to government policies and investment (Liefert & Liefert, 2012; Fellmann et al., 2014; Rada et al., 2017). As early as 2014, civil society organizations invested in agricultural outreach and training to eliminate agricultural burning in Krasnodar and Rostov (ICCI, 2020). Evidence of a link between the temporal shift in the fire season in southwest Russia and modernization in the agricultural system may be found in the record of wheat yields, which are correlated to fertilizer use and farm machinery efficiency (Liefert et al., 2013; Deppermann et al., 2018). Indeed, we see higher winter wheat yields and temporal shifts in Krasnodar and Adygea (2.69-2.8 days yr^{-1}, $p < 0.05$) than in Rostov and Stavropol (1.59-1.93 days yr^{-1}, $p < 0.05$) (Figure F.3, Table F.4).

Second, high water withdrawal for competing uses in residential, industrial, and agricultural sectors has led to moderate to severe water stress in southwest Russia (Alcamo et al., 2007). Rodell et al. (2018) attributes the downward trend in freshwater storage from 2003-2016 to groundwater depletion and drought. Within our study region, GRACE observations indicate a decrease in freshwater availability of 1.43 cm yr^{-1} (Figure 6.3d), which is comparable to that in northwest India (-1.44 cm yr^{-1}). In particular, changes in vapor pressure deficit (VPD) are most pronounced during summer and early autumn days, with increases up to ~30-70 Pa yr^{-1} from 2003-2018 (Figure 6.3c). Dryness can delay winter wheat sowing (Wegren, 2011; USDA, 2020), which may partly explain the increase in late season fires. Additionally, drought in tandem with federal government policies may have exacerbated delays in winter wheat sowing in this region. In August 2010, after intense heatwaves, drought, and

wildfires devastated crop production elsewhere in Russia, the government banned wheat exports in an effort to stabilize domestic food prices (Figure 6.3e) (Wegren, 2011). While southwest Russia was spared damage to its winter wheat, the export ban disrupted the supply chain in this region, and wheat prices plummeted (Wegren, 2011; ROSSTAT, 2020a). Anecdotally, some farmers in Krasnodar waited to sell their wheat crop to return a higher profit (de Sousa, 2019), and the wheat price then strongly rebounded. In contrast, no export restrictions were imposed in 2012, a severe drought year with low wheat production and exports similar to those in 2010 (Götz et al., 2016). Nevertheless, like in 2010, wheat producer prices in 2012 sharply rose starting in July, indicating that farmers may have again waited to sell their wheat crop (Figure 6.3e). These price swings and related delays in selling wheat may have also delayed sowing if farmers relied on these profits to buy seeds and fertilizer for the following year's crop.

In summary, factors that may have driven the 39-day delay in fires in southwest Russia include improvements in agricultural management and technology, drought and groundwater depletion, and fluctuations in wheat prices due to export restrictions and bans.

6.4.3 Case study 2: north Australia

The primary fire season in the savannas of north Australia occurs during the dry season primarily from May through November. We estimate that the midpoint of the fire season has shifted by -2.41 days yr^{-1}, or 39 days earlier from 2003-2018 (Table 6.1, Figure 6.2b, Figure F.6). This shift is consistent across breakpoints in the fire season, varying from -3.06 to -2.29 days yr^{-1}. We find the trend is induced by a 40% increase during the early dry season (EDS) from May to July and a 67% decrease in fires during the late dry season (LDS) from September to November, with the transition point from the EDS to LDS defined as July 31 (Price et al., 2012).

During the LDS, fires tend to burn out of control due to favorable fire weather, such as high VPD values. The resurgence of Aboriginal fire management practices in north Australia, which began in the 1990s, has spurred the decrease in fires during the LDS, most notably in Arnhem Land (Figure F.9a) (Yibarbuk et al., 2001; Whitehead et al., 2003; Price et al., 2012; Price, 2015; Ansell et al., 2020; Evans & Russell-Smith, 2020). Since 2005-06, the West Arnhem Land Fire Abatement (WALFA) project has built on the collaboration with Indigenous fire managers and landowners to reduce greenhouse gas emissions by curbing large, destructive fires in the LDS (Price et al., 2012; Ansell et al., 2020). Following WALFA, there are four other ALFA projects in operation: CALFA (central Arnhem), NEALFA (northeast Arnhem), SEALFA (southeast Arnhem), and SEALFA Stage 2 (Price,

2015; Ansell et al., 2020). In the past decade, dozens of savanna burning projects in the Top End have emulated WALFA. Registered under the Australian government's Carbon Credits (Carbon Farming Initiative) Act 2011 and Emissions Reduction Fund, these projects can earn Australian carbon credit units (ACCUs) (Figure F.6) (Ansell et al., 2020). The economic incentive for Aboriginal people involved in these carbon abatement projects adds to inherent environmental, social, and cultural co-benefits of such projects (Andersen et al., 2005; Ansell et al., 2020).

Our results provide quantitative evidence of the success of these policy efforts to reduce fire size, especially later in the dry season when fires are more likely to burn out of control. We find that fire management within the savanna burning project areas in the Top End and Cape York drives the temporal shifts toward an earlier fire season, with spatially cohesive shifts within the domain of Aboriginal freehold lands and ALFA projects. This domain accrued over 2.5 million ACCUs from 2012-13 to 2018-19 (Figures F.5-6). Within the study region, we find a temporal shift in the midpoint of the primary fire season of -3.48 days yr^{-1} ($p < 0.05$) in savanna burning project areas, which comprise ~56% of the annual burned area, compared to just -0.9 days yr^{-1} in other areas ($p = 0.18$) (Table F.5). Moreover, ALFA project areas, which have a long history of fire management (Price et al., 2012; Price, 2015; Ansell et al., 2020), exhibit a larger overall temporal shift of -4.3 days yr^{-1} ($p < 0.05$), particularly in WALFA at -6.13 days yr^{-1} ($p < 0.05$), than the region overall.

In north Australia fire management, prescribed burning creates a mosaic of burned and unburned areas during the EDS, decreasing overall fuel availability across the landscape (Andersen et al., 2005; Trauernicht et al., 2015; Russell-Smith et al., 2019). The fuel-limited areas, where prescribed burning has occurred, act like a patchwork of endpoints for fast-spreading wildfires in the LDS, thus limiting the maximum extent of the final burn perimeters (Price et al., 2012; Petty & Bowman, 2007; Petty et al., 2015). This phenomenon is widespread across Arnhem Land, where small fires have become more prevalent during the EDS and widely dispersed across the landscape (Figure 3a-d). During the EDS, we see a 60% decline in the average distance to the closest fire and a 50-60% increase in the number of distinct fire perimeters from 2003-2018 (Figure 4e). The increase in EDS fires and their spatial coverage suggest fewer open spaces for fires later in the season to spread across, and indeed, we see a 49-54% decrease in the average area per fire during the LDS (Figure 6.4f). The decrease in LDS fire activity is consistent across burned area and fire emissions datasets, as described in Appendix F.5.

Finally, we investigate the influence of meteorology on the 59% decrease in LDS burned area (Figure F.9b-c). If meteorology played a major role, we would expect wetter and cooler conditions, or decreases in VPD and

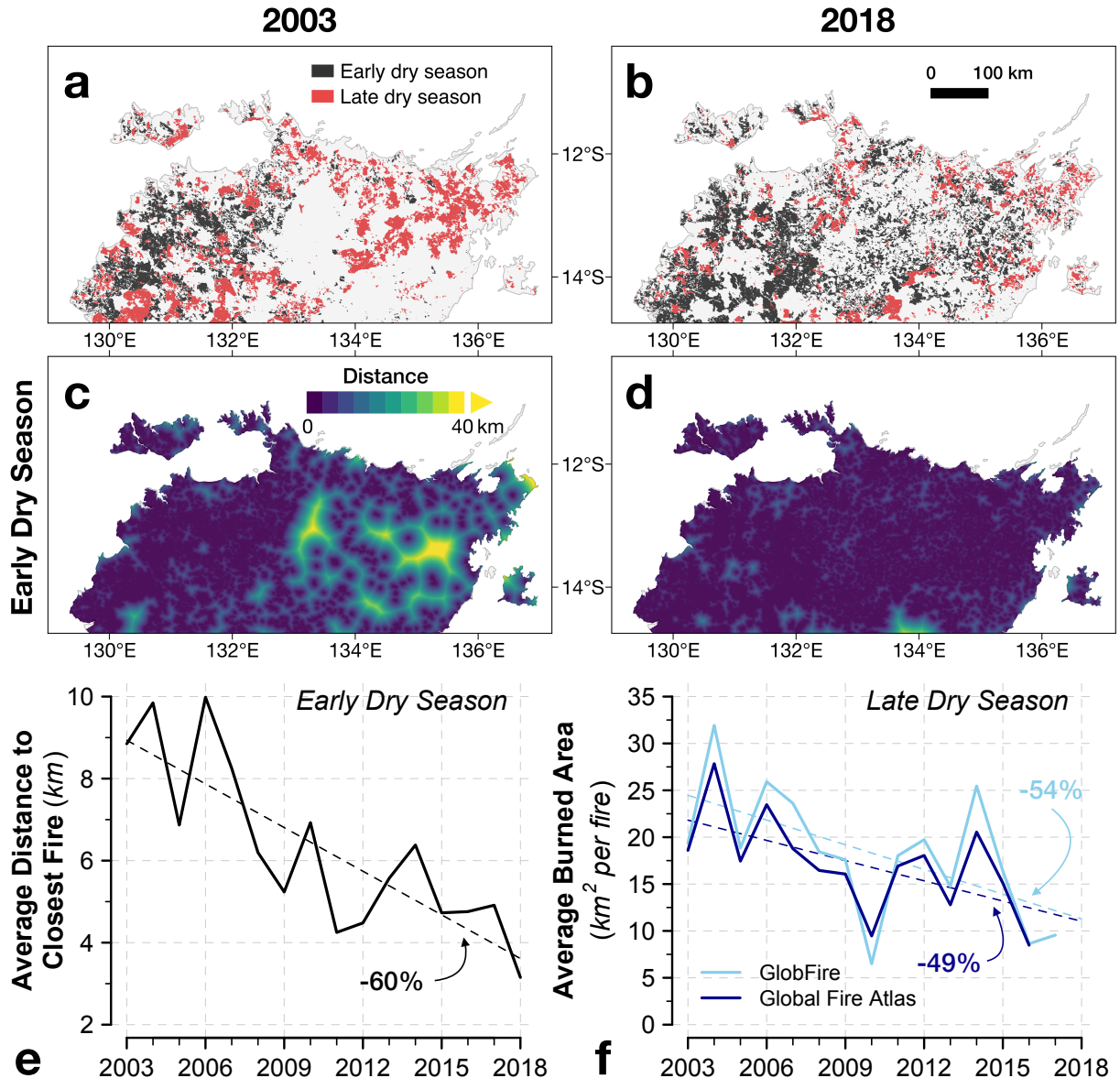


Figure 6.4: Trends in early and late dry season fires in north Australia from 2003-2018: Spatial comparison of MCD64A1 burned area during the early dry season (EDS, black shading) and late dry season (LDS, red shading) in the Top End of the Northern Territory in (a) 2003 and (b) 2018. Smaller islands without observed fire activity are excluded. Spatial distribution of the per-pixel distance in km to the closest burned area during the EDS in (c) 2003 and (d) 2018. The more uniform blue shading in 2018 indicates smaller distances between fires. (e) Annual trend in the distance to closest fire during the EDS from 2003 to 2018, averaged over all pixels in the Top End. This calculation excludes those pixels in which burning took place, i.e., areas with a distance of 0 km to the closest fire. Maximum distance is capped at 100 km. (f) Average burned area per fire (in km2) during the LDS based on the GlobFire (2003-2017) and Global Fire Atlas (2003-2016) datasets (Artés et al., 2019; Andela et al., 2019). The linear trends shown in (e) and (f) are statistically significant at $p < 0.05$.

FWI over the 2003-2018 timeframe. In fact, we see the opposite — a 6% increase in VPD and 3% increase in FWI, although these trends are not statistically significant (Figure F.9b-c). When detrended, however, VPD and FWI are moderately to strongly correlated with burned area, with the correlation $r = 0.57$ for VPD and $r = 0.79$ for FWI ($p < 0.05$). Thus, meteorology appears to drive the interannual variability but not the decrease in LDS burned area over this time period that caused the fire season to shift earlier. Our hypothesis is consistent with Andela et al. (2017), who concluded on a global scale that precipitation is strongly related to the interannual variability in burned area, yet human activity drives the overall decrease in burned area, inferred from proxies such as GDP, population growth, and widespread wildland to agricultural transition.

In summary, our approach using temporal shifts and distance to nearest fire strengthens the conclusion of previous studies that EDS prescribed burning, particularly in Arnhem Land, has shifted the fire season earlier and lowered LDS burned area and emissions.

6.4.4 Drivers of temporal shifts

In north India and the two case study regions — southwest Russia and north Australia — humans play an integral part in shaping the landscape by using prescribed burns, either to clear fields in an agricultural context or as a tool to prevent larger, more destructive fires in savannas. Although we do not find large changes in meteorological variability in line with the 39-day temporal shifts in the fire season, climate shocks, such as droughts and heatwaves, or concerns about rising greenhouse gas emissions may spur human actions that affect the use of fire, either through fire management or changes in government policy and agricultural practices. For example, in response to groundwater depletion and drought, state governments in north India delayed rice sowing closer to the monsoon onset, whereas in Russia, the federal government enacted wheat export bans and restrictions to protect domestic supply. In north Australia, Indigenous fire managers use prescribed burns to limit greenhouse gas emissions from LDS fires. Our probe of the potential human and climatic drivers is not exhaustive, and further study, such as through household surveys, is needed to systematically detail and confirm the mechanisms for the temporal shifts in each region described here, especially in southwest Russia.

Through the lens of the two case study regions, we briefly discuss five other ROIs, grouped by the two broad land cover types: croplands and savannas, grasslands, and shrublands. For croplands, the southwest Russia case study and studies on north India (Liu et al., 2021a; Jethva et al., 2019; Balwinder-Singh et al., 2019) suggest that water stress, as well as increasing mechanization, modernization, and productivity, in agricultural systems are

likely causes of changes in the timing of peak burning. In both south Russia and Thailand, the primary fire season coincides with the post-harvest period for spring wheat and rice, respectively (Hall et al., 2016; Vadrevu et al., 2015). GRACE observations of freshwater availability show an increase in south Russia of +0.52 cm yr^{-1} from 2003-2016, coinciding with earlier peak burning. Thailand, on the other hand, reveals a decline in freshwater availability of -0.53 cm yr^{-1} — that is, drought and/or groundwater depletion — coinciding with a delay in the fire season. For savannas, grasslands, and shrublands, the north Australia case study suggests that proactive fire management practices are key to limiting the fires with fast spread rates and high fuel consumption that occur later in the season. In contrast, poor fire management, in combination with drought, may drive fire seasons later. Fire is mainly used pasture management for grazing cattle in central Madagascar, whereas deforestation is common in Brazil, and careless use of fire, both deliberate and accidental, has led to destructive "veld" fires in Zimbabwe (Aragão et al., 2018; Kull, 2012; Nyamadzawo et al., 2013). In fact, for Zimbabwe, Nyamadzawo et al. (2013) recommends a shift from fire suppression to fire management, with early season prescribed burns to curb the fire activity later in the season. Globally, Lipsett-Moore et al. (2018) find widespread potential in EDS prescribed burning to both mitigate fire emissions and improve livelihoods.

6.5 Conclusion

In conclusion, we use 16 years of daily satellite-derived burned area to quantify the temporal shifts in the primary fire season at global scale. While earlier studies have diagnosed trends in annual fire activity (Andela et al., 2017; Andela & van der Werf, 2014; Giglio et al., 2010), this is, to our knowledge, the first global study of trends in the timing of peak fire activity. We focus on regions where fires consistently recur year after year, and in particular, we select southwest Russia and north Australia as two case study regions, where the fire season has shifted by a total of nearly 40 days. No matter the setting, either croplands in southwest Russia or savannas in north Australia, we find human action as likely an important contributor of these temporal shifts. Pinpointing regions where such shifts in the fire season occur is critical for contextualizing broader changes in agricultural systems, fire management practices, and government policies and for understanding the consequences of these changes. In India, government efforts to conserve water in spring have delayed the onset of rice residue burning during the post-monsoon season and inadvertently led to degraded air quality. In southwest Russia, human innovations and investment in agricultural technology and management have limited the need for fire to clear wheat residue. Meanwhile in north Australia, widespread adoption of Aboriginal fire management with increased prescribed

burning have curbed the frequency of large fires over a broad region and potentially limited greenhouse gas emissions.

A

Supplemental Material for Chapter 1

A.1 Data and Methods

We primarily use Google Earth Engine (Gorelick et al., 2017), a cost-free cloud-based computing platform for geospatial analysis, to access and process satellite-derived datasets and R software for statistical analysis.

Table A.1: Satellite-derived fire, surface reflectance, aerosol, and land cover datasets used in this study.

Dataset	Satellite	Sensor	Product	Collection	Temporal	Spatial
Fire Radiative Power (FRP)	Terra	MODIS[1]	MOD14A1	C6	Daily	1 km
	Aqua		MYD14A1			
Fire Counts	Terra/Aqua	MODIS	MCD14ML	C6	Daily	1 km
	S-NPP[2]	VIIRS[3]	VNP14IMGML	C1		375 m
Burned Area	Terra/Aqua	MODIS	MCD64A1	C6	Monthly	500 m
Fire Emissions	Terra/Aqua	MODIS	GFED[4]	4s	Monthly, Daily	0.25°
Surface Reflectance	Terra	MODIS	MOD09GA	C6	Daily	500 m
	Aqua		MYD09GA			
Aerosol Optical Depth	Terra	MODIS	MOD_04	C6.1	Daily	10 km
Land Cover	Terra/Aqua	MODIS	MCD12Q1	C6	Annual	500 m

[1] Moderate Resolution Imaging Spectroradiometer
[2] Suomi National Polar-orbiting Partnership
[3] Visible Infrared Imaging Radiometer Suite
[4] Global Fire Emissions Database

A.1.1 Active fires

For analysis of fire activity, we use the Collection 6 active fire products, MOD14A1 and MYD14A1, derived from the Moderate Resolution Imaging Spectroradiometer (MODIS), aboard the Terra and Aqua satellites (Table A.1). The MxD14A1 Level-3 products grid daily observations of maximum Fire Radiative Power (FRP) at 1-km spatial resolution. We exclude non-agricultural areas using the extent of croplands classified by Scheme 2 (University of Maryland) of the Collection 6 MODIS MCD12Q1 global land cover product. Giglio (2015) recommends the 1-km gridded MODIS fire products (MxD14A1) rather than fire pixel geolocations (MCD14ML) due to several caveats associated with the latter, such as possible spatial and temporal biases and omitted known fires. However, to perform ancillary inter-satellite comparison analyses, we use the geolocations of 1-km MODIS/Terra and Aqua (MCD14ML) and 375-m S-NPP/Visible Infrared Imaging Radiometer Suite (VIIRS) active fires (VNP14IMGML), available from the University of Maryland, Department of Geographical Sciences (`ftp://fuoco.geog.umd.edu/`). Each geolocation represents the centroid of a pixel (MODIS: 1 km x 1 km; VIIRS: 375 m x 375 m) with one or more active fires. We consider daytime MODIS active fires from 2003-2016 and VIIRS active fires from 2012-2016.

In addition to FRP, we consider the MODIS MCD64A1 burned area product (500 m x 500 m) and fire emissions from the Global Fire Emissions Database, version 4, with small fires boost (GFEDv4s) (Randerson et al., 2012; van der Werf et al., 2017; Giglio et al., 2018). MCD64A1 uses active fire detections to guide its burned area classification based on changes in surface reflectance (Giglio et al., 2009, 2018). GFEDv4s emissions are derived from the Carnegie Ames Stanford Approach (CASA) biogeochemical model (van der Werf et al., 2010) with MODIS MCD64A1 burned area and MCD14ML active fires as inputs (Randerson et al., 2012; van der Werf et al., 2017). The default monthly fire emissions can be partitioned to daily resolution based on the temporal variability of active fire counts and burned area (Mu et al., 2011).

In India, satellite detection of small, cool agricultural fires that last no more than half an hour is challenging due to the moderate spatial resolution of the sensor and the limited number of overpasses, just twice daily (Thumaty et al., 2015). Still, despite absolute differences in fire detection, we find temporal agreement in the timing of the post-monsoon fire season at various breakpoints using MODIS and VIIRS FRP. The absolute difference in the timing of $k_{peak}(FRP)$, $k_{midpoint}(FRP)$, $k_{start}(FRP)$, and $k_{end}(FRP)$ from 2012-2016 between the two satellites is small, ranging from 0-1 days for Punjab, depending on the year. In addition, persistent thick haze and intermit-

tent cloud cover over high fire regions further limits detection (Cusworth et al., 2018). High fire intensity days, which predominantly occur during the latter half of the post-monsoon fire season, can lead to especially hazy and smoggy conditions. Consequently, satellites may be unable to "see" late fire-intensive days, and trends at k_{peak} and k_{end} may be underestimated.

A.1.2 Vegetation indices

The Normalized Burn Ratio (NBR) is closely related to two other SWIR-based indices: Normalized Difference Water Index (NDWI) and Land Surface Water Index (LSWI), which also use SWIR bands (van Wagtendonk et al., 2004). Both of these indices have been used to analyze crop phenology, vegetation liquid water, and land use (Chen et al., 2005; Brown et al., 2013). Because SWIR wavelengths are dominated by water absorption, SWIR-based vegetation indices are more sensitive to variations in vegetation water content and more closely track crop growth than indices that include visible bands, such as NDVI (Chen et al., 2005).

We use the daily 500-m Collection 6 MOD09GA surface reflectance product from the MODIS sensor, aboard the Terra satellite (Table A.1), to derive NDVI and NBR. As with active fires, we mask out non-agricultural areas. We use surface reflectance data from Terra, because it has an earlier overpass (10:30 a.m. local time) compared to Aqua (1:30 p.m. local time). Fire energy peaks in the afternoon in India (Giglio, 2007; Vadrevu et al., 2011), and so thick haze is likely to be relatively more intense during the Aqua overpass, obscuring the satellite observing area over Punjab (Cusworth et al., 2018). We filter valid pixels further using two simple cloud/haze indicators, based on Xiang et al. (2013), that exploit the sensitivity of visible bands to cloud contamination and the normalized surface reflectance difference between the Red and SWIR-2 bands. Put another way, cloud contamination results in differences in the spectral signatures of visible and infrared bands which we can use to filter the data. Clouds exhibit relative maximum spectral reflectance at visible wavelengths and relative minimum spectral reflectance at the SWIR wavelengths (Bowker et al., 1985). We thus retain pixels that satisfy the following requirements, based on Xiang et al. (2013):

$$0 < \frac{\rho_1}{\rho_7} < 1 \text{ and } \rho_1 < 0.3 \tag{A.1}$$

where ρ_i is the surface reflectance of MODIS band i. The wavelength range of the bands is as follows: 620-670 nm for band 1 (red) and 2105-2155 nm for band 7 (shortwave infrared). We additionally mask anomalous values

of ρ_1 and ρ_7, which we define as surface reflectance below 0 and above 1. We further note that the $0 < \rho_1/\rho_7 < 1$ criterion proposed by Xiang et al. (2013) is mathematically equivalent to $(\rho_7 - \rho_1)/(\rho_7 + \rho_1) > 0$ for the range of valid reflectance values (0-1); the alternate normalized difference formulation emulates existing cloud and snow/ice indices (Qiang et al., 2014).

As described in Chapter 1.3.3.2, we estimate the timing of the maximum monsoon greenness through application of weighted cubic splines smoothing. A disadvantage of cubic splines smoothing is that each of these "knots" affects the interpolation globally. Minimizing the "generalized" cross-validation, an objective criterion for model selection, tends to overfit, resulting in artificial curves. We thus manually select a smoothing parameter of 0.75 to reduce these artificial curves. We also adjust for leap years by selecting the day (February 28-29) with the highest usable fraction as day 59 of the year. This method allows the day-month to be consistent across leap and non-leap years.

To further assess whether the 2008-09 policy implementations were associated with abrupt shifts in monsoon peak greenness or post-monsoon trough greenness, we quantify the mean difference between the 2003-2007 and 2008-2016 time periods. As we will see, the observed shifts are primarily localized in 2 years from 2008-09 with little change thereafter, and so the overall linear trend may overestimate delays in peak or trough greenness. To find the mean delay, we use weighted two-sample t-tests with bootstrapped statistics. The weights are $1/\sigma^2$, in which σ is associated with bootstrapped estimates of the timing in peak or trough greenness over the two time periods.

In addition to daily vegetation indices from MOD09GA (Terra) surface reflectance, we derive daily vegetation indices from MYD09GA (Aqua) surface reflectance to check the Terra-Aqua agreement. In general, we find good agreement between Terra and Aqua in the estimated linear trend from 2003-2016 and mean difference in the timing of peak or trough greenness between the 2003-2007 and 2008-2016 time periods (Table A.5).

A.1.3 Aerosol optical depth

For analysis of aerosol optical depth (AOD) exceedances, we use the Collection 6.1 Level-2 Deep Blue (DB) AOD product from MODIS/Terra, available at 10-km pixel resolution (Levy et al., 2013). Mid-visible AOD retrievals at 0.55 μm are used in this study. AOD is not retrieved over cloudy or foggy pixels. The Level-2 AOD retrievals are available on a daily basis, which were then uniformly gridded to produce a per-pixel AOD mean spatial distribution at 10 x 10 km grid cells, for Punjab, Haryana, Delhi, and western Uttar Pradesh, for the period 2003-

2016. In terms of accuracy of the 10 km product, the expected error envelope is reported to be $\pm(0.03 + 0.2\tau)$ for DB retrievals (Sayer et al., 2013), where τ represents AOD. In this study, we use the best-quality flagged retrievals of the Deep Blue AOD data. Unlike the Dark Target retrieval algorithm, Deep Blue consistently retrieves AOD over pixels with thick haze.

We find that daily Terra AOD is less noisy than Aqua AOD, suggesting that burning source attribution using Terra AOD could be more effective in our AOD exceedance analysis; Aqua AOD could be associated with greater turbulent mixing in the boundary layer during the Aqua afternoon overpass (1:30 pm) relative to the earlier Terra morning overpass (10:30 am). Nevertheless, the magnitude in the AOD exceedance trends is consistent between Terra (+0.09 yr^{-1}) and Aqua (+0.08 yr^{-1}) in November, thus corroborating the overall increase in daytime aerosol loading. Additionally, MODIS/Aqua AOD exceedances yield a similar trend in $k_{peak}(AOD)$ of 0.8 days yr^{-1} and slightly higher increase in magnitude of 62% compared to MODIS/Terra (Figure 1.4a).

A.1.4 Population count

To estimate the total population over the Indo-Gangetic Plain (IGP), we use the United Nations-adjusted Global Population of the World, version 4.1 dataset (UN-adjusted GPW), available in 5-year intervals from 2000-2020 and 1 km x 1 km spatial resolution (CIESIN, 2017). We use the population count for 2015 and define the spatial bounds of the IGP, which includes parts of India, Pakistan, Nepal, and Bangladesh, following Narang & Virmani (2001).

A.2 India state-level agricultural fire activity

Total all-India pre-monsoon fire activity, which generally spans March to May, is 12% higher than post-monsoon fire activity during October to November, in terms of total FRP. The relatively broad temporal distribution of pre-monsoon fires suggests diverse timing in rabi harvests across India (Figure A.1). In contrast, post-monsoon fires are largely concentrated in Punjab, which contributes 84% of total all-India fire intensity from October to November and accounts for 38-65% of annual fire intensity and emissions from 2003-2016 (Figures 1.1, A.1, A.2).

All-India agricultural emissions, estimated by GFEDv4s, increased on average by 0.3 Tg DM yr^{-1} (95% CI: [0.12, 0.48]) from 2003-2016, while total FRP increased on average by 73 GW yr^{-1} (95% CI: [45, 102]) (Figure

A.2). In our "all-India" totals, we exclude the Seven Sister States (Arunachal Pradesh, Assam, Manipur, Meghalaya, Mizoram, Nagaland, Tripura) and two island states (Lakshadweep, Andaman and Nicobar Island), which are geographically distant and agriculturally and climatically distinct from other states. Punjab alone accounts for over half of all-India agricultural dry matter (DM) emissions, but its DM emissions have increased at less than half the rate of the all-India total (Figure A.2, Table A.4). In 2007, the central Indian state Madhya Pradesh considerably increased both its share of fire emissions and intensity. As the fire activity in other states, including Madhya Pradesh, increases — largely during the pre-monsoon — Punjab's contribution to total fire intensity has decreased by 20% and fire emissions by 10% over the 14-year study period.

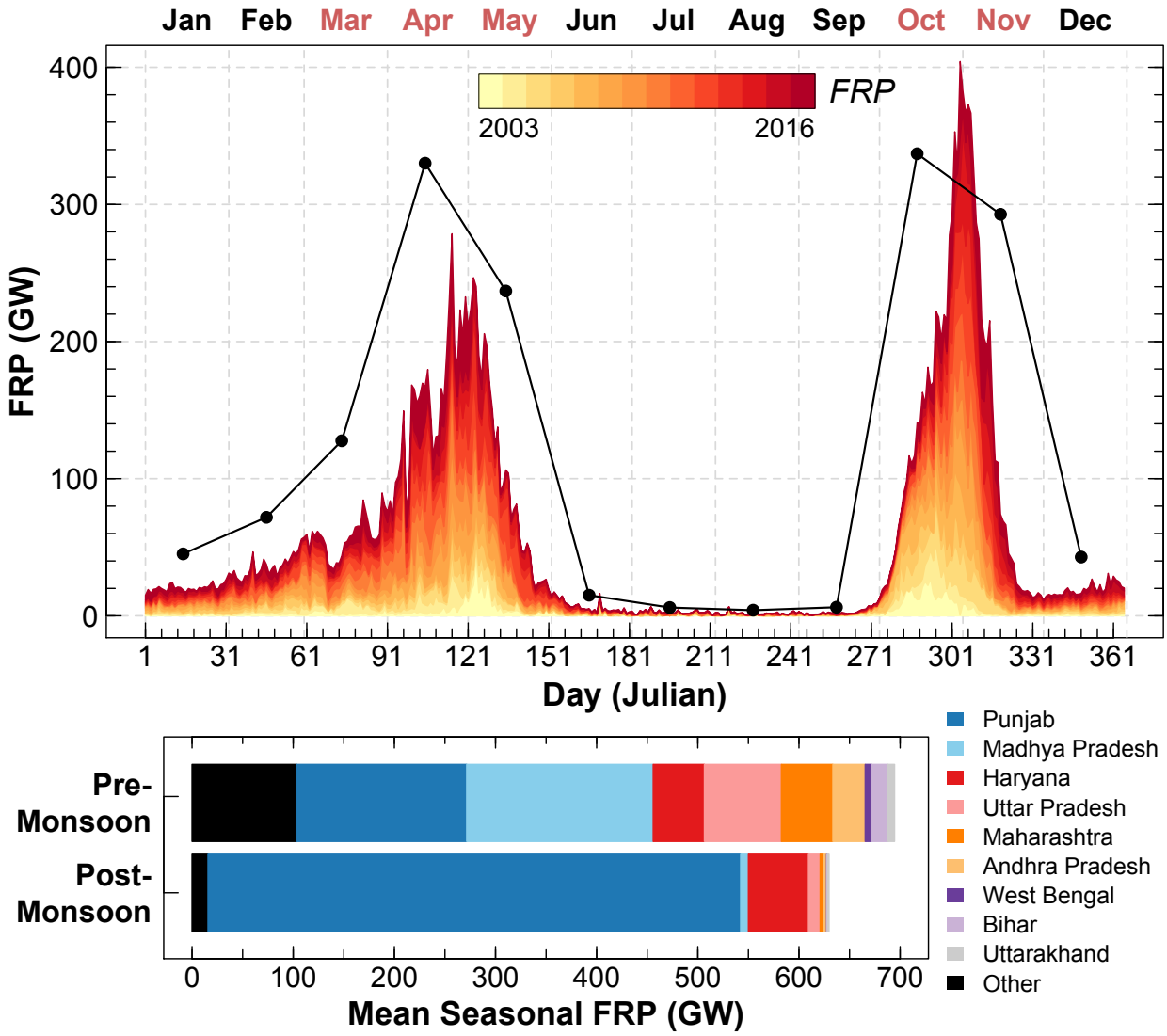


Figure A.1: Overview of pre-monsoon and post-monsoon fire activity in India at state-level. Top panel: All-India stacked daily MODIS Aqua + Terra FRP (GW) in agricultural areas, from 2003-2016. The line overplotted with points denotes the monthly FRP, averaged over 2003-2016 (same scale as stacked daily FRP). Bottom panel: Mean pre-monsoon and post-monsoon FRP. Colors represent the contributions from different states.

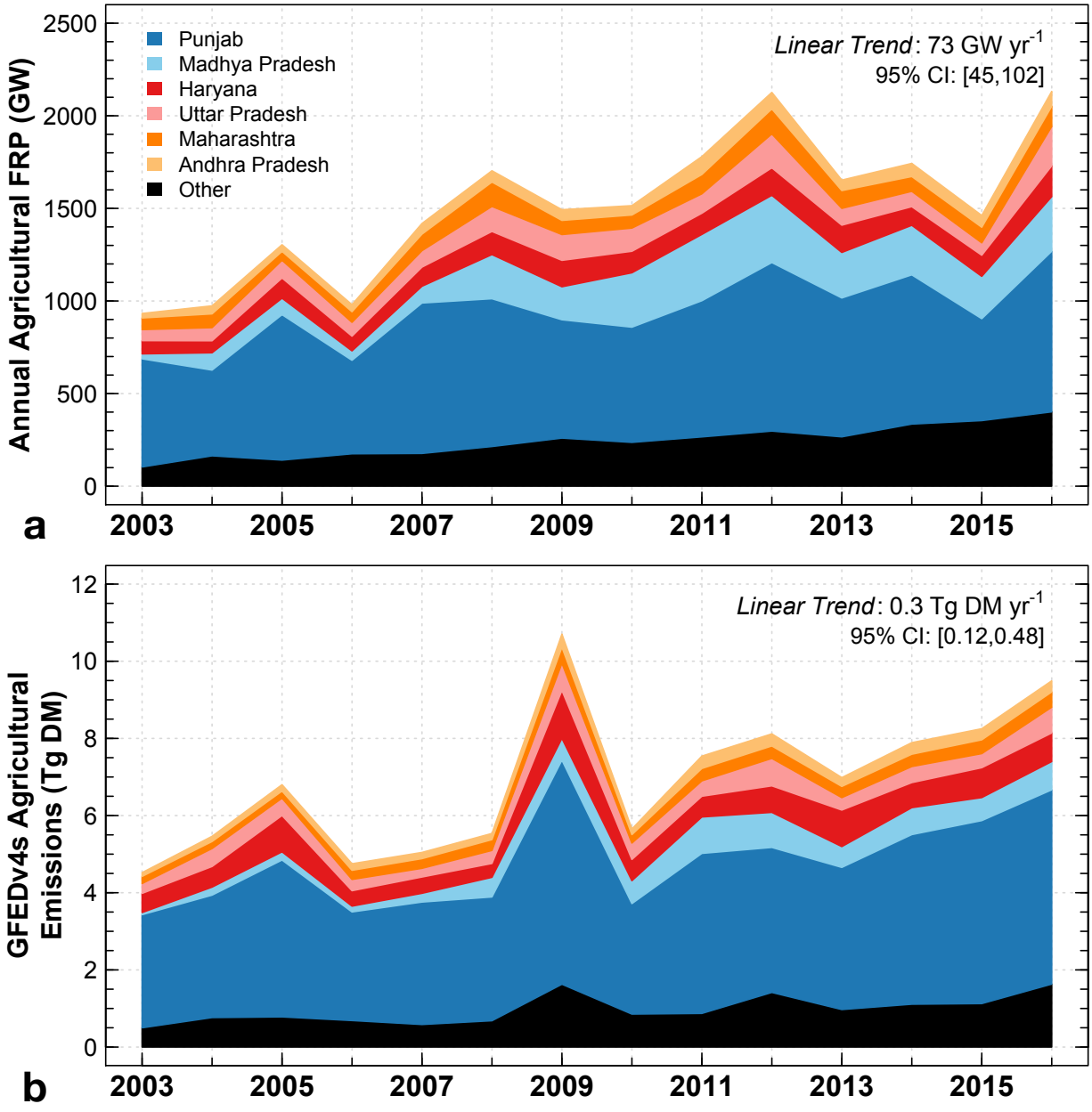


Figure A.2: Trends in all-India agricultural FRP and fire emissions. (a) Annual FRP (GW) and (b) GFEDv4s agricultural dry matter emissions (Tg) by state. Inset shows the bootstrapped linear increase and 95% confidence interval.

A.3 Temporal shifts in fires and vegetation greenness in Punjab

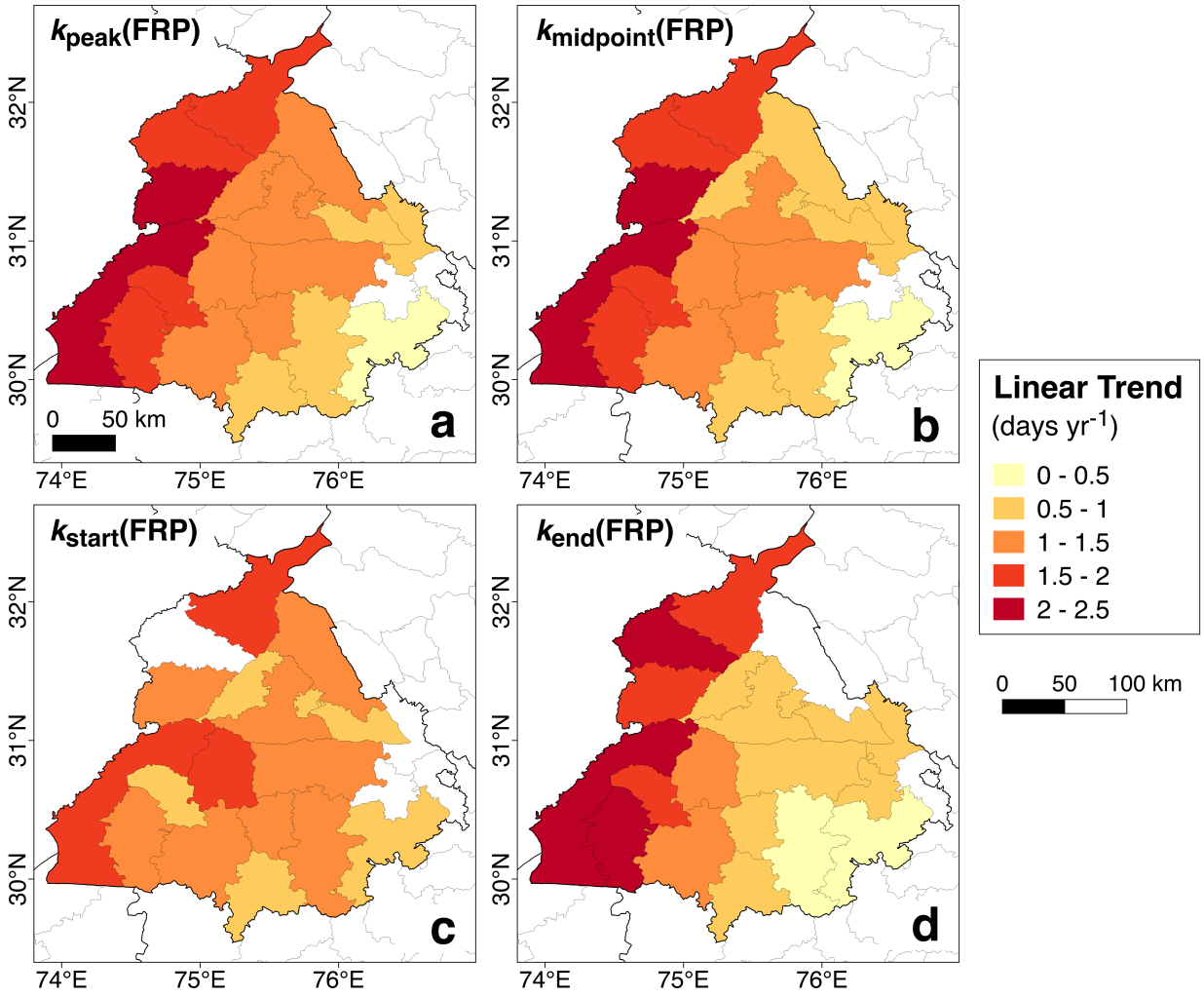


Figure A.3: Trends in peak post-monsoon burning of in Punjab by district. Timing of (a) $k_{peak}(FRP)$, (b) $k_{midpoint}(FRP)$, (c) $k_{start}(FRP)$, and (d) $k_{end}(FRP)$, based on post-monsoon MODIS Aqua + Terra FRP over Punjab from 2003-2016. The bootstrapped mean delay (days yr^{-1}) is shown for linear trends statistically significant at the 95% confidence level. White denotes regions with insignificant trends in these variables.

Table A.2: Temporal shifts (days yr^{-1}) in pre-monsoon and post-monsoon FRP in Punjab, from 2003-2016, with bootstrapped 95% confidence intervals.

	Pre-monsoon (Apr. 1-May 30)		**Post-monsoon** (Sep. 20-Nov. 30)	
	Mean	*95% CI*	*Mean*	*95% CI*
k_{peak}	0.37	[-0.27, 1.03]	1.17*	[0.86, 1.49]
$k_{midpoint}$ ($k_{\beta=0.5}$)	0.39	[-0.23, 1.02]	1.14*	[0.88, 1.39]
k_{start} ($k_{\beta=0.1}$)	0.6*	[0.12, 1.12]	1.22*	[0.95, 1.48]
k_{end} ($k_{\beta=0.9}$)	0.32	[-0.29, 0.89]	0.93*	[0.64, 1.24]
$k_{midpoint,w}$	0.4	[-0.18, 0.98]	1.11*	[0.89, 1.35]

*Bootstrapped trend is statistically significant at the 95% confidence level

Table A.3: Temporal shifts (days yr^{-1}) in fire intensity (MxD14A1), active fire counts (MCD14ML), burned area (MCD64A1), and agricultural fire dry matter (DM) emissions (GFEDv4s) in Punjab, from 2003-2016, during the post-monsoon burning season.

	Active Fire Counts (MCD14ML)		**Burned Area** (MCD64A1)		**Agricultural DM Emissions** (GFEDv4s)	
	Mean	*95% CI*	*Mean*	*95% CI*	*Mean*	*95% CI*
k_{peak}	1.13*	[0.84, 1.41]	1.56*	[1.71, 2.41]	1.23*	[0.84, 1.64]
$k_{midpoint}$ ($k_{\beta=0.5}$)	1.02*	[0.8, 1.25]	1.41*	[0.92, 1.89]	1.22*	[0.85, 1.59]
k_{start} ($k_{\beta=0.1}$)	1.05*	[0.79, 1.31]	2.27*	[1.54, 2.97]	1.42*	[0.99, 1.81]
k_{end} ($k_{\beta=0.9}$)	0.89*	[0.6, 1.18]	0.81*	[0.41, 1.18]	0.88*	[0.51, 1.26]
$k_{midpoint,w}$	1.03*	[0.8, 1.28]	1.46*	[1.03, 1.89]	1.2*	[0.86, 1.52]

*Bootstrapped trend is statistically significant at the 95% confidence level

Table A.4: Trends (yr^{-1}) in fire intensity (MxD14A1), active fire counts (MCD14ML), burned area (MCD64A1), and agricultural fire dry matter emissions (GFEDv4s) in Punjab during the post-monsoon burning season over 2003-2016.

Dataset	**Mean**	**95% CI**	**Units**
FRP *(MxD14A1)*	13.6*	[0.8, 27.6]	GW
Active Fire Counts *(MCD14ML)*	322*	[80, 568]	--
Burned Area *(MCD64A1)*	598*	[455, 733]	km^2
Agricultural DM Emissions *(GFEDv4s)*	0.15*	[0.06, 0.23]	Tg DM

*Bootstrapped trend is statistically significant at the 95% confidence level

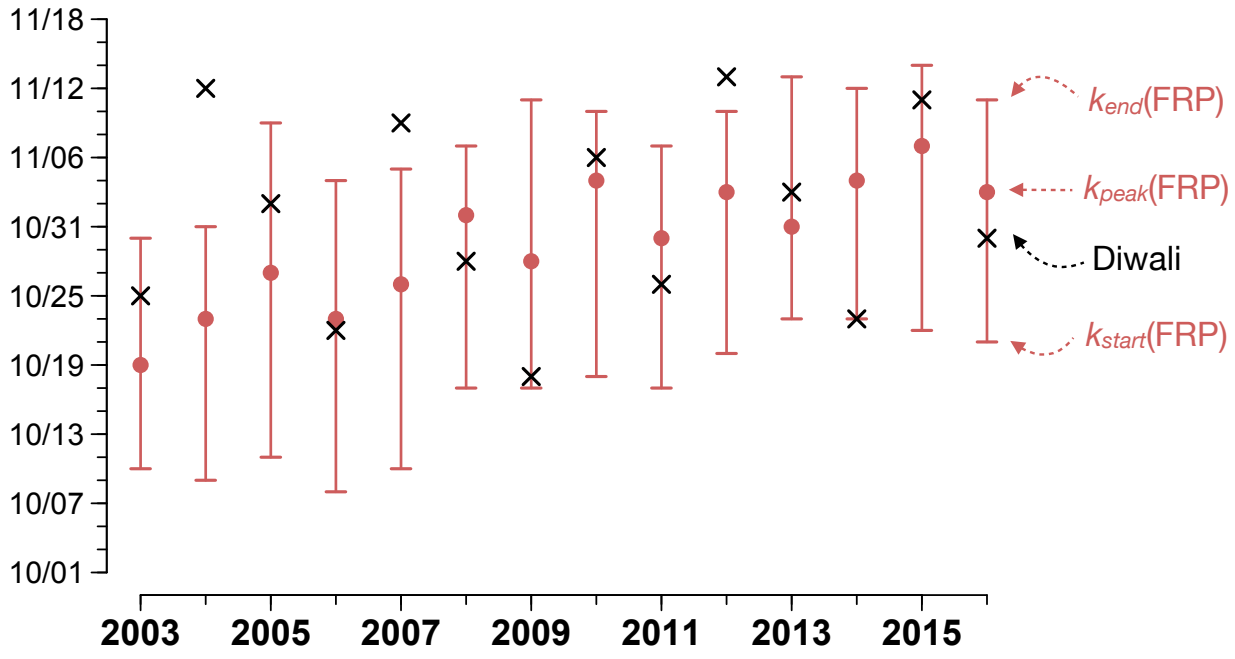


Figure A.4: Timing of the Diwali festival and post-monsoon burning season in Punjab. The timing of the start and end of post-monsoon burning season is shown as red intervals, while peak burning dates are denoted as red dots. The main day of celebration during the 5-day Diwali festival is denoted as a black x.

Table A.5: Step difference in the timing of peak monsoon greenness and trough post-monsoon greenness from the 2003-2007 to 2008-2016 time period and linear trends in the timing and magnitude of peak monsoon and trough post-monsoon greenness in Punjab.

Index	Season	Dataset	**Timing** (days yr^{-1})				**Value** (decade^{-1})	
			Step Difference		**Linear Trend**		**Linear Trend**	
			Mean	*SE*	*Mean*	*95% CI*	*Mean*	*95% CI*
NBR	Monsoon	MOD09GA	9.33*	1.2	1.09*	[0.74, 1.42]	0.06*	[0.04, 0.08]
		MYD09GA	9.01*	1.04	1.14*	[0.84, 1.43]	0.06*	[0.04, 0.08]
	Post-Monsoon	MOD09GA	4.41*	1.56	0.42*	[0.07, 0.78]	0	[-0.02, 0.02]
		MYD09GA	4.66*	1.57	0.42*	[0.06, 0.77]	0	[-0.02, 0.02]
NDVI	Monsoon	MOD09GA	7.43*	1.71	0.78*	[0.34, 1.23]	0.07*	[0.05, 0.09]
		MYD09GA	7.51*	1.57	0.81*	[0.46, 1.16]	0.06*	[0.04, 0.09]
	Post-Monsoon	MOD09GA	3.55*	1.33	0.29	[-0.06, 0.65]	0.01	[-0.01, 0.03]
		MYD09GA	3.77*	1.28	0.32	[-0.01, 0.64]	0	[-0.02, 0.02]

*Bootstrapped trend is statistically significant at the 95% confidence level

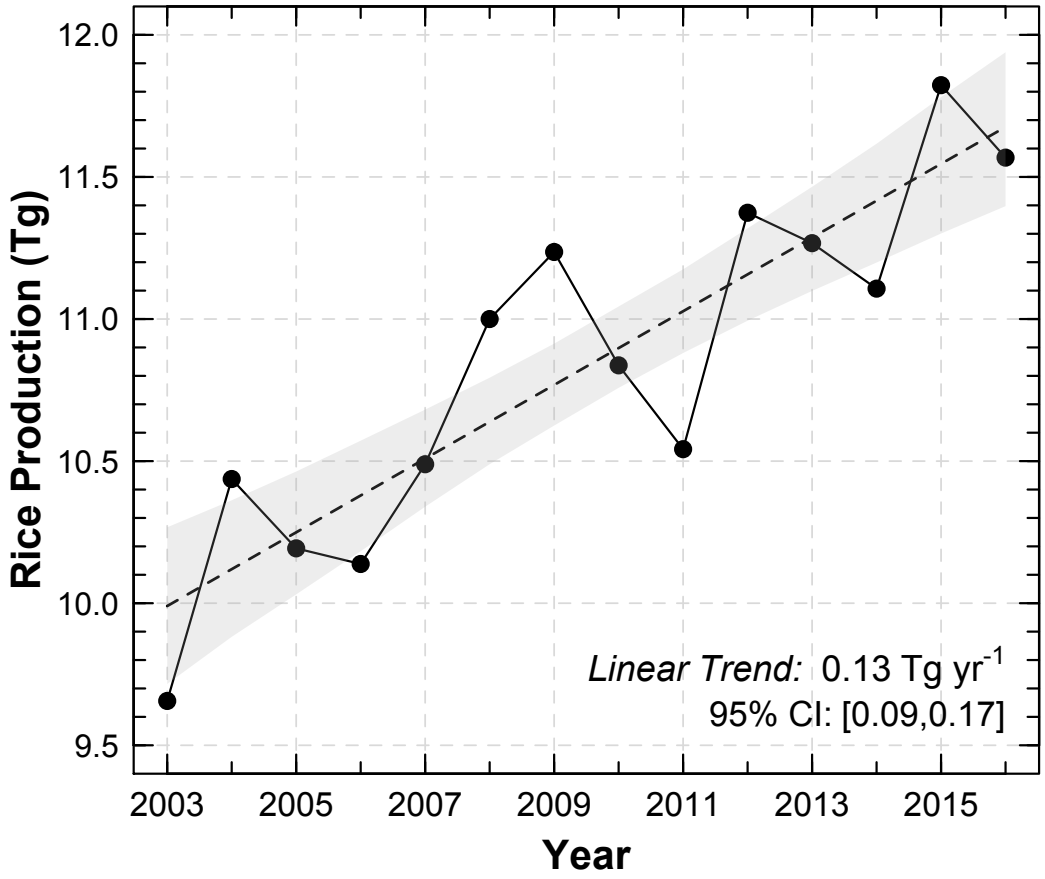


Figure A.5: Rice production in Punjab. Annual total *kharif* rice production (Indiastat, 2000) in Punjab, from 2003-2016. Inset shows linear trend estimated with residuals bootstrapping and the 95% confidence interval.

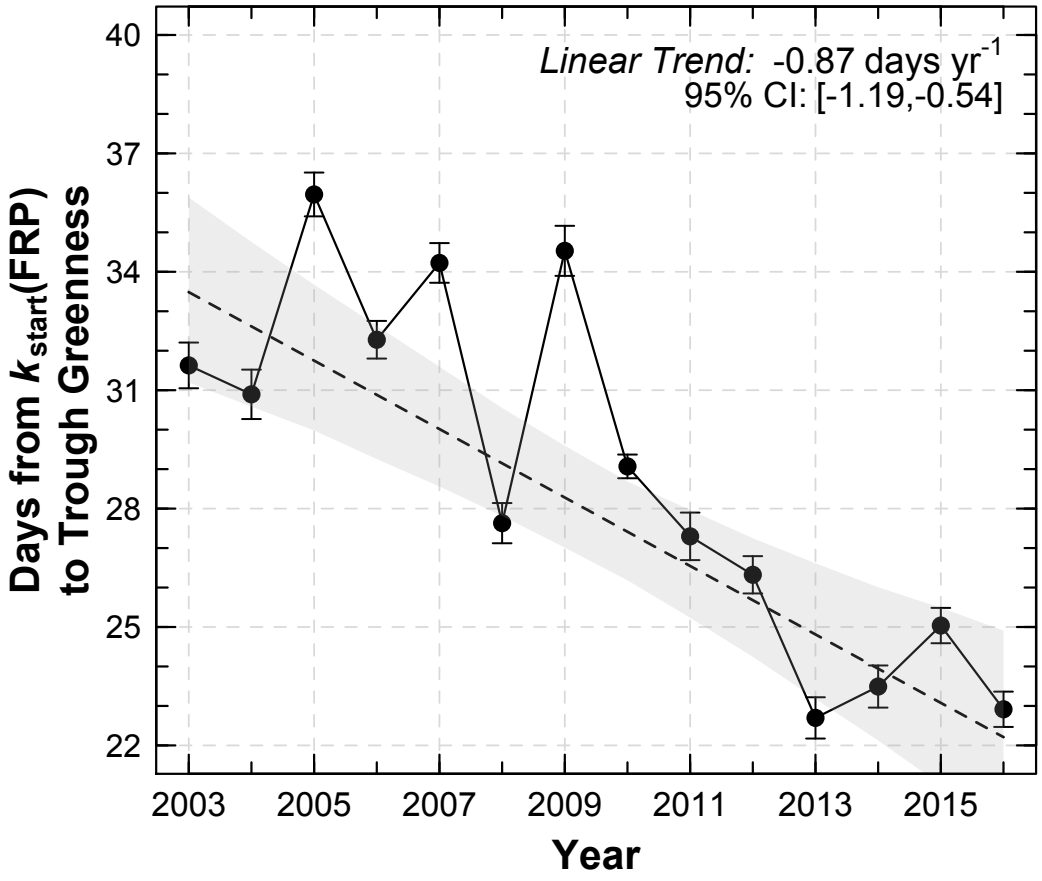


Figure A.6: Temporal compression of the duration from the onset of post-monsoon burning season to trough greenness in Punjab. The duration, with bootstrapped 95% confidence interval, from the onset of post-monsoon burning, $k_{start}(FRP)$, to post-monsoon minimum greenness. Inset shows linear trend estimated with residuals bootstrapping and the 95% confidence interval. The trend is similar using trough greenness derived from NDVI, at a mean decrease of 0.87 days yr^{-1} (95% CI: [-1.19, -0.54]).

A.4 Vegetation indices: NBR and NDVI

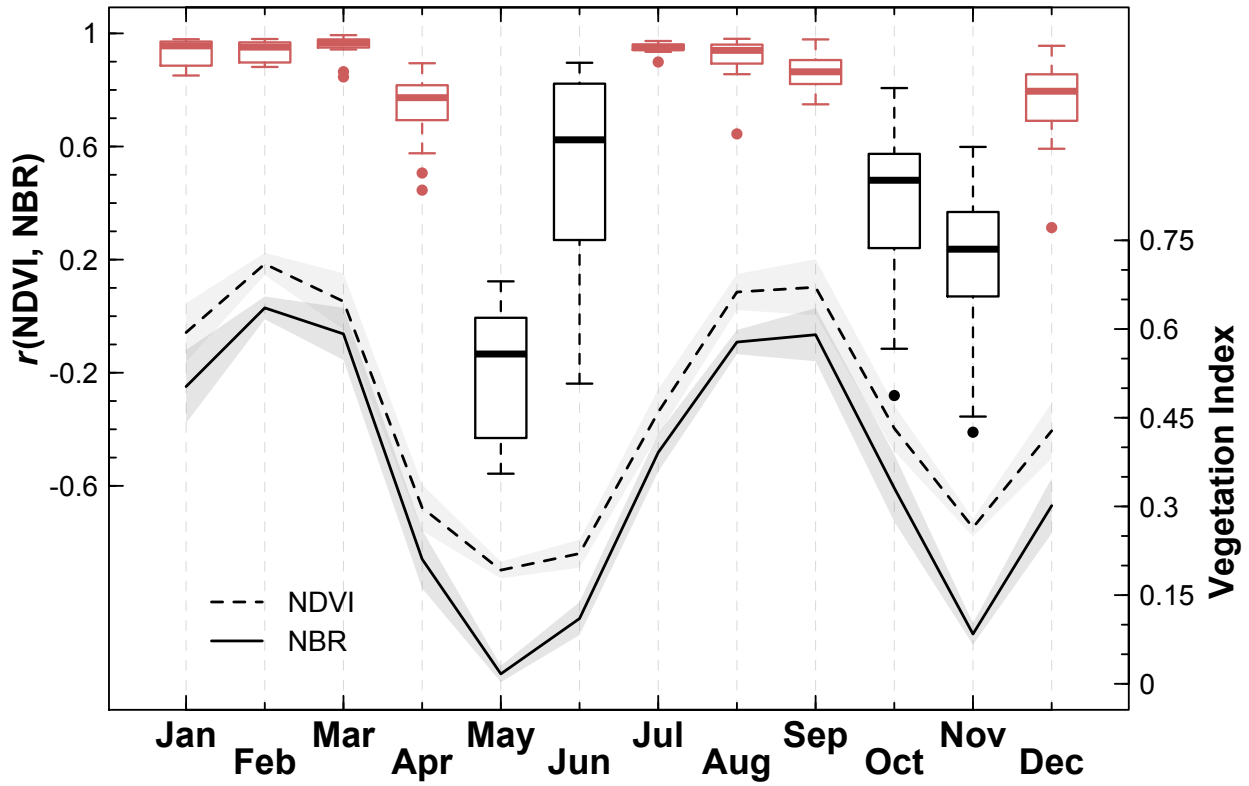


Figure A.7: Detrended correlation between daily median NDVI and NBR, by month, in Punjab. Monthly boxplots denote correlation coefficients (r) from 2003 to 2016. Mean monthly NDVI and NBR are denoted as the dashed line and solid line, respectively, with gray $\pm 1\sigma$ envelopes. Months with no or weak correlations (May, June, October, and November) are shown as black boxplots, while other months with higher correlations are shown as red boxplots. Correlations for these other months are all statistically significant at $p < 0.1$.

A.5 Thick haze and fog over the Indo-Gangetic Plain

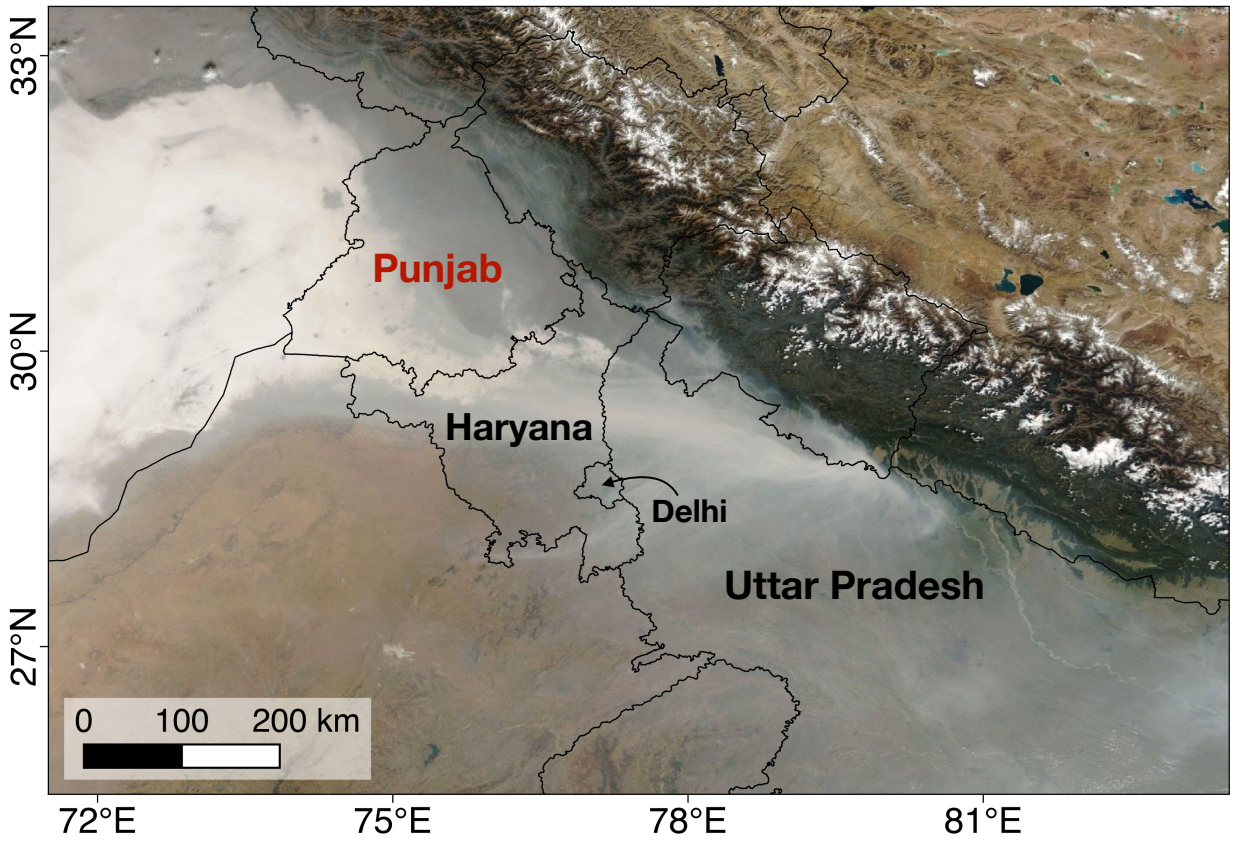


Figure A.8: Example of thick haze and fog over the Indo-Gangetic Plain. MODIS/Terra corrected reflectance image of thick haze and fog extending across northern India and Punjab, Pakistan on November 6, 2017 (NASA Worldview; https://worldview.earthdata.nasa.gov/).

A.6 Variations in Monsoon Onset and Withdrawal

The India Meteorological Department (IMD) reports the annual onset and withdrawal of the southwest monsoon spatially (http://www.imd.gov.in/pages/monsoon_main.php; last accessed: February 23, 2019). Using maps provided by the IMD from 1951-2007, Singh & Ranade (2010) approximated the dates of the monsoon onset and withdrawal for 19 sub-regions in India by interpreting isochrone maps from the IMD. We use the monsoon onset dates from Singh & Ranade (2010) for sub-region 19 (western IGP) and extend the record to 2016 by using IMD annual reports. We approximate the monsoon onset date as the earliest date and the withdrawal date as the latest date of the isochrones across Punjab. There is no statistically significant trend ($p < 0.05$) in the monsoon onset or withdrawal date from 2003-2016 (Figure A.9).

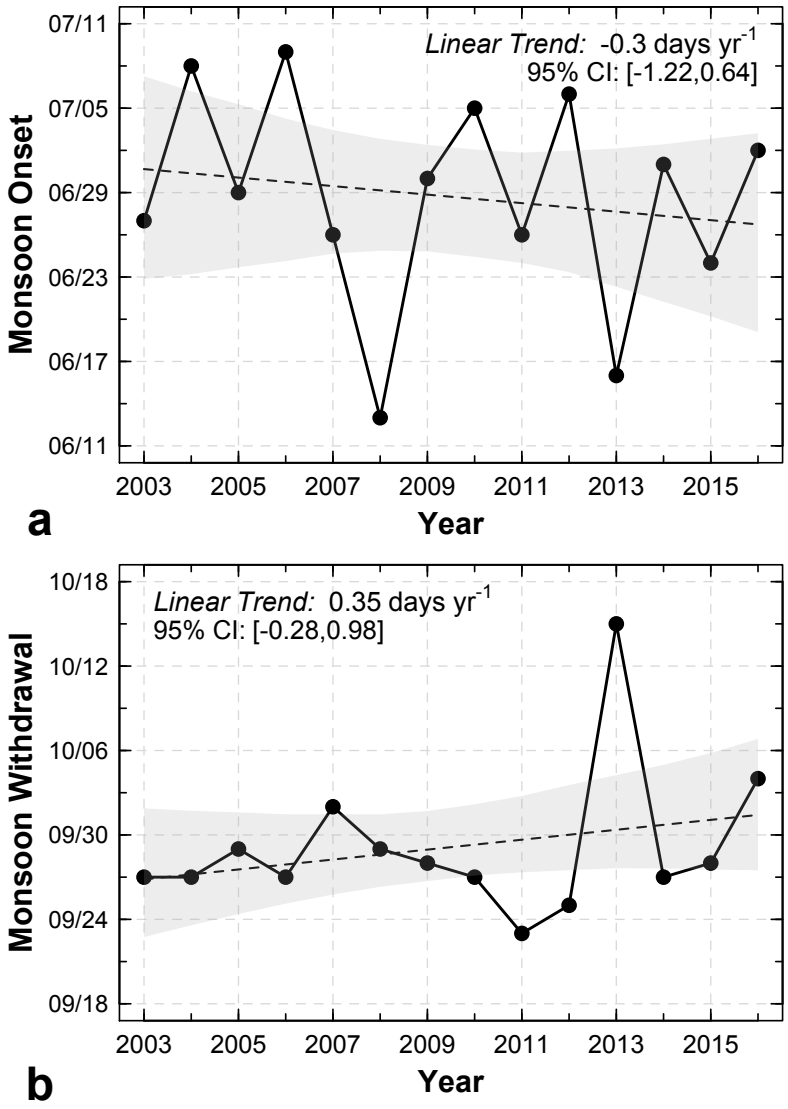


Figure A.9: Monsoon onset and withdrawal date in Punjab from 2003-2016. The (a) onset and (b) withdrawal dates are derived from maps provided by the India Meteorological Department (IMD) (Singh & Ranade, 2010).

A.7 Synthesis of the potential drivers and consequences of delays in agricultural burning associated with the double-crop cycle

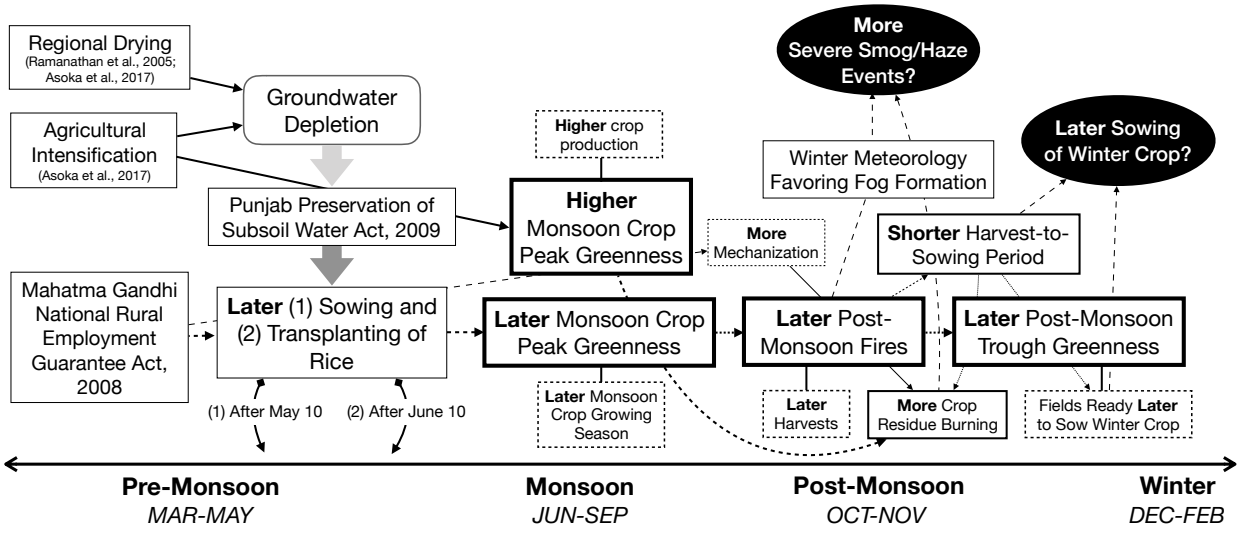


Figure A.10: Potential drivers and consequences of the temporal shifts in the double crop-fire cycle for Punjab. Rice transplanting is the practice of moving seedlings raised in nurseries to flooded paddy fields and re-planting with some spacing. The transition from solid to dotted to dashed arrows denotes increasing uncertainty. Boxes delineated by heavy solid lines highlight observed results from this study, while those with thin solid lines denote the effects of policy implementations and other related observations from literature. Dotted boxes denote implications based on observed variables, linked to these observations with solid lines.

B

Supplemental Material for Chapter 2

B.1 Household survey

The survey was a structured-household survey, where the most common responses were coded for each question. The most common responses were determined based on pilot surveys that we conducted in each study region before the actual survey was conducted. When enumerators surveyed farmers, all questions were posed as open-ended questions, and no responses were given to farmers. In other words, farmers were not primed with potential responses while being asked each question. For each question, "other" was also included as a response choice where enumerators could write in farmers' responses if they did not match existing coded responses. We ensured quality of survey responses in several ways. First, a member of our research team (Sukhwinder Singh) trained all enumerators in the survey prior to implementation. This involved conducting mock interviews with farmers prior to the implementation of the survey. During these mock interviews, any potential problems in the way that enumerators were asking questions or recording answers were addressed. Second, since the survey was conducted using an application, Singh was also able to review survey responses after they were collected and checked random samples for any potential inconsistencies. The margin of error for the survey was 2% considering our sample size ($n = 2184$) and the estimated total population across our study region ($n > 350$ million people).

Table B.1 lists the relevant household survey questions and possible responses pertaining to this study. There are three types of questions: (1) single response, (2) multiple responses possible, and (3) numerical response. Tables B.2-B.3 summarize the responses to the survey questions.

Table B.1: Questions from the 2017-18 household survey on agricultural practices across the Indo-Gangetic Plain and possible responses. The total number n of valid responses is 2184, with the following per state: in Haryana (n = 417), Punjab (n = 573), Uttar Pradesh (n = 836), and Bihar (n = 358).

Description	Survey Question	Responses	*n*
Took part in survey in 2016-17	Did you take part in our survey last year? [*]	(1) yes (0) no	2184
Method of harvesting rice	How do you harvest your rice crop? [*]	(1) fully mechanical (e.g. combine harvester) (2) partially mechanical (e.g. thresher) (3) manually (4) both manual and mechanical	1842
Rice residue burning	Did you burn rice crop before planting wheat? [*]	(1) yes (2) no	1872
Method of burning	Do you burn the entire field (whole field burning) or stack residue in the center of the field and burn (partial field burning)? [*]	(1) whole (2) partial	474
Duration between harvest and burning	How long did you wait (days) after harvest to burn? [***]	*n* days	
Time of day for burning	What time in the day did you burn? [**]	(1) early morning [4 a.m. - 10 a.m.] (2) mid-day [10 a.m. - 2 p.m.] (3) evening [2 p.m. - 6 p.m.] (4) late night [6 p.m. - 11 p.m.]	
Start year of crop residue burning	Which year did you first start to burn crop residue? [***]	*x* year	
Reasons for burning crop residue	Why did you burn the crop residue? [**]	(1) cannot use residue as cattle feed (2) difficult to cut and manage residue (3) small time window to prepare land to sow the next crop (4) no technology to manage residue (5) burning does not hamper soil health (6) burning improves soil heath (7) no incentive from government to not burn	
Negative effects of crop residue burning on soil	Have you seen any negative effects of crop residue burning on soil? [*]	(1) yes (2) no	2184
	If yes (negative effects of crop residue burning on soil), which ones? [**]	(1) lower yield (2) crop demands more fertilizers (3) change in soil color (4) change in soil texture	687
Positive effects of crop residue burning on soil	Have you seen any positive effects of crop residue burning on soil? [*]	(1) yes (0) no	2184
	If yes (positive effects of crop residue burning on soil), which ones? [**]	(1) save the cost of cutting and management of rice residue (2) higher yield (3) crop demands less fertilizers (4) change in soil color (5) change in soil texture	717
Effect of crop residue burning on air quality	Do you believe that burning is affecting air quality in nearby cities? [*]	(1) yes (2) no	2023

* single response, ** multiple responses possible, ** numerical response

Table B.2: 2017-18 household survey data on crop residue burning and mechanization in the IGP.

Description	IGP	Punjab	Haryana	UP	Bihar
Method of harvesting rice	(1) 50% *fully mechanical* (2) 2% *partially mechanical* (3) 41% *manually* (4) 7% *both manual and mechanical* ***n* = 1842**	(1) 93% (2) 0% (3) 3% (4) 4% ***n* = 561**	(1) 57% (2) 5% (3) 28% (4) 10% ***n* = 322**	(1) 21% (2) 2% (3) 71% (4) 6% ***n* = 673**	(1) 26% (2) 3% (3) 61% (4) 11% ***n* = 286**
Rice residue burning	25% *burned rice residue before planting wheat* ***n* = 1872**	53% ***n* = 554**	10% ***n* = 299**	9% ***n* = 667**	30% ***n* = 342**
Method of burning	(1) 62% *complete burns* (2) 38% *partial burns* ***n* = 474**	(1) 70% (2) 30% ***n* = 296**	(1) 57% (2) 43% ***n* = 30**	(1) 50% (2) 50% ***n* = 62**	(1) 43% (2) 57% ***n* = 86**
Duration between harvest and burning	9 days [95% CI: 3, 20] ***n* = 474**	10 days [4, 23] ***n* = 296**	6.5 days [4, 25] ***n* = 30**	8 days [3, 15] ***n* = 62**	5 days [2, 8] ***n* = 86**
Time of day for burning	(1) 1% *early morning* (2) 36% *mid-day* (3) 51% *evening* (4) 26% *late night* ***n* = 474**	(1) 0% (2) 44% (3) 41% (4) 27% ***n* = 296**	(1) 3% (2) 43% (3) 53% (4) 20% ***n* = 30**	(1) 8% (2) 15% (3) 71% (4) 27% ***n* = 62**	(1) 1% (2) 23% (3) 70% (4) 22% ***n* = 86**
Start year of crop residue burning	2004 [95% CI: 1979, 2017] ***n* = 474**	2000 [1979, 2017] ***n* = 296**	2009 [1997, 2017] ***n* = 30**	2008 [1964, 2016] ***n* = 62**	2009 [1997, 2015] ***n* = 86**

Table B.3: 2017-18 household survey data on the reasons for and effects of crop residue burning in the IGP.

Description	IGP	Punjab	Haryana	UP	Bihar
Reasons for burning crop residue	(1) 68% *cannot use residue as cattle feed* (2) 67% *difficult to cut and manage residue* (3) 70% *small time window to prepare land to sow the next crop* (4) 42% *no technology to manage residue* (5) 26% *burning does not hamper soil health* (6) 16% *burning improves soil heath* (7) 52% *no incentive from government to not burn* ***n* = 474**	(1) 76% (2) 61% (3) 65% (4) 39% (5) 21% (6) 17% (7) 81% ***n* = 296**	(1) 67% (2) 73% (3) 83% (4) 33% (5) 13% (6) 3% (7) 13% ***n* = 30**	(1) 42% (2) 73% (3) 56% (4) 29% (5) 27% (6) 21% (7) 10% ***n* = 62**	(1) 57% (2) 80% (3) 92% (4) 64% (5) 43% (6) 17% (7) 1% ***n* = 86**
Negative effects of crop residue burning on soil	(1) 32% *yes* (0) 68% *no* ***n* = 2184**	(1) 54% (0) 46% ***n* = 573**	(1) 51% (0) 49% ***n* = 417**	(1) 18% (0) 82% ***n* = 836**	(1) 8% (0) 92% ***n* = 358**
	(1) 39% *lower yield* (2) 40% *crop demands more fertilizers* (3) 39% *change in soil color* (4) 44% *change in soil texture* ***n* = 687**	(1) 42% (2) 35% (3) 34% (4) 42% ***n* = 308**	(1) 45% (2) 48% (3) 40% (4) 41% ***n* = 208**	(1) 25% (2) 39% (3) 49% (4) 50% ***n* = 153**	(1) 45% (2) 45% (3) 34% (4) 62% ***n* = 28**
Positive effects of crop residue burning on soil	(1) 33% *yes* (0) 67% *no* ***n* = 2184**	(1) 58% (0) 42% ***n* = 573**	(1) 30% (0) 70% ***n* = 417**	(1) 19% (0) 81% ***n* = 836**	(1) 27% (0) 73% ***n* = 358**
	(1) 80% *save the cost of cutting and management of rice residue* (2) 28% *higher yield* (3) 29% *crop demands less fertilizers* (4) 11% *change in soil color* (5) 7% *change in soil texture* ***n* = 717**	(1) 98% (2) 19% (3) 17% (4) 11% (5) 7% ***n* = 334**	(1) 93% (2) 17% (3) 24% (4) 6% (5) 5% ***n* = 126**	(1) 62% (2) 32% (3) 42% (4) 9% (5) 6% ***n* = 161**	(1) 28% (2) 69% (3) 58% (4) 17% (5) 10% ***n* = 96**
Effect of crop residue burning on air quality	(1) 90% *yes* (2) 10% *no* ***n* = 2023**	(1) 89% (2) 11% ***n* = 565**	(1) 94% (2) 6% ***n* = 373**	(1) 88% (2) 12% ***n* = 741**	(1) 90% (2) 10% ***n* = 344**

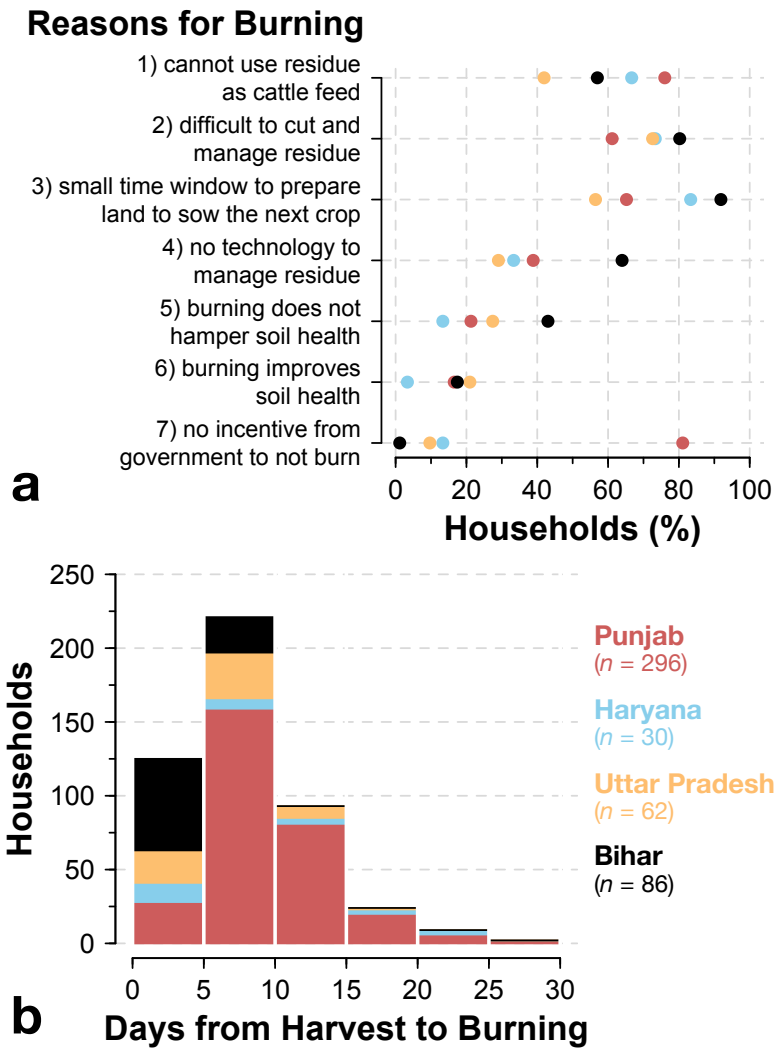


Figure B.1: Drivers of rice residue burning across the Indo-Gangetic Plain inferred from household survey data for the 2017-18 growing season: (a) Primary reasons and incentives for rice residue burning by per cent households; each household was allowed multiple reasons and incentives. (b) Histogram of the time window (in days) between rice harvests and subsequent burning of residues. Colors indicate different states.

Table B.4: Potential increase in post-monsoon burning, weighted by operational landholding area, across the Indo-Gangetic Plain for a hypothetical scenario in which all farmers use fully mechanical harvesting (combine harvesters). For each state, only households that harvest rice are considered. "All" provides the percentage of rice-growing households that burn residue; "Combine Harvester" states the percentage of these households that use combine harvesters before burning. The range of estimates for burn rate and combine harvester use is from differing survey responses in 2016 and 2017. Note that both the state-level burn rate and combine harvester use are calculated using landholding area rather than a simple count of household responses and therefore differ from Figure 2.4.

State	Current Use of Combine Harvesters [%]	Burn Rate [%]		Potential Increase in Burn Rate [%]	*n*
		All	*Combine Harvester*		
Punjab	94-96	71-89	72-91	2 (1-2)	554-568
Haryana	64-69	12-28	14-37	27 (13-34)	299-302
UP	24-26	13-15	39-45	207 (203-211)	665-671
Bihar	14-39	23-46	37-78	67 (63-68)	285-329

Table B.5: State-level fraction of partial and complete-field burns and fractional fire diurnal cycle, weighted by operational landholding area, derived from the 2017 household survey.

State	Type of Burning		Fire Diurnal Cycle				Total Area (ha)
	Partial	*Complete*	*4-10 a.m.*	*10 a.m.-2 p.m.*	*2-6 p.m.*	*6-11 p.m.*	
Punjab[1]	0.3	0.7	0	0.44	0.28	0.27	1911
Haryana[2]	0.51	0.49	0.03	0.41	0.43	0.14	182
UP[3]	0.5	0.5	0.08	0.11	0.56	0.26	172
Bihar[4]	0.57	0.43	0.02	0.11	0.77	0.11	334

Districts represented in household survey for each state: [1]Amritsar, Bathinda, Gurdaspur, Muktsar, Sangrur; [2]Kurukshetra, Fatehabad; [3]Hardoi, Kushinagar, Rampur, Sant Kabir Nagar; [4]Rohtas

B.2 Characterizing fires, crop phenology, and rainfall using satellite data

For each of the four states, we use satellite observations to characterize the fire activity, crop phenology, and rainfall at daily scale from 2003-2018 (Table B.6).

Table B.6: Satellite datasets used in this study.

Description	Dataset	Satellite	Sensor	Resolution		Time Range
				Temporal	Spatial	
Gridded fire mask/ maximum FRP	MOD14A1	Terra	MODIS	Daily	1 km	from 2000
	MYD14A1	Aqua				from 2002
Active fire geolocations	MCD14ML	Terra+Aqua				from 2000
	VNP14IMGML	S-NPP	VIIRS	Daily	375 m	from 2012
Surface reflectance	MOD09GA	Terra	MODIS	Daily	500 m	from 2000
	MYD09GA	Aqua				from 2002
Land cover	MCD12Q1	Terra+Aqua		Annual	500 m	from 2001
Rainfall	CHIRPS	—	—	Daily	0.05°	from 1981

For fire activity, we use the MODIS Collection 6 active fire datasets (MOD14A1/MYD14A1, 1 km) and sum the daily maximum FRP. We additionally estimate the day of the start, midpoint, and end of the pre-monsoon (defined here as March-May) and post-monsoon (October-December) fire seasons as described in Chapter 2.3.3. We use the University of Maryland (UMD) scheme in the MODIS MCD12Q1 land cover product to identify agricultural regions, or class 12 under the MCD12Q1 UMD classification. To characterize the phenology of vegetation greenness, we use the MODIS Collection 6 surface reflectance datasets (MOD09GA/MYD09GA, 500 m). As an indicator of crop phenology and vegetation greenness, we derive the Normalized Difference Vegetation Index (NDVI) from near infrared (NIR) and red surface reflectance as follows:

$$NDVI < \frac{\rho_2 - \rho_1}{\rho_2 + \rho_1} \tag{B.1}$$

where ρ_i is the surface reflectance of MODIS band i. The wavelength range is 841-876 nm for band 2 (NIR) and 620-670 nm for band 1 (red). To obtain a reference greenness curve for the 2003-2018 period, we calculate average NDVI for each day of the year, using the daily fractional area free of clouds and haze, or "usable fraction,"

as weights (Liu et al., 2021a). The usable fraction is based on two simple criteria from Xiang et al. (2013) using surface reflectance:

$$\frac{\rho_1 - \rho_7}{\rho_1 + \rho_7} < 0 \text{ and } \rho_1 < 0.3 \tag{B.2}$$

where the wavelength range of band 7 (SWIR-2) is 2105-2155 nm. Saturation of surface reflectance in the visible bands relative to SWIR bands generally indicates hazy or cloudy conditions.

For rainfall, we use the Climate Hazards Infrared Precipitation with Stations (CHIRPS) dataset, version 2, available at 0.05° x 0.05° spatial resolution (Funk et al., 2015). We sum the daily rainfall, in units of mm, across each state.

B.3 Gridded inventory for agricultural fire emissions across the Indo-Gangetic Plain

B.3.1 Additional details on VIIRS FRP boost

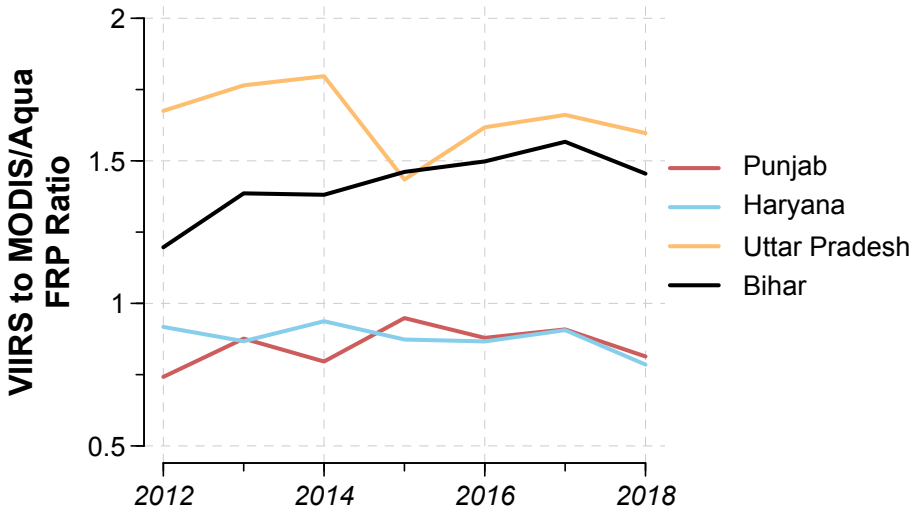


Figure B.2: Interannual variability in the VIIRS to MODIS/Aqua FRP ratio by state. VIIRS and MODIS/Aqua FRP are summed over September to December of each year before calculating the ratio from 2012-2018. Colors refer to the four states in the study region.

We derive the VIIRS boost to MODIS FRP by calculating the VIIRS to MODIS/Aqua FRP ratio (Figure B.2). We use only those daytime VIIRS fire detections that do not intersect with MODIS/Aqua FRP within a 1-km buffer and are also designated as vegetation type fires (Schroeder & Giglio, 2018). We tested the sensitivity of the buffer size using a larger 1.5-km buffer and find a small difference (∼7%) in the resulting VIIRS FRP boost. For MODIS/Terra, we assume that the same ratio of fires missed by MODIS but detected by VIIRS is consistent across the Terra and Aqua overpasses, and thus apply the same VIIRS to MODIS/Aqua ratio to MODIS/Terra FRP.

In the context of north India, adjacent fire detections are unlikely to be duplicates, because individual fields are small (∼2-3 ha); at fine spatial resolution (< 5 m), satellite images show that a single MODIS or VIIRS pixel covers many fields and that large swaths of neighboring fields often burn around at the same time (Liu et al., 2019). We quantified the percentage of duplicate observations by tagging detections that are within 200 m of each other. We found that consistently, ∼6% of active fires each year are tagged possible duplicates. To remove the influence of duplicates, we apply a scaling factor of 0.97 to both the MODIS and VIIRS FRP.

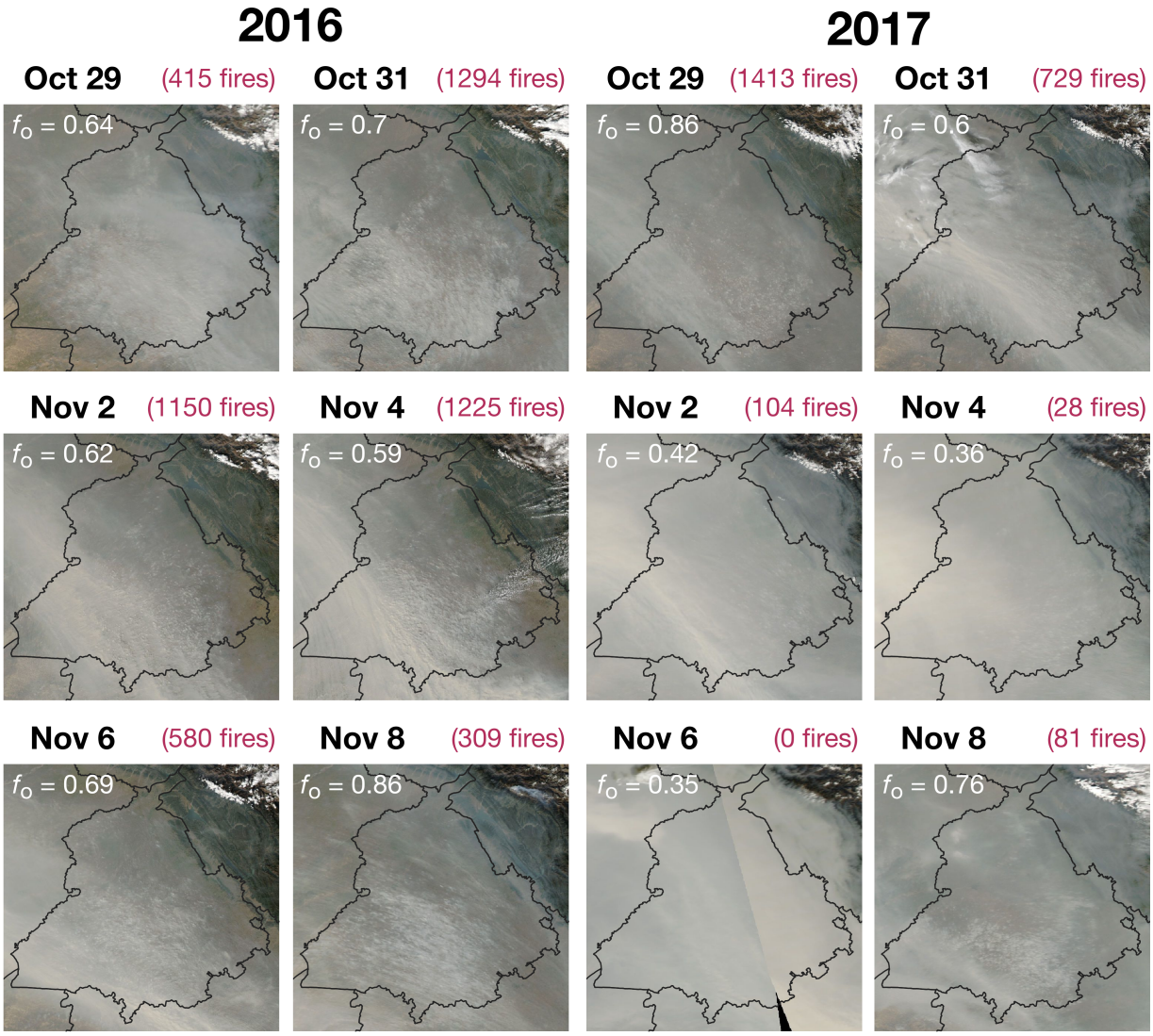


Figure B.3: Haze and cloud cover over Punjab, India from Oct 28-Nov 8 in 2016 and 2017: Corrected MODIS/Aqua reflectance images (RGB, bands 1-4-3) are from NASA Worldview (https://worldview.earthdata.nasa.gov/). Inset shows the number of active fires detected by MODIS/Aqua during the daytime overpass and the MODIS/Aqua satellite observable fraction, f_o, for Punjab. Images are shown for every other day to avoid the sampling cycle artifacts due to the day-to-day variability in satellite viewing angles.

Using the clouds/haze cutoff in Equation B.2, we can assign the fire detection probability for cloud/hazy pixels as 0 and clear pixels as 1. However, we then obtain a step function with a discontinuity at $\rho_1 = 0.3$, and as we will see, some fires are detected when $\rho_1 > 0.3$. We thus smooth this step function by creating a continuous piecewise function with a descending limb about $\rho_1 = 0.3$. To do so, we first derive a fire detection curve for the entire study region, showing the distribution of ρ_1 at active fire geolocations (MCD14ML), binned at intervals of 0.01

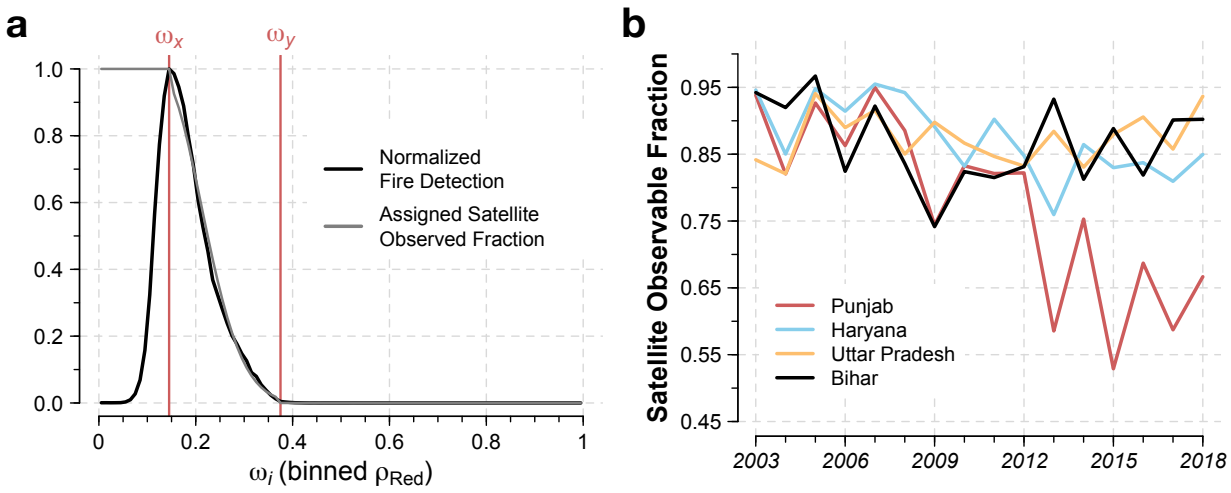


Figure B.4: Satellite observable fraction in the IGP during September to December from 2003-2018, weighted by FRP: (a) Normalized fire detection curve (black) and assigned value for the satellite observed fraction, or γ_{ω_i}, (gray) for binned ρ_1 from 0-1 (ω_i). For each day and bin, we divide the active fire count across the IGP by the maximum active fire count of all bins to obtain the associated fire detection curve. The red lines labeled ω_x and ω_y represent the start and end ρ_1 values used to approximate the descending limb of the observed fraction curve from 1 to 0, which is labeled here as the "assigned" curve. (b) Timeseries of satellite observable fraction for each state from 2003-2018. The methods used to calculate the fire detection curve and satellite observable fraction are described in detail in Chapter 2.3.4.1.

from 0 to 1. We denote the binned ρ_1 as ω_i, where i refers to the median of each ρ_1 bin. In constructing the ρ_1 distribution, we mask out areas with zero active fire detections from 2003-2018. For each day and satellite, we identify the bin with the maximum active fire counts summed across the study region, and then we divide the active fire count in each bin by this maximum count to obtain the daily normalized fire detection curve as a function of ρ_1. We obtain the final detection curve by averaging all daily detection curves, weighted by the IGP-wide FRP for that day and satellite to place more emphasis on satellite observing conditions coinciding with high fire activity. We find that the detection curve peaks at the bin centered at 0.145 (ω_x) and drops to 0 at the bin centered at 0.375 (ω_y) (Figure B.4a).

We next calculate f_o, the statewide Terra or Aqua fractional observable area, on any given day. For ω_i less than the peak value ω_x, we assume that atmospheric conditions are relatively clear and set the fraction as 1. For values of ω_i between ω_x and ω_y, the fraction is a value from 1 to 0 as a function of ρ_1. For values of ω_i greater than ω_y, the fraction is 0. Figure B.4a reveals that we can approximate f_o as a quadratic function of ω_i in the log-linear space. Put another way,

$$f_o = \sum_{i=1}^{100} \frac{A_{\omega_i}}{A} \times \gamma_{\omega_i}$$

$$\text{where } \gamma_{\omega_i} = \begin{cases} 1 & \text{if } \omega_i \leq \omega_x \\ e^{-69.986\omega_i^2 + 17.713\omega_i - 1.142} & \text{if } \omega_x \leq \omega_i \leq \omega_y \\ 0 & \text{if } \omega_i \geq \omega_y \end{cases} \tag{B.3}$$

where A_{ω_i} is the area for which ρ_1 falls within ω_i, A is the total area in the state with ≥ 1 fire detection, and γ_{ω_i} is the detection rate associated with ω_i.

Next, we gap-fill the temporal distribution of total FRP over each state separately, boosting fire activity during each season according to cloud/haze cover. For each day, we first average the Terra and Aqua fractional observable areas f_o, with the respective Terra and Aqua FRP as weights. We hereafter refer to the combined Terra/Aqua f_o as the "satellite observable fraction"; the complement of this quantity is the "satellite non-observable fraction." We calculate an initial cloud/haze correction by multiplying the observed, daily statewide FRP with the satellite non-observable fraction and then adding this increment to the observed FRP. This assumes that the satellite FRP per unit area is the same in non-observable areas as in observable areas. This initial gap-fill step leads to a conservative estimate of FRP on days with no or few active fire detections, since there are likely to be even more fires where heavy smoke is obscuring detection. In such cases, this method alone may not suffice to correct for missing fires. Take, for example, a day with near zero FRP at the peak of the fire season, as in Punjab during 2017. The satellite observable fraction would need to be unrealistically low (« 0.1) for the FRP on that day to be adjusted to the expected level.

For Punjab and Haryana, where satellites can more consistently detect post-monsoon fires, we can use iterative methods to apply further cloud/haze corrections and reduce underestimates in FRP during particularly cloudy/hazy periods. Here, for days within the burning season, we gap-fill FRP by iteratively nudging the observed FRP toward a Gaussian distribution within a moving 15-day window. We find that shorter time windows are more likely to introduce artificial noise in the daily timeseries adjusted FRP. For each day, we adjust the partial sums by adding the increment derived from the slope of a simple linear regression of FRP versus time for the 15-day window, weighted by the satellite non-observable fraction for that day. In this way, days with higher cloud/haze cover are prioritized in the adjustment. For days near the start and end of the burning season, the increment is calculated using a truncated 15-day window that excludes days before or after the burning season,

which have specified partial sums of FRP of ∼0 or 1, respectively. The impact of FRP outliers when calculating the slope is minimized by using state-level FRP and cumulative sums.

Each iteration of the gap-filling exercise smooths the temporal evolution of FRP over the state. To determine when to stop nudging, we derive a target Gaussian curve from the derivative of the sigmoid-smoothed cumulative FRP, or FRP_{σ}, as described in detail in Chapter 2.3.3. The maximum of the Gaussian curve is normalized to the maximum daily FRP. Iterations stop upon convergence of the ratio of adjusted to Gaussian FRP or when the maximum of 50 iterations is reached. During each iteration, the nudging is repeated for each day until the following criterion is met: the ratio of FRP on a given day to the maximum FRP of its neighborhood window must be at least 0.75 times the same ratio of these values for a Gaussian-smoothed FRP distribution. While we tested other sensitivity parameters, we select 0.75 to avoid overcompensating for unobserved FRP while preserving some likely daily variability in FRP. For days prior to the midpoint of the burning season, the neighborhood window consists of all days prior to a selected day. For days after the midpoint, the neighborhood window consists of all days prior and after a selected day. Unlike in Chapter 2.3.3, here we calculate the midpoint as a fractional value by weighting each day of the burning season, from 1 to n total days, by the corresponding daily FRP and take the average. As an added constraint to prevent overcorrection from the cloud/haze gap-fill, the cloud-gap fill adjustment is rejected if the resulting FRP is greater than FRP from the Gaussian curve. The cloud/haze gap-filling step ultimately yields a ratio of 2016 to 2017 FRP that more closely matches the ratio in the burn rates derived from household surveys for the 2016-17 post-monsoon burning seasons.

We also gap-fill days that have zero FRP if prior days have non-zero FRP. For such days, we simply re-assign its FRP as the average of FRP observed on the day prior and after. Without this additional gap-filling step, discontinuities in fire emissions at state borders may emerge at a later stage of our algorithm (Chapter 2.3.4.3).

Finally, the iterative statistical adjustment may introduce error in the cloud/haze boosted FRP time series. To help overcome this error, for each day, we take the average of FRP with the initial cloud/haze gap-fill and with both the initial and iterative cloud/haze gap-fill, using the factors $(1 - f_o)$ and f_o as weights. The resulting adjusted FRP is closer to the cloud/haze gap-filled FRP (Steps 1-3) on days with low satellite observable fraction f_o, but also closer to the FRP without gap-filling (Steps 1-2 only) on days with high f_o. This step temporally redistributes the cloud/haze boost and helps to preserve the temporal variability in the satellite observations while incorporating our cloud/haze gap-fill.

B.3.3 Additional details on the adjustment for the diurnal cycle of fire activity

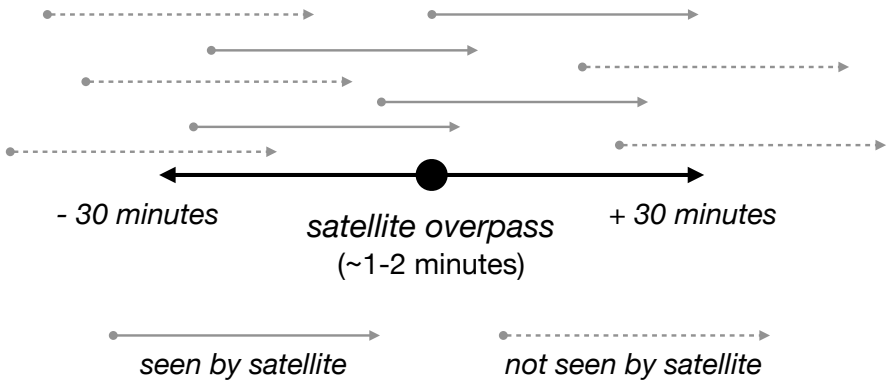


Figure B.5: Graphic depiction of which fires are seen by a satellite during its overpass over north India: The timing of the satellite overpass, which lasts 1-2 minutes, is denoted by the filled-in circle. Each arrow denotes an individual fire detection, assuming that the fire lasts 30 minutes. Arrows with solid lines denote fires seen by the satellite, while arrows with dashed lines denote fires not seen by the satellite.

To adjust FRP to the diurnal cycle of fire activity, we assume that MODIS, with the Terra and Aqua overpasses, accounts for 1.5 hours of fire activity, or 45 minutes for each overpass. Figure B.5 depicts the basis for this assumption. According to the orbital track, MODIS/Terra and Aqua and S-NPP/VIIRS retrieve active fire detections within 1-2 minutes over the study region. Assuming that fires last half an hour, the satellites can thus see fires that started up to 30 minutes before the overpass, accounting for 1 hour of fire activity in total. However, some fires that burn within this 1-hour period may be missed by the satellites, namely those fires that end less than 30 minutes before the overpass and start less than 30 minutes after the overpass, as depicted by the dashed arrows in Figure B.5. We account for these missed fires by assuming that each overpass captures 45 minutes of fire activity rather than 1 hour.

Figure B.6 shows the binned active fire counts from MODIS and VIIRS at 15-minute intervals. About a third of fires from MODIS/Aqua and VIIRS/S-NPP are detected after 2 p.m. local time. We assume that FRP is consistent across the distribution of Aqua overpass times. Here we do not take into account the day-to-day variability in overpass time, and further study is needed to develop a detailed correction for this issue. While an "A1" product exists for VIIRS at 750-m, one does not yet exist for VIIRS at 375-m (Schroeder and Giglio, 2018). To temporarily account for differences in FRP between "A1" and "ML" products, we derive an adjustment based on the ratio of FRP from MxD14A1 and MCD14ML, which varies from 1.8-2.34 among the four states. Instances of multiple fires occurring within each pixel is reduced at higher resolution, so this ratio is likely dampened with

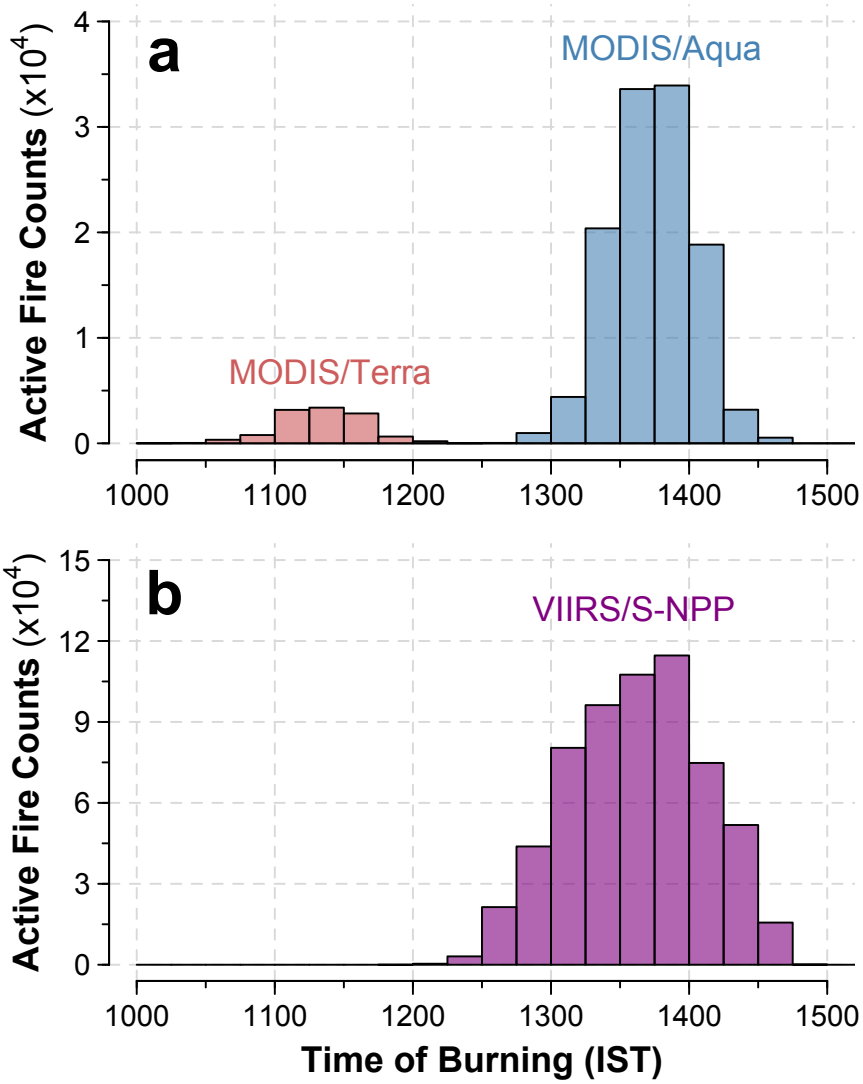


Figure B.6: Temporal distribution of daytime active fire detections by MODIS and VIIRS in north India from 2012-2018. Cumulative active fire counts, binned at 15-minute intervals, from September to December from (a) MODIS/Terra and MODIS/Aqua and (b) VIIRS/S-NPP.

smaller pixels. We thus adjust the ratio by an area-derived factor f, or $(375/1000)^2$, as in,

$$FRP_{A1,VIIRS} = FRP_{ML,VIIRS} + FRP_{ML,VIIRS}(\frac{FRP_{A1,MODIS} - FRP_{ML,MODIS}}{FRP_{ML,MODIS}})f \tag{B.4}$$

B.3.4 Hourly diurnal cycle of fire activity

As an ancillary dataset for our inventory, we disaggregate the diurnal cycle of fire activity, derived from household survey data, to hourly timesteps for each state, since the time intervals from the household survey are irregular. For atmospheric modeling, the hourly diurnal fractions, which can be aggregated to a coarser temporal resolution, allow end-users to readily apply SAGE-IGP emissions at sub-daily resolution. Like our inventory with daily timesteps, the hourly fraction of fire activity is mapped onto a 0.25° x 0.25° grid. For grid cells where states overlap, we weight the hourly fraction of fire activity by the total statewide DM from 2003-2018.

Figure B.7 shows the 3-hourly fire diurnal cycle from GFEDv4s (Mu et al., 2011; van der Werf et al., 2017). GFEDv4s uses active fire data from the Geostationary Operational Environmental Satellite (GOES) satellites to derive the 3-hourly diurnal cycle by land cover and region. We find general agreement in the fire diurnal cycles for Punjab and Haryana, but for UP and Bihar, the peak fraction of fire activity occurs later in our survey-based dataset by several hours compared to GFEDv4s (Figure 2.1c, Figure B.7). Additionally, no farmers burned rice residues from 11 p.m. to 4 a.m. in our household survey, while GFEDv4s indicates that a small fraction of fires occurred during these hours. It is possible that either the sample size of our household survey is too small to reveal crop residue burning at these hours, farmers did not report burning at these hours even though it occurred, or the GOES-derived GFEDv4s 3-hourly fractions are not representative of fire activity in north India.

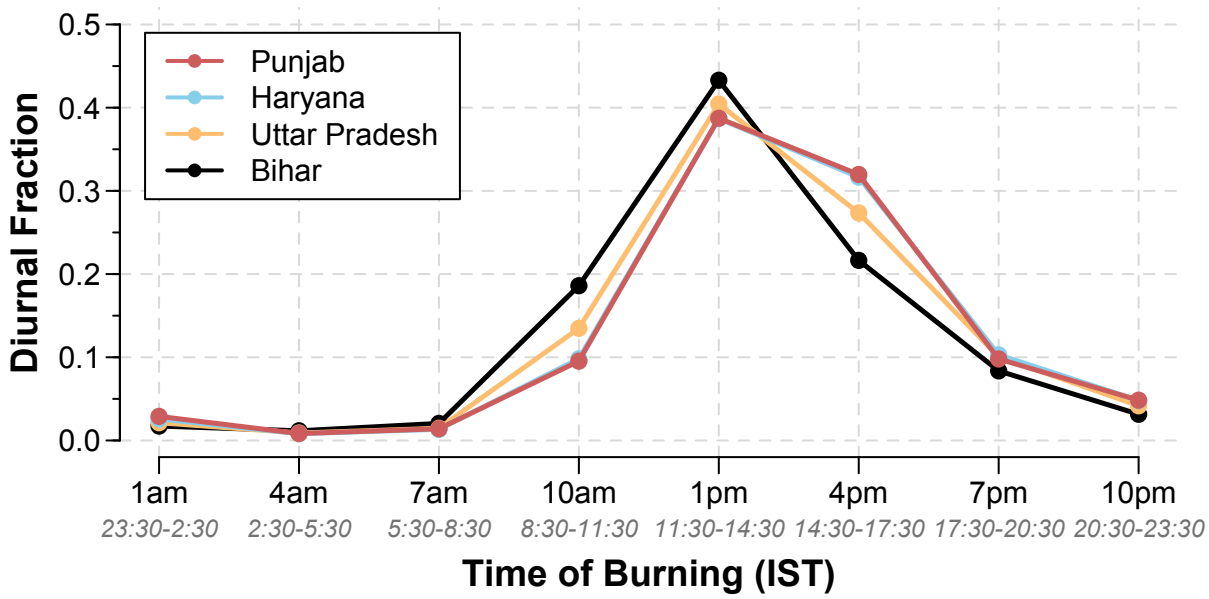


Figure B.7: GFEDv4s diurnal cycle of fire activity in Punjab, Haryana, UP, and Bihar: The GFEDv4s diurnal cycle of fire activity is in 3-hourly intervals. The median (black) and bounds (gray) of the 3-hour windows are labeled on the x-axis.

B.3.5 Uncertainty analysis

Global fire emissions inventories do not provide formal uncertainty estimates due to the difficulty in assessing uncertainty at every step of the calculation (van der Werf et al., 2017; Wiedinmyer et al., 2011). This is especially the case for satellite observations of fires, because observations often represent the lower bound of fire activity, and it is difficult to quantify what satellites do not see. Below, we attempt to quantify the uncertainty associated with satellite observations, household survey results, conversion factor (α) for FRP to dry matter burned, and emissions factors.

Satellite observations of fires (Step 1-3). To gauge the state-level relative uncertainty in MODIS and VIIRS observations of FRP and from year to year, we calculate the ratio of cloud/haze gap-filled FRP to MODIS + VIIRS FRP (Figure B.8). A higher ratio indicates higher relative uncertainty in satellite-observed FRP due to a greater degree of haziness and/or cloudiness obscuring fires from satellite detection. For instance, the high relative uncertainty for 2015 fire emissions reflects the poor observing conditions of that year (Figure B.4b, S8). Additional uncertainty stems from the application of the mean VIIRS boost factor — i.e., the mean ratio of VIIRS to MODIS/Aqua FRP from 2012-2018 — to MODIS FRP from 2003-2011, when VIIRS observations are not available (Figure B.2, Table B.7). However, we note that the VIIRS to MODIS/Aqua FRP ratio is consistent from year to year with a low coefficient of variation at < 10% (Figure B.2).

Table B.7: Uncertainty in VIIRS FRP boost, calculated per season using the ratio of VIIRS to MODIS/Aqua FRP from 2012-2018, when applied to post-monsoon burning seasons from 2003-2011. The mean and standard deviation are weighted by the sum of MODIS and VIIRS FRP, and CV is the coefficient of variation across the bootstrapped hold-out samples.

State	VIIRS FRP boost	
	Weight. Mean (SD)	CV
Punjab	0.85 (0.07)	8%
Haryana	0.88 (0.05)	5%
Uttar Pradesh	1.64 (0.12)	7%
Bihar	1.43 (0.13)	9%

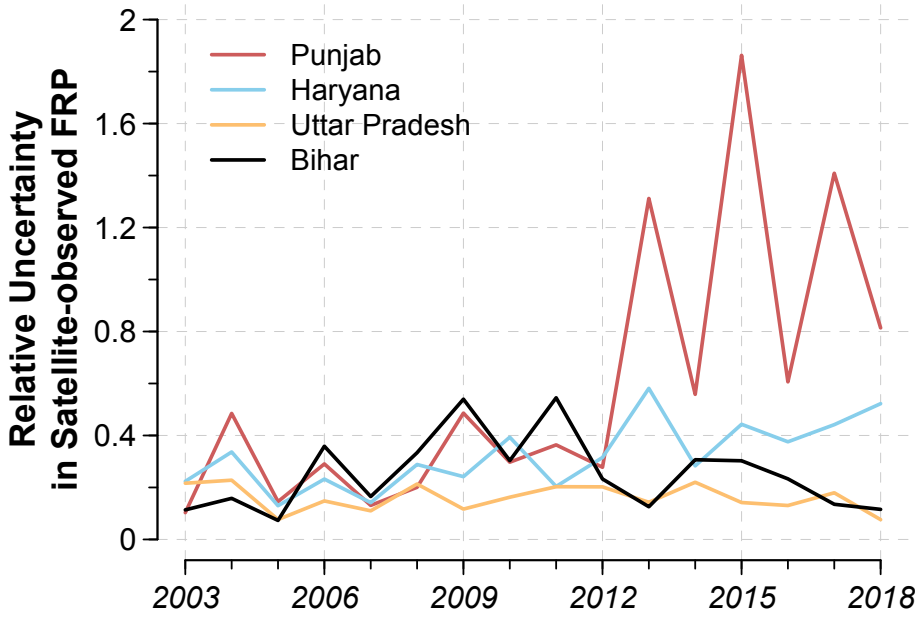


Figure B.8: Relative uncertainty in satellite-derived FRP due to cloud/haze gaps in observations. The relative uncertainty for satellite-observed FRP is expressed as the ratio of cloud/haze-gap-filled FRP to MODIS + VIIRS observed FRP.

Partial-field burning and fire diurnal cycle (Steps 4-5). Here we describe our approach to estimate uncertainty in adjusted FRP from our two survey components: partial-field burns and the diurnal cycle of fire activity. For each state, we randomly sample two-thirds of the survey responses 1000 times. In each iteration, we calculate the partial-field burn and mid-day fire (10 a.m. to 2 p.m.) fractions using only the two-thirds subset. The mean of the bootstrapped hold-out samples (Table B.8) is similar to that used with the entire survey sample (Table B.5). The coefficient of variation (CV) for the bootstrapped hold-out samples provides an estimate of uncertainty on the partial burn and mid-day fire fractions. Generally, the CV is lowest for states with high sample sizes (e.g., Punjab) and highest for those states with small sample sizes (e.g. Uttar Pradesh, Haryana).

Table B.8: Uncertainty in partial burn and mid-day fire fractions (10 a.m. to 2 p.m.) from household survey responses. The mean with a 90% confidence interval is shown along with the coefficient of variation (CV), or the ratio of the standard deviation to the mean.

State	*n*	Partial burn		Mid-day fires	
		Mean [90% CI]	CV	Mean [90% CI]	CV
Punjab	296	0.31 [0.25, 0.38]	13%	0.44 [0.34, 0.51]	14%
Haryana	30	0.5 [0.36, 0.64]	17%	0.41 [0.27, 0.54]	20%
Uttar Pradesh	62	0.5 [0.38, 0.68]	18%	0.11 [0.03, 0.18]	42%
Bihar	86	0.56 [0.48, 0.65]	10%	0.11 [0.06, 0.15]	26%

FRP to dry matter burned conversion factor. The conversion factor α is used to convert Fire Radiative Energy (FRE) to dry matter burned (Equation 2.3). First, we convert FRP to FRE by assuming that fires last half an hour in north India. As we note in Chapter 2.3.4.2, our estimates of FRE are insensitive to this assumption, because any changes must be compensated for in Step 5 to adjust for the diurnal cycle of fire activity. Conversion factor α is dependent on fuel load and combustion completeness, or fuel consumption. Because fuel consumption cannot be directly multiplied by FRE to estimate DM, α is derived from bottom-up inventories, such as GFEDv4s, as a proxy to convert FRE to DM burned. We discuss uncertainties in fuel consumption in more detail in Appendix B.4.3. Additionally, in our bottom-up validation for Punjab (Figure 2.6a), we take into account a range of values for some fuel consumption components, namely residue-to-crop ratio and fraction of dry matter (Table 2.1).

Emissions factors. In this study, we use emissions factors (EFs) for agricultural fires from Andreae (2019), which updates the earlier compilations by Andreae & Merlet (2001) and Akagi et al. (2011) used in the standard global fire inventories. We note the differences in the EFs used by these global inventories in Table B.11 in Appendix B.4.3. Here we also compile EFs specific to rice straw burning in Asia — mainly in China and none in

India — from the literature (Table B.9). Overall, the EFs from Andreae (2019) and our compilation are within ± 1 standard deviation of the mean. There is, however, substantial variability of the rice straw burning EFs reported for China, and it is not known how EFs for north India may differ from these existing studies. For example, both rice straw and stubble are typically burned in India, but only rice straw is burned in at least some regions (Lasko et al., 2017). As new field studies are conducted in north India, end-users of our SAGE-IGP inventory will be able to apply region-specific EFs.

Table B.9: Average emissions factors and associated uncertainty (±1 SD) for OC, BC, CO, and CO_2 for agricultural burning.

Species	**Andreae (2019)**	**Rice straw**	
		Average	*References*
OC	4.9 (3.6)	5.5 (2.8)	**a, b, c, d**
BC	0.42 (0.28)	0.74 (0.2)	**a, b, c, d, e**
CO	76 (55)	61 (21)	**a, b, c, e, f, g**
CO_2	1430 (230)	1355 (217)	**a, b, c, e, f, g**

a = Cao et al. (2008), **b** = Zhang et al. (2013), **c** = Ni et al. (2015), **d** = Li et al. (2017a), **e** = Zhang et al. (2015), **f** = Kim Oanh et al. (2011), **g** = Irfan et al. (2014)

B.4 Estimates of agricultural fire emissions based on active fires and burned area

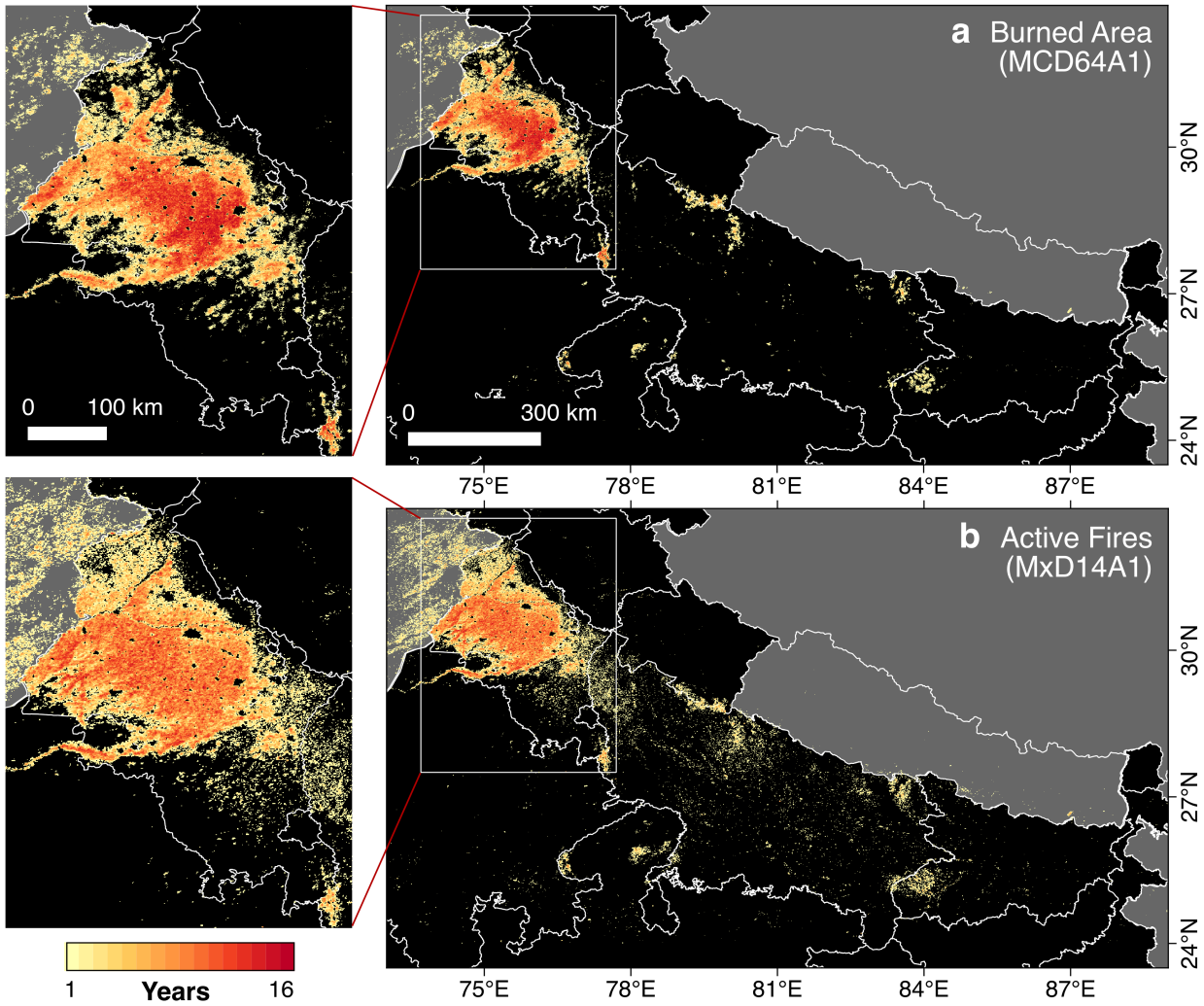


Figure B.9: Post-monsoon burn footprint over the Indo-Gangetic Plain derived from: (a) MCD64A1 burned area and (b) MxD14A1 active fires. The agricultural burn footprint is calculated as the stack of all years from 2003-2018; for each year, a pixel burned on any day from September-December is assigned a value of 1.

Table B.10: Regional and global fire emissions inventories.

Fire Emissions Inventory	Fire Product	Temporal Range	Spatial Resolution	Reference
SAGE-IGP [r]	FRP	2003-2018	0.25° x 0.25°	*this study*
GFEDv4s [g]	BA	1997-*	0.25° x 0.25°	van der Werf et al. (2017)
FINNv1.5 [g]	AFA	2002-	0.1° x 0.1°**	Wiedinmyer et al. (2011)
GFASv1.2 [g]	FRP	2003-	0.1° x 0.1°	Kaiser et al. (2012)
QFEDv2.5r1 [g]	FRP	2000-	0.1° x 0.1°	Darmenov and da Silva (2013)
FEERv1.0-G1.2 [g]	FRP	2003-	0.1° x 0.1°	Ichoku and Ellison (2014)

[r] = regional, [g] = global inventory
FRP = Fire Radiative Power, BA = burned area, AFA = active fire area
* GFEDv4s emissions from 2017-present are preliminary, based on active fires and historical emissions; emissions from 1997-2002 are at monthly scale only
** regridded to 0.1° from FINNv1.5's native 1-km spatial resolution

B.4.1 BA/AFA-based inventories

For inventories derived from burned area, fire emissions are calculated as follows (van der Werf et al., 2017; Wiedinmyer et al., 2011):

$$E_i = BA \times FL \times f_{CC} \times EF_i \tag{B.5}$$

where E_i is the emissions of species i (g species), BA is burned area (m^2), FL is fuel loading (kg m^{-2}), f_{CC} is combustion completeness, and E_i is the emissions factor for species i (g species kg^{-1} DM). For estimates of BA, GFEDv4s uses the burned area product MCD64A1, while FINNv1.5 uses the near-real-time active fire product MCD14DL.

One major source of uncertainty is the fuel loading applied. Despite similar burned area estimates over Punjab and Haryana in GFEDv4s and FINNv1.5, FINN emissions are more than twice that of GFED (Liu et al., 2019). FINN primarily assumes static land cover-dependent fuel loading from Hoelzemann et al. (2004) (Wiedinmyer et al., 2011), while GFED calculates these values as a function of climate and fire persistence in the Carnegie-Ames-Stanford-Approach (CASA) biogeochemical model (van der Werf et al., 2010). For GFEDv4s, the fuel consumption is ~288 g m^{-2} on average over Punjab during the post-monsoon burning season, 73% lower than that used by FINN (~1093 g m^{-2}).

B.4.2 FRP-based inventories

FRP-based emission inventories rely on conversion factors to translate fire energy into dry matter burned. For the Global Fire Assimilation System (GFASv1.0), Kaiser et al. (2012) used a factor of 0.29 kg dry matter per MJ^{-1} for agricultural fires, derived from the relationship between GFASv1.0 and GFEDv3, which did not at that time include a small fires boost (Randerson et al., 2012). Kaiser et al. (2014) later revised this conversion factor to 0.41 kg MJ^{-1}, which is equivalent to the average of the conversion factor derived in Wooster et al. (2005) and Freeborn et al. (2008) (Liu et al., 2015). GFASv1.2, as well as two other FRP-based inventories, Quick Fire Emissions Dataset (QFEDv2.5r1) and Fire Energetics and Emissions Research (FEERv1.0-G1.2), include adjustments to FRP to fill in cloud gaps. QFEDv2.5r1 and FEERv1.0-G1.2 also scale aerosol emissions to aerosol optical depth (AOD) by land cover — QFED globally and FEER by region (Darmenov & da Silva, 2013; Ichoku & Ellison, 2014). Carter et al. (2020) adjusted QFED aerosol emissions using a scaling factor of 0.69 to account for differences in model treatment of aerosols. In addition, the high AOD scaling factor over north India compared to

other regions may explain the high bias of FEER emissions for the study region.

B.4.3 Uncertainties in burned area, fuel consumption, and emissions factors

Table B.11: Different fuel consumption (FC) assumptions for Punjab, India from 2003-2016.

Source	FC (g m^{-2}, $\pm 1\sigma$)	Linear Trend	
		trend and SE (g m^{-2} yr^{-1})	total change (% 14-yr^{-1})
GFEDv4s	289 (33)	-6.9* (1.1)	-27%
FINNv1.5	1093 (83)	-14.5* (3.9)	-16%
Indiastat	*min*: 370 (10) *max:* 510 (14)	*min*: 0.7 (0.7) *max*: 1 (0.9)	+3%

SE = standard error; *p-value < 0.05

To explore the statistically significant decreases in FINNv1.5 and GFEDv4s fuel consumption (Table B.11), we consider additional datasets. We use the 250-m MODIS/Terra Vegetation Continuous Fields (VCF) product (MOD44B C6), which subdivides pixels into tree cover, non-tree-cover vegetated, and non-vegetated by percent area on a yearly basis.

Table B.12: Range of emissions factors (g kg^{-1} DM) used for agricultural waste burning in global fire emissions inventories. Percentages denote the relative difference between emissions factors used by each inventory and those suggested by Andreae (2019).

Species	Andreae (2019)	GFEDv4s[1]	FINNv1.0[2]	GFASv1.0[3]	QFEDv2.4[4]
OC	4.9	2.3 (-53%)	3.3 (-33%)	4.2 (-14%)	3.4 (-31%)
BC	0.42	0.75 (+79%)	0.69 (+64%)	0.42 (–)	0.48 (+14%)
CO	76	102 (+34%)	111 (+46%)	92 (+21%)	65 (-14%)
CO_2	1430	1585 (+11%)	1537 (+7%)	1308 (-14%)	1613 (+13%)

[1] van der Werf et al. (2017); Akagi et al. (2011)
[2] Wiedinmyer et al. (2011); Akagi et al. (2011); Andreae & Merlet (2001)
[3] Kaiser et al. (2012); Andreae & Merlet (2001)
[4] Darmenov & da Silva (2013); Andreae & Merlet (2001); emissions factors are for savanna/grassland fires, since QFED does not delineate agricultural areas in its land use and land cover classification

Table B.13: Uncertainties in bottom-up and top-down emissions inventories and range of average post-monsoon fire emissions in Punjab, India, compared to this study, from 2003-2016. Percentages denote the contribution of each variable (burned area, fuel consumption, and emissions factor) to the uncertainty in emissions for each species.

Species	Burned Area[1]		Fuel Consumption[2]		Emission Factors[3]		Emissions Range	Emissions (*this study*)
	km^2	%	$g\ m^{-2}$	%	$g\ kg^{-1}$ DM	%	$Gg\ yr^{-1}$	
OC	7206-16060	24	289-1093	54	2.3-4.9	22	5-86	43
BC		26		58	0.42-0.75	16	1-13	4
CO		26		59	65-111	15	135-1948	547
CO_2		29		66	1308-1613	5	2721-28310	10295

[1] from GFEDv4s, FINNv1.5, and ModL2T

[2] from GFEDv4s, FINNv1.5, and Indiastat; weighted average by year using burned area

[3] from GFEDv4s, FINNv1.0, GFASv1.0, QFEDv2.4 (savanna/grassland), and Andreae (2019); see Table B.10

B.5 Delays in post-monsoon fire activity in Punjab, India

Recent delays in the post-monsoon burning season — more than a 2-week shift in peak burning from 2003-2016 — indicate later rice harvests, which may lead to later winter crop sowing and increased risk of wheat senescence from springtime heat (Balwinder-Singh et al., 2019; Liu et al., 2021a; Lobell et al., 2012).

Here we revisit the findings of Liu et al. (2021a) by recalculating the temporal shifts in crop residue burning with adjusted FRP. We apply sigmoid-fitting on the daily timeseries of adjusted FRP and estimate that the timing of peak post-monsoon burning has shifted by 1.07 days yr^{-1}, or 17 days in total from 2003-2018. Use of the adjusted FRP amplifies the magnitude of the delay by 1-5 days compared to Liu et al. (2021a) at the start, midpoint, and peak of the post-monsoon burning season (Table B.14, Figure B.10). These delays likely reflect the implementation of a statewide groundwater policy as well as variability in the summer monsoon onset (Balwinder-Singh et al., 2019; Liu et al., 2021a, 2019). In order to counter severe groundwater depletion (Asoka et al., 2017; Rodell et al., 2018), the Preservation of Sub-Soil Water Act of 2009 (ordinance in 2008) delayed the earliest date by which farmers can sow rice, a water-intensive crop (Tripathi et al., 2016), which in turn has likely delayed rice harvests Liu et al. (2021a).

Another method we use to estimate the midpoint date of each burning season, $k_{midpoint}(FRP)$, is to weight each day of the burning season, from 1 to n total days, by the corresponding daily sum of Terra and Aqua MODIS FRP and take the average across all days. The timing of the start and end date of burning for that season, $k_{start}(FRP)$ and $k_{end}(FRP)$, can be approximated as $k_{midpoint}(FRP) \pm 1.25\sigma$, where σ, also weighted by daily FRP, is one standard deviation (Table B.14). The value of $k_{midpoint}(FRP) \pm 1.25\sigma$ is approximately equivalent to $k_{\beta=0.1}(FRP)$ and $k_{\beta=0.9}(FRP)$ for Gaussian distributions.

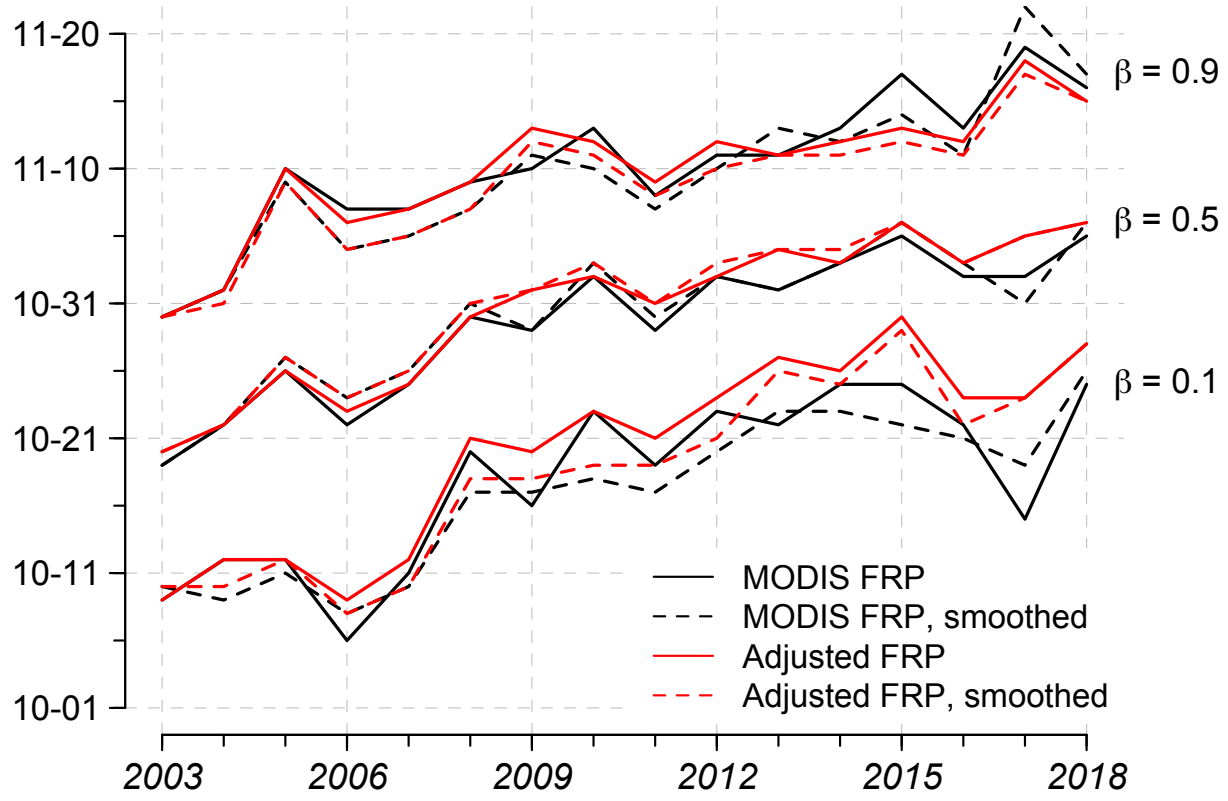


Figure B.10: Delays in the post-monsoon burning season in Punjab, India from 2003-2018: the timing of the start (β = 0.1), midpoint (β = 0.5), and end (β = 0.9) of the burning season is shown for MODIS FRP and adjusted FRP (this study) for unsmoothed and sigmoid-smoothed timeseries.

Table B.14: Temporal shifts (days yr^{-1}) in the post-monsoon burning season in Punjab, India from 2003-2018. The standard error of the slope is shown in parentheses. The table demonstrates that the magnitude of the temporal shift in start, midpoint, and peak of burning in this region is amplified when using the adjusted FRP, regardless of the method of calculation.

	MODIS FRP		**Adjusted FRP**	
	Sigmoid-smoothed	*No smoothing*	*Sigmoid-smoothed*	*No smoothing*
Partial sums				
$k_{\beta=0.1}(FRP)$, *start*	1.01 (0.23)	1.08 (0.14)	1.32 (0.18)	1.33 (0.16)
$k_{\beta=0.5}(FRP)$, *midpoint*	1 (0.12)	0.96 (0.14)	1.09 (0.11)	1.05 (0.12)
$k_{\beta=0.9}(FRP)$, *end*	0.97 (0.14)	1.07 (0.15)	0.85 (0.15)	0.93 (0.14)
Weighted mean				
$k_{\beta=0.1}(FRP)$, *start*	1.05 (0.23)	1.04 (0.17)	1.37 (0.18)	1.28 (0.14)
$k_{\beta=0.5}(FRP)$, *midpoint*	1 (0.12)	1.03 (0.11)	1.09 (0.11)	1.09 (0.11)
$k_{\beta=0.9}(FRP)$, *end*	0.96 (0.14)	0.99 (0.12)	0.84 (0.15)	0.94 (0.12)
Gaussian fit				
$k_{peak}(FRP)$	0.89 (0.19)		1.07 (0.14)	

C

Supplemental Material for Chapter 3

C.1 Satellite-observed temporal shifts in crop phenology and fire activity

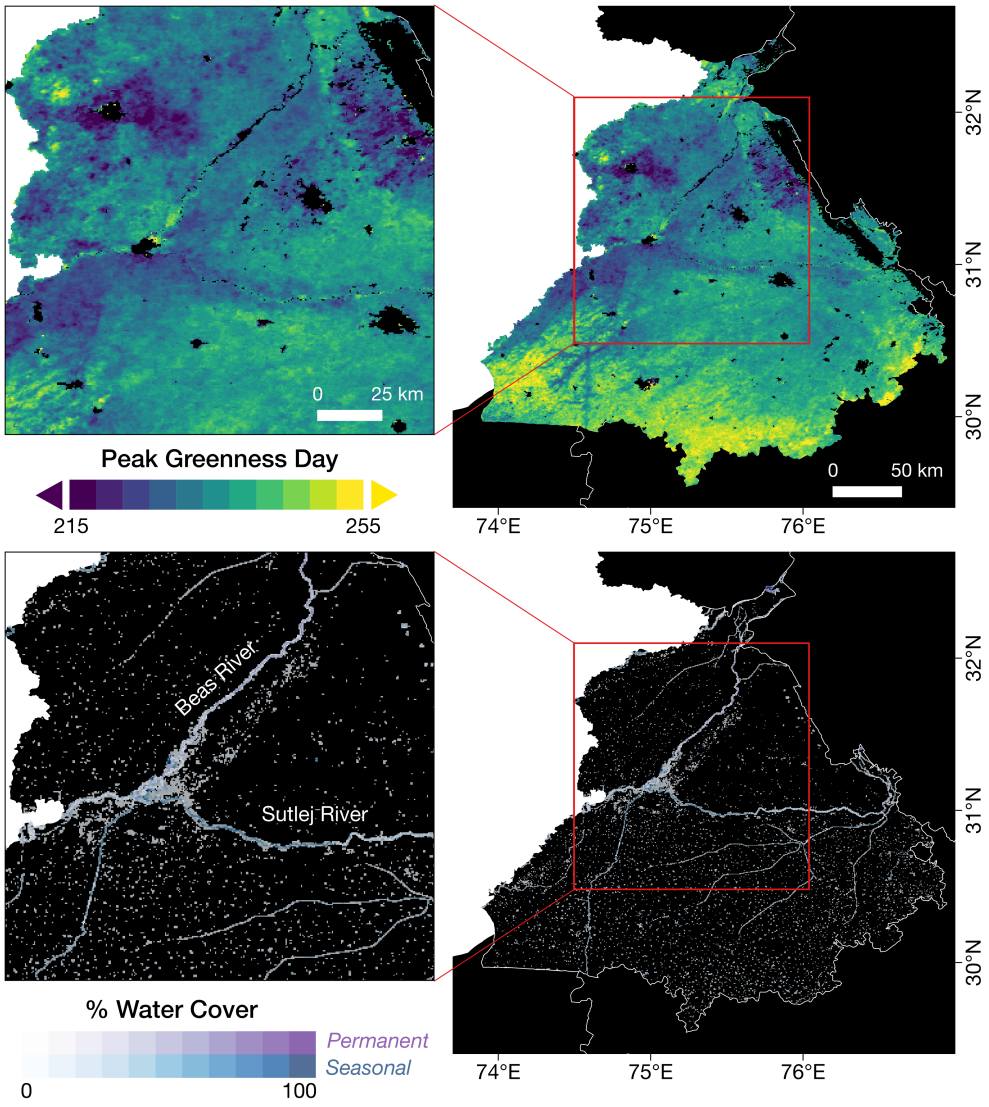


Figure C.1: Spatial variability in monsoon crop phenology in Punjab during the 2003-2007 period: (Top panel) Day of the year of peak monsoon greenness derived from MODIS MCD12Q2, averaged across 2003-2007. (Bottom panel) Location of seasonal (blue shades) and permanent (purple shades) water cover derived from the Copernicus Dynamic Global Land Cover (CGLS-LC100) from 2015-2019. Areas with greatest water coverage (i.e., darkest shades) are located near the intersection of the Beas and Sutlej Rivers. Most of the water cover pixels are classified as seasonal. The CGLS land cover is upsampled to 500 m for visibility.

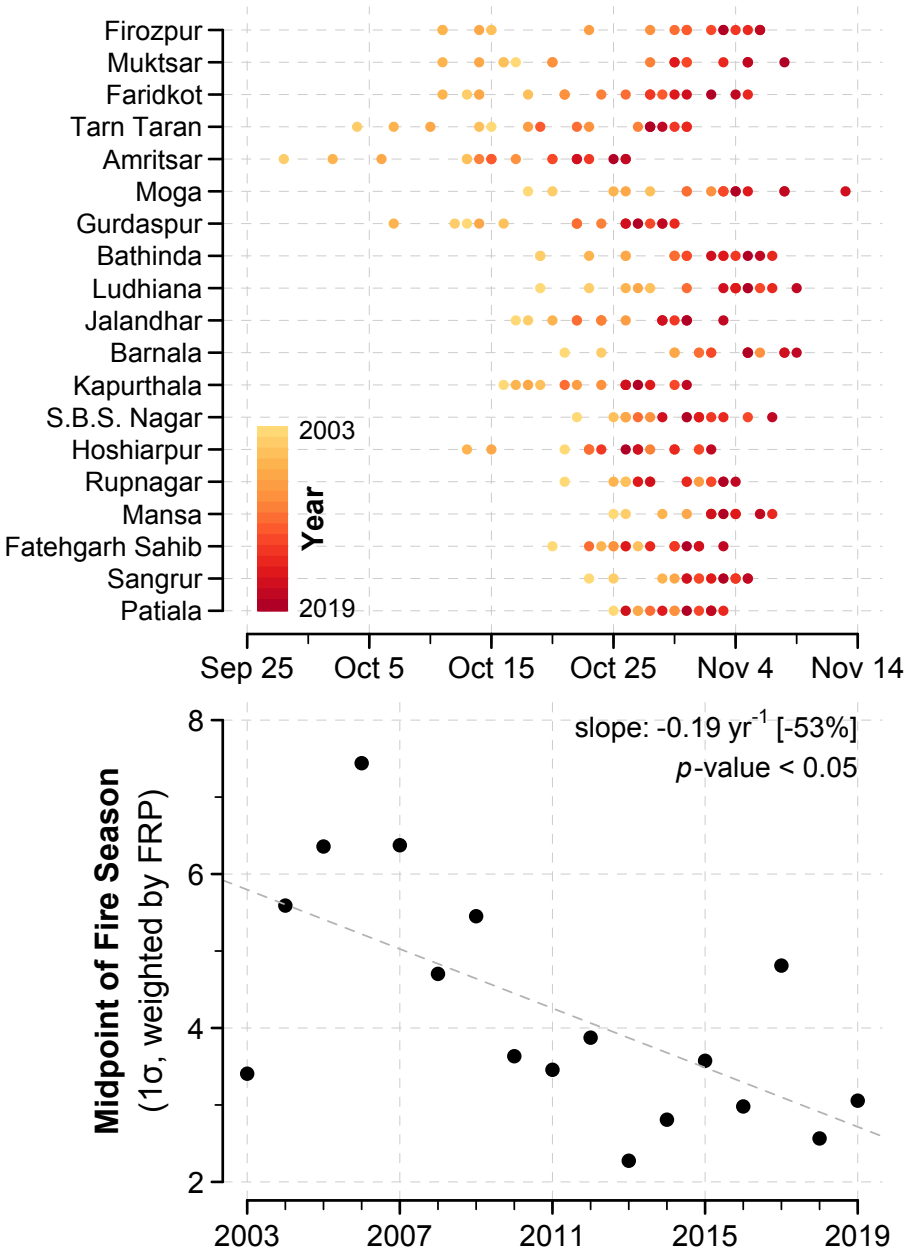


Figure C.2: Spatial variability in the midpoint of the post-monsoon fire season among Punjab districts from 2003-2019: (Top panel) The midpoint of post-monsoon fire seasons in 19 districts (same as in Figure 3.1) in Punjab from 2003-2019, colored by year. The districts shown are ordered by the magnitude of the temporal shift, from highest to lowest. (Bottom panel) The standard deviation of the spatial distribution of district-level post-monsoon fire season midpoint dates, weighted by the overall FRP of each district, from 2003-2019. The slope and p-value of the linear trend are shown inset.

Groundwater levels. In addition to groundwater data from India-WRIS and Dacnet, we use household survey data from the 2017-18 crop season to estimate the usage of canal irrigation in three regions in Punjab: Amritsar (north), Sangrur (southeast), and Bathinda/Muktsar (southwest) districts. 573 households in Punjab are represented in the subset of the household survey we used in this study. Methodology for the household survey is described in Liu et al. (2021a).

C.1.1 Spatial heterogeneity in groundwater usage and trends in context of temporal shifts in the monsoon growing season and post-monsoon fires

Visual inspection of the spatial heterogeneity in peak monsoon greenness at the native MODIS spatial resolution (500 m) reveals that regions with initially early monsoon crop cycles (i.e., in northern and western Punjab), as well as the greatest cascading delays, are near major rivers integral to canal irrigation (Figure C.1). Remote sensing and ground measurements suggest that these districts are less affected by groundwater depletion (Asoka et al., 2017). Annual maps of the pre-monsoon depth to water level by India's Central Groundwater Board, based on interpolated well data, show shallower depths in western Punjab (< 20 m) than eastern Punjab (20-40 m) (`https://indiawris.gov.in/wris/#/gwyearbook`), suggesting more abundant water resources in the west.

Household survey data of irrigation practices collected in 2018 in three Punjab regions (Amritsar, Bathinda/Muktsar, and Sangrur districts) show similar spatial variation (Figure C.3). While access to tubewells is nearly universal, canal irrigation is high in southwestern Punjab (Bathinda/Muktsar: 88%) but low in southeastern and northern Punjab (Sangrur: 34%, Amritsar: 11%) (Table C.1). Recent structural collapses in the canal networks in districts such as Amritsar may increase groundwater dependence further (The Tribune India, 2019). Although paddy growing depends on groundwater rather than canal irrigation, the latter's availability may have alleviated the water table decline. Aside from differences in irrigation, crop varieties may also contribute to spatial variation in peak monsoon greenness, which is tied to the duration of the growing season (Figure C.4). Compared to eastern and central Punjab, farmers in western Punjab tend to plant crops earlier in the season (Figure C.1) and favor varieties with shorter growing periods (Figure C.4). While western Punjab experienced the greatest delays, farmers there use shorter duration crop varieties, which produce less residue and require less irrigation and may help to reduce fire emissions and offset groundwater use (Dhillon & Kumar, 2021; Mahajan et al., 2009).

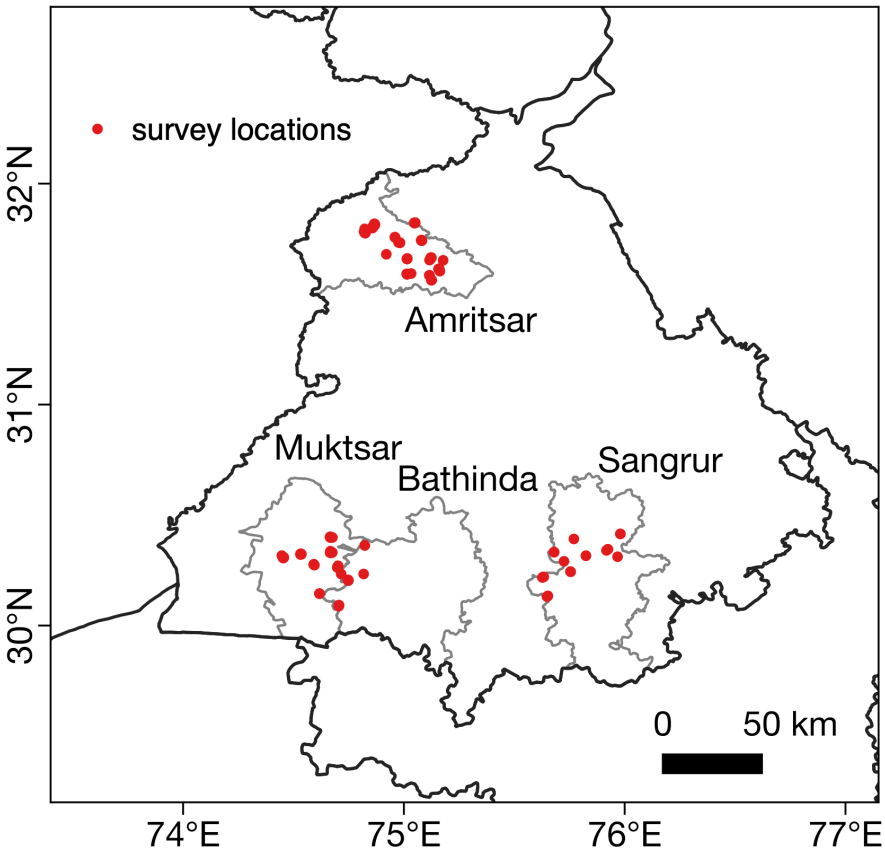


Figure C.3: Household survey locations in Punjab: Red dots correspond to household survey locations in Punjab, mainly within the Amritsar, Muktsar, Bathinda, and Sangrur districts.

Table C.1: Irrigation practices in Punjab, India by district from household survey data.

	Irrigation	Amritsar	Muktsar/ Bathinda	Sangrur
Household survey, 2018	Canal	11%	88%	34%
	Groundwater			
	tubewell, owned	78%	85%	82%
	tubewell, shared	19%	7%	18%
	tubewell, rented	6%	9%	2%

Amritsar (n=186), Muktsar/Bathinda (n=196), Sangrur (n=191)

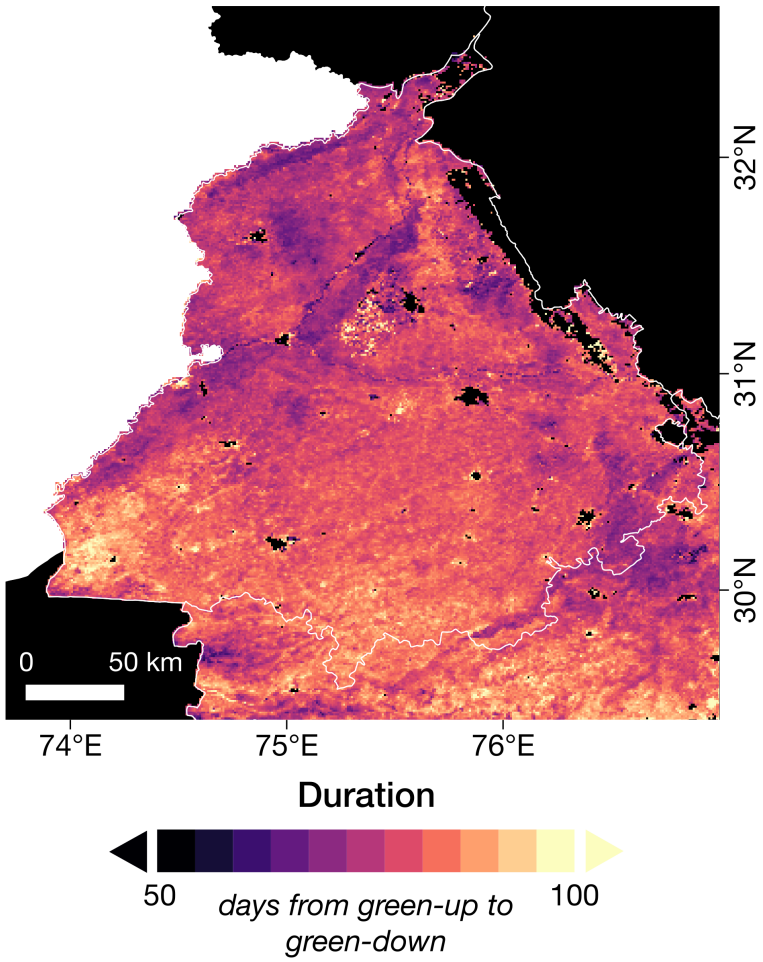


Figure C.4: Duration from green-up to green-down during the monsoon growing season in northwest India: average number of days between green-up and green-down from 2003-2019 derived from the MCD12Q2 phenology dataset.

C.2 Atmospheric Transport Modeling of Smoke $PM_{2.5}$

C.2.1 STILT modeling

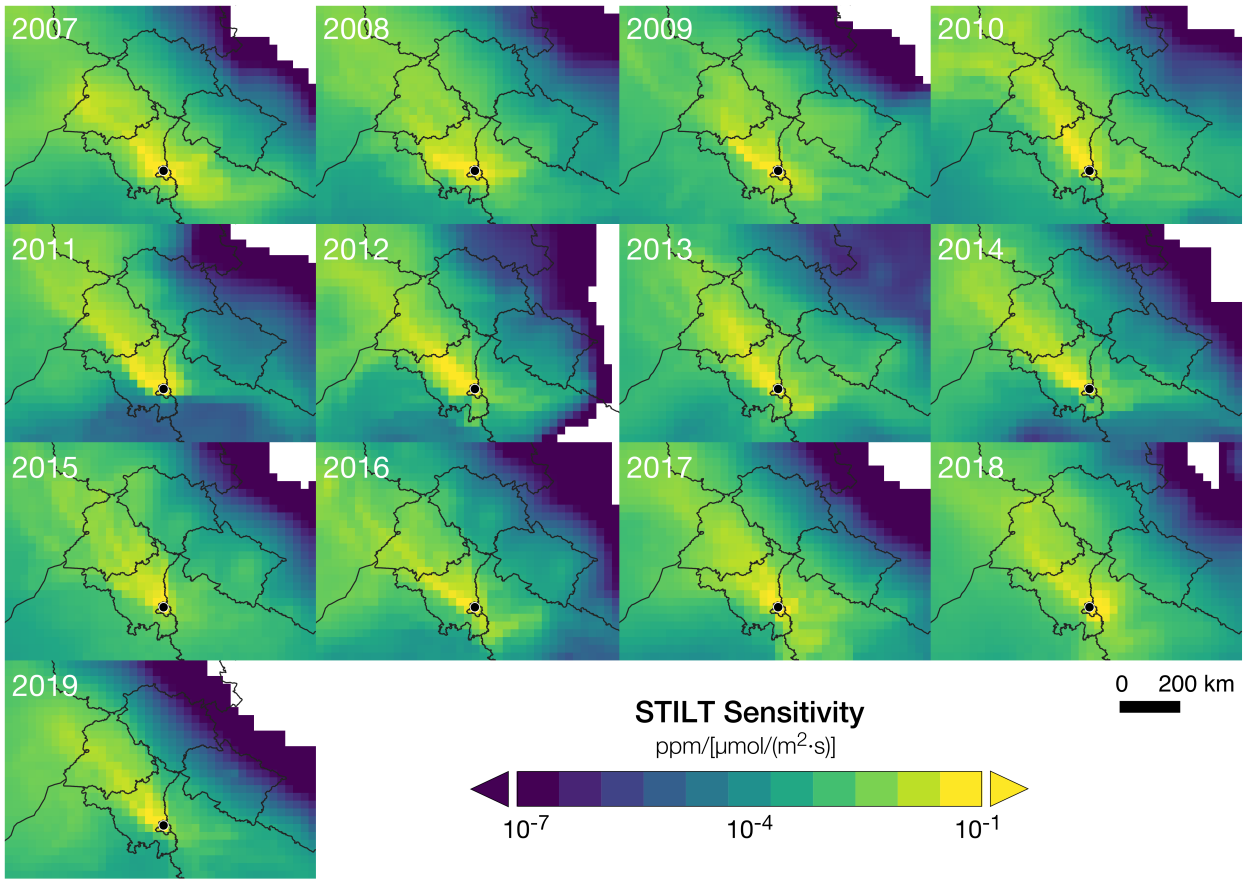


Figure C.5: Annual variation in STILT sensitivities from 2007-2019 with New Delhi as the receptor: STILT sensitivity maps are averaged using the daily smoke $PM_{2.5}$ at New Delhi as weights. To calculate the $PM_{2.5}$ weights, STILT sensitivities of a given meteorological year are applied to each year's post-monsoon fire emissions from 2008-2019. The $PM_{2.5}$ is then averaged by day across the fire emissions years to standardize the fire season, account for the delay and increase in fires during this period, and focus the year-to-year comparison of the STILT sensitivities on meteorological patterns.

C.2.2 Background $PM_{2.5}$

We use $PM_{2.5}$ observed at the U.S. Embassy in New Delhi from 2013-2019 to quantify the increase in background $PM_{2.5}$ from October to December. For each year, we use quantile regression to fit a linear trend to the timeseries of daily average $PM_{2.5}$ at the 20th percentile, which results in a fitted line apparently consistent with observations dominated by background $PM_{2.5}$ and not strongly influenced by outliers or by $PM_{2.5}$ spikes associ-

ated with crop residue burning. We extend the $PM_{2.5}$ timeseries from October to December to prevent inflation of the estimated trend in background $PM_{2.5}$ due to high $PM_{2.5}$ days during November.

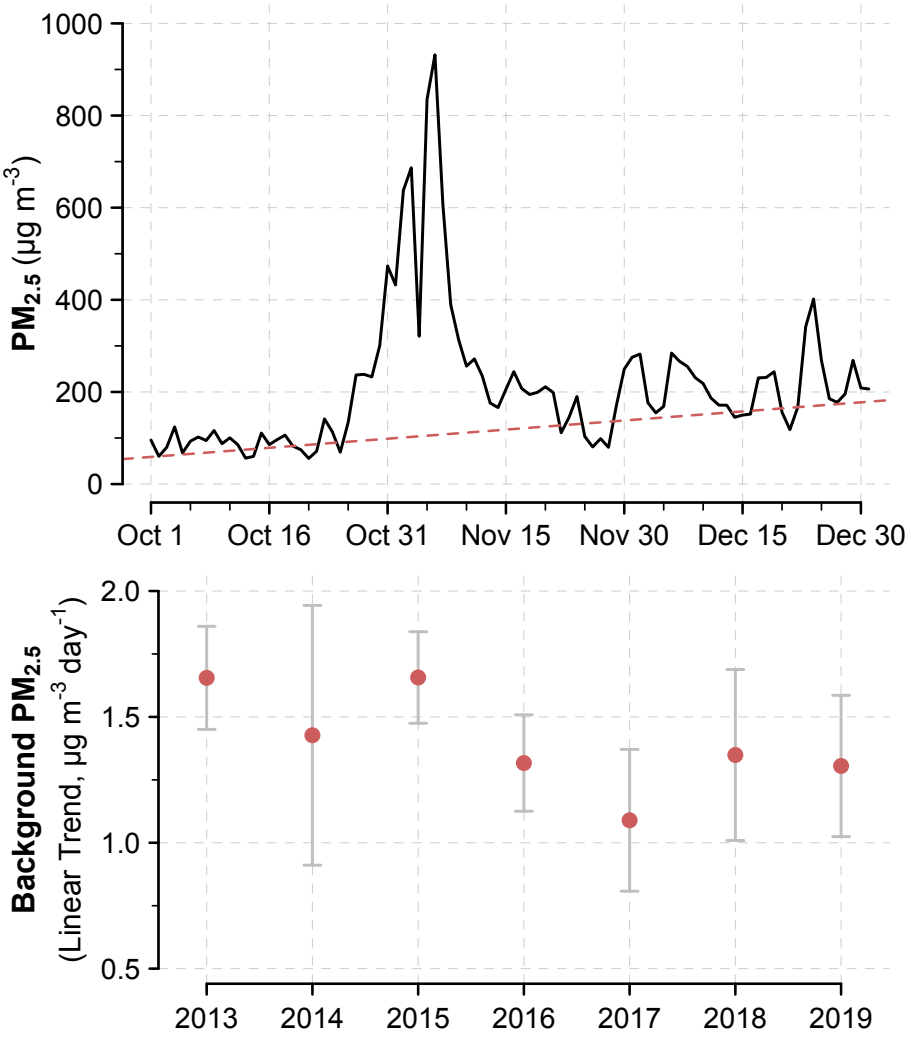


Figure C.6: Increase in daily background $PM_{2.5}$ in New Delhi from post-monsoon to winter, 2013-2019: (Top panel) Example timeseries of daily average $PM_{2.5}$ (black line) observed at the U.S. Embassy in New Delhi from Oct 1 to Dec 30, 2016. The linear increase in background $PM_{2.5}$ (red dashed line) is estimated using quantile regression at the 20th percentile. (Bottom panel) The slope ± 1 standard error of the linear trend in background $PM_{2.5}$ from 2013-2019.

GEOS-Chem chemical transport model (CTM). We use the GEOS-Chem CTM, version 12.8.2 (https://zenodo.org/record/3860693), to simulate daily background $PM_{2.5}$ concentrations for a 3-year period from 2015-2017 (Bey et al., 2001). We use the global 2° x 2.5° full chemistry simulation with a 6-month spin-up to generate boundary conditions for the nested grid simulation (0.5° x 0.625°) of the Asia domain, both driven by MERRA2 reanalysis meteorology (Wang et al., 2004). Anthropogenic emissions are from the MIX inventory for Asia (Li et al., 2017b). Fire emissions are from a combined GFEDv4s and SAGE-IGP dataset, with SAGE-IGP

replacing GFEDv4s agricultural fire emissions over north India.

We use the GEOS-Chem simulated background $PM_{2.5}$ to calculate how much smoke $PM_{2.5}$ contributes to the total $PM_{2.5}$ at each receptor (Table C.2). STILT and GEOS-Chem smoke $PM_{2.5}$ concentrations are consistent for New Delhi, Kanpur, and Bathinda, whereas GEOS-Chem tends to overestimate smoke $PM_{2.5}$ in Lahore, Ludhiana, and Jind relative to STILT. Discrepancies between the models may arise due to differences in spatial resolution and input meteorology. In GEOS-Chem, emissions inventories are first upscaled to the nested grid resolution (0.5° x 0.625°), while in STILT, we generate sensitivity footprints at the native resolution of the SAGE-IGP inventory (0.25° x 0.25°).

In addition, we find that GEOS-Chem is unable to capture the increase in observed background $PM_{2.5}$ as seen by its > 50% underestimate in December compared to October, two months with much less influence from biomass burning than from anthropogenic sources (Figure C.7). Such biases in anthropogenic emissions inventories or incomplete chemical mechanisms in the model may in turn lead to underestimates in total $PM_{2.5}$ and highly polluted days in November.

Table C.2: Background and smoke $PM_{2.5}$ ($\mu g\ m^{-3}$) in the six receptor cities from 2015-2017. The $PM_{2.5}$ concentrations shown are the maximum of 21-day rolling means from October to November. Ranges within the parentheses refer to the minimum and maximum from 2015-2017. Smoke $PM_{2.5}$ is simulated using STILT and GEOS-Chem, while background $PM_{2.5}$ is simulated only in GEOS-Chem. Here, smoke $PM_{2.5}$ is defined as the sum of primary OC and BC emitted by fires, or 2.1 × OC + BC, to make the STILT and GEOS-Chem estimates consistent. The 2.1 factor converts OC to organic matter, as suggested in Turpin & Lim (2001).

Receptor	**Background $PM_{2.5}$** (GEOS-Chem, no fire simulation)	**STILT**		**GEOS-Chem**	
		Smoke $PM_{2.5}$	%	Smoke $PM_{2.5}$	%
New Delhi	133 (110-173)	32 (27-37)	20 (14-24)	35 (31-40)	21 (18-22)
Kanpur	116 (95-149)	13 (9-20)	10 (6-16)	16 (9-20)	11 (7-15)
Lahore	119 (91-151)	28 (26-30)	20 (15-25)	66 (44-100)	35 (26-47)
Ludhiana	134 (107-166)	39 (18-57)	23 (10-35)	179 (91-235)	55 (35-66)
Bathinda	105 (82-145)	158 (145-179)	61 (51-67)	209 (148-244)	66 (63-73)
Jind	115 (93-152)	64 (50-78)	36 (25-44)	143 (112-176)	56 (42-63)

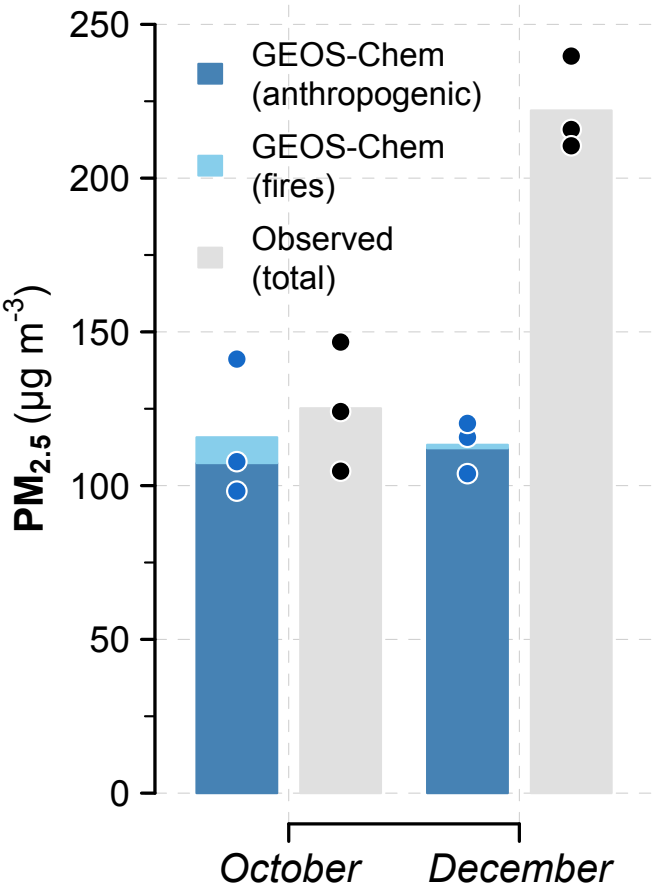


Figure C.7: Observed and modeled $PM_{2.5}$ in New Delhi in October and December from 2015-2017: Monthly average $PM_{2.5}$ from observations (gray) and GEOS-Chem nested grid model simulations partitioned into anthropogenic (dark blue) and biomass burning (light blue) sources. Dots represent monthly averages of total $PM_{2.5}$ in individual years.

D

Supplemental Material for Chapter 4

D.1 Inventory-specific relative fire confidence scores

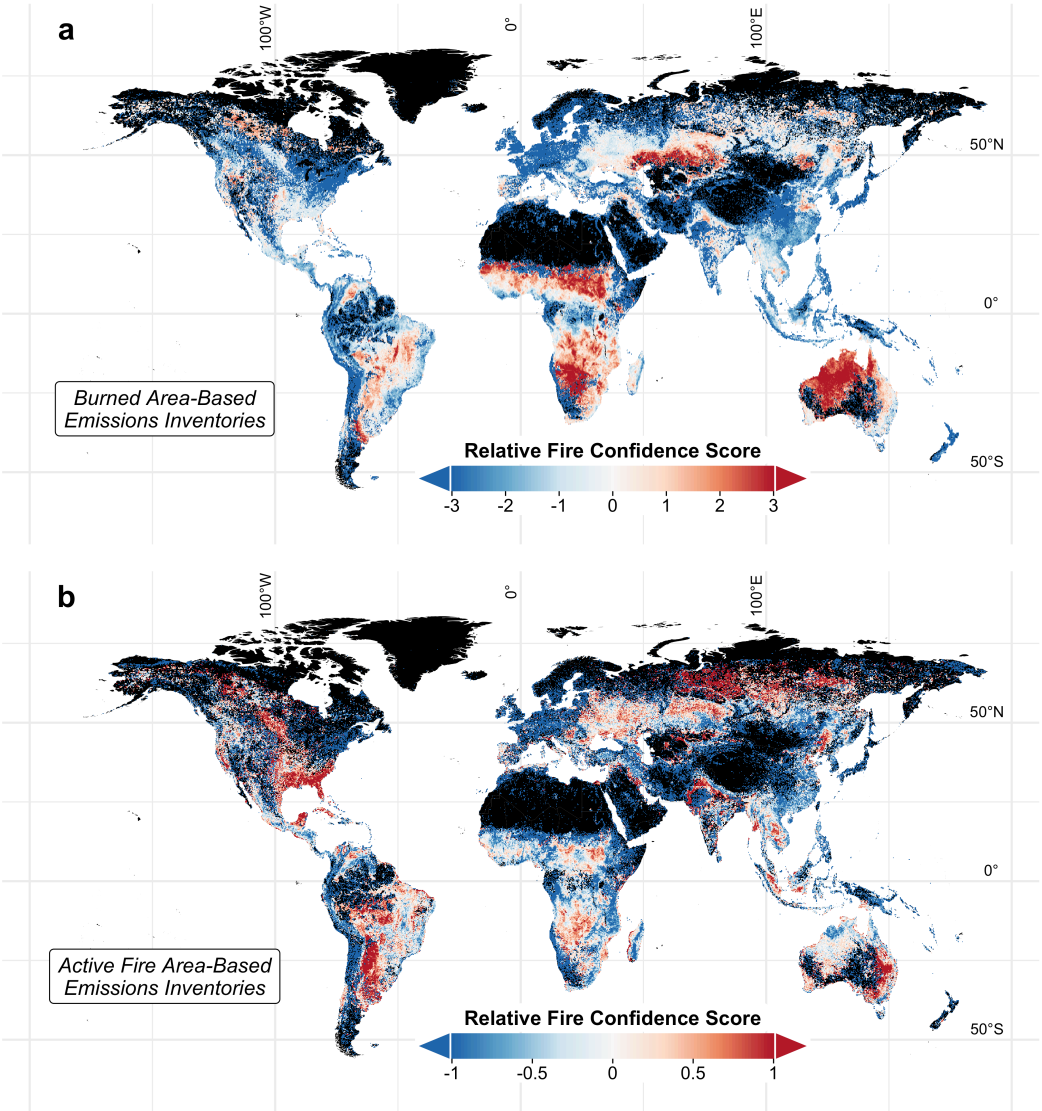


Figure D.1: Relative fire confidence score for bottom-up emissions inventories based primarily on (a) MODIS MCD64A1 burned area (BA-score; e.g. GFEDv4s) and (b) MODIS MxD14A1 active fire pixel area (AFA-score; e.g. FINN). The darkest blue pixels represent grid cells with (a) active fire observations but no burned area over 2003-2017 or (b) burned area but no active fire observations over this time frame. Thus, these grid cells indicate low confidence for (a) burned area inventories or (b) active fire pixel inventories.

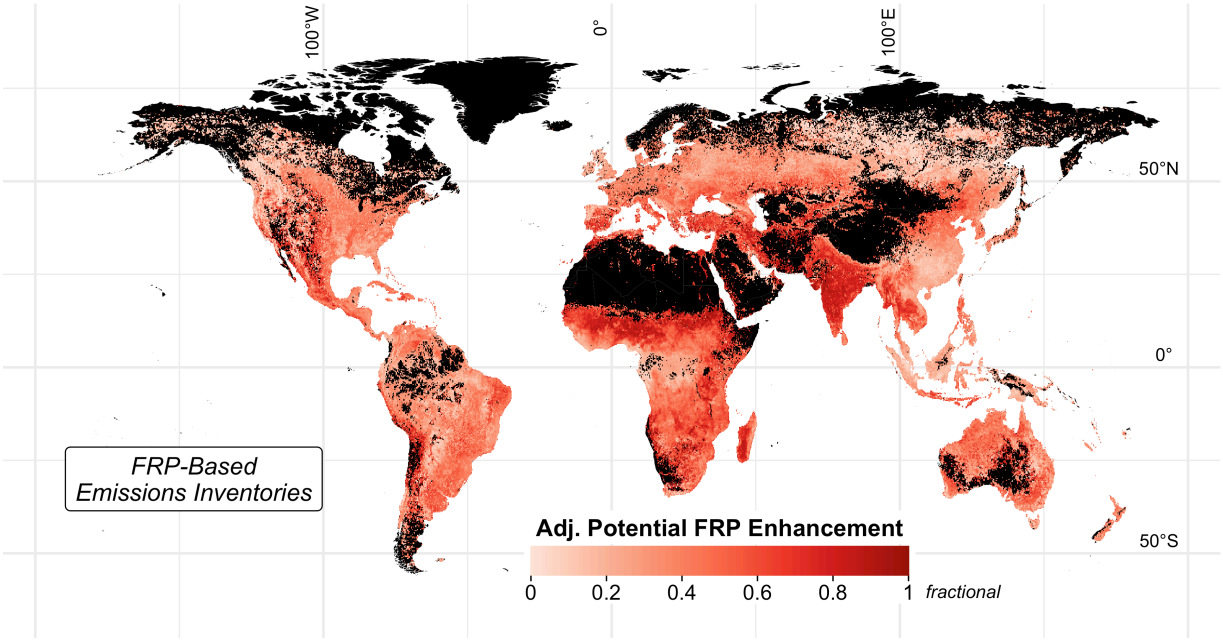


Figure D.2: Adjusted potential FRP enhancement (pFRP), expressed as fractional fire energy, for top-down FRP-based emissions inventories. The potential FRP enhancement diagnoses additional fire energy, unaccounted for by the MODIS active fires product but indicated by large burn scars from the MODIS burned area product or very small fires from the 375-m VIIRS active fires product. It is the sum of fractional MODIS/Terra + Aqua MxD14A1 FRP outside MCD64A1 burned area and fractional VIIRS FRP outside the MODIS burn extent, then adjusted by the FRP-weighted cloud/haze obscuration fraction. High pFRP is associated with lower confidence, as many MODIS active fire observations are not co-located with MODIS burned area or VIIRS FRP observations.

D.2 Global fire emissions inventories: "bottom-up" and "top-down" methods

D.2.1 Bottom-up emissions inventories: GFED and FINN

Bottom-up emission inventories (e.g. GFED and FINN) multiply burned area, fuel load, combustion completeness, and emissions factors to estimate fire emissions:

$$E_i = BA \times f_b \times \gamma \times EF_i \tag{D.1}$$

where E_i is emissions of species i, BA is burned area, f_b is the fraction of biomass burned or fuel load, γ is combustion completeness, and EF_i is the emissions factor of species i (van der Werf et al., 2017; Wiedinmyer et al., 2011). GFEDv4s relies on 500-m burned area observations with a "small fires boost" (SFB) from active fire geolocations to estimate monthly emissions (van der Werf et al., 2017). FINN uses daily 1-km active fire area as "burned area" (Wiedinmyer et al., 2011).

GFEDv4s is available at 0.25° x 0.25° spatial resolution and monthly timesteps with daily fraction based on active fire counts and burned area (Mu et al., 2011). This inventory uses active fire detections from Tropical Rainfall Measuring Mission (TRMM) Visible and Infrared Scanner (VIRS) and Along Track Scanning Radiometer (ASTR) to estimate monthly emissions for the pre-MODIS era (from 1997-2000). GFEDv4s also projects fire emissions (2017-2018) based on the observed relationships between historical GFEDv4s emissions and MODIS active fires. For the small fires boost, GFEDv4s uses MCD14ML C6 active fire geolocations (Randerson et al., 2012), but for burned area, the inventory currently relies on MCD64A1 C5.1, rather than C6 (Giglio et al., 2013). GFED uses the Carnegie Ames Stanford Approach (CASA) biogeochemical model to estimate fire carbon and dry matter (DM) emissions using burned area, meteorology, net primary production, and land cover as input variables (van der Werf et al., 2010).

FINNv1.5 is available at the native MODIS 1-km spatial resolution from 2002 and available at near real time. FINNv1.5 derives active fire area from MCD14DL C5 (C6 from 2017-present) active fire geolocations, which is the near-real-time equivalent of MCD14ML. FINN assumes an upper-bound estimate of burned area (1 km^2) for each fire detection for most fires except for grassland or savanna fires, which are assigned a burned area of 0.75 km^2 (Wiedinmyer et al., 2011). FINN assigns fuel loadings by region and land cover, based on Hoelzemann et al. (2004). A newer version of this inventory, FINNv1.6 is no longer available as of April 2018 due to dataset issues

and has been reverted back to FINNv1.5 (http://bai.acom.ucar.edu/Data/fire/).

For land cover, GFEDv4s and FINNv1.5 use the 500-m MCD12Q1 C5.1 land cover product. Neither GFEDv4s nor FINNv1.5 has updated the respective LULC maps from C5.1 to C6. GFEDv4s separately incorporates peat maps (Olson et al., 2001) and emissions factors (Christian et al., 2003). FINNv1.5 subdivides the broader savanna, grassland, and shrubland class into savanna/grassland and woody savanna/shrubland subclasses and further delineates a temperate evergreen forest subclass from the broader temperate forest class.

D.2.2 Top-down emissions inventories: GFAS, QFED, and FEER

Top-down emissions inventories (e.g. GFAS, QFED, and FEER) integrate daily FRP to fire radiative energy (FRE) and scale this quantity linearly to obtain fire emissions:

$$FRE = \int_{t_1}^{t_2} FRP(t)dt \tag{D.2}$$

$$E_i = FRE \times \beta \times EF_i \text{ OR} \tag{D.3}$$

$$E = FRE \times C_e \tag{D.4}$$

where FRE is the integral of FRP from time t_1 to t_2, β is a coefficient converting FRP to dry matter, and C_e is the coefficient of emissions that is equivalent to the product of β and EF_i for total particulate matter (TPM) in Equation D.2 (Darmenov & da Silva, 2013; Ichoku & Ellison, 2014; Kaiser et al., 2012). Equation D.3 applies to GFAS and QFED, while Equation D.4 applies to FEER. In some inventories, such as GFAS, the coefficient β varies with class of LULC. The FRP-based inventories also statistically adjust FRP for spatial and temporal gaps in the observations due to cloud cover (Kaiser et al., 2012), but by assuming that fire persists through cloudy days, such adjustments may result in unrealistic emissions (Di Giuseppe et al., 2017). GFAS and QFED directly use MxD14 FRP, while FEER relies on the GFAS FRP after adjustment for cloud gaps.

To convert FRP to DM burned, GFASv1.2 uses conversion factors derived from GFEDv3 DM combustion rates (Kaiser et al., 2012). QFED globally calibrates emissions coefficients with GFEDv2 but further boosts the emissions of aerosols (OC, BC, $PM_{2.5}$). Based on constraints from observed smoke AOD, QFED applies global emission strength factors that range from 1.8-4.5, depending on land cover (Darmenov & da Silva, 2013). Similarly, Kaiser et al. (2012) recommended a global scaling factor of 3.4 for GFAS OC and BC emissions to reconcile with smoke AOD observations. FEER estimates TPM emissions by directly applying smoke AOD-derived emis-

sions coefficients to FRP observations by region and land cover, and then converts TPM to other species using emissions factors (Ichoku & Ellison, 2014).

QFEDv2.5r1, GFASv1.2, and FEERv1.0-G1.2 are available on a daily basis at near real time and 0.1° x 0.1° spatial resolution. GFASv1.2 switched from using C5 to C6 MxD14 FRP after December 2016, but has not retroactively updated emissions from before that; this discrepancy may lead to inconsistencies in the timeseries of GFASv1.2 emissions Giglio et al. (2016). FEERv1.0-G1.2 relies on GFASv1.2 FRP as input. QFEDv2.5r1 uses the MxD14 C6 FRP. For land cover, GFASv1.2 currently considers only the LULC with the highest emissions in each 0.5° x 0.5° grid cell, which it derives from GFED3. Like GFEDv4s, GFASv1.2 separately delineates peatland emissions (Heil et al., 2010). FEER uses a dominant fire-prone LULC map, derived from MODIS, at 1° x 1° spatial resolution. QFEDv2.5r1 uses the simplest LULC classification, without either peatland or agricultural classes; in addition, while QFED separates the grassland and savanna classes, they are treated as the same LULC both in terms of emissions factors and aerosol emissions enhancements.

Table D.1: Emissions factors (g species kg^{-1} dry matter) for CO_2, CO, CH_4, organic carbon (OC), black carbon (BC) and fine particulate matter ($PM_{2.5}$) used in the global fire emissions inventories.

Inventory	Species	Land Use and Land Cover (LULC)					
		SAVA *Savanna, Grassland, Shrubland*	**BORF** *Boreal Forest*	**TEMF** *Temperate Forest*	**DEFO** *Tropical Forest*	**PEAT** *Peatland*	**AGRI** *Agricultural*
GFEDv4s	CO_2	1686	1489	1647	1643	1703	1585
FINNv1.0		1716/1692[a]	1514	1630	1643	—	1537
GFASv1.0		1646	1572[b]		1626	1703	1308
QFEDv2.4		1613	1569[b]		1580	—	—
GFEDv4s	CO	63	127	88	93	210	102
FINNv1.0		68/59[a]	118	102	92	—	111
GFASv1.0		61	106[b]		101	210	92
QFEDv2.4		65	107[b]		104	—	—
GFEDv4s	CH_4	1.94	5.96	3.36	5.07	20.8	5.82
FINNv1.0		2.6/1.5[a]	6	5	5.1	—	6
GFASv1.0		2.2	4.8[b]		6.6	20.8	8.4
QFEDv2.4		2.3	4.7[b]		6.8	—	—
GFEDv4s	OC	2.62	9.6	9.6	4.71	6.02	2.3
FINNv1.0		6.6/2.6[a]	7.8	9.2	4.7	—	3.3
GFASv1.0		3.2	9.1[b]		4.3	6.0	4.2
QFEDv2.4		3.4	8.6-9.7[b]		5.2	—	—
GFEDv4s	BC	0.37	0.5	0.5	0.52	0.04	0.75
FINNv1.0		0.5/0.37[a]	0.2	0.56	0.52	—	0.69
GFASv1.0		0.46	0.56[b]		0.57	0.04	0.42
QFEDv2.4		0.48	0.56[b]		0.66	—	—
GFEDv4s	$PM_{2.5}$	7.17	15.3	12.9	9.1	9.1	6.26
FINNv1.0		15.4/8.3[a]	13	13	9.7	—	5.8
GFASv1.0		4.9	13.8[b]		9.1	9.1	8.3
QFEDv2.4		5.4	13[b]		9.1	—	—

[a] Woody savanna/shrubland and savanna/grassland. [b] Extratropical forest (BORF and TEMF). [c] Peatland and agricultural regions are treated as tropical forest, temperate forest, boreal forest, or savanna/grassland if specific emission factor is not indicated.

D.3 Validation of smoke exposure in Equatorial Asia from Indonesia fires

D.3.1 Singapore

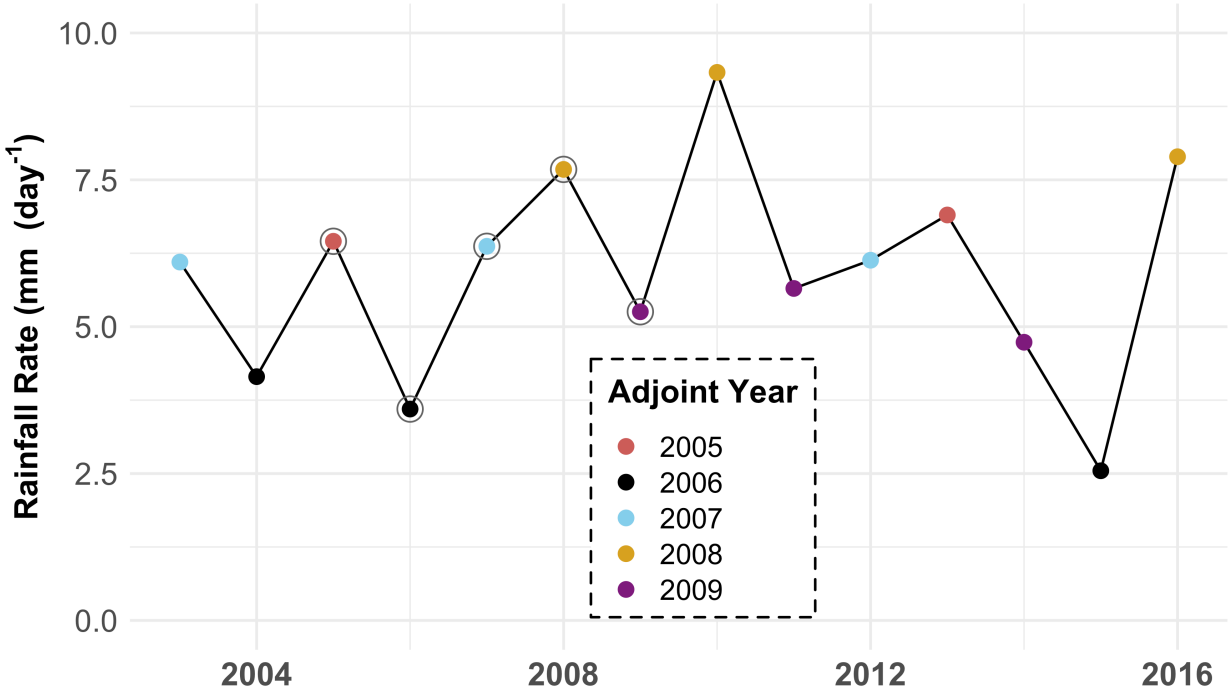


Figure D.3: Average CHIRPS rainfall rate (mm day^{-1}) over Sumatra and Kalimantan, from 2003-2016. The years 2003-2004 and 2010-2016 are colored according to their closest match in the average rainfall rate during years with adjoint sensitivities (2005-2009), which are also colored but circled with dark gray outlines.

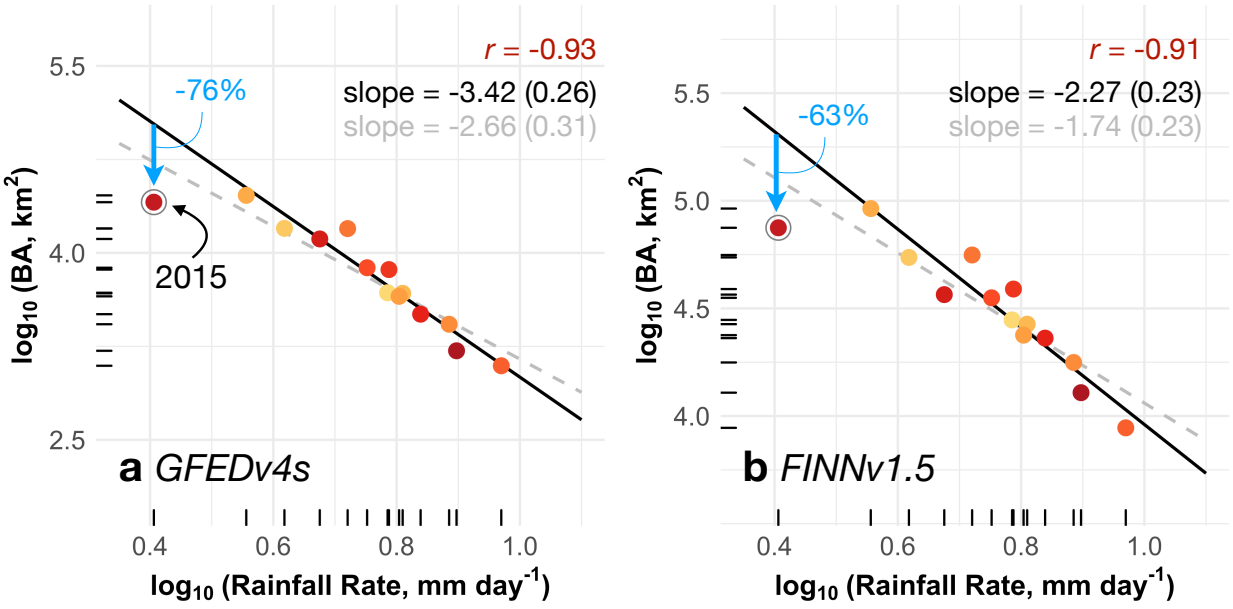


Figure D.4: Under-detection of 2015 Indonesia fires in burned area relative to the 2003-2016 period (similar to Figure 4.9). CHIRPS rainfall rates (mm day^{-1}) are plotted against MODIS (a) GFEDv4s burned area and (b) FINNv1.5 active fire area in log-log space. All variables are averaged temporally over July-October and spatially over Sumatra and Kalimantan, Indonesia. Colors denote different years from 2003-2016, with later years depicted by redder shades; values for 2015 are circled. Inset shows the correlation (r, $p < 0.01$), slope of the linear regression (gray dashed line), and slope with 2015 removed (black line) for each pair of observations. Standard errors for the slopes are shown in parentheses. There is no statistically significant linear trend in any variable. Blue arrows show that observed burned area is lower than expected based on prediction from the linear regression of rainfall and fires that excludes 2015 observations. Percent underestimate of each fire variable based on these predictions is shown in blue.

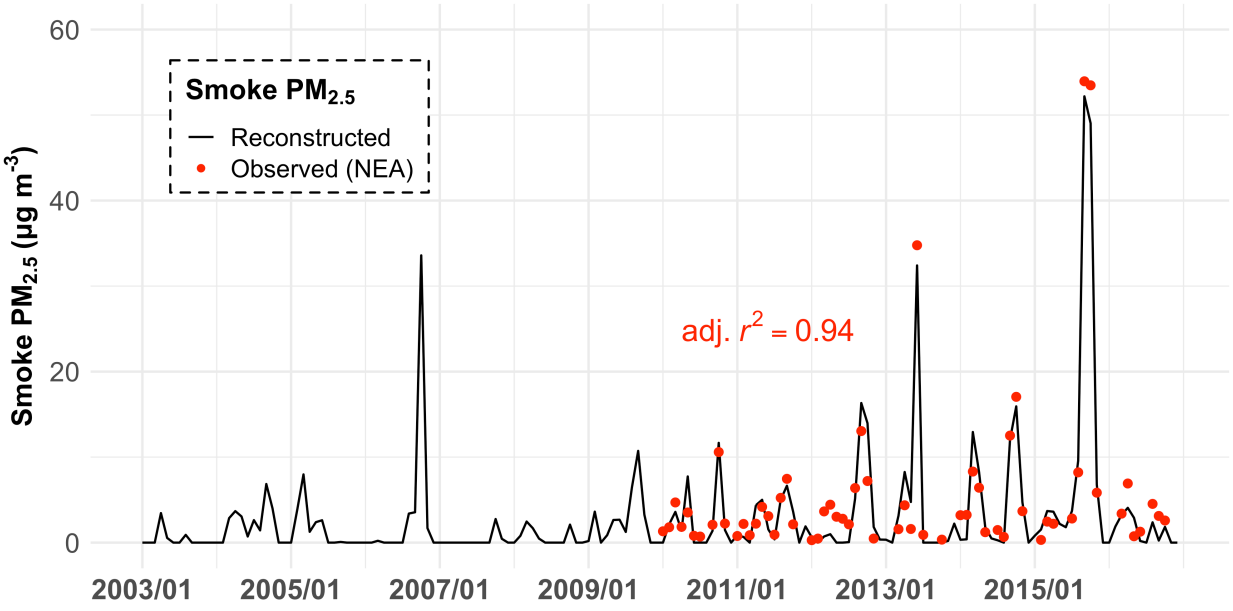


Figure D.5: Observed (red) and reconstructed (black) smoke $PM_{2.5}$ in Singapore for 2003-2016. Observations are from the Singapore NEA. We reconstruct $PM_{2.5}$ over 2003 to 2009 by building a model based on the observed 2010-2016 $PM_{2.5}$ record and four meteorological variables (visibility, air temperature, wind speed, and rainfall) observed at the Singapore Changi Airport. Adjusted R^2 for the model versus observations over 2010-2016 is 0.94. A baseline $PM_{2.5}$ of 13.77 μg m^{-3}, calculated as the median of $PM_{2.5}$ during non-fire season months (January to June, November to December), is subtracted from observations to obtain smoke $PM_{2.5}$.

D.3.2 Malaysia and Indonesia

Malaysia. We use PM_{10} observations across a network of 59 residential and industrial Continuous Air Quality Monitoring (CAQM) stations in Malaysia, maintained by the Malaysian Department of Environment since 1996, to further validate our modeled population-weighted smoke exposure (Figure D.6) (Khan et al., 2015; Kuwata et al., 2018). Two stations, CAE 022 and CAK 029, do not have observations from 2003-2015, so we exclude these stations in our analysis (Table D.2). To weight these observations by population, we use the population density estimates from the Gridded Population of the World, version 4.1, adjusted to the country totals from the United Nations' World Population Prospects country totals (UN WPP-adjusted GPWv4.1), at the native 1 km x 1 km spatial resolution (CIESIN, 2017). We first interpolate the 5-yearly population density linearly to annual values and extract the population density in the grid cell co-located with each station. We subtract the background PM_{10}, here defined as median PM_{10} during non-fire season months, from monthly mean PM_{10} observations at each station, and then take the population-weighted average across all stations, yielding the monthly smoke PM_{10} for the 2003-2015 time period.

Indonesia. Due to the lack of ground observations of $PM_{2.5}$ and PM_{10} in Indonesia, we use monthly satellite-derived AOD, from MODIS/Terra and Aqua MOD/MYD08_M3, from 2003-2016, for validation of Indonesia population-weighted exposure. We use the MxD08_M3 C6 aerosol optical thickness (AOT) at 0.55 μm, available at 1° x 1° spatial resolution and in the GEE data catalog. We subtract monthly AOD, averaged over Indonesia, by mean AOD of non-fire season months to estimate smoke AOD.

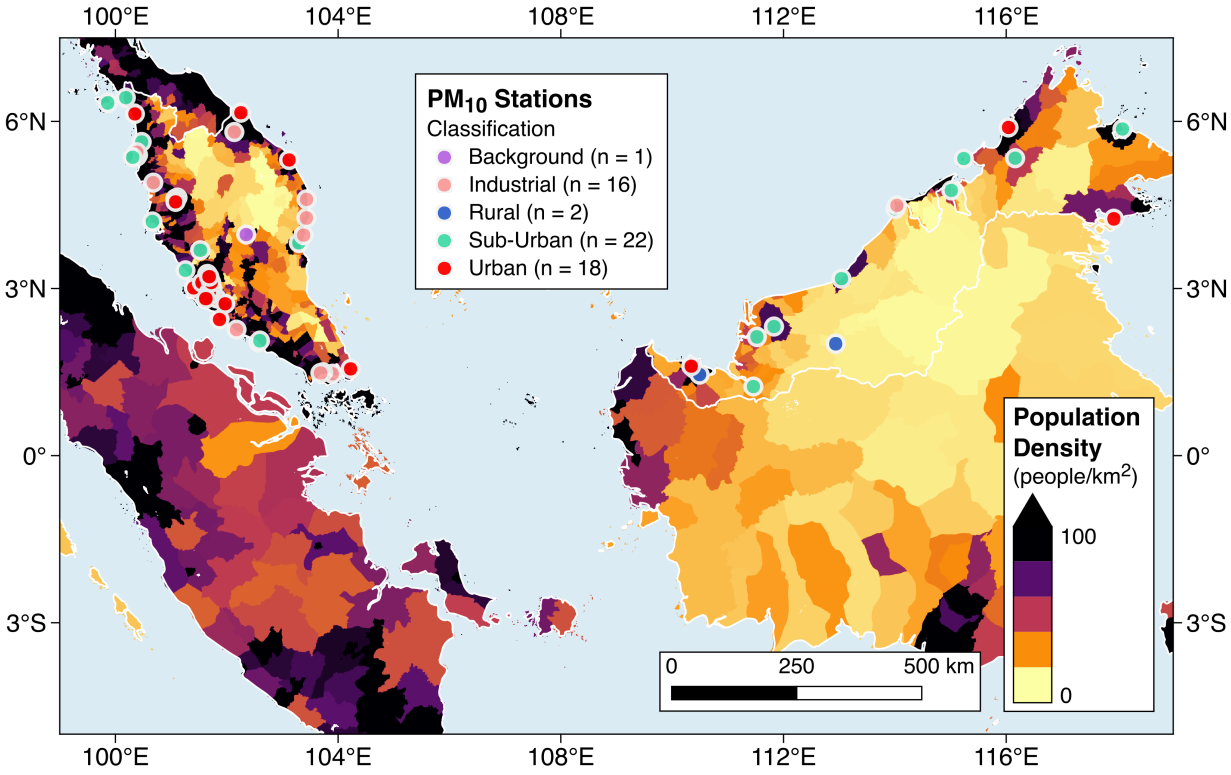


Figure D.6: PM_{10} station network (n = 59) in Malaysia overlaid on population density in 2010. The different colors of the station sites denote different environments, classified according to the locations of the stations (background, industrial, rural, sub-urban, or urban).

Table D.2: Details on PM_{10} stations in Malaysia used for validation of modeled population-weighted exposure.

Station ID	Location		Time Period	Pop. Density (people/km^2)	Classification
	Coordinates	State			
CAS 001	103.9°E, 1.5°N	Johor	2003-2015	1975	Industrial
CAE 002	103.4°E, 4.3°N	Terengganu	2003-2015	334	Industrial
CAN 003	100.4°E, 5.4°N	Pulau Pinang	2003-2015	2447	Industrial
CAK 004	110.4°E, 1.6°N	Sarawak	2003-2015	451	Industrial
CAC 005	101.7°E, 3.3°N	Selangor	2003-2008	2271	Sub-Urban
CAS 006	102.2°E, 2.3°N	Melaka	2003-2015	1161	Industrial
CAE 007	102.3°E, 4°N	Pahang	2003-2015	97	Background
CAN 008	101.1°E, 4.6°N	Perak	2003-2015	906	Industrial
CAN 009	100.4°E, 5.4°N	Pulau Pinang	2003-2015	2437	Sub-Urban
CAC 010	101.8°E, 2.8°N	Negeri Sembilan	2003-2015	466	Industrial
CAC 011	101.4°E, 3°N	Selangor	2003-2015	1451	Urban
CAC 012	101.7°E, 3.1°N	Kuala Lumpur	2003-2004	5334	Urban
CAN 013*	101.1°E, 4.6°N	Perak	1997-1999	906	Sub-Urban
CAE 014	103.3°E, 3.8°N	Pahang	2003-2015	426	Sub-Urban
CAE 015	103.4°E, 4°N	Pahang	2003-2015	203	Industrial
CAC 016	101.6°E, 3.1°N	Selangor	2003-2015	3875	Industrial
CAN 017	100.5°E, 5.6°N	Kedah	2003-2015	2135	Sub-Urban
CAN 018*	100.4°E, 5.4°N	Pulau Pinang	1996-1998	4205	Industrial
CAS 019	103.7°E, 1.5°N	Johor	2003-2015	3502	Industrial
CAN 020	100.7°E, 4.9°N	Perak	2003-2015	1597	Industrial
CAE 022	102.3°E, 6.2°N	Kelantan	2003-2015	1326	Urban
CAC 023	101.7°E, 3°N	Selangor	2003-2010	2726	Sub-Urban
CAE 024	103.4°E, 4.6°N	Terengganu	2003-2015	215	Industrial
CAC 025	101.6°E, 3.1°N	Selangor	2003-2015	3762	Urban
CAK 026	111.8°E, 2.3°N	Sarawak	2003-2015	79	Sub-Urban
CAK 027	113°E, 3.2°N	Sarawak	2003-2015	80	Sub-Urban
CAK 028	114°E, 4.4°N	Sarawak	2003-2015	489	Sub-Urban
CAK 029	111.5°E, 2.1°N	Sarawak	2003-2015	48	Sub-Urban
CAH 030	116°E, 5.9°N	Sabah	2003-2015	1493	Urban
CAK 031	115°E, 4.8°N	Sarawak	2003-2015	51	Sub-Urban
CAN 032	99.9°E, 6.3°N	Kedah	2003-2015	211	Sub-Urban
CAN 033	100.2°E, 6.4°N	Perlis	2003-2015	740	Sub-Urban

Table D.2 (continued): Details on PM_{10} stations in Malaysia used for validation of modeled population-weighted exposure

CAE 034	103.1°E, 5.3°N	Terengganu	2003-2015	3068	Urban
CAK 035	110.5°E, 1.5°N	Sarawak	2003-2015	205	Rural
CAK 036	111.5°E, 1.2°N	Sarawak	2003-2015	25	Sub-Urban
CAN 038	100.3°E, 5.4°N	Pulau Pinang	2003-2015	6313	Sub-Urban
CAH 039	117.9°E, 4.2°N	Sabah	2003-2015	67	Urban
CAN 040	100.3°E, 6.1°N	Kedah	2003-2015	2205	Urban
CAN 041	100.7°E, 4.2°N	Perak	2003-2015	257	Sub-Urban
CAH 042	115.2°E, 5.3°N	Labuan	2003-2015	919	Sub-Urban
CAS 043	102.6°E, 2°N	Melaka	2003-2015	2274	Urban
CAS 044	102.6°E, 2.1°N	Johor	2003-2015	2274	Sub-Urban
CAC 045	101.5°E, 3.7°N	Perak	2003-2015	103	Sub-Urban
CAN 046	101.1°E, 4.6°N	Perak	2003-2015	906	Urban
CAC 047	102°E, 2.7°N	Negeri Sembilan	2003-2015	1899	Urban
CAC 048	101.3°E, 3.3°N	Selangor	2003-2015	460	Sub-Urban
CAH 049	116.2°E, 5.3°N	Sabah	2003-2015	48	Sub-Urban
CAH 050	118.1°E, 5.9°N	Sabah	2003-2015	172	Sub-Urban
CAS 051	103.7°E, 1.5°N	Johor	2003-2008	1745	Industrial
CAK 052	110.3°E, 1.6°N	Sarawak	2003-2007	451	Urban
CAC 053	101.7°E, 2.9°N	W. P. Putrajaya	2003-2015	1392	Urban
CAC 054	101.7°E, 3.1°N	Kuala Lumpur	2004-2015	5774	Urban
CAK 055	112.9°E, 2°N	Sarawak	2004-2015	4	Rural
CAC 056	101.9°E, 2.4°N	Negeri Sembilan	2007-2015	162	Urban
CAS 057	104.2°E, 1.6°N	Johor	2008-2015	83	Urban
CAC 058	101.7°E, 3.2°N	Kuala Lumpur	2009-2015	6243	Urban
CAE 059	102.1°E, 5.8°N	Kelantan	2009-2015	393	Industrial
CAC 060	101.6°E, 2.8°N	Selangor	2010-2015	299	Urban
CAK 061	114°E, 4.5°N	Sarawak	2010-2015	489	Industrial

* Stations CAN 013 and CAN 018 do not have any observations during the 2003-2015 study period, and so are not included in our analysis.

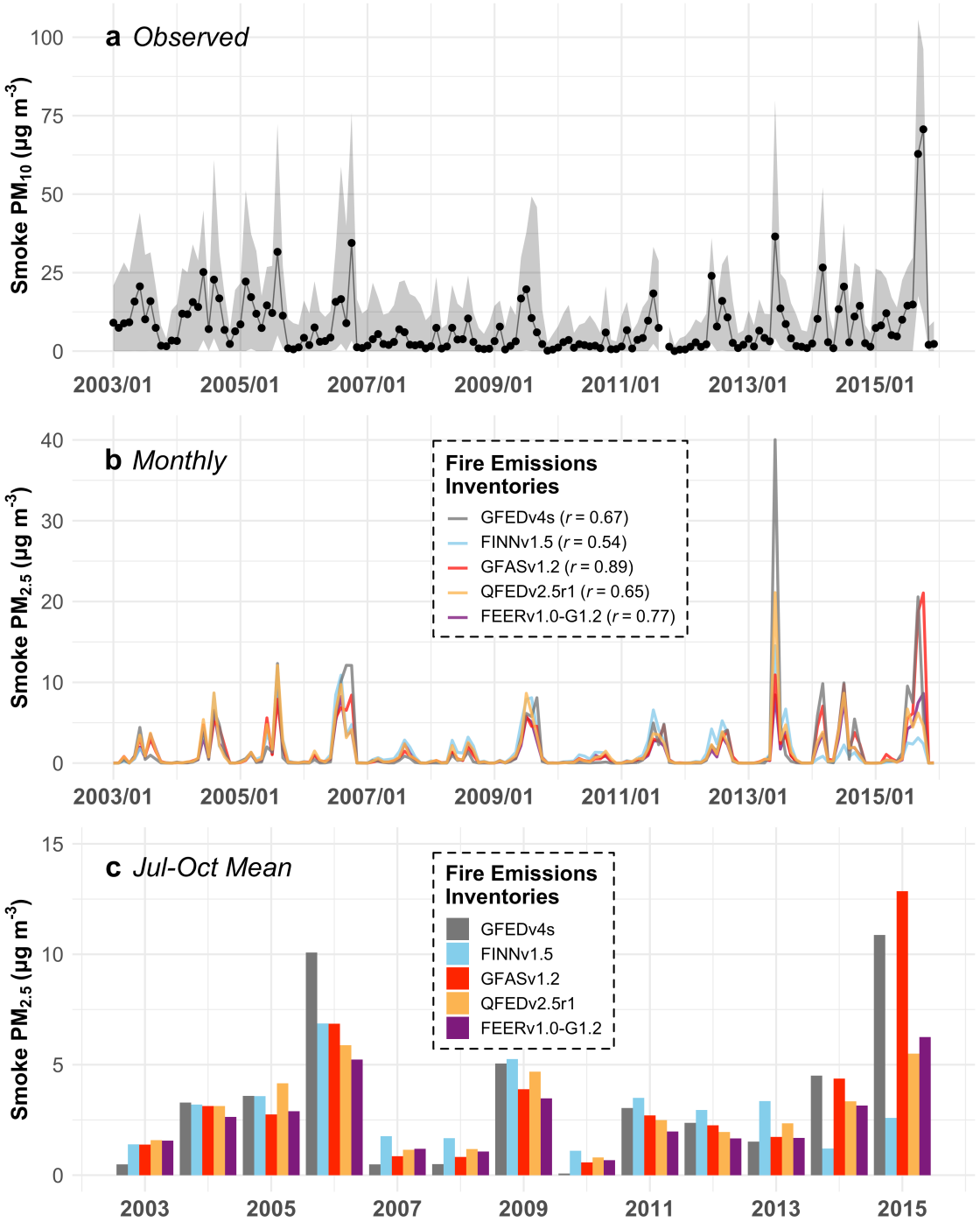


Figure D.7: Smoke $PM_{2.5}$ exposure in Malaysia, from 2003-2015. (a) Observed, population-weighted observed smoke PM_{10} from 2003-2015, using 57 stations (Table D.2), with the gray envelope showing the 5th-95th quantile range. (b) Modeled, population-weighted smoke $PM_{2.5}$ calculated by the GEOS-Chem adjoint with different global fire emissions inventories: GFEDv4s, FINNv1.5, GFASv1.2, QFEDv2.5r1, and FEERv1.0-G1.2. Correlations between observed smoke PM_{10} and modeled smoke $PM_{2.5}$ are shown inset for each inventory. All correlations are statistically significant ($p < 0.01$). (c) Jul-Oct mean smoke $PM_{2.5}$ by inventory.

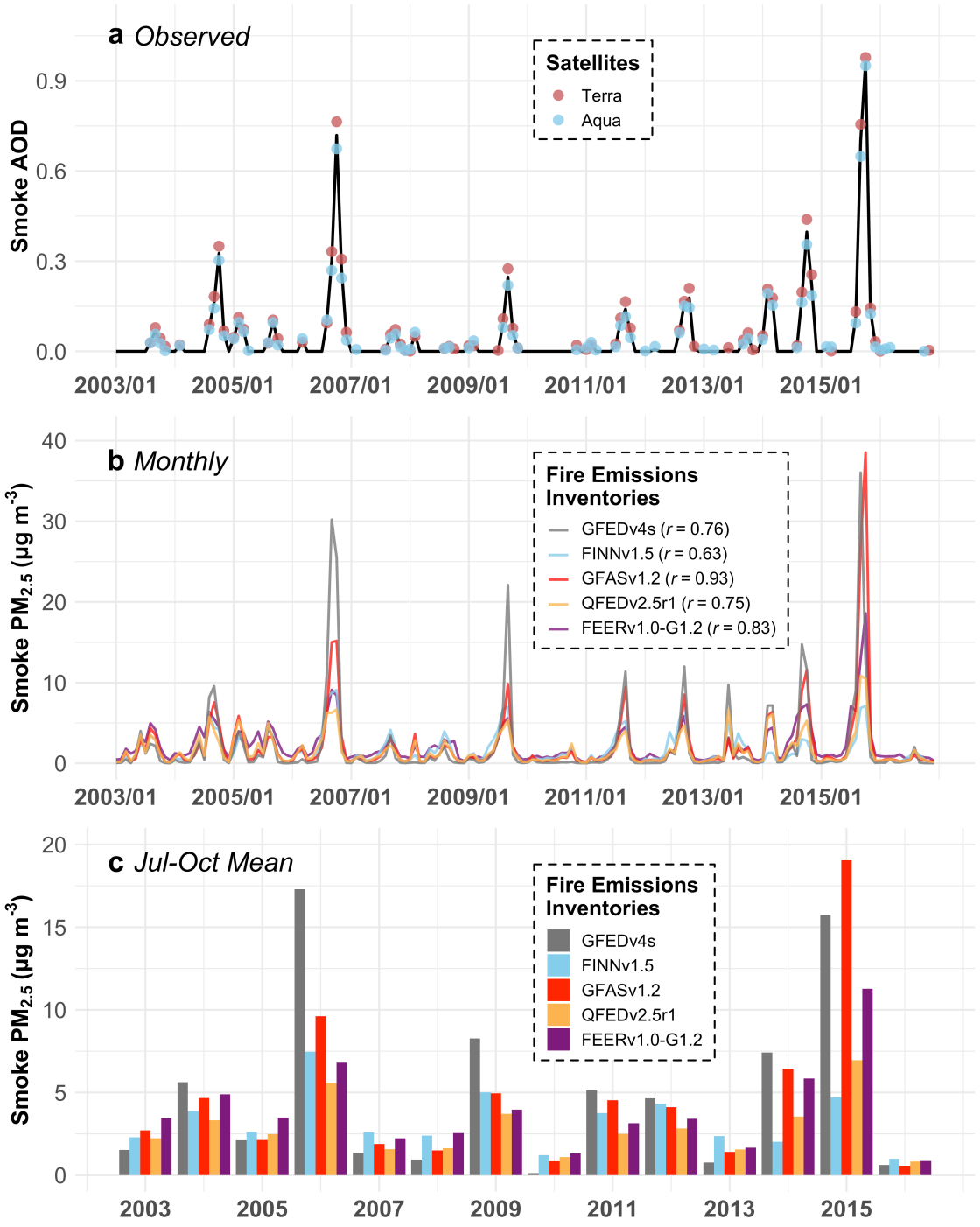


Figure D.8: Smoke AOD and $PM_{2.5}$ exposure in Indonesia, from 2003-2016. (a) Smoke aerosol optical depth (AOD) from 2003-2016, derived from the average of MODIS Terra (red circles) and Aqua (blue circles) smoke AOD over Indonesia (Sumatra and Kalimantan). (b) Modeled, population-weighted smoke $PM_{2.5}$ calculated by the GEOS-Chem adjoint for this region, using different global fire emissions inventories: GFEDv4s, FINNv1.5, GFASv1.2, QFEDv2.5r1, and FEERv1.0-G1.2. Correlations between observed smoke AOD and modeled smoke $PM_{2.5}$ are shown inset for each inventory. All correlations are statistically significant ($p < 0.01$). (c) Jul-Oct mean smoke $PM_{2.5}$ by inventory.

D.4 Ancillary information on burn date uncertainty, fire diurnal cycle, and land use/ land cover

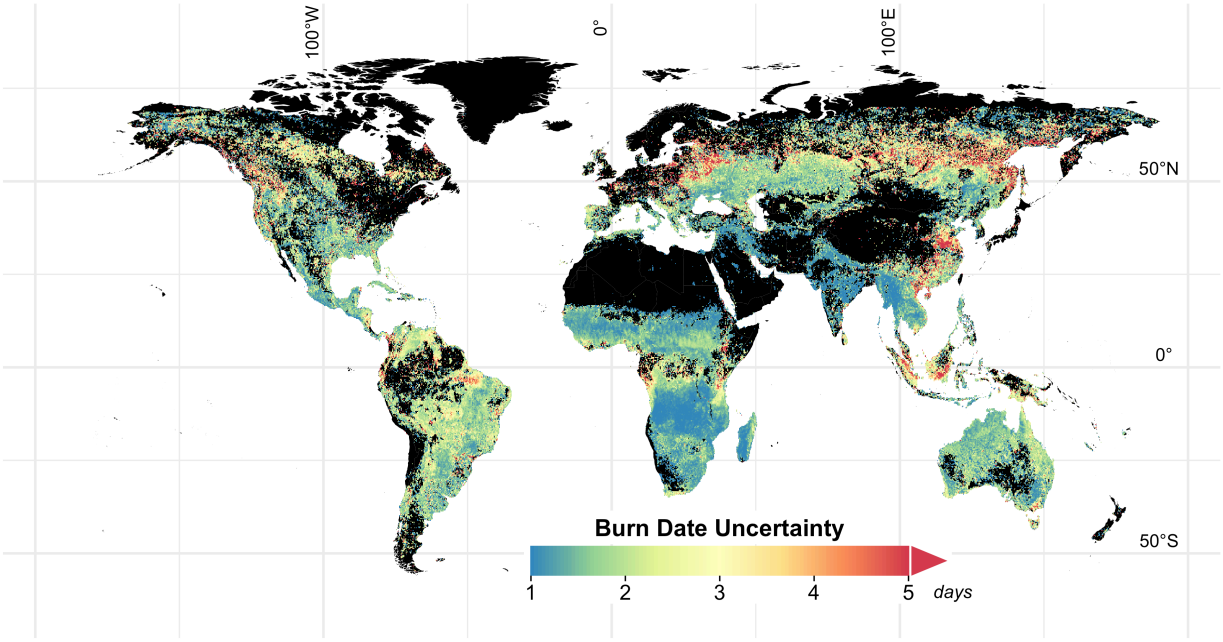


Figure D.9: Average burn date uncertainty (in days), over 2003-2017, for burned area estimates from the MODIS MCD64A1 burned area product. The average burn date uncertainty is averaged over each grid cell at monthly timesteps and weighted by monthly burned area.

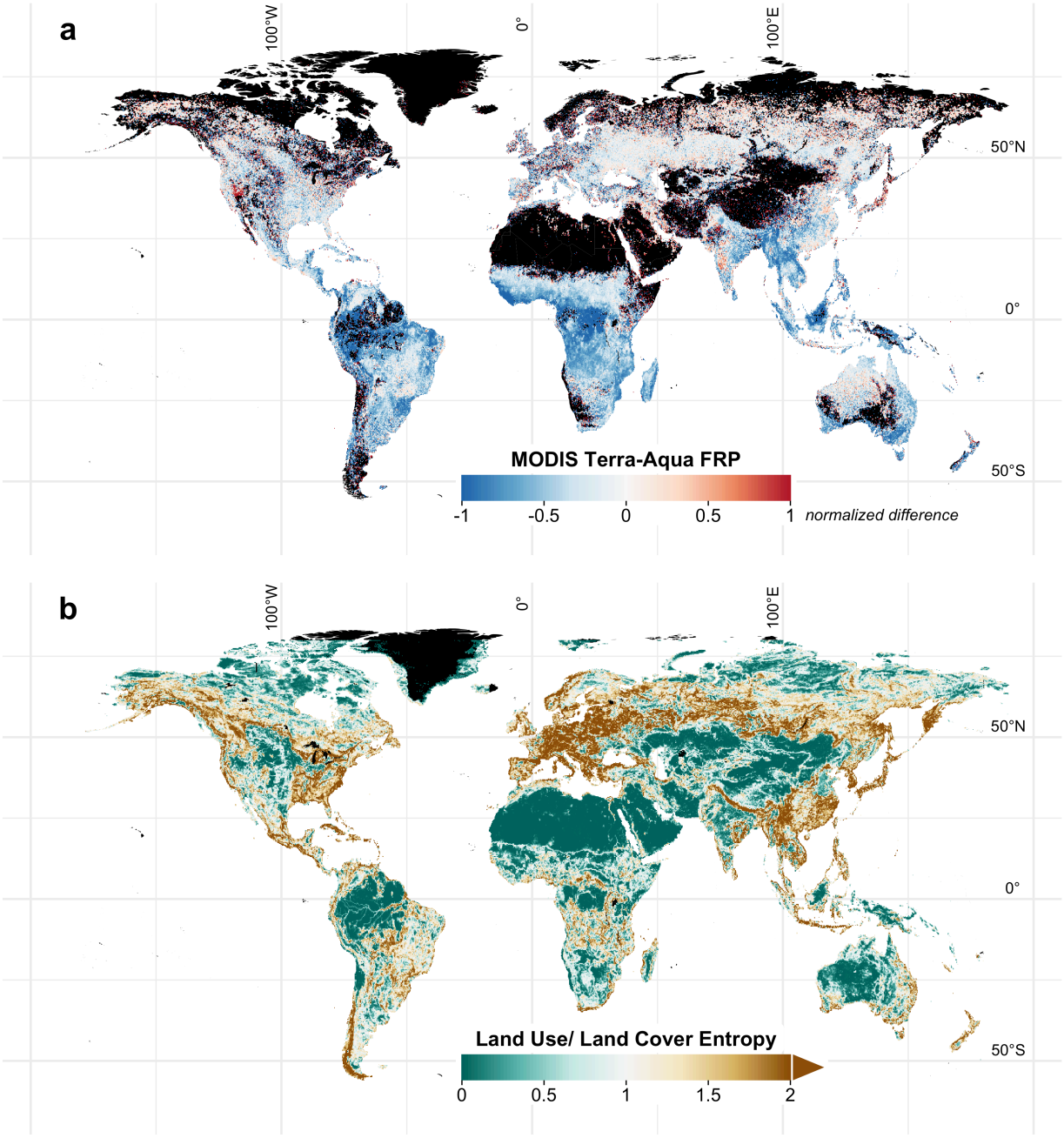


Figure D.10: Ancillary information on the diurnal cycle in fire energy and entropy of land use/land cover classification, mapped at 0.25° x 0.25° spatial resolution. (a) MODIS FRP, from 2003-2017, expressed as the normalized difference of Terra and Aqua FRP. Positive values (red) indicate fire energy dominated by contribution from Terra (10:30 am overpass, morning), while negative values indicate fire energy dominated by contribution from Aqua (1:30 pm overpass, early afternoon). (b) Average entropy from MODIS MCD12Q1 Scheme 1 (IGBP) and Scheme 2 (UMD) land use/ land cover (LULC), from 2003-2016. We exclude pixels classified as water bodies or permanent snow/ice. Higher entropy (brown) indicates more heterogenous LULC; conversely, lower entropy (green) indicates more homogenous LULC.

D.5 Fire Inventories: Regional Evaluation, Comparison, and Metrics (FIRECAM) online tool

We present an online tool called "Fire Inventories: Regional Evaluation, Comparison, and Metrics" (FIRECAM; https://globalfires.earthengine.app/view/firecam), hosted on Earth Engine Apps, that allows users to compare regional differences in five global fire emissions inventories (GFEDv4s, FINNv1.5, GFASv1.2, QFEDv2.5, and FEERv1.0-G1.2) for six species (CO_2, CO, CH_4, OC, BC, $PM_{2.5}$; Figure D.11) and diagnose regional challenges in satellite observations of fires by using the five relative fire confidence metrics. We use the 14 "basis" regions defined in GFEDv4s as default, but users can also select a country, pixel, or custom region (Figure D.12) (van der Werf et al., 2017). Due to differences in spatial resolution, we aggregate all inventories to 0.5° x 0.5°.

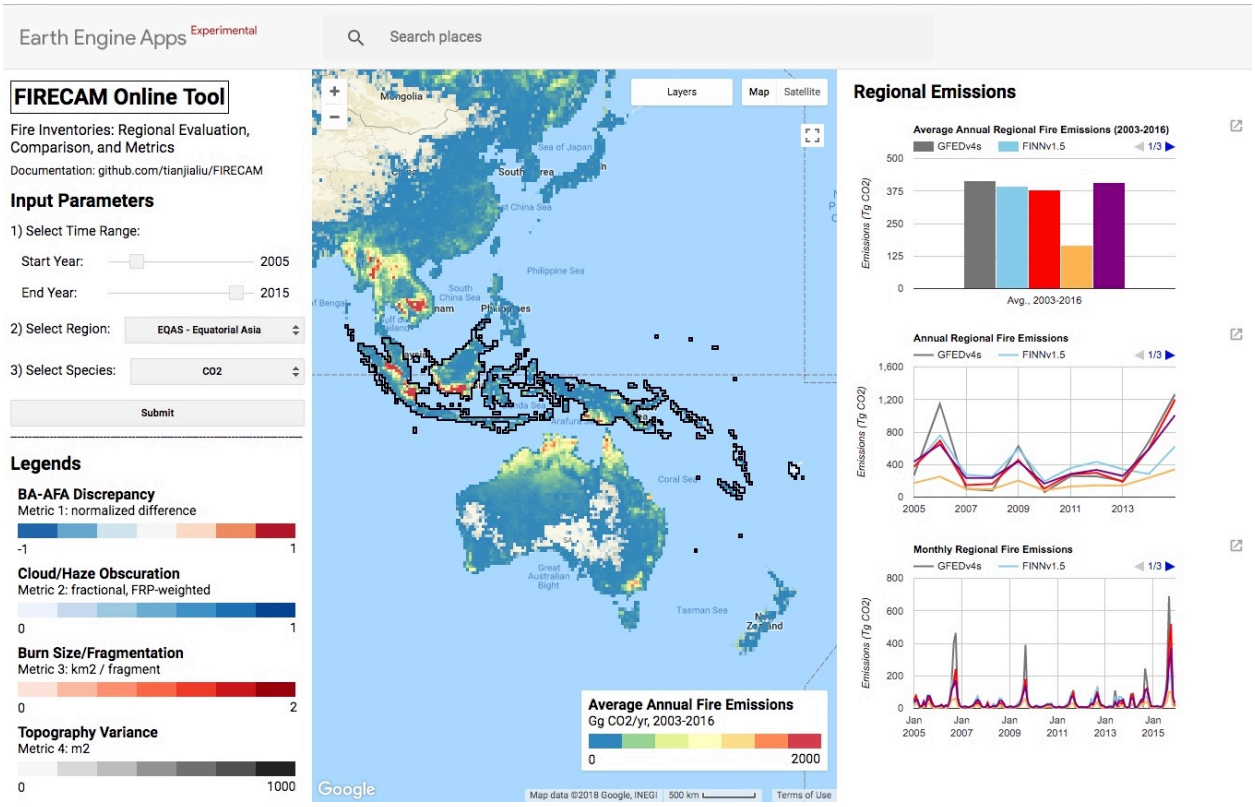


Figure D.11: Screenshot of the Fire Inventories: Regional Evaluation, Comparison, and Metrics (FIRECAM) online tool (https://globalfires.earthengine.app/view/firecam).

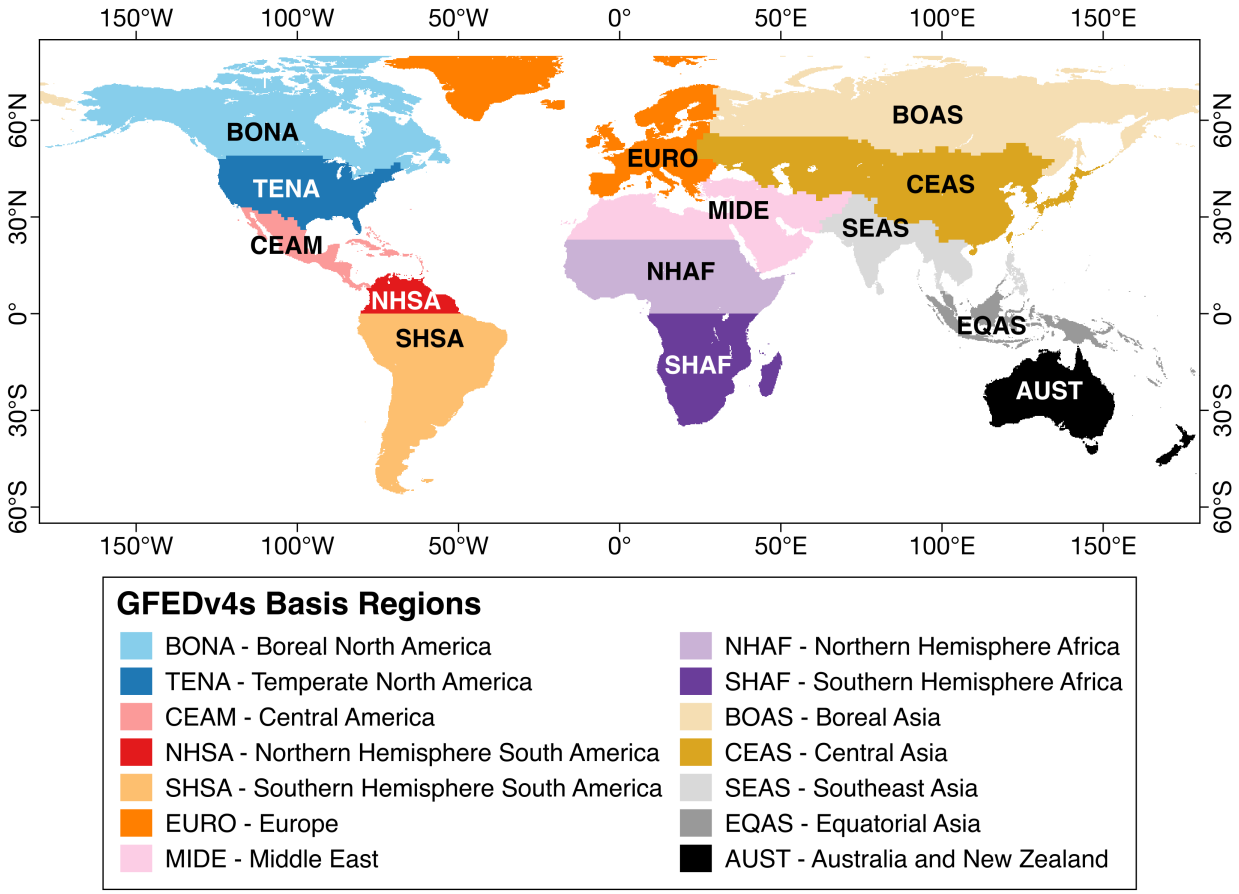


Figure D.12: The 14 basis regions defined in GFEDv4s (van der Werf et al., 2017).

D.6 Relative fire confidence metrics: consistency with other regional studies

The relative fire confidence metrics can be used to probe causes of region-specific uncertainties in satellite-observed fire activity. For example, how comparable are the challenges in estimating burned area in the agricultural region of eastern China compared to that in northern India? Given that eastern China has rougher terrain (metric 4) and much higher FRP-weighted cloud/haze fraction (metric 2) than India, we hypothesize that agricultural fire emissions in eastern China are more poorly constrained than those in India. We can further probe within-region differences in fire emissions estimates using the relative fire confidence metrics, as discussed below for wildland fires in the United States and for agricultural fires in India.

United States. Koplitz et al. (2018b) compared wildland burned area and fire emissions from GFEDv4s, FINNv1.5, and the National Emission Inventory (NEI) from the U.S. Environmental Protection Agency (EPA). The NEI integrates satellite sources and on-the-ground reports and is considered most accurate of these inventories. These authors found that using FINNv1.5 and GFEDv4s in a regional model led to severe underestimates of 0.52-0.73 μg m^{-3} in the annual average $PM_{2.5}$ enhancement due to wildland fires over 2002-2014, relative to the NEI. However, compared to GFEDv4s, FINNv1.5 better captured the variability in burned area and pollutant concentrations in the U.S. Southeast. This last result is consistent with the high AFA-scores and low BA-scores over the U.S. Southeast, where small, fragmented fires dominate, as shown by metrics 1, 3, and 5 (McCarty et al., 2008). Given the moderate cloud/haze burden in this region (metric 2), top-down inventories that account for cloud gaps in the FRP record may be better suited for this region than bottom-up inventories.

India. During the post-monsoon season (Oct-Nov), smoke from agricultural fires in the northwestern states of Punjab and Haryana travels southeast across northern India, with severe consequences for air quality downwind. Small, fragmented fires dominate northwestern India (metrics 1, 3, and 5), leading to low BA-scores and high AFA-scores over the region; the flat topography (metric 4) and low cloud/haze fraction (metric 2) indicate that these two factors are not as important for evaluating satellite-derived fire activity in this region. High pFRP suggests that emissions from top-down inventories are uncertain, as many small fires may be missed. Using four different fire inventories (GFEDv4s, FINNv1.5, GFASv1.2, and QFEDv2.4), Cusworth et al. (2018) modeled smoke enhancement over Delhi during the 2012-2016 burning seasons. GFAS and GFEDv4s both strongly underestimated the smoke enhancement, compared to surface observations, while FINNv1.5 best captured this enhancement. Aside from the inherent difficulty of quantifying emissions from small agricultural fires, the strong

afternoon peak in fire activity in northwestern India may also partially explain the GFEDv4s underestimate. This is because the small fires boost in GFED4s is derived from an average of Terra (morning) and Aqua (afternoon) estimates of active fires (Figure D.10a) (van der Werf et al., 2017). QFED leads to inconsistent smoke $PM_{2.5}$ enhancement over the 5 years, most notably yielding low enhancements in 2014 and 2016, when the influence of smoke on Delhi air quality appears to be greater. Both GFAS and QFED derive the conversion factor β of FRP to DM emissions based on earlier versions of GFED that do not apply a small fires boost, and this may explain the relatively low smoke $PM_{2.5}$ enhancement, at least for GFAS. QFED enhances aerosol emissions by a factor of 1.8 for savannas and grasslands, thus adjusting OC and BC emissions that might otherwise be too low.

D.7 Trends in global fire emissions

The importance of inventory choice can further be seen in the estimated linear trends in global fire emissions. Trends in GFEDv4s and GFASv1.2 emissions, from 2003-2016, are statistically insignificant for most species while those in the other three inventories show statistically significant decreases (Table D.3). While global burned area has declined over the past two decades (Andela et al., 2017), the trend in global fire emissions is not as clear due to the disproportionate contribution in emissions over burned area from some regions, such as Indonesia (van der Werf et al., 2017). The strong link between the El Niõ Southern Oscillation and pan-tropical fires — Indonesian peat fires in particular — is responsible for emissions spikes in strong El Niõ years, such as 2006 and 2015 (Chen et al., 2017; van der Werf et al., 2017). Peat delineation may be one factor that explain differences in trends using GFEDv4s and GFASv1.2 versus the three other inventories. However, further analysis is needed to determine the reasons for the presence or lack of statistically significant decreases in global fire emissions.

Evaluation of linear trends is an important application of global fire emissions inventories. As an example, Worden et al. (2017) pointed to linear trends in GFEDv4s emissions of CH_4 and to CO/CH_4 observations as evidence for the hypothesis that a decline in biomass burning over 2007-2014 can help explain isotopic changes in atmospheric methane after 2007. In fact, methane emissions from fires have not appreciably decreased according to GFEDv4s when this time period is extended to 2016. In any event, it is clear that inventory bias is an important factor to consider when drawing conclusions.

Table D.3: Linear trends in global fire emissions, from 2003-2016, by inventory and species.

	CO_2	**CO**	**CH_4**	**OC**	**BC**	**$PM_{2.5}$**
GFEDv4s	-68 (36)	-2.1 (2.6)	-0.03 (0.2)	-0.09 (0.12)	-0.02 (0.01)	-0.27 (0.21)
FINNv1.5	**-180 (48)**	**-9.3 (2.6)**	**-0.43 (0.13)**	**-0.57 (0.16)**	**-0.05 (0.01)**	**-1.0 (0.28)**
GFASv1.2	-71 (36)	-3 (2.8)	-0.12 (0.24)	-0.15 (0.14)	**-0.03 (0.01)**	-0.32 (0.21)
QFEDv2.5r1	**-113 (32)**	**-5.5 (1.4)**	**-0.26 (0.06)**	**-0.74 (0.24)**	**-0.08 (0.02)**	**-1.17 (0.36)**
FEERv1.0-G1.2	**-169 (53)**	**-8.3 (2.6)**	**-0.43 (0.14)**	**-0.4 (0.14)**	**-0.05 (0.02)**	**-0.69 (0.23)**

D.8 Implementation of global fire emissions inventories in GEOS-Chem

As an example of how the emissions implemented into chemical transport models (CTMs) may be outdated, we examine the implementation of GFED, FINN, and QFED into GEOS-Chem. The GEOS-Chem CTM (geos-chem.org) is paired with the Harvard-NASA Emissions Component (HEMCO) (Keller et al., 2014), an interface for emissions inventories. The default global fire emissions inventory in GEOS-Chem CTM is GFED, with an option to use QFED or FINN. The current versions of GFED, FINN, and QFED available in HEMCO are GFEDv4s, FINNv1.5, and QFEDv2.5.

First, as new versions of emissions inventories become available, such updates may lag months to years before full incorporation into GEOS-Chem. For example, GFEDv4s updated emissions factors in 2017 (van der Werf et al., 2017), but this change was made available only in March 2018 and fully implemented in GEOS-Chem v12 in August 2018. Using updated emissions factors decreases average annual global emissions, from 2003-2016, of CH_4, OC, and BC by 8.6-13%, and the other emissions by lesser amounts (Table D.4). In particular, the BC emissions factor for peatlands decreased by 93% from 0.566 to 0.04 g BC/kg DM with updated emissions factors (Table D.5) (van der Werf et al., 2017). This is more consistent with measurements that suggest the peat BC emissions factor is almost negligible due to the lack of flaming fires in peatlands (Stockwell et al., 2016). Further, QFED was updated to v2.5r1 in HEMCO in July 2018 with no intermediate versions (e.g., v2.4r8) superseding v2.4r6 since September 2014. QFEDv2.5r1, which reflects the update in MODIS active fires from C5 to C6, has been available from the NASA Center for Climate Simulation (NCCS) data portal (`https://portal.nccs.nasa.gov/datashare/iesa/aerosol/emissions/QFED/v2.5r1/`) since December 2016, and QFEDv2.4r8 since April 2015.

Second, we find inconsistencies between emissions from the "out-of-box" FINNv1.5, downloaded from http://bai.acom.ucar.edu/Data/fire/, and FINNv1.5 in HEMCO. FINNv1.5 in HEMCO is gridded to 0.25° x 0.25° for CO_2 only. Scaling factors are then used to convert CO_2 to other species. This approach, which is also used with GFED dry matter (DM) emissions, conserves storage and limits computational cost. We separately calculate the average yearly emissions from 2003-2016 for CO_2, CO, CH_4, OC, and BC for "out-of-box" and HEMCO versions. While CO_2, CO, CH_4 emissions differ by < 1%, OC emissions are 14% lower in HEMCO than in FINNv1.5, and BC emissions 36% higher (Table S6). Discrepancies are present for all scaling factors, but appreciable differences in CO_2/OC and CO_2/BC for class 2, or woody savanna, are primarily responsible for

the large relative error in OC and BC emissions (Table D.7). Additionally, FINNv1.5 in HEMCO is missing class 6, or temperate evergreen forest. For classes 3-5, we find two unique scaling factors each for "out-of-box" FINNv1.5. These discrepancies imply that FINNv1.5 must be implemented with all species independently calculated, similar to QFED in HEMCO, or that FINNv1.5 LULC should be further subdivided to account for the unique scaling factors.

In summary, emissions inventories may lag in version as implemented in CTMs, as in the case of QFED in GEOS-Chem. Our results imply non-negligible impacts on the emissions budget from (1) outdated emissions factors for GFEDv4s and (2) errors in the implementation of FINNv1.5 in GEOS-Chem, with implications for studies that used these inventories in GEOS-Chem.

Table D.4: Differences in mean annual global GFEDv4s CO_2, CO, CH_4, OC, and BC emissions (Tg yr^{-1}, $\pm 1\sigma$) using the original and updated emissions factors.

	CO_2	**CO**	**CH_4**	**OC**	**BC**
Old EFs, *pre-GCv12* (Tg)	6825 (584)	331 (40)	17 (3)	17 (2)	2.1 (0.2)
New EFs, *GCv12* (Tg)	6986 (595)	336 (39)	15 (3)	16 (2)	1.8 (0.2)
Relative Diff. (%)	2.4	1.5	-13	-8.6	-13

Table D.5: Differences in original and updated emissions factors (EFs; g species kg^{-1} dry matter) for GFEDv4s. The original EFs were available with the July 2015 release of GFEDv4s and updated in June 2017 in van der Werf et al. (2017)

		CO_2	CO	CH_4	OC	BC
Class 1: SAVA *Savannas, grasslands, shrublands*	Original EFs	1650	62.3	2.2	3.21	0.46
	Updated EFs	1686	63	1.94	2.62	0.37
Class 2: BORF *Boreal forests*	Original EFs	1570	106	4.81	9.15	0.562
	Updated EFs	1489	127	5.96	9.6	0.5
Class 3: TEMF *Temperate forests*	Original EFs	1570	106	4.81	9.15	0.562
	Updated EFs	1647	88	3.36	9.6	0.5
Class 4: DEFO *Tropical forests and deforestation*	Original EFs	1630	101	6.59	4.3	0.566
	Updated EFs	1643	93	5.07	2.71	0.52
Class 5: PEAT *Peatlands*	Original EFs	1710	210	20.8	4.3	0.566
	Updated EFs	1703	210	20.8	6.02	0.04
Class 6: AGRI *Agricultural*	Original EFs	1310	92.1	8.79	4.14	0.42
	Updated EFs	1585	102	8.4	2.3	0.75

Table D.6: Differences in mean annual global CO_2, CO, CH_4, OC, and BC emissions (Tg yr^{-1}, $\pm 1\sigma$) between "out-of-box" and HEMCO FINNv1.5.

	CO_2	CO	CH_4	OC	BC
Out-of-box (Tg)	6292 (1137)	330 (60)	16 (3)	20 (4)	1.9 (0.3)
HEMCO (Tg)	6309 (1019)	330 (53)	16 (3)	17 (3)	2.6 (0.4)
Relative Error (%)	0.3	-0.2	0.3	-14	36

Table D.7: Differences in scaling factors from CO_2 to CO, CH_4, OC, and BC emissions between "out-of-box" and HEMCO FINNv1.5.

		CO_2/CO (mole/mole)	**CO_2/CH_4** (mole/mole)	**CO_2/OC** (mole/g)	**CO_2/BC** (mole/g)
Class 1 *Savanna, grasslands*	Out-of-box	18.3	411.1	14.8	103.9
	HEMCO	17	316.7	14.7	103.5
Class 2 *Woody savanna*	Out-of-box	16.1	240.5	5.9	78
	HEMCO	15.3	226.5	10.5	29.8
Class 3 *Tropical forest*	Out-of-box	7.9, 11.4	98.1, 117.4	4.5, 7.9	61.3, 71.8
	HEMCO	11.2	118.1	7.9	71.8
Class 4 *Temperate forest*	Out-of-box	7.5, 7.9	90.4, 98.1	4.3, 4.5	61.3, 169.2
	HEMCO	10.3	127.7	4	65.1
Class 5 *Boreal forest*	Out-of-box	7.5, 7.9	90.4, 98.1	4.3, 4.5	61.3, 169.2
	HEMCO	7.5	91.1	4.3	169.2
Class 6 *Temperate evergreen forest*	Out-of-box	11.9	178.7	4.9	66.8
	HEMCO	x	x	x	x
Class 9 *Agricultural*	Out-of-box	8.8	93.4	10.6	50.6
	HEMCO	9.9	99.3	15.7	48

E

Supplemental Material for Chapter 5

E.1 The φ and ε metrics: complications and limitation

For φ, errors in the allocation of burned area at monthly resolution may result in mismatches between active fire area and burned area. However, assessing the temporal discrepancy in burned area and active fire area as a potential cause of the tiling artifacts is beyond the scope of this study. The average uncertainty in burn date in MCD64A1 is mostly less than five days, suggesting that the chance of misallocating burned area in the incorrect month is relatively small (Liu et al., 2020a). Here, we primarily focus on regions with pronounced, large-scale tiling artifacts persisting across multiple months throughout the fire season.

ε and its priority class should be characterized as an indicator of the likelihood of tile edge artifacts. The lower the ε and the higher the priority class, the higher the likelihood of tile edge artifacts. Interpreting ε requires end-users to contextualize the level of expected continuity across tiles with the type of fire. For example, agricultural fires are largely constrained to small, individual fields, though clusters of fields often burn around the same time. In forests and savannas, fires can spread to very large areas very quickly. Due to low burned area per ignition, it is more likely that tile edge artifacts in croplands are not tiling artifacts but rather indicate the heterogeneity in farmers' decisions to burn crop residues. For future analyses, stronger inferences can be made using additional pixels past the tile edge. However, quantifying the continuity of burned pixels is increasingly computationally intensive past one pixel because the end-user must assess continuity across each subsequent row (horizontal tile edges) or column (vertical tile edges) of pixels in a cascading manner.

While clouds and thick haze can negatively impact burned area classification, we do not expect the cloud detection algorithm to produce the same degree of tiling artifacts as the burned area algorithm. The burned area algorithm is more complex, because its classification thresholds are heavily dependent on land cover and land

use, and each classification requires a long time series of valid surface reflectance observations (Giglio et al., 2018; Lizundia-Loiola et al., 2020). Nevertheless, end-users can use the quality assurance (QA) flags of the burned area products to rule out missing burned area due to clouds or other inherent surface reflectance issues. For MCD64A1, we also find tiling artifacts in the QA flags for unburned pixels. The discontinuities between tiles are associated with the lack of training observations or separability between spectral classes. These tiling artifacts may point to differences in applied thresholds to separate burned and unburned pixels due to variability in land cover and land use composition in each tile. FireCCI has a simplified set of flags that do not reveal a probable cause for its tiling artifacts. Further study is needed to pinpoint which parts of the burned area algorithm cause tiling artifacts to occur and subsequently update the algorithm to ensure continuity in the final burned area product.

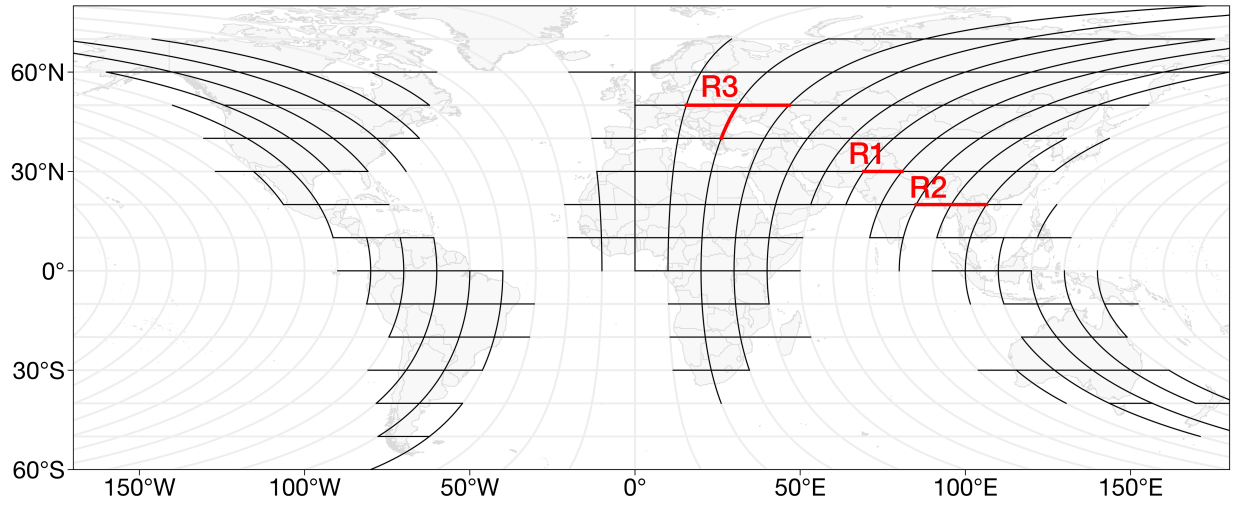


Figure E.1: Regions with large-scale tiling artifacts. R1: northwest India and Pakistan, R2: Myanmar and Thailand, and R3: Ukraine and southwest Russia. The tile edges for these regions are highlighted in red, and other land-crossing tile edges are highlighted in black.

Table E.1: Regions with tiling artifacts in MCD64A1 and FireCCI according to the φ and ε metrics. To aggregate ε across 2003-2019, we define priority as a continuous variable with a range of 0-100. ε is averaged using the continuous priority as weights. The % years (over 2003-2019) with $\varepsilon_{T1,T2}$ < 0.3 at medium or high priority is also listed. Bolded text denotes the presence of tiling artifacts in two methods: by visual interpretation from φ maps and quantitatively from mean $\varepsilon_{T1,T2} < 0.3$ with medium or high priority.

Region	MODIS Tiles	Month	MCD64A1			FireCCI		
			ϕ	$\varepsilon_{T1,T2}$ [*priority*]	*% years*	ϕ	$\varepsilon_{T1,T2}$ [*priority*]	*% years*
R1. *NW India, Pakistan*	h24v05 | h24v06 *north / south*	Apr	**Yes**	**0.24 [h]**	**71%**	No	0.54 [m]	6%
		May	**Yes**	**0.22 [h]**	**82%**	**Yes**	**0.17 [m]**	**65%**
		Oct	No	0.41 [h]	12%	**Yes**	**0 [h]**	**100%**
		Nov	No	0.5 [h]	18%	**Yes**	**0 [h]**	**100%**
R2. *Myanmar, Thailand*	h26v06 | h26v07 *north / south*	Jan	No	0.28 [l]	6%	**Yes**	**0 [m]**	**35%**
		Feb	No	0.56 [m]	12%	**Yes**	**0.07 [m]**	**76%**
		Mar	No	0.41 [m]	29%	**Yes**	**0.09 [h]**	**82%**
		Apr	No	0.57 [m]	18%	Yes	0 [l]	6%
	h27v06 | h27v07 *north / south*	Jan	No	0.26 [m]	18%	**Yes**	**0 [m]**	**41%**
		Feb	No	0.48 [h]	24%	**Yes**	**0.21 [h]**	**76%**
		Mar	No	0.49 [h]	18%	**Yes**	**0.28 [h]**	**59%**
		Apr	No	0.33 [h]	53%	**Yes**	**0.22 [m]**	**53%**
R3. *Ukraine, SW Russia*	h19v03 | h19v04 *north / south*	Mar	**Yes**	**0.1 [m]**	**29%**	No	0.15 [m]	29%
		Apr	Yes	0 [l]	18%	**Yes**	**0.03 [m]**	**35%**
		Jul	Yes	0 [l]	18%	Yes	0 [l]	6%
		Aug	**Yes**	**0.27 [m]**	**24%**	**Yes**	**0.15 [m]**	**65%**
		Sep	**Yes**	**0.25 [m]**	**29%**	**Yes**	**0.05 [m]**	**59%**
		Oct	**Yes**	**0.18 [m]**	**24%**	No	0.15 [m]	35%
	h20v03 | h20v04 *north / south*	Mar	**Yes**	**0.07 [m]**	**35%**	No	0.07 [m]	35%
		Apr	**Yes**	**0.05 [m]**	**47%**	**Yes**	**0.08 [m]**	**59%**
		Jul	**Yes**	**0.15 [m]**	**29%**	No	0.17 [m]	29%
		Aug	**Yes**	**0.17 [m]**	**47%**	No	0.16 [h]	71%
		Sep	**Yes**	**0.07 [m]**	**71%**	No	0.13 [m]	59%
		Oct	**Yes**	**0.19 [m]**	**47%**	No	0.21 [m]	47%
	h19v04 | h20v04 *east / west*	Jul	**Yes**	**0 [m]**	**47%**	No	0.27 [m]	47%
		Aug	**Yes**	**0.01 [m]**	**88%**	No	0.26 [h]	47%
		Sep	Yes	0 [l]	24%	No	0.07 [m]	65%
		Oct	**Yes**	**0.2 [m]**	**12%**	No	0.11 [m]	53%

priority classes: [h] = high, [m] = medium, [l] = low

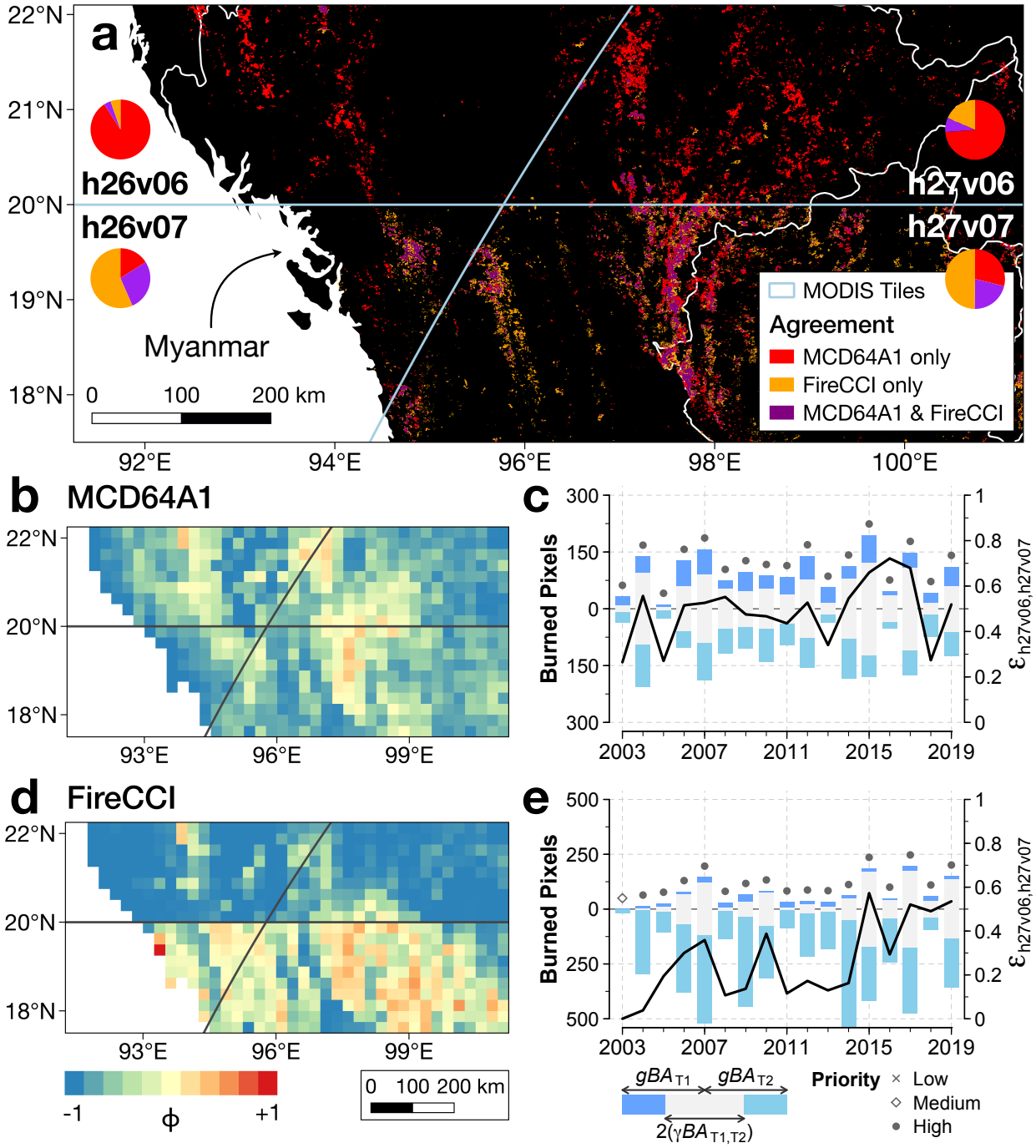


Figure E.2: Example of the tiling artifacts in FireCCI in March in Myanmar. (a) Agreement between FireCCI and MCD64A1 in 2012 in the MODIS tiles h26v06, h26v07, h27v06 and h27v07. Pie charts denote the per-tile proportion of burned area derived from MCD64A1 only (red), FireCCI only (orange), and both products (purple). (b) φ metric for MCD64A1 burned area and MOD/MYD14A1 active fire area, aggregated over 2003-2019. (c) ε metric for the h27v06 (T1) and h27v07 (T2) tiles (shown as lines). Bars show the number of burned pixels adjacent to the tile edge, with priority classes denoted by gray symbols above the bars. Pixels in adjacent pixel pairs are denoted in gray, and others are denoted in blue (T1: dark blue, T2: light blue). (d-e) Same as (b-c) but for FireCCI burned area.

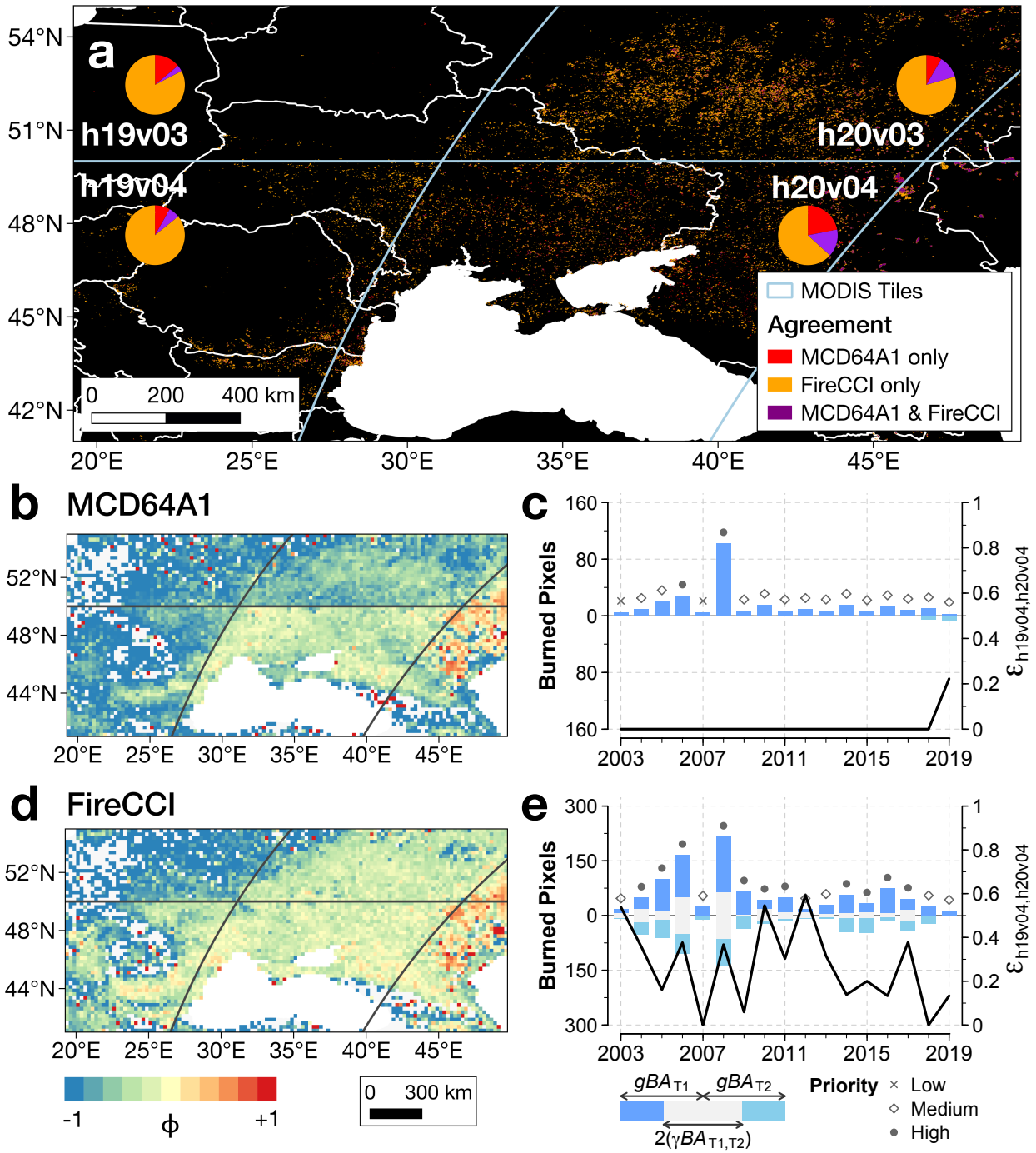


Figure E.3: Example of the tiling artifacts in MCD64A1 in August in Ukraine and southwest Russia. (a) Agreement between FireCCI and MCD64A1 in 2005 in the MODIS tiles h19v03, h19v04, h20v03, and h20v04. Pie charts denote the per-tile proportion of burned area derived from MCD64A1 only (red), FireCCI only (orange), and both products (purple). (b) φ metric for MCD64A1 burned area and MOD/MYD14A1 active fire area, aggregated over 2003-2019. (c) ε metric for the h19v04 (T1) and h20v04 (T2) tiles (shown as lines). Bars show the number of burned pixels adjacent to the tile edge, with priority classes denoted by gray symbols above the bars. Pixels in adjacent pixel pairs are denoted in gray, and others are denoted in blue (T1: dark blue, T2: light blue). (d-e) Same as (b-c) but for FireCCI burned area.

F

Supplemental Material for Chapter 6

F.1 Datasets

Table F.1: Details on the primary satellite fire datasets used in this study.

Description	Dataset	Resolution		Time Range
		Temporal	*Spatial*	
Fire atlas	GlobFire, v1	Daily	—	2000-2018[a]
	Global Fire Atlas, v1	Daily	—	2003-2016
Meteorology	ERA5	Daily	0.25°	from 1979
Fire weather	GFWED/MERRA-2	Daily	0.5° x 0.625°	from 1980
Freshwater storage	GRACE/GRCTellus*	Daily	0.5°	2002-2017
Surface reflectance	MODIS/Terra MOD09GA*	Daily	500 m	from 2000
Land cover	MCD12Q1, C6*	Annual	500 m	from 2001
Fire emissions	GFEDv4s	Monthly, Daily	0.25°	from 1997[b]
	FINNv1.5	Daily	1 km	from 2002
	GFASv1.2	Daily	0.1°	from 2003
	QFEDv2.5r1	Daily	0.1°	from 2000
	FINNv1.0-G1.2	Daily	0.1°	from 2003

* available from Google Earth Engine's public data catalog (https://developers.google.com/earth-engine/datasets)

The MCD64A1 algorithm estimates the burn date by detecting changes in a multi-week timeseries of near-

infrared and shortwave infrared surface reflectance and assumes that each pixel can burn at most once per month (Giglio et al., 2009). In contrast, the MxD14A1 algorithm detects thermal hotspots in near real time, independent of detections from previous overpasses (Giglio et al., 2016), and so active fires can be detected in the same pixel on multiple days within a month. The burned area product tends to outperform the active fire products in regions with large, contiguous fires, while the opposite is true for small, fragmented fire landscapes (Liu et al., 2020a). Because our objective here is to identify large temporal shifts in areas with high fire activity, we primary use MCD64A1 burned area with MxD14A1 active fire area as a check on our temporal shift estimates. Satellite detection of fire using both approaches is limited by observational gaps from cloud and thick smoke/haze cover. Unlike estimates of trends in the absolute magnitude of fire activity, those of temporal shifts are less sensitive to fluctuations in satellite observing conditions (Liu et al., 2020b). While a year with poor observing conditions will yield severe underestimates in total burned area, it is still possible to estimate with some accuracy the timing of the fire season, which generally varies little from year to year, based on the distribution of available fire observations.

Following Andela et al. (2017), who quantified the annual trend in the magnitude of burned area, we use a 0.25° x 0.25° grid to perform our initial search of temporal shifts in the primary fire season. This spatial resolution balances the need to have enough burned area observations within each grid cell to confidently quantify the midpoint date of the primary season with our aim to preserve sufficiently small-scale spatial patterns to define our regions of interest.

F.2 Ancillary Datasets

Table F.2: Details on the ancillary satellite-based and reanalysis datasets used in this study.

Description	Dataset	Resolution		Time Range
		Temporal	*Spatial*	
Fire atlas	GlobFire, v1	Daily	—	2000-2018[a]
	Global Fire Atlas, v1	Daily	—	2003-2016
Meteorology	ERA5	Daily	0.25°	from 1979
Fire weather	GFWED/MERRA-2	Daily	0.5° x 0.625°	from 1980
Freshwater storage	GRACE/GRCTellus*	Daily	0.5°	2002-2017
Surface reflectance	MODIS/Terra MOD09GA*	Daily	500 m	from 2000
Land cover	MCD12Q1, C6*	Annual	500 m	from 2001
Fire emissions	GFEDv4s	Monthly, Daily	0.25°	from 1997[b]
	FINNv1.5	Daily	1 km	from 2002
	GFASv1.2	Daily	0.1°	from 2003
	QFEDv2.5r1	Daily	0.1°	from 2000
	FINNv1.0-G1.2	Daily	0.1°	from 2003

* available from Google Earth Engine's public data catalog (https://developers.google.com/earth-engine/datasets)

[a] emissions estimates from 2017 onward are preliminary, daily emissions are available from 2003

[b] until June 2018

We investigate potential drivers of the temporal shifts in fire activity using several ancillary global datasets (Table F.2). Unless otherwise noted, the datasets span the entire time range of the study, or from 2003-2018.

F.3 Southwest Russia

Meteorology. We use GRACE-based estimates of freshwater storage, derived from satellite observations of anomalies in Earth's gravity field and calculated in terms of equivalent liquid water thickness (LWE), or the vertical extent of water (Rodell et al., 2018). We use the average of monthly GRACE Tellus LWE estimates by JPL (NASA Jet Propulsion Laboratory), CSR (University of Texas/ Center for Space Research), and GFZ (GeoForschungsZentrum Potsdam). Following Rodell et al. (2018), we interpolate monthly LWE to gap-fill months with limited observations and remove the seasonal cycle. We use GRACE data from 2003-2016. To complement GRACE freshwater storage, we use ERA5, the fifth generation of global atmospheric reanalysis products from ECMWF (Hersbach et al., 2020), to calculate the vapor pressure deficit (VPD), or the difference between saturation and actual vapor pressure. VPD is a skillful indicator of crop stress or wildfire risk (Lobell et al., 2014; Seager et al., 2015) and one of the leading predictors of fire activity on sub-seasonal to seasonal timescales (Chen et al., 2020).

Human activity. To characterize the timing of the winter wheat crop cycle, we use the U.S. Department of Agriculture Crop Calendar (`https://ipad.fas.usda.gov/`) and derive daily Normalized Difference Vegetation Index (NDVI) from MODIS surface reflectance observations for use as a proxy for greenness (Table 6.2). However, we find that MODIS-derived NDVI does not reveal shifts in crop phenology consistent with delays in the fire season (not shown). Because winter wheat fields lie dormant over the winter for 4-5 months with little change in greenness (Figure 6.3a), it is difficult to derive planting dates from satellite data or track changes in the harvest-to-sowing period that might propagate to the timing of peak growth in the following year. Further, we assess trends in winter wheat production, exports, and producer prices at the country and oblast level using data from Russia's Federal State Statistic Service, ROSSTAT (`https://gks.ru/`).

F.4 North Australia

Fires. To assess the efficacy of prescribed burning during the early dry season (EDS) to reduce fuel-abundant areas leading into the late dry season (LDS), we calculate the distance from each pixel to the nearest burned pixel, according to MCD64A1. We quantify the annual trends in the mean distance to nearest fire, averaged across Arnhem Land, in the EDS and LDS. As a check on MCD64A1, we repeat the analysis with regional fire perimeters from the North Australia and Rangelands Fire Information (NAFI, https://firenorth.org.au/) dataset, which is derived from MODIS 250-m surface reflectance. To investigate the characteristics of individual fire events, we use the GlobFire and Global Fire Atlas datasets, which spatially and temporally aggregate clusters of MODIS burned area (Artés et al., 2019; Andela et al., 2019). Based on data availability, we use GlobFire from 2003-2017 and Global Fire Atlas from 2003-2016.

To check whether the decrease in LDS burned area shows a similar trend in fire emissions, we use the Global Fire Emissions Database, version 4s (GFEDv4s). GFEDv4s uses satellite fire observations, biogeochemical modeling of fuel load and combustion completeness, and compilations of emissions factors to estimate gaseous and aerosol emissions from landscape fires (Table F.2) (van der Werf et al., 2017). We also use fire emissions estimates from four other global inventories, which differ in input datasets and methodology: Fire Inventory from NCAR (FINNv1.5), Global Fire Assimilation System (GFASv1.2), Quick Fire Emissions Dataset (QFEDv2.5r1), and Fire Energetics and Emissions Research (FEERv1.0-G1.2) (Wiedinmyer et al., 2011; Kaiser et al., 2012; Darmenov & da Silva, 2013; Ichoku & Ellison, 2014).

Meteorology. We use the Global Fire Weather Database (GFWED), in addition to ERA5-derived VPD, to investigate meteorological conditions during the fire season. GFWED uses reanalysis or forecast meteorology (MERRA-2 and GEOS-5) to compute the Fire Weather Index (FWI) (Field et al., 2015). FWI is a composite of six indices on fuel moisture conditions and fire behavior, including fuel buildup and initial spread, derived using surface meteorology, namely wind speed, temperature, relative humidity, and precipitation. FWI is a skillful indicator of fire danger in short-term forecasts and when validated against satellite observations of burned area, including in north Australia (Di Giuseppe et al., 2016; Field, 2020). We use the MERRA-2 version of GFWED with precipitation bias-corrected with rain gauge data.

Human activity. We obtain data from Australia's Clean Energy Regulator (http://www.cleanenergyregulator.gov.au/) on savanna burning projects that aim to reduce greenhouse gas emissions

from fires under the auspices of the Emissions Reduction Fund. For each savanna burning project in Arnhem Land and Cape York, we sum the Australia carbon credit units (ACCUs) issued from the 2012-13 to the 2018-19 financial year as a proxy for the level of fire management activity.

F.5 Temporal shifts in regions of interest

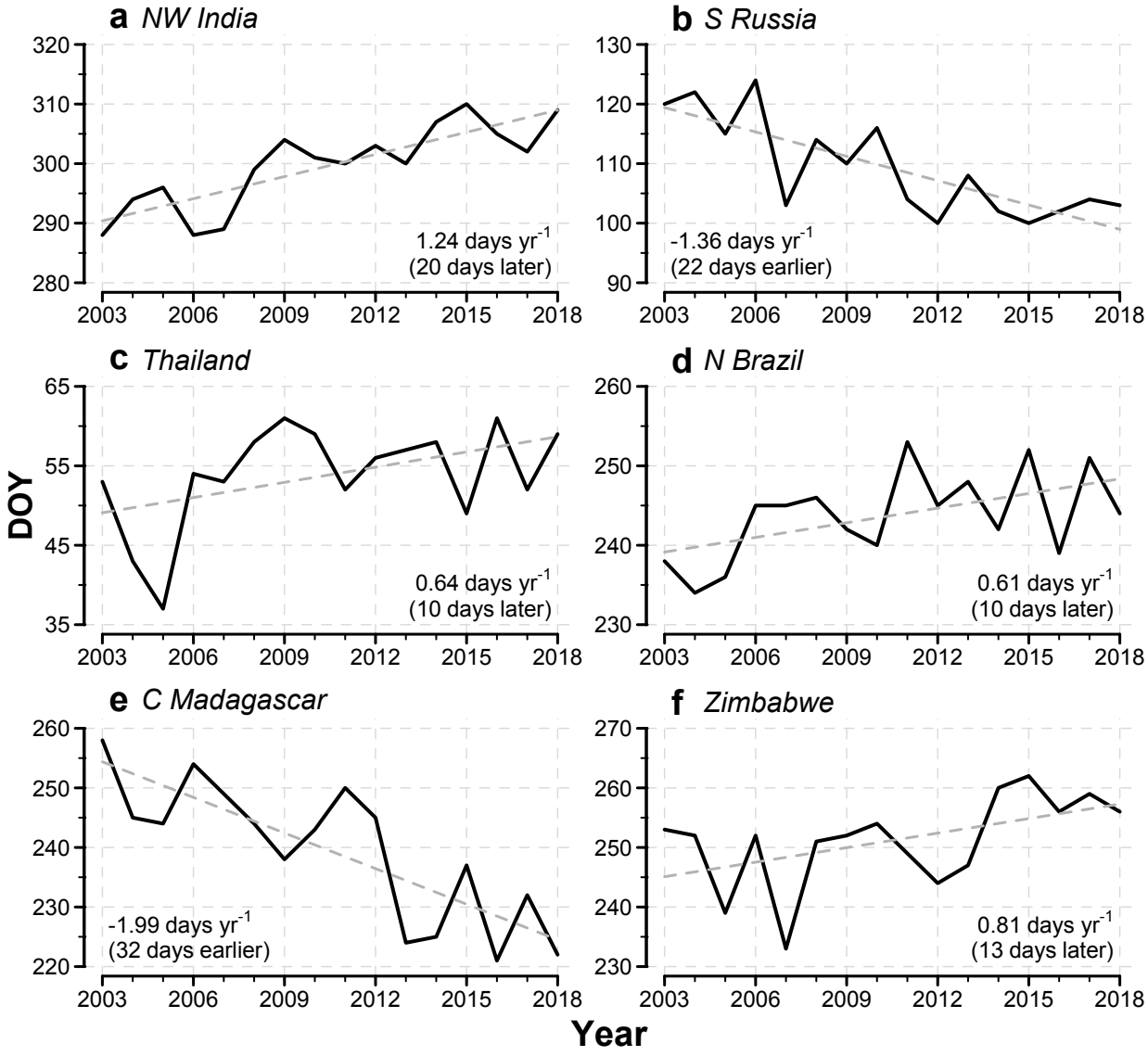


Figure F.1: Temporal shifts in the primary fire season over a 16-year period from 2003-2018 in secondary regions of interest: (a) north-west India, (b) south Russia (Siberia), (c) Thailand, (d) north Brazil (Pará), (e) central Madagascar, and (f) Zimbabwe. These ROIs are the same as described in Table 6.1. Black lines depict the day of year of the midpoint of the primary fire season, and gray, dashed lines denote the linear fit across the 2003-2018 time period. All trends are statistically significant at $p < 0.1$.

Table F.3: Regions of interest with coherent spatial signals of a temporal shift in the midpoint of the primary fire season from 2003-2018. Here we expand Table 6.1 to compare temporal shifts derived from MCD64A1 burned area with those derived from MxD14A1 active fire area.

Code	Region	MCD64A1		MxD14A1	
		Trend (days yr^{-1}; total 16-yr shift)	*p-value*	*Trend* (days yr^{-1}; total 16-yr shift)	*p-value*
1a	NW India	+1.24 (20 days)	< 0.01	+0.99 (16 days)	< 0.01
1b*	SW Russia	+2.41 (39 days)	< 0.01	+2.52 (40 days)	< 0.01
1c	S Russia	-1.36 (22 days)	< 0.01	-0.92 (15 days)	< 0.01
1d	Thailand	+0.64 (10 days)	0.07	+0.39 (6 days)	0.27
2a*	N Australia	-2.41 (39 days)	< 0.01	-1.92 (32 days)	< 0.01
2b	C Madagascar	-1.99 (32 days)	< 0.01	-0.94 (15 days)	0.02
2c	Zimbabwe	+0.81 (13 days)	0.04	+0.93 (15 days)	0.02
2d	N Brazil	+0.61 (10 days)	0.04	+0.7 (11 days)	0.01

* Case study regions; N = North, S = South, W = West, E = East, C = Central

F.6 Case study 1: southwest Russia

Table F.4: Temporal shifts in the midpoint of the primary fire season in oblasts in southwest Russia.

Region	*Trend* (days yr^{-1}; total 16-yr shift)	*p-value*	*Mean Annual BA* (km^2)	
SW Russia	**+2.41 (39 days)**	**< 0.01**	**10932 ± 6511**	
Krasnodar	+2.69 (43 days)	< 0.01	3861 ± 1692	35%
Adygea	+2.8 (45 days)	< 0.01	229 ± 120	2%
Rostov	+1.59 (25 days)	0.01	3269 ± 2559	30%
Stavropol	+1.93 (31 days)	< 0.01	3573 ± 2493	33%

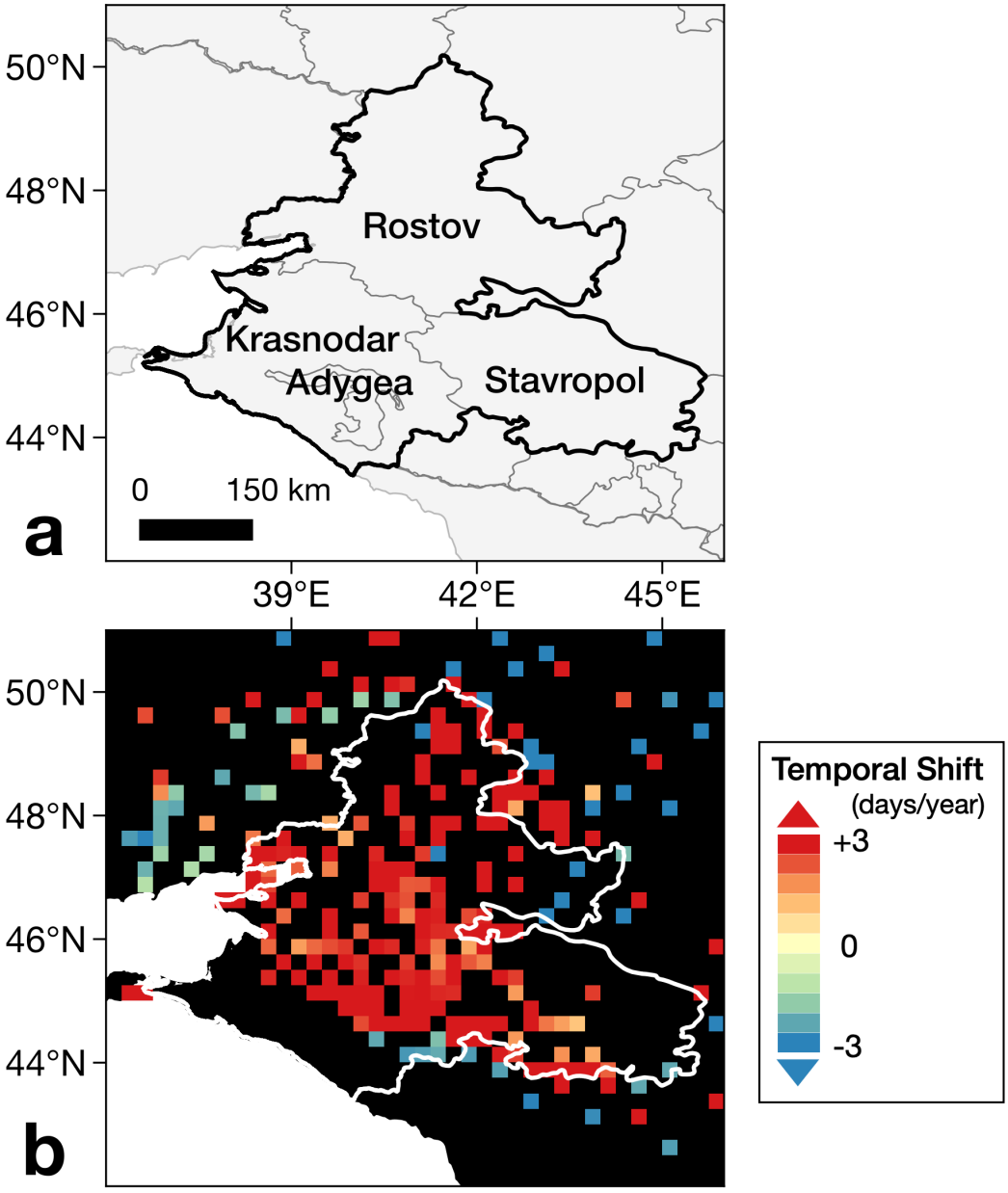


Figure F.2: Study area in southwest Russia. (a) Oblasts within the southwest Russia study region: Krasnodar Krai, Republic of Adygea, Rostov Oblast, and Stavropol Krai. (b) Gridded temporal shifts in the midpoint of the primary fire season from 2003-2018 (same as Figure 6.1).

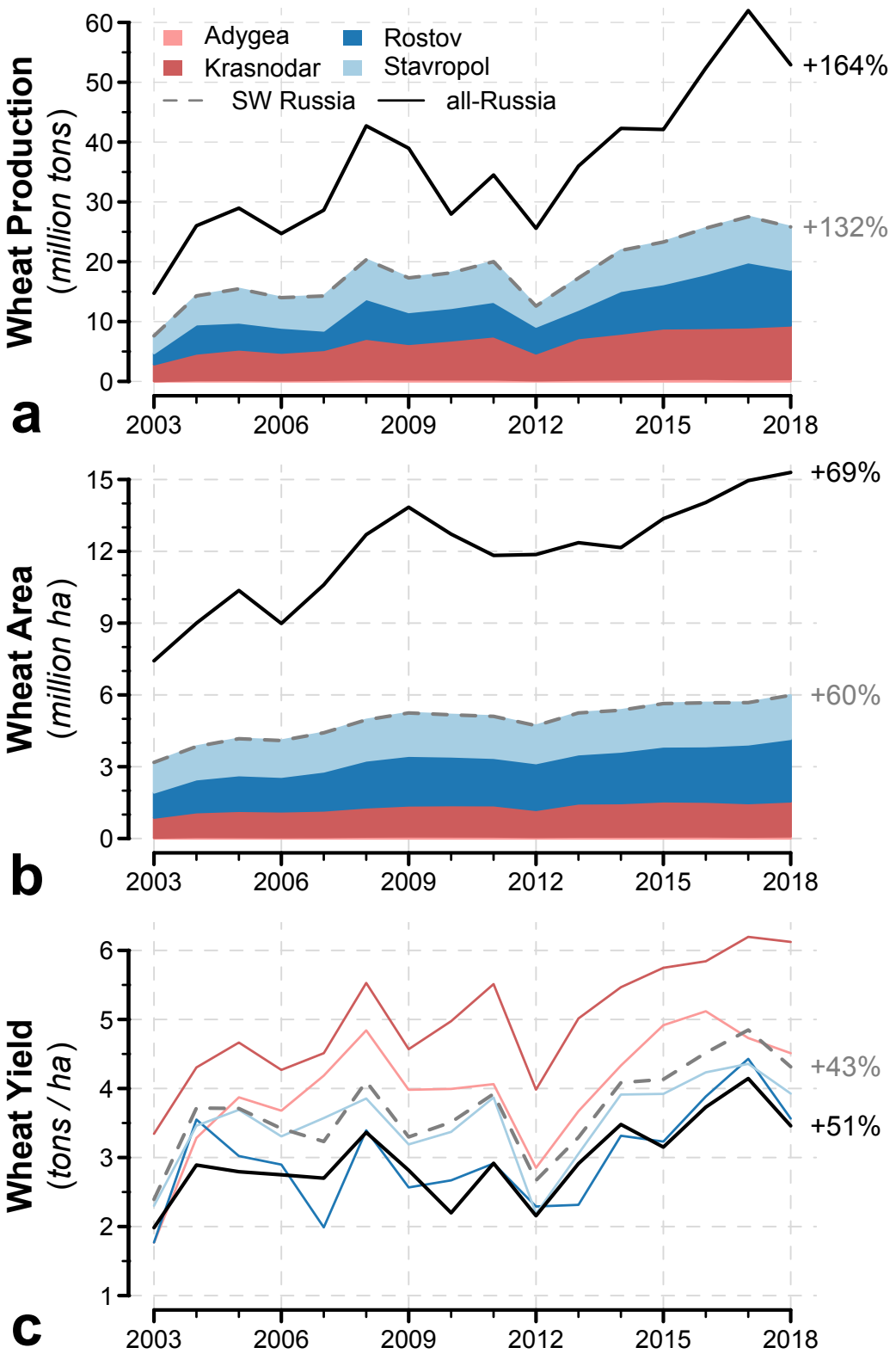


Figure F.3: Winter wheat in southwest Russia from 2003-2018: (a) production, (b) sown area, and (c) yield (ROSSTAT, 2020a,b). Non-grayscale colors correspond to federal provinces within the study region: Republic of Adygea, Rostov, Krasnodar, and Stavropol. The black and gray lines denote the all-Russia and southwest Russia aggregates, respectively.

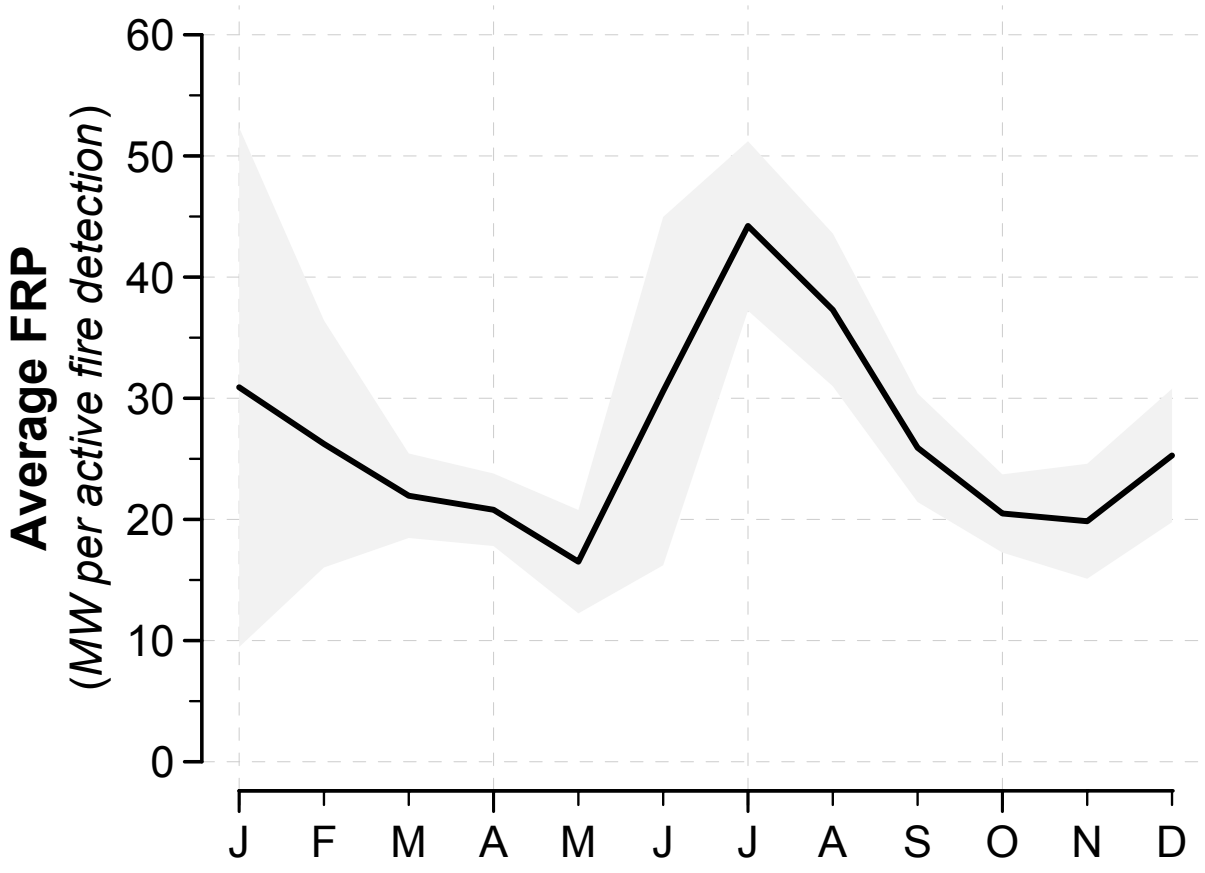


Figure F.4: Average fire intensity per active fire detection in southwest Russia by month from 2003-2018: Fire Radiative Power (FRP, in MW) is from MODIS MCD14ML active fire product. The black line shows the average FRP, and the gray envelope denotes ±1SD.

F.7 Case study 2: north Australia

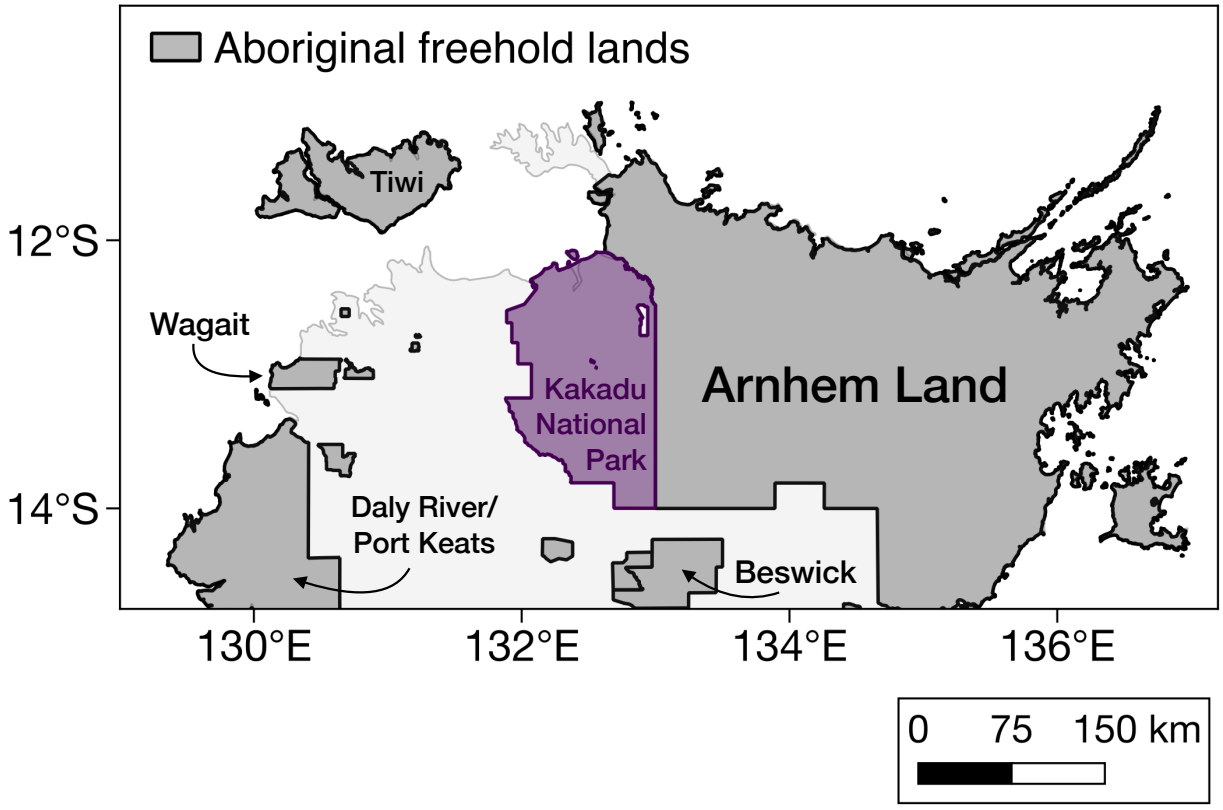


Figure F.5: Aboriginal freehold lands in north Australia: Major Aboriginal freehold lands in the Top End of the Northern Territory, including Arnhem Land, as well as Kakadu National Park (Data: Global Forest Watch/World Resources Institute, Australian open government data: `data.gov.au`)

The Arnhem Land Fire Abatement (ALFA) projects follow an earlier joint fire management project launched in the 1990s in the adjacent Kakadu National Park but avoids the missteps in Kakadu — namely, marginalization of Indigenous fire managers in planning and implementation of the project and, eventually, over-burning practices criticized by Aboriginal people (Figure F.5) (Price et al., 2012; Petty et al., 2015).

As a check, we compared our results using MCD64A1 burned area with those using NAFI fire perimeters. The two datasets yield similar results (Figure F.7). In line with the observed decrease in LDS burned area, we find that five global emissions inventories report decreases in fire-related CO_2 emissions from this region 48-56% during the LDS. However, increases in fuel consumption, as indicated by the Global Fire Emissions Database (GFEDv4s), as well as satellite observations of vegetation greenness and model projections of fuel load, may partly offset these reductions in fire emissions (Figure F.8) (Clarke et al., 2016; van der Werf et al., 2017; Chen

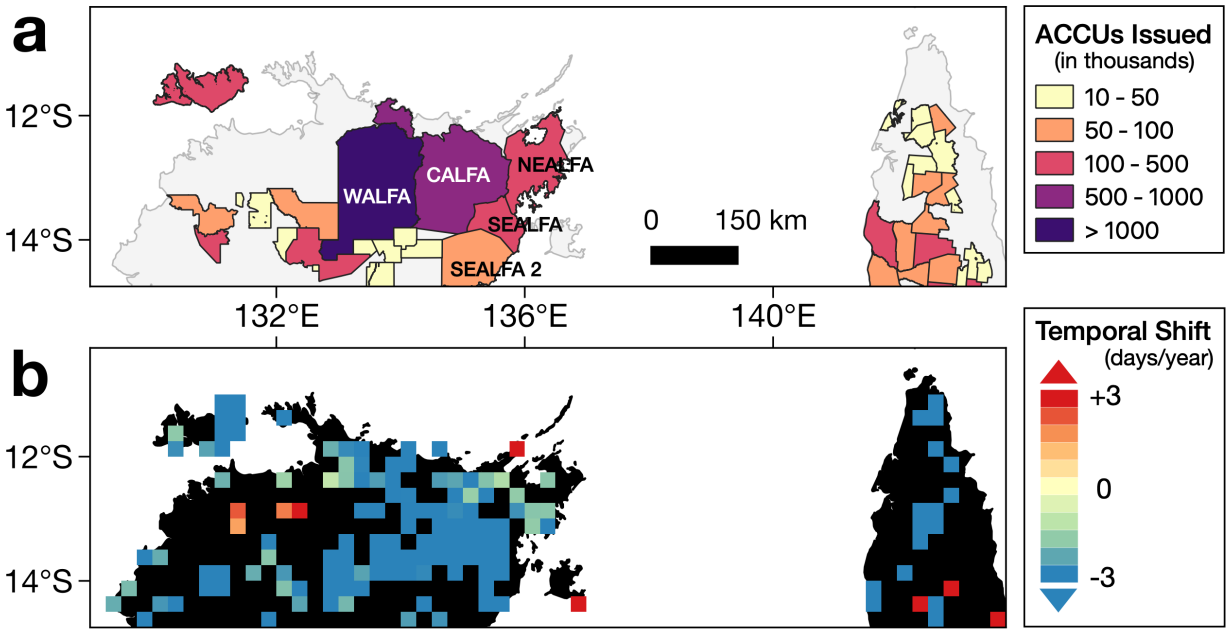


Figure F.6: Savanna burning projects in north Australia: Savanna burning projects in the Top End of the Northern Territory and Cape York in Queensland under the Australian government's Emissions Reduction Fund. (a) Total Australia carbon credit units (ACCUs) issued from the 2012-13 to the 2018-19 financial year. The five Arnhem Land Fire Abatement (ALFA) projects are labeled. Only projects with non-zero ACCUs accrued are shown. (Data: Clean Energy Regulator: `http://www.cleanenergyregulator.gov.au/`). (b) Gridded temporal shifts in the midpoint of the primary fire season from 2003-2018 (same as Figure 6.1).

et al., 2019).

According to the five global inventories, fire-related CO_2 emissions during the LDS have similarly decreased by 48-56% (Figure F.8a). CO_2 emissions peak during the LDS in August and September when fuel consumption is highest (Figure F.8b,d). However, fuel consumption, the product of fuel load and combustion completeness, is a complicating factor, because it is either directly used or indirectly accounted for to calculate dry matter emissions in fire inventories. Methodology on fuel consumption differs among inventories: for example, while FINNv1.5 assumes a static fuel load, GFEDv4s dynamically models fuel load at monthly timesteps (Wiedinmyer et al., 2011; van der Werf et al., 2010). In particular, the 48% decrease in GFEDv4s CO_2 is the smallest among the five inventories, and increases in GFEDv4s fuel consumption (+13% from 2003-2016) — consistent with recent "greening" trends that indicate greater fuel load (Chen et al., 2019) — partly offset the decrease in its fire emissions (Figure F.8c). Clarke et al. (2016) projects an increase in fuel load (i.e., fine litter) across Australia in the upcoming decades under climate change.

Table F.5: Temporal shifts in the midpoint of the primary fire season in savanna burning project areas in north Australia.

Region	*Trend* (days yr^{-1}; total 16-yr shift)	*p-value*	*Mean Annual BA* (km^2)	
SW Russia	**+2.41 (39 days)**	**< 0.01**	**10932 ± 6511**	
Krasnodar	+2.69 (43 days)	< 0.01	3861 ± 1692	35%
Adygea	+2.8 (45 days)	< 0.01	229 ± 120	2%
Rostov	+1.59 (25 days)	0.01	3269 ± 2559	30%
Stavropol	+1.93 (31 days)	< 0.01	3573 ± 2493	33%

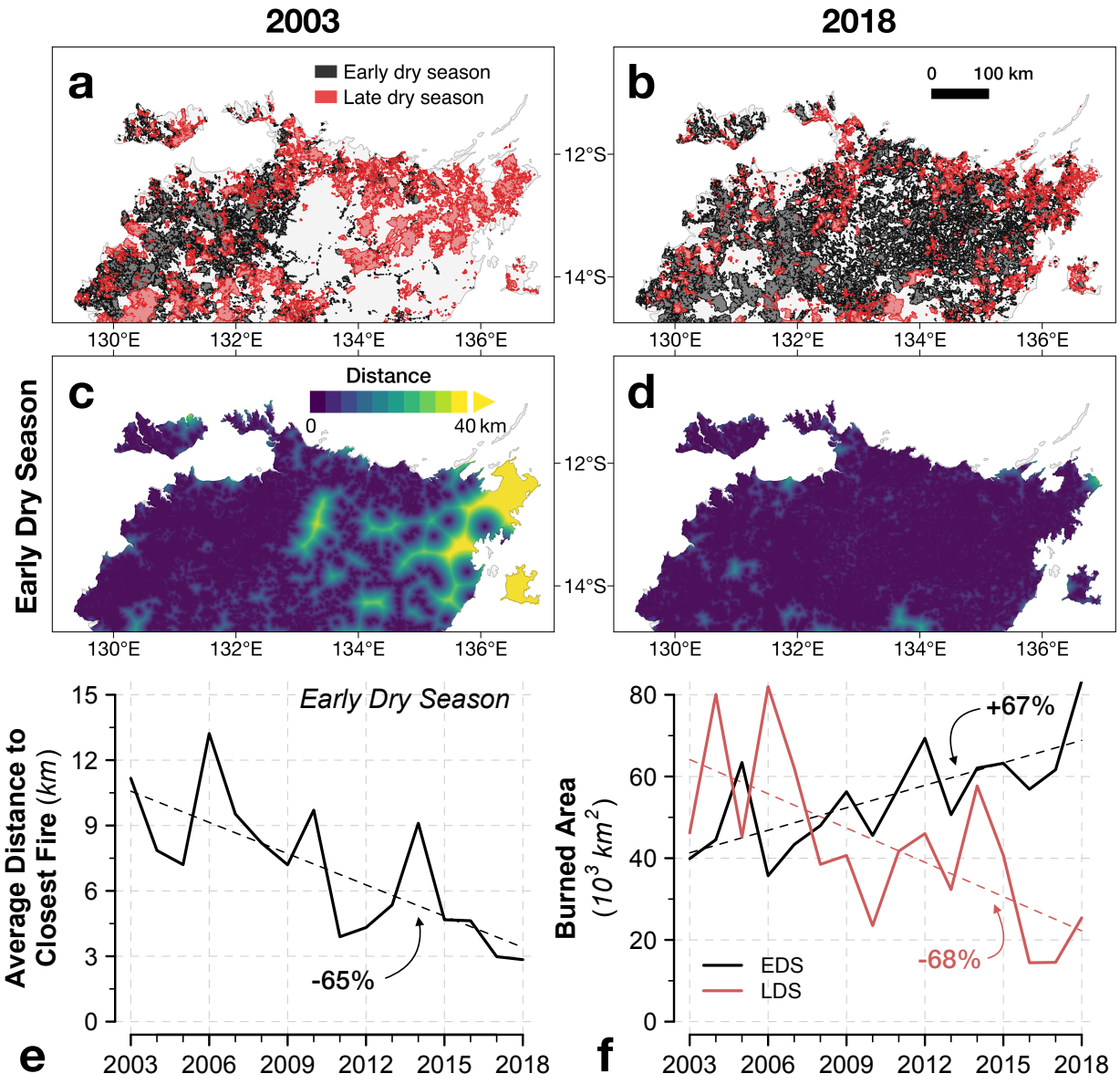


Figure F.7: Trends in early and late dry season fires in north Australia from 2003-2018: Same as Figure 6.4 but using fire perimeters from North Australia and Rangelands Fire Information (NAFI). Spatial comparison of NAFI burned area during the early dry season (EDS, black shading) and late dry season (LDS, red shading) in the Top End of the Northern Territory in (a) 2003 and (b) 2018. Smaller islands without burned area are excluded. Spatial distribution of the per-pixel distance in km to the closest burned area during the EDS in (c) 2003 and (d) 2018. (e) Annual trend in the average distance (in km) to closest fire during the EDS from 2003 to 2018, averaged over all pixels. This calculation excludes burned pixels, or areas with a distance of 0 km to the closest fire. Maximum distance is capped at 100 km. (f) Trends in EDS and LDS burned area. The linear trends shown in (e) and (f) are statistically significant at $p < 0.05$.

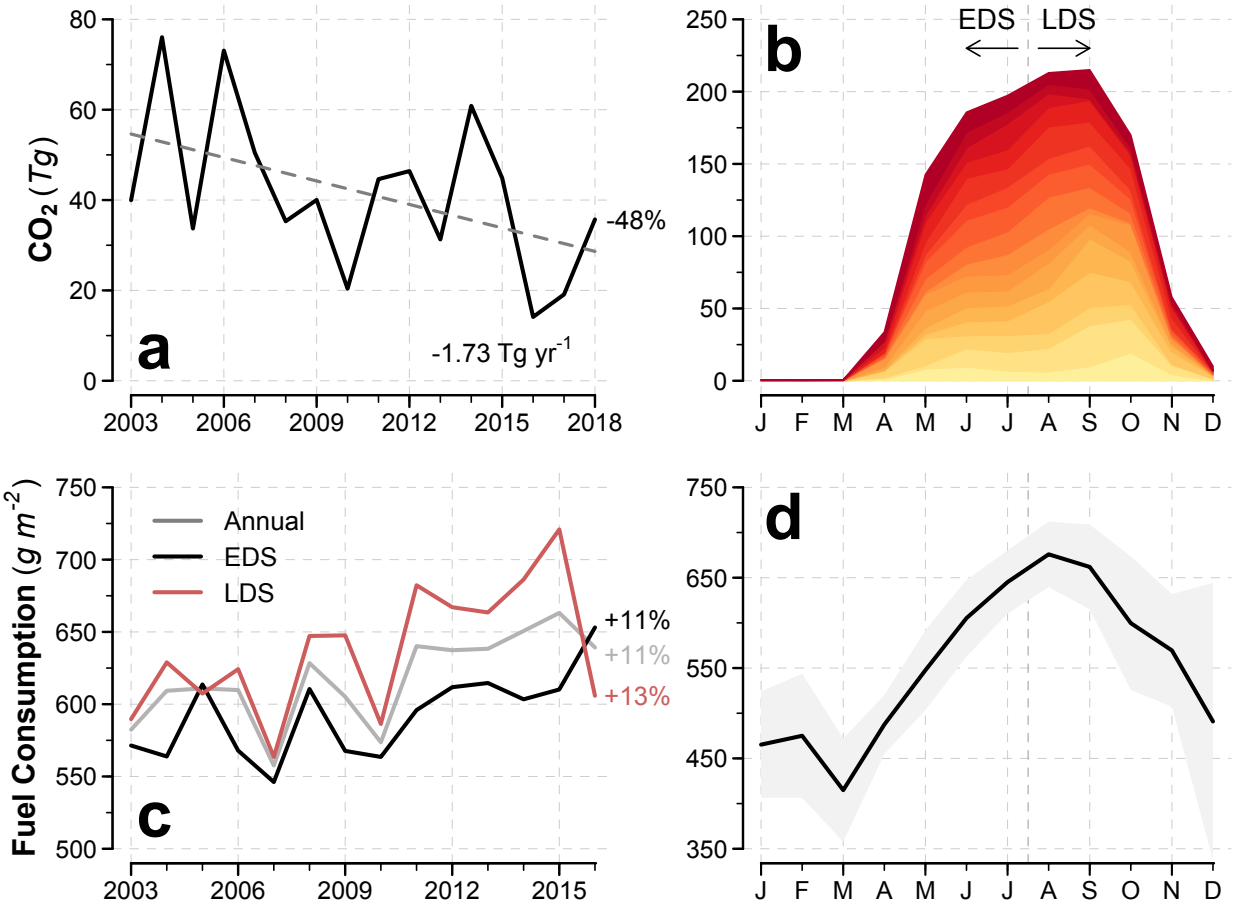


Figure F.8: Trends in GFEDv4s CO_2 emissions and fuel consumption in north Australia: (a) Trend in annual LDS CO_2 emissions and (b) Stacked monthly CO_2 emissions from 2003-2018. (c) Trend in fuel consumption (in terms of grams dry matter per m^2 burned), averaged across the EDS, LDS, and annually from 2003-2016. (d) Average monthly fuel consumption with ±1SD denoted by the gray envelope. All trends shown in (c) and (d) are statistically significant at $p < 0.1$.

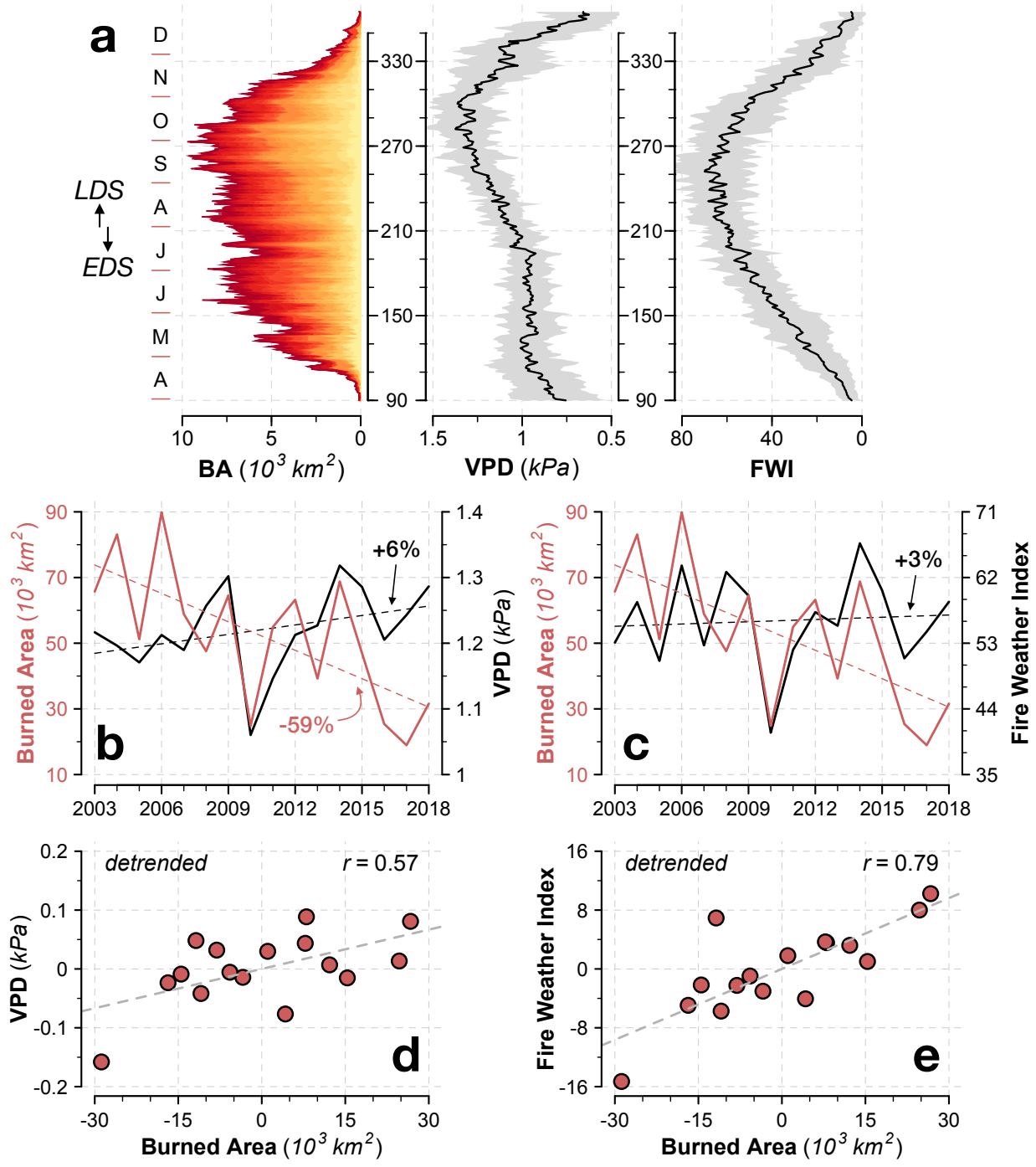


Figure F.9: Meteorology drives the inter-annual variability in burned area in north Australia during the late dry season: (a) Daily burned area, vapor pressure deficit (VPD), and fire weather index (FWI) across the early dry season (EDS) and late dry season (LDS) from 2003-2018. Burned area is summed by day, while VPD and FWI are averaged with ±1SD depicted by the gray envelopes. Interannual trends in (b, c) LDS burned area ($p < 0.05$), (b) VPD ($p = 0.18$), and (c) FWI ($p = 0.77$). Annual mean VPD and FWI are temporally averaged using the daily mean burned area as weights to place greater emphasis on VPD and FWI on consistently fire-intensive days of the year. Detrended correlation between (d) LDS burned area and VPD, and (e) LDS burned area and FWI. Correlation coefficients are inset.

References

Aalde, H., Gonzalez, P., Gytarsky, M., Krug, T., Kurz, W. A., Lasco, R. D., Martino, D. L., McConkey, B. G., Ogle, S., Paustian, K., Raison, J., Ravindranath, N., Schoene, D., Smith, P., Somogyi, Z., van Amstel, A., & Verchot, L. (2006). Chapter 2: Generic Methodologies Applicable to Multiple Land-Use Categories. In *2006 IPCC Guidel. Natl. Greenh. Gas Invent. Vol 4 Agric. For. Other L. Use*.

Akagi, S. K., Yokelson, R. J., Wiedinmyer, C., Alvarado, M. J., Reid, J. S., Karl, T., Crounse, J. D., & Wennberg, P. O. (2011). Emission factors for open and domestic biomass burning for use in atmospheric models. *Atmos. Chem. Phys.*, 11(9), 4039–4072.

Alcamo, J., Dronin, N., Endejan, M., Golubev, G., & Kirilenko, A. (2007). A new assessment of climate change impacts on food production shortfalls and water availability in Russia. *Glob. Environ. Chang.*, 17(3-4), 429–444.

Amann, M., Purohit, P., Bhanarkar, A. D., Bertok, I., Borken-Kleefeld, J., Cofala, J., Heyes, C., Kiesewetter, G., Klimont, Z., Liu, J., Majumdar, D., Nguyen, B., Rafaj, P., Rao, P. S., Sander, R., Schöpp, W., Srivastava, A., & Vardhan, B. H. (2017). Managing future air quality in megacities: A case study for Delhi. *Atmos. Environ.*, 161, 99–111.

Andela, N., Morton, D. C., Giglio, L., Chen, Y., van der Werf, G. R., Kasibhatla, P. S., DeFries, R. S., Collatz, G. J., Hantson, S., Kloster, S., Bachelet, D., Forrest, M., Lasslop, G., Li, F., Mangeon, S., Melton, J. R., Yue, C., & Randerson, J. T. (2017). A human-driven decline in global burned area. *Science.*, 356, 1356–1362.

Andela, N., Morton, D. C., Giglio, L., Paugam, R., Chen, Y., Hantson, S., van der Werf, G. R., & Randerson, J. T. (2019). The Global Fire Atlas of individual fire size, duration, speed, and direction. *Earth Syst. Sci. Data*, 11, 529–552.

Andela, N. & van der Werf, G. R. (2014). Recent trends in African fires driven by cropland expansion and El Niño to la Niña transition. *Nat. Clim. Chang.*, 4(9), 791–795.

Andersen, A. N., Cook, G. D., Corbett, L. K., Douglas, M. M., Eager, R. W., Russell-Smith, J., Setterfield, S. A., Williams, R. J., & Woinarski, J. C. (2005). Fire frequency and biodiversity conservation in Australian tropical savannas: Implications from the Kapalga fire experiment. *Austral Ecol.*, 30, 155–167.

Andreae, M. O. (2019). Emission of trace gases and aerosols from biomass burning – An updated assessment. *Atmos. Chem. Phys.*, 19, 8523–8546.

Andreae, M. O. & Merlet, P. (2001). Emissions of trace gases and aerosols from biomass burning. *Global Biogeochem. Cycles*, 15(4), 955–966.

Ansell, J., Evans, J., Rangers, A., Rangers, A. S., Rangers, D., Rangers, J., Rangers, M., Rangers, N. N., Rangers, W., Rangers, Y., & Rangers, Y. M. (2020). Contemporary Aboriginal savanna burning projects in Arnhem Land: a regional description and analysis of the fire management aspirations of Traditional Owners. *Int. J. Wildl. Fire*, 29(5), 371–385.

Aragão, L. E., Anderson, L. O., Fonseca, M. G., Rosan, T. M., Vedovato, L. B., Wagner, F. H., Silva, C. V., Silva Junior, C. H., Arai, E., Aguiar, A. P., Barlow, J., Berenguer, E., Deeter, M. N., Domingues, L. G., Gatti, L., Gloor, M., Malhi, Y., Marengo, J. A., Miller, J. B., Phillips, O. L., & Saatchi, S. (2018). 21st Century drought-related fires counteract the decline of Amazon deforestation carbon emissions. *Nat. Commun.*, 9, 536.

Artés, T., Oom, D., de Rigo, D., Durrant, T. H., Maianti, P., Libertà, G., & San-Miguel-Ayanz, J. (2019). A global wildfire dataset for the analysis of fire regimes and fire behaviour. *Sci. Data*, 6(1), 296.

Asner, G. P. & Lobell, D. B. (2000). A Biogeophysical Approach for Automated SWIR Unmixing of Soils and Vegetation. *Remote Sens. Environ.*, 74(1), 99–112.

Asoka, A., Gleeson, T., Wada, Y., & Mishra, V. (2017). Relative contribution of monsoon precipitation and pumping to changes in groundwater storage in India. *Nat. Geosci.*, 10(2), 109–117.

Avery, T. E. & Berlin, G. L. (1992). *Fundamentals of remote sensing and airphoto interpretation*. New York, NY: Macmillan Publishing Company, 5 edition.

Azzari, G., Jain, M., & Lobell, D. B. (2017). Towards fine resolution global maps of crop yields: Testing multiple methods and satellites in three countries. *Remote Sens. Environ.*, 202, 129–141.

Azzari, G. & Lobell, D. B. (2017). Landsat-based classification in the cloud: An opportunity for a paradigm shift in land cover monitoring. *Remote Sens. Environ.*, 202, 64–74.

Badarinath, K. V. S., Kharol, S. K., & Sharma, A. R. (2009). Long-range transport of aerosols from agriculture crop residue burning in Indo-Gangetic Plains-A study using LIDAR, ground measurements and satellite data. *J. Atmos. Solar-Terrestrial Phys.*, 71(1), 112–120.

Badarinath, K. V. S., Kiran Chand, T. R., & Krishna Prasad, V. (2006). Agriculture crop residue burning in the Indo-Gangetic Plains - A study using IRS-P6 AWiFS satellite data. *Curr. Sci.*, 91(8), 1085–1089.

Balwinder-Singh, Humphreys, E., Gaydon, D. S., & Eberbach, P. L. (2016). Evaluation of the effects of mulch on optimum sowing date and irrigation management of zero till wheat in central Punjab, India using APSIM. *F. Crop. Res.*, 197, 83–96.

Balwinder-Singh, McDonald, A. J., Srivastava, A. K., & Gerard, B. (2019). Tradeoffs between groundwater conservation and air pollution from agricultural fires in northwest India. *Nat. Sustain.*, 2, 580–583.

Bey, I., Jacob, D. J., Yantosca, R. M., Logan, J. A., Field, B. D., Fiore, A. M., Li, Q., Liu, H. Y., Mickley, L. J., & Schultz, M. G. (2001). Global modeling of tropospheric chemistry with assimilated meteorology: Model description and evaluation. *J. Geophys. Res. Atmos.*, 106(D19), 23073–23095.

Bhuvaneshwari, S., Hettiarachchi, H., & Meegoda, J. N. (2019). Crop residue burning in India: Policy challenges and potential solutions. *Int. J. Environ. Res. Public Health*, 16(5).

Bikkina, S., Andersson, A., Kirillova, E. N., Holmstrand, H., Tiwari, S., Srivastava, A. K., Bisht, D. S., & Gustafsson, Ö. (2019). Air quality in megacity Delhi affected by countryside biomass burning. *Nat. Sustain.*, 2, 200–205.

Bowker, D. E., Davis, R. E., Myrick, D. L., Stacy, K., & Jones, W. T. (1985). *Spectral Reflectances of Natural Targets for Use in Remote Sensing Studies*. Technical report.

Bowman, D. M. J. S., Kolden, C. A., Abatzoglou, J. T., Johnston, F. H., van der Werf, G. R., & Flannigan, M. (2020). Vegetation fires in the Anthropocene. *Nat. Rev. Earth Environ.*, 1, 500–515.

Brown, J. C., Kastens, J. H., Coutinho, A. C., Victoria, D. d. C., & Bishop, C. R. (2013). Classifying multiyear agricultural land use data from Mato Grosso using time-series MODIS vegetation index data. *Remote Sens. Environ.*, 130, 39–50.

Burney, J. & Ramanathan, V. (2014). Recent climate and air pollution impacts on Indian agriculture. *Proc. Natl. Acad. Sci.*, 111(46), 16319–16324.

Cao, G., Zhang, X., Gong, S., & Zheng, F. (2008). Investigation on emission factors of particulate matter and gaseous pollutants from crop residue burning. *J. Environ. Sci.*, 20, 50–55.

Carter, T., Heald, C., Jimenez, J., Campuzano-Jost, P., Kondo, Y., Moteki, N., Schwarz, J., Wiedinmyer, C., Darmenov, A., & Kaiser, J. (2020). How emissions uncertainty influences the distribution and radiative impacts of smoke from fires in North America. *Atmos. Chem. Phys.*, 20, 2073–2097.

Casu, F., Manunta, M., Agram, P. S., & Crippen, R. E. (2017). Big Remotely Sensed Data: tools, applications and experiences. *Remote Sens. Environ.*, 202(September), 1–2.

Chakrabarti, S., Khan, M. T., Kishore, A., Roy, D., & Scott, S. P. (2019). Risk of acute respiratory infection from crop burning in India: estimating disease burden and economic welfare from satellite and national health survey data for 250 000 persons. *Int. J. Epidemiol.*, 48, 1113–1124.

Chen, C., Park, T., Wang, X., Piao, S., Xu, B., Chaturvedi, R. K., Fuchs, R., Brovkin, V., Ciais, P., Fensholt, R., Tømmervik, H., Bala, G., Zhu, Z., Nemani, R. R., & Myneni, R. B. (2019). China and India lead in greening of the world through land-use management. *Nat. Sustain.*, 2(2), 122–129.

Chen, D., Huang, J., & Jackson, T. J. (2005). Vegetation water content estimation for corn and soybeans using spectral indices derived from MODIS near- and short-wave infrared bands. *Remote Sens. Environ.*, 98(2-3), 225–236.

Chen, Y., Morton, D. C., Andela, N., van der Werf, G. R., Giglio, L., & Randerson, J. T. (2017). A pan-tropical cascade of fire driven by El Niño/Southern Oscillation. *Nat. Clim. Chang.*, 7(12), 906–911.

Chen, Y., Randerson, J. T., Coffield, S. R., Foufoula-Georgiou, E., Smyth, P., Graff, C. A., Morton, D. C., Andela, N., van der Werf, G. R., Giglio, L., & Ott, L. E. (2020). Forecasting Global Fire Emissions on Subseasonal to Seasonal (S2S) Time Scales. *J. Adv. Model. Earth Syst.*, 12(9), e2019MS001955.

Choudhury, S., Rajpal, H., Saraf, A. K., & Panda, S. (2007). Mapping and forecasting of North Indian winter fog: an application of spatial technologies. *Int. J. Remote Sens.*, 28(15-16), 3649–3663.

Christian, T. J., Kleiss, B., Yokelson, R. J., Holzinger, R., Crutzen, P. J., Hao, W. M., Saharjo, B. H., & Ward, D. E. (2003). Comprehensive laboratory measurements of biomass-burning emissions: 1. Emissions from Indonesian, African, and other fuels. *J. Geophys. Res.*, 108(D23), 4719.

Chuvieco, E., Lizundia-loiola, J., Pettinari, M. L., Ramo, R., Padilla, M., Mouillot, F., Laurent, P., Storm, T., Heil, A., & Plummer, S. (2018). Generation and analysis of a new global burned area product based on MODIS 250m reflectance bands and thermal anomalies. *Earth Syst. Sci. Data*, 10, 2015–2031.

CIESIN (2017). Gridded Population of the World, Version 4 (GPWv4): Population Count Adjusted to Match 2015 Revision of UN WPP Country Totals, Revision 10.

Clarke, H., Pitman, A. J., Kala, J., Carouge, C., Haverd, V., & Evans, J. P. (2016). An investigation of future fuel load and fire weather in Australia. *Clim. Change*, 139(3-4), 591–605.

Crippa, P., Castruccio, S., Archer-Nicholls, S., Lebron, G. B., Kuwata, M., Thota, A., Sumin, S., Butt, E., Wiedinmyer, C., & Spracklen, D. V. (2016). Population exposure to hazardous air quality due to the 2015 fires in Equatorial Asia. *Sci. Rep.*, 6, 37074.

Crowley, M. A., Cardille, J. A., White, J. C., & Wulder, M. A. (2019a). Generating intra-year metrics of wildfire progression using multiple open-access satellite data streams. *Remote Sens. Environ.*, 232, 111295.

Crowley, M. A., Cardille, J. A., White, J. C., & Wulder, M. A. (2019b). Multi-sensor, multi-scale, Bayesian data synthesis for mapping within-year wildfire progression. *Remote Sens. Lett.*, 10(3), 302–311.

Cusworth, D. H., Mickley, L. J., Sulprizio, M. P., Liu, T., Marlier, M. E., Defries, R. S., Guttikunda, S. K., & Gupta, P. (2018). Quantifying the influence of agricultural fires in northwest India on urban air pollution in Delhi, India. *Environ. Res. Lett.*, 13(4), 044018.

Darmenov, A. S. & da Silva, A. (2013). *The Quick Fire Emissions Dataset (QFED) - Documentation of versions 2.1, 2.2, and 2.4*. Technical report.

de Sousa, A. (2019). The Pessimist's Guide to 2019: Fires, Floods, and Famine.

Dekker, I. N., Houweling, S., Pandey, S., Krol, M., Röckmann, T., Borsdorff, T., Landgraf, J., & Aben, I. (2019). What caused the extreme CO concentrations during the 2017 high pollution episode in India? *Atmos. Chem. Phys.*, 19, 3433–3445.

Dennis, R. A., Mayer, J., Applegate, G., Chokkalingam, U., Colfer, C. J. P., Kurniawan, I., Lachowski, H., Maus, P., Permana, R. P., Ruchiat, Y., Stolle, F., Suyanto, & Tomich, T. P. (2005). Fire, people and pixels: Linking social science and remote sensing to understand underlying causes and impacts of fires in Indonesia. *Hum. Ecol.*, 33(4), 465–504.

Deppermann, A., Balkovič, J., Bundle, S. C., Di Fulvio, F., Havlik, P., Leclère, D., Lesiv, M., Prishchepov, A. V., & Schepaschenko, D. (2018). Increasing crop production in Russia and Ukraine - Regional and global impacts from intensification and recultivation. *Environ. Res. Lett.*, 13(2), 025008.

Dey, S. (2018). On the theoretical aspects of improved fog detection and prediction in India. *Atmos. Res.*, 202, 77–80.

Dhillon, B. S. & Kumar, R. (2021). Short-duration paddy varieties can turn the tide.

Di Giuseppe, F., Pappenberger, F., Wetterhall, F., Krzeminski, B., Camia, A., Libertá, G., & Miguel, J. S. (2016). The potential predictability of fire danger provided by numerical weather prediction. *J. Appl. Meteorol. Climatol.*, 55(11), 2469–2491.

Di Giuseppe, F., Rémy, S., Pappenberger, F., & Wetterhall, F. (2017). Improving forecasts of biomass burning emissions with the fire weather index. *J. Appl. Meteorol. Climatol.*, 56(10), 2789–2799.

Dickinson, M. B., Hudak, A. T., Zajkowski, T., Loudermilk, E. L., Schroeder, W., Ellison, L., Kremens, R. L., Holley, W., Martinez, O., Paxton, A., Bright, B. C., O'Brien, J. J., Hornsby, B., Ichoku, C., Faulring, J., Gerace, A., Peterson, D., & Mauceri, J. (2016). Measuring radiant emissions from entire prescribed fires with ground, airborne and satellite sensors - RxCADRE 2012. *Int. J. Wildl. Fire*, 25, 48–61.

Eck, T. F., Holben, B. N., Giles, D. M., Slutsker, I., Sinyuk, A., Schafer, J. S., Smirnov, A., Sorokin, M., Reid, J. S., Sayer, A. M., Hsu, N. C., Shi, Y. R., Levy, R. C., Lyapustin, A., Rahman, M. A., Liew, S. C., Salinas Cortijo, S. V., Li, T., Kalbermatter, D., Keong, K. L., Yuggotomo, M. E., Aditya, F., Mohamad, M., Mahmud, M., Chong, T. K., Lim, H. S., Choon, Y. E., Deranadyan, G., Kusumaningtyas, S. D., & Aldrian, E. (2019). AERONET Remotely Sensed Measurements and Retrievals of Biomass Burning Aerosol Optical Properties During the 2015 Indonesian Burning Season. *J. Geophys. Res. Atmos.*, 124(8), 4722–4740.

Eva, H. & Lambin, E. F. (1998). Burnt area mapping in Central Africa using ATSR data. *Int. J. Remote Sens.*, 18, 3473–3497.

Evans, J. & Russell-Smith, J. (2020). Delivering effective savanna fire management for defined biodiversity conservation outcomes: an Arnhem Land case study. *Int. J. Wildl. Fire*, 29(5), 386–400.

Fanin, T. & van der Werf, G. R. (2017). Precipitation – fire linkages in Indonesia (1997 – 2015). *Biogeosciences*, 14, 3995–4008.

Fasoli, B., Lin, J. C., Bowling, D. R., Mitchell, L., & Mendoza, D. (2018). Simulating atmospheric tracer concentrations for spatially distributed receptors: Updates to the Stochastic Time-Inverted Lagrangian Transport model's R interface (STILT-R version 2). *Geosci. Model Dev.*, 11(7), 2813–2824.

Fellmann, T., Hélaine, S., & Nekhay, O. (2014). Harvest failures, temporary export restrictions and global food security: the example of limited grain exports from Russia, Ukraine and Kazakhstan. *Food Secur.*, 6(5), 727–742.

Fernandes, K., Verchot, L., Baethgen, W., Gutierrez-Velez, V., Pinedo-Vasquez, M., & Martius, C. (2017). Heightened fire probability in Indonesia in non-drought conditions: the effect of increasing temperatures. *Environ. Res. Lett.*, 12(5), 054002.

Fernandes, P. M. & Botelho, H. S. (2003). A review of prescribed burning effectiveness in fire hazard reduction. *Int. J. Wildl. fire*, 12, 117–128.

Field, R. (2020). Evaluation of Global Fire Weather Database re-analysis and short-term forecast products. *Nat. Hazards Earth Syst. Sci.*, 20, 1123–1147.

Field, R. D., Spessa, A. C., Aziz, N. A., Camia, A., Cantin, A., Carr, R., De Groot, W. J., Dowdy, A. J., Flannigan, M. D., Manomaiphiboon, K., Pappenberger, F., Tanpipat, V., & Wang, X. (2015). Development of a Global Fire Weather Database. *Nat. Hazards Earth Syst. Sci.*, 15(6), 1407–1423.

Fornacca, D., Ren, G., & Xiao, W. (2017). Performance of Three MODIS fire products (MCD45A1, MCD64A1, MCD14ML), and ESA Fire_CCI in a mountainous area of Northwest Yunnan, China, characterized by frequent small fires. *Remote Sens.*, 9, 1131.

Freeborn, P. H., Wooster, M. J., Hao, W. M., Ryan, C. A., Nordgren, B. L., Baker, S. P., & Ichoku, C. (2008). Relationships between energy release, fuel mass loss, and trace gas an aerosol emissions during laboratory biomass fires. *J. Geophys. Res. Atmos.*, 113, D01301.

Funk, C., Peterson, P., Landsfeld, M., Pedreros, D., Verdin, J., Shukla, S., Husak, G., Rowland, J., Harrison, L., Hoell, A., & Michaelsen, J. (2015). The climate hazards infrared precipitation with stations - A new environmental record for monitoring extremes. *Sci. Data*, 2, 1–21.

Gao, Y., Zhang, M., Liu, Z., Wang, L., Wang, P., Xia, X., Tao, M., & Zhu, L. (2015). Modeling the feedback between aerosol and meteorological variables in the atmospheric boundary layer during a severe fog-haze event over the North China Plain. *Atmos. Chem. Phys.*, 15(8), 4279–4295.

Gautam, R., Hsu, N. C., Kafatos, M., & Tsay, S. (2007). Influences of winter haze on fog/low cloud over the Indo-Gangetic plains. *J. Geophys. Res. Atmos.*, 112, D05207.

Gautam, R., Patel, P., Singh, M., Liu, T., Mickley, L., Jethva, H., & DeFries, R. (2021). Extreme smog challenge of northern India intensified by increasing lower tropospheric stability. *Proc. Natl. Acad. Sci.*, (pp. (in review)).

Gautam, R. & Singh, M. K. (2018). Urban Heat Island Over Delhi Punches Holes in Widespread Fog in the Indo-Gangetic Plains. *Geophys. Res. Lett.*, 45, 1114–1121.

Ghude, S. D., Bhat, G. S., Prabhakaran, T., Jenamani, R. K., Chate, D. M., Safai, P. D., Karipot, A. K., Konwar, M., Pithani, P., Sinha, V., Rao, P. S., Dixit, S. A., Tiwari, S., Todekar, K., Varpe, S., Srivastava, A. K., Bisht, D. S., Murugavel, P., Ali, K., Mina, U., Dharua, M., Jaya Rao, Y., Padmakumari, B., Hazra, A., Nigam, N., Shende, U., Lal, D. M., Chandra, B. P., Mishra, A. K., Kumar, A., Hakkim, H., Pawar, H., Acharja, P., Kulkarni, R., Subharthi, C., Balaji, B., Varghese, M., Bera, S., & Rajeevan, M. (2017). Winter fog experiment over the Indo-Gangetic plains of India. *Curr. Sci.*, 112(4), 767–784.

Ghude, S. D., Jena, C. K., Beig, G., Kumar, R., Kulkarni, S. H., & Chate, D. M. (2016). Impact of emission mitigation on ozone-induced wheat and rice damage in India. *Curr. Sci.*, 110(8), 1452–1458.

Giglio, L. (2007). Characterization of the tropical diurnal fire cycle using VIRS and MODIS observations. *Remote Sens. Environ.*, 108, 407–421.

Giglio, L. (2015). *MODIS Collection 6 Active Fire Product User's Guide Revision A*. Technical report.

Giglio, L., Boschetti, L., Roy, D. P., Humber, M. L., & Justice, C. O. (2018). The Collection 6 MODIS burned area mapping algorithm and product. *Remote Sens. Environ.*, 217, 72–85.

Giglio, L., Csiszar, I., & Justice, C. O. (2006). Global distribution and seasonality of active fires as observed with the Terra and Aqua Moderate Resolution Imaging Spectroradiometer (MODIS) sensors. *J. Geophys. Res. Biogeosciences*, 111(2), G02016.

Giglio, L., Descloitres, J., Justice, C. O., & Kaufman, Y. J. (2003). An enhanced contextual fire detection algorithm for MODIS. *Remote Sens. Environ.*, 87, 273–282.

Giglio, L., Loboda, T., Roy, D. P., Quayle, B., & Justice, C. O. (2009). An active-fire based burned area mapping algorithm for the MODIS sensor. *Remote Sens. Environ.*, 113(2), 408–420.

Giglio, L., Randerson, J. T., & van der Werf, G. R. (2013). Analysis of daily, monthly, and annual burned area using the fourth-generation global fire emissions database (GFED4). *J. Geophys. Res. Biogeosciences*, 118, 1–12.

Giglio, L., Randerson, J. T., van der Werf, G. R., Kasibhatla, P. S., Collatz, G. J., Morton, D. C., & DeFries, R. S. (2010). Assessing variability and long-term trends in burned area by merging multiple satellite fire products. *Biogeosciences*, 7, 1171–1186.

Giglio, L., Schroeder, W., & Justice, C. O. (2016). The collection 6 MODIS active fire detection algorithm and fire products. *Remote Sens. Environ.*, 178, 31–41.

Goodwin, N. R. & Collett, L. J. (2014). Development of an automated method for mapping fire history captured in Landsat TM and ETM+ time series across Queensland, Australia. *Remote Sens. Environ.*, 148, 206–221.

Gorelick, N., Hancher, M., Dixon, M., Ilyushchenko, S., Thau, D., & Moore, R. (2017). Google Earth Engine: Planetary-scale geospatial analysis for everyone. *Remote Sens. Environ.*, 202, 18–27.

Götz, L., Djuric, I., & Nivievskyi, O. (2016). Regional Price Effects of Extreme Weather Events and Wheat Export Controls in Russia and Ukraine. *J. Agric. Econ.*, 67(3), 741–763.

Gras, J. L. & Jensen, J. B. (1999). Some Optical Properties of Smoke Aerosol in Indonesia. *Geophys. Res. Lett.*, 26(10), 1393–1396.

Gray, J., Sulla-Menashe, D., & Friedl, M. A. (2019). User Guide to Collection 6 MODIS Land Cover Dynamics (MCD12Q2) Product.

Hall, J. V., Loboda, T. V., Giglio, L., & McCarty, G. W. (2016). A MODIS-based burned area assessment for Russian croplands: Mapping requirements and challenges. *Remote Sens. Environ.*, 184, 506–521.

Harrison, M. E., Page, S. E., & Limin, S. H. (2009). The global impact of Indonesian forest fires. *Biologist*, 56(3), 156–163.

Hawbaker, T. J., Vanderhoof, M. K., Beal, Y.-J., Takacs, J. D., Schmidt, G. L., Falgout, J. T., Williams, B., Fairaux, N. M., Caldwell, M. K., Picotte, J. J., Howard, S. M., Stitt, S., & Dwyer, J. L. (2017). Mapping burned areas using dense time-series of Landsat data. *Remote Sens. Environ.*, 198, 504–522.

Hayasaka, H., Noguchi, I., Putra, E. I., Yulianti, N., & Vadrevu, K. (2014). Peat-fire-related air pollution in Central Kalimantan, Indonesia. *Environ. Pollut.*, 195, 257–266.

Heil, A., Kaiser, J. W., van der Werf, G. R., Wooster, M. J., Schultz, M. G., & van der Gon, H. D. (2010). *Assessment of the Real-Time Fire Emissions (GFASvo) by MACC*. Technical report.

Hersbach, H., Bell, B., Berrisford, P., Hirahara, S., Horányi, A., Muñoz-Sabater, J., Nicolas, J., Peubey, C., Radu, R., Schepers, D., Simmons, A., Soci, C., Abdalla, S., Abellan, X., Balsamo, G., Bechtold, P., Biavati, G., Bidlot, J., Bonavita, M., Chiara, G. D., Dahlgren, P., Dee, D., Diamantakis, M., Dragani, R., Flemming, J., Forbes, R., Fuentes, M., Geer, A., Haimberger, L., Healy, S., Hogan, R. J., Hólm, E., Janisková, M., Keeley, S., Laloyaux, P., Lopez, P., Lupu, C., Radnoti, G., de Rosnay, P., Rozum, I., Vamborg, F., Villaume, S., & Thépaut, J.-N. (2020). The ERA5 Global Reanalysis. *Q. J. R. Meteorol. Soc.*

Heymann, J., Reuter, M., Buchwitz, M., Schneising, O., Bovensmann, H., Burrows, J. P., Massart, S., Kaiser, J. W., & Crisp, D. (2017). CO2 emission of Indonesian fires in 2015 estimated from satellite-derived atmospheric CO2 concentrations. *Geophys. Res. Lett.*, 44(3), 1537–1544.

Hoelzemann, J. J., Schultz, M. G., Brasseur, G. P., Granier, C., & Simon, M. (2004). Global Wildland Fire Emission Model (GWEM): Evaluating the use of global area burnt satellite data. *J. Geophys. Res. D Atmos.*, 109(14).

Hoscilo, A., Page, S. E., Tansey, K. J., & Rieley, J. O. (2011). Effect of repeated fires on land-cover change on peatland in southern Central Kalimantan, Indonesia, from 1973 to 2005. *Int. J. Wildl. Fire*, 20(4), 578–588.

Humber, M. L., Boschetti, L., Giglio, L., & Justice, C. O. (2019). Spatial and temporal intercomparison of four global burned area products. *Int. J. Digit. Earth*, 12(4), 460–484.

Humphreys, E., Kukal, S. S., Christen, E. W., Hira, G. S., Balwinder-Singh, Sudhir-Yadav, & Sharma, R. K. (2010). Halting the groundwater decline in north-west India-which crop technologies will be winners? *Adv. Agron.*, 109, 155–217.

ICCI (2020). Krasnodar Krai Field Day: «Different Methods for the Use of Agricultural Residue other than Burning».

Ichoku, C. & Ellison, L. (2014). Global top-down smoke-aerosol emissions estimation using satellite fire radiative power measurements. *Atmos. Chem. Phys.*, 14(13), 6643–6667.

Indiastat (2000). Indiastat.com: revealing India – statistically.

Irfan, M., Riaz, M., Arif, M. S., Shahzad, S. M., Saleem, F., Rahman, N. U., van den Berg, L., & Abbas, F. (2014). Estimation and characterization of gaseous pollutant emissions from agricultural crop residue combustion in industrial and household sectors of Pakistan. *Atmos. Environ.*, 84, 189–197.

Jain, M., Mondal, P., DeFries, R. S., Small, C., & Galford, G. L. (2013). Mapping cropping intensity of smallholder farms: A comparison of methods using multiple sensors. *Remote Sens. Environ.*, 134, 210–223.

Jain, M., Mondal, P., Galford, G., Fiske, G., & DeFries, R. (2017). An Automated Approach to Map Winter Cropped Area of Smallholder Farms across Large Scales Using MODIS Imagery. *Remote Sens.*, 9(6), 566.

Jethva, H., Chand, D., Torres, O., Gupta, P., Lyapustin, A., & Patadia, F. (2018). Agricultural Burning and Air Quality over Northern India: A Synergistic Analysis using NASA's A-train Satellite Data and Ground Measurements. *Aerosol Air Qual. Res.*, 18(7), 1756–1773.

Jethva, H., Torres, O., Field, R. D., Lyapustin, A., Gautam, R., & Kayetha, V. (2019). Connecting Crop Productivity, Residue Fires, and Air Quality over Northern India. *Sci. Rep.*, 9, 16594.

Johnston, F., Henderson, S., Chen, Y., Randerson, J., Marlier, M., DeFries, R., Kinney, P., Bowman, D., & Brauer, M. (2012). Estimated global mortality attributable to smoke from landscape fires. *Environ. Health Perspect.*, 120(5), 695–701.

Justice, C. O., Townshend, J. R. G., Holben, B. N., & Tucker, C. J. (1985). Analysis of the phenology of global vegetation using meteorological satellite data. *Int. J. Remote Sens.*, 6(8), 1271–1318.

Kaiser, J. W., Andela, N., Atherton, J., de Jong, M., Heil, A., Paugam, R., Remy, S., Schultz, M. G., van der Werf, G. R., van Leeuwen, T. T., & Wooster, M. J. (2014). Recommended Fire Emission Service Enhancements.

Kaiser, J. W., Heil, A., Andreae, M. O., Benedetti, A., Chubarova, N., Jones, L., Morcrette, J. J., Razinger, M., Schultz, M. G., Suttie, M., & van der Werf, G. R. (2012). Biomass burning emissions estimated with a global fire assimilation system based on observed fire radiative power. *Biogeosciences*, 9, 527–554.

Kant, Y., Chauhan, P., Natwariya, A., Kannaujiya, S., & Mitra, D. (2022). Long term influence of groundwater preservation policy on stubble burning and air pollution over North-West India. *Sci. Rep.*, 12, 2090.

Kasischke, E. S. & Bruhwiler, L. P. (2002). Emissions of carbon dioxide, carbon monoxide, and methane from boreal forest fires in 1998. *J. Geophys. Res.*, 108(D1), 8146.

Kaskaoutis, D. G., Kumar, S., Sharma, D., Singh, R. P., Kharol, S. K., Sharma, M., Singh, A. K., Singh, S., Singh, A., & Singh, D. (2014). Effects of crop residue burning on aerosol properties, plume characteristics, and long-range transport over northern India. *J. Geophys. Res. Atmos.*, 119, 5424–5444.

Keller, C. A., Long, M. S., Yantosca, R. M., Da Silva, A. M., Pawson, S., & Jacob, D. J. (2014). HEMCO v1.0: A versatile, ESMF-compliant component for calculating emissions in atmospheric models. *Geosci. Model Dev.*, 7(4), 1409–1417.

Kennedy, R. E., Yang, Z., Gorelick, N., Braaten, J., Cavalcante, L., Cohen, W. B., & Healey, S. (2018). Implementation of the LandTrendr algorithm on Google Earth Engine. *Remote Sens.*, 10(5), 1–10.

Khan, M. F., Latif, M. T., Juneng, L., Amil, N., Nadzir, M. S. M., & Hoque, H. M. S. (2015). Physicochemical factors and sources of particulate matter at residential urban environment in Kuala Lumpur. *J. Air Waste Manag. Assoc.*, 65(8), 958–969.

Kim, P. S., Jacob, D. J., Mickley, L. J., Koplitz, S. N., Marlier, M. E., DeFries, R. S., Myers, S. S., Chew, B. N., & Mao, Y. H. (2015). Sensitivity of population smoke exposure to fire locations in Equatorial Asia. *Atmos. Environ.*, 102, 11–17.

Kim Oanh, N. T., Ly, B. T., Tipayarom, D., Manandhar, B. R., Prapat, P., Simpson, C. D., & Liu, L. J. S. (2011). Characterization of particulate matter emission from open burning of rice straw. *Atmos. Environ.*, 45, 493–502.

Koplitz, S., Mickley, L., Jacob, D., Marlier, M., DeFries, R., Gaveau, D., Locatelli, B., Reid, J., Xian, P., & Myers, S. (2018a). Role of the Madden-Julian Oscillation in the Transport of Smoke From Sumatra to the Malay Peninsula During Severe Non-El Niño Haze Events. *J. Geophys. Res. Atmos.*, 123(11), 6282–6294.

Koplitz, S., Mickley, L., Marlier, M., Buonocore, J., Kim, P., Liu, T., Sulprizio, M., DeFries, R., Jacob, D., Schwartz, J., Pongsiri, M., & Myers, S. (2016). Public health impacts of the severe haze in Equatorial Asia in September–October 2015: demonstration of a new framework for informing fire management strategies to reduce downwind smoke exposure. *Environ. Res. Lett.*, 11(9), 094023.

Koplitz, S., Nolte, C., Pouliot, G., Vukovich, J., & Beidler, J. (2018b). Influence of uncertainties in burned area estimates on modeled wildland fire PM2.5 and ozone pollution in the contiguous U.S. *Atmos. Environ.*, 191, 328–339.

Korontzi, S., McCarty, J., Loboda, T., Kumar, S., & Justice, C. (2006). Global distribution of agricultural fires in croplands from 3 years of Moderate Resolution Imaging Spectroradiometer (MODIS) data. *Global Biogeochem. Cycles*, 20(2), GB2021.

Kull, C. A. (2012). Fire and people in tropical island grassland landscapes: Fiji and Madagascar. *J. Pacific Stud.*, 32, 121–129.

Kumar, P., Kumar, S., & Joshi, L. (2015). *Socioeconomic and Environmental Implications of Agricultural Residue Burning: A Case Study of Punjab, India*.

Kuwata, M., Neelam-Naganathan, G. G., Miyakawa, T., Khan, M. F., Kozan, O., Kawasaki, M., Sumin, S., & Latif, M. T. (2018). Constraining the Emission of Particulate Matter From Indonesian Peatland Burning Using Continuous Observation Data. *J. Geophys. Res. Atmos.*, 123(17), 9828–9842.

Lasko, K. & Vadrevu, K. (2018). Improved rice residue burning emissions estimates: Accounting for practice-specific emission factors in air pollution assessments of Vietnam. *Environ. Pollut.*, 236, 795–806.

Lasko, K., Vadrevu, K. P., Tran, V. T., Ellicott, E., Nguyen, T. T., Bui, H. Q., & Justice, C. (2017). Satellites may underestimate rice residue and associated burning emissions in Vietnam. *Environ. Res. Lett.*, 12(8), 085006.

Levy, R. C., Mattoo, S., Munchak, L. A., Remer, L. A., Sayer, A. M., Patadia, F., & Hsu, N. C. (2013). The Collection 6 MODIS aerosol products over land and ocean. *Atmos. Meas. Tech.*, 6(11), 2989–3034.

Li, C., Hu, Y., Zhang, F., Chen, J., Ma, Z., Ye, X., Yang, X., Wang, L., Tang, X., Zhang, R., Mu, M., Wang, G., Kan, H., Wang, X., & Mellouki, A. (2017a). Multi-pollutant emissions from the burning of major agricultural residues in China and the related health-economic effects. *Atmos. Chem. Phys.*, 17(8), 4957–4988.

Li, F., Martin, M. V., Andreae, M. O., Arneth, A., Hantson, S., Kaiser, J. W., Lasslop, G., Yue, C., Bachelet, D., Forrest, M., Kluzek, E., Liu, X., Mangeon, S., Melton, J. R., Ward, D. S., Darmenov, A. S., Hickler, T., Ichoku, C., Magi, B. I., Sitch, S., van der Werf, G. R., Wiedinmyer, C., & Rabin, S. (2019). Historical (1700–2012) Global Multi-model Estimates of the Fire Emissions from the Fire Modeling Intercomparison Project (FireMIP). *Atmos. Chem. Phys.*, 19, 12545–12567.

Li, F., Zhang, X., Kondragunta, S., & Csiszar, I. (2018). Comparison of Fire Radiative Power Estimates From VIIRS and MODIS Observations. *J. Geophys. Res. Atmos.*, 123(9), 4545–4563.

Li, M., Zhang, Q., Kurokawa, J. I., Woo, J. H., He, K., Lu, Z., Ohara, T., Song, Y., Streets, D. G., Carmichael, G. R., Cheng, Y., Hong, C., Huo, H., Jiang, X., Kang, S., Liu, F., Su, H., & Zheng, B. (2017b). MIX: A mosaic Asian anthropogenic emission inventory under the international collaboration framework of the MICS-Asia and HTAP. *Atmos. Chem. Phys.*, 17(2), 935–963.

Li, Z., Guo, J., Ding, A., Liao, H., Liu, J., Sun, Y., Wang, T., Xue, H., Zhang, H., & Zhu, B. (2017c). Aerosol and boundary-layer interactions and impact on air quality. *Natl. Sci. Rev.*, 4(6), 810–833.

Liefert, O., Liefert, W., & Luebehusen, E. (2013). *Rising grain exports by the former Soviet Union region: Causes and outlook*. Technical report.

Liefert, W. M. & Liefert, O. (2012). Russian agriculture during transition: Performance, global impact, and outlook. *Appl. Econ. Perspect. Policy*, 34, 37–75.

Lipsett-Moore, G. J., Wolff, N. H., & Game, E. T. (2018). Emissions mitigation opportunities for savanna countries from early dry season fire management. *Nat. Commun.*, 9, 2247.

Liu, J. C., Mickley, L. J., Sulprizio, M. P., Dominici, F., Yue, X., Ebisu, K., Anderson, G. B., Khan, R. F., Bravo, M. A., & Bell, M. L. (2016). Particulate air pollution from wildfires in the Western US under climate change. *Clim. Change*, 138(3-4), 655–666.

Liu, M., Song, Y., Yao, H., Kang, Y., Li, M., Huang, X., & Hu, M. (2015). Estimating emissions from agricultural fires in the North China Plain based on MODIS fire radiative power. *Atmos. Environ.*, 112, 326–334.

Liu, T. & Crowley, M. A. (2021). Detection and impacts of tiling artifacts in MODIS burned area classification. *IOP SciNotes*, 2, 14003.

Liu, T., Marlier, M. E., DeFries, R. S., Westervelt, D. M., Xia, K. R., Fiore, A. M., Mickley, L. J., Cusworth, D. H., & Milly, G. (2018). Seasonal impact of regional outdoor biomass burning on air pollution in three Indian cities: Delhi, Bengaluru, and Pune. *Atmos. Environ.*, 172, 83–92.

Liu, T., Marlier, M. E., Karambelas, A., Jain, M., Singh, S., Singh, M. K., Gautam, R., & DeFries, R. S. (2019). Missing emissions from post-monsoon agricultural fires in northwestern India: regional limitations of MODIS burned area and active fire products. *Environ. Res. Commun.*, 1, 011007.

Liu, T., Mickley, L., Patel, P., Gautam, R., Jain, M., Singh, S., Singh, B., DeFries, R., & Marlier, M. (2022). Cascading delays in the monsoon growing season and post-monsoon fires may exacerbate poor air quality in north India. *J. Geophy. Res. Atmos.*, in review.

Liu, T., Mickley, L. J., Gautam, R., Singh, M. K., DeFries, R. S., & Marlier, M. E. (2021a). Detection of delay in post-monsoon agricultural burning across Punjab, India: potential drivers and consequences for air quality. *Environ. Res. Lett.*, 16, 014014.

Liu, T., Mickley, L. J., Marlier, M. E., DeFries, R. S., Khan, M. F., Latif, M. T., & Karambelas, A. (2020a). Diagnosing spatial biases and uncertainties in global fire emissions inventories: Indonesia as regional case study. *Remote Sens. Environ.*, 237, 111557.

Liu, T., Mickley, L. J., & McCarty, J. L. (2021b). Global search for temporal shifts in fire activity: potential human influence on southwest Russia and north Australia fire seasons. *Environ. Res. Lett.*, 16, 044023.

Liu, T., Mickley, L. J., Singh, S., Jain, M., DeFries, R. S., & Marlier, M. E. (2020b). Crop residue burning practices across north India inferred from household survey data: bridging gaps in satellite observations. *Atmos. Environ. X*, 8, 100091.

Lizundia-Loiola, J., Otón, G., Ramo, R., & Chuvieco, E. (2020). A spatio-temporal active-fire clustering approach for global burned area mapping at 250 m from MODIS data. *Remote Sens. Environ.*, 236, 111493.

Lobell, D. B., Ortiz-Monasterio, J. I., Sibley, A. M., & Sohu, V. S. (2013). Satellite detection of earlier wheat sowing in India and implications for yield trends. *Agric. Syst.*, 115, 137–143.

Lobell, D. B., Roberts, M. J., Schlenker, W., Braun, N., Little, B. B., Rejesus, R. M., & Hammer, G. L. (2014). Greater sensitivity to drought accompanies maize yield increase in the U.S. Midwest. *Science.*, 344(6183), 516–519.

Lobell, D. B., Sibley, A., & Ivan Ortiz-Monasterio, J. (2012). Extreme heat effects on wheat senescence in India. *Nat. Clim. Chang.*, 2(3), 186–189.

Maasakkers, J. D., Jacob, D. J., Sulprizio, M. P., Turner, A. J., Weitz, M., Wirth, T., Hight, C., DeFigueiredo, M., Desai, M., Schmeltz, R., Hockstad, L., Bloom, A. A., Bowman, K. W., Jeong, S., & Fischer, M. L. (2016). Gridded National Inventory of U.S. Methane Emissions. *Environ. Sci. Technol.*, 50(23), 13123–13133.

Mahajan, G., Bharaj, T. S., & Timsina, J. (2009). Yield and water productivity of rice as affected by time of transplanting in Punjab, India. *Agric. Water Manag.*, 96(3), 525–532.

Marlier, M. E., DeFries, R. S., Kim, P. S., Koplitz, S. N., Jacob, D. J., Mickley, L. J., & Myers, S. S. (2015). Fire emissions and regional air quality impacts from fires in oil palm, timber, and logging concessions in Indonesia. *Environ. Res. Lett.*, 10(8), 085005.

Marlier, M. E., Liu, T., Yu, K., Buonocore, J. J., Koplitz, S. N., DeFries, R. S., Mickley, L. J., Jacob, D. J., Schwartz, J., Wardhana, B. S., & Myers, S. S. (2019). Fires, Smoke Exposure, and Public Health: An Integrative Framework to Maximize Health Benefits from Peatland Restoration. *GeoHealth*, 3(7), 178–189.

McCarty, J. L., Loboda, T., & Trigg, S. (2008). A hybrid remote sensing approach to quantifying crop residue burning in the United States. *Appl. Eng. Agric.*, 24(4), 515–527.

Miao, Y., Li, J., Miao, S., Che, H., Wang, Y., Zhang, X., Zhu, R., & Liu, S. (2019). Interaction Between Planetary Boundary Layer and PM2.5 Pollution in Megacities in China: a Review. *Curr. Pollut. Reports*, 5(4), 261–271.

Mondal, P., Jain, M., DeFries, R. S., Galford, G. L., & Small, C. (2015). Sensitivity of crop cover to climate variability: Insights from two Indian agro-ecoregions. *J. Environ. Manage.*, 148, 21–30.

Mondal, P., Jain, M., Robertson, A. W., Galford, G. L., Small, C., & DeFries, R. S. (2014). Winter crop sensitivity to inter-annual climate variability in central India. *Clim. Change*, 126(1-2), 61–76.

Mu, M., Randerson, J. T., Van Der Werf, G. R., Giglio, L., Kasibhatla, P., Morton, D., Collatz, G. J., Defries, R. S., Hyer, E. J., Prins, E. M., Griffith, D. W., Wunch, D., Toon, G. C., Sherlock, V., & Wennberg, P. O. (2011). Daily and 3-hourly variability in global fire emissions and consequences for atmospheric model predictions of carbon monoxide. *J. Geophys. Res. Atmos.*, 116, D24303.

Mukherjee, T., Vinoj, V., Midya, S. K., Puppala, S. P., & Adhikary, B. (2020). Numerical simulations of different sectoral contributions to post monsoon pollution over Delhi. *Heliyon*, 6, e03548.

Narang, R. S. & Virmani, S. M. (2001). Rice-wheat cropping systems of the Indo-Gangetic Plain of India. In *Rice-Wheat Consort. Pap. Ser. 11. Rice-Wheat Consort. Indo-Gangetic Plains, New Delhi, Int. Crop. Res. Inst. Semi-Arid Trop. (ICRISAT), Patancheru, India.*

Ni, H., Han, Y., Cao, J., Chen, L.-W. A., Tian, J., Wang, X., Chow, J. C., Watson, J. G., Wang, Q., Wang, P., Li, H., & Huang, R.-J. (2015). Emission characteristics of carbonaceous particles and trace gases from open burning of crop residues in China. *Atmos. Environ.*, 123, 399–406.

Nyamadzawo, G., Gwenzi, W., Kanda, A., Kundhlande, A., & Masona, C. (2013). Understanding the causes, socio-economic and environmental impacts, and management of veld fires in tropical Zimbabwe. *Fire Sci. Rev.*, 2(1), 2.

Ojha, N., Sharma, A., Manish, K., Girach, I., Ansari, T. U., Sharma, S. K., Singh, N., Pozzer, A., & Gunthe, S. S. (2020). On the widespread enhancement in fine particulate matter across the Indo-Gangetic Plain towards winter. *Sci. Rep.*, 10, 5862.

Olson, D. M., Dinerstein, E., Wikramanayake, E. D., Burgess, N. D., Powell, G. V. N., Underwood, E. C., D'amico, J. A., Itoua, I., Strand, H. E., Morrison, J. C., Loucks, C. J., Allnutt, T. F., Ricketts, T. H., Kura, Y., Lamoreux, J. F., Wettengel, W. W., Hedao, P., & Kassem, K. R. (2001). Terrestrial Ecoregions of the World: A New Map of Life on Earth. *Bioscience*, 51(11), 933.

Page, S., Hoscilo, A., Langner, A., Tansey, K., Siegert, F., Limin, S., & Rieley, J. (2009). Tropical peatland fires in Southeast Asia. In *Trop. Fire Ecol. Clim. Chang. L. Use, Ecosyst. Dyn.* (pp. 263–287). Berlin, Heidelberg: Springer Berlin Heidelberg.

Palanisami, K., Kakumanu, K. R., Nagothu, U. S., & Ranganathan, C. R. (2019). *Climate Change and Future Rice Production in India: A Cross Country Study of Major Rice Growing States of India*. Springer Singapore.

Palinkas, L. A., Horwitz, S. M., Green, C. A., Wisdom, J. P., Duan, N., & Hoagwood, K. (2015). Purposeful sampling for qualitative data collection and analysis in mixed method implementation research Lawrence. *Adm. Policy Ment. Heal. Ment. Heal. Serv. Res.*, 42(5), 533–544.

Palm, B. B., Peng, Q., Fredrickson, C. D., Lee, B. H., Garofalo, L. A., Pothier, M. A., Kreidenweis, S. M., Farmer, D. K., Pokhrel, R. P., Shen, Y., Murphy, S. M., Permar, W., Hu, L., Campos, T. L., Hall, S. R., Ullmann, K., Zhang, X., Flocke, F., Fischer, E. V., & Thornton, J. A. (2020). Quantification of organic aerosol and brown carbon evolution in fresh wildfire plumes. *Proc. Natl. Acad. Sci. U. S. A.*, 117(47), 29469–29477.

Pan, X., Chin, M., Gautam, R., Bian, H., Kim, D., Colarco, P. R., Diehl, T. L., Takemura, T., Pozzoli, L., Tsigaridis, K., Bauer, S., & Bellouin, N. (2015). A multi-model evaluation of aerosols over South Asia: Common problems and possible causes. *Atmos. Chem. Phys.*, 15(10), 5903–5928.

Patel, K., Bhandari, S., Gani, S., Campmier, M. J., Kumar, P., Habib, G., Apte, J., & Hildebrandt Ruiz, L. (2021). Sources and Dynamics of Submicron Aerosol during the Autumn Onset of the Air Pollution Season in Delhi, India. *ACS Earth Sp. Chem.*, 5, 118–128.

Pechony, O. & Shindell, D. T. (2010). Driving forces of global wildfires over the past millennium and the forthcoming century. *Proc. Natl. Acad. Sci. U. S. A.*, 107(45), 19167–19170.

Petäjä, T., Järvi, L., Kerminen, V. M., Ding, A. J., Sun, J. N., Nie, W., Kujansuu, J., Virkkula, A., Yang, X., Fu, C. B., Zilitinkevich, S., & Kulmala, M. (2016). Enhanced air pollution via aerosol-boundary layer feedback in China. *Sci. Rep.*, 6(November 2015), 1–6.

Petty, A. M. & Bowman, D. M. (2007). A Satellite Analysis of Contrasting Fire Patterns in Aboriginal- and Euro-Australian Lands in Tropical North Australia. *Fire Ecol.*, 3, 32–47.

Petty, A. M., DeKoninck, V., & Orlove, B. (2015). Cleaning, Protecting, or Abating? Making Indigenous Fire Management "Work" in Northern Australia. *J. Ethnobiol.*, 35, 140–162.

Prentice, I. C., Kelley, D. I., Foster, P. N., Friedlingstein, P., Harrison, S. P., & Bartlein, P. J. (2011). Modeling fire and the terrestrial carbon balance. *Global Biogeochem. Cycles*, 25(3), GB3005.

Price, O. F. (2015). Potential role of ignition management in reducing unplanned burning in Arnhem Land, Australia. *Austral Ecol.*, 40(7), 857–868.

Price, O. F., Russell-Smith, J., & Watt, F. (2012). The influence of prescribed fire on the extent of wildfire in savanna landscapes of western Arnhem Land, Australia. *Int. J. Wildl. Fire*, 21(3), 297–305.

Qiang, B., Lei, H., & Zhao, C. Y. (2014). Monitoring glacier changes of recent 50 years in the upper reaches of heihe river basin based on remotely-sensed data. *IOP Conf. Ser. Earth Environ. Sci.*, 17, 012138.

Qiu, Y., Liao, H., Zhang, R., & Hu, J. (2017). Simulated impacts of direct radiative effects of scattering and absorbing aerosols on surface layer aerosol concentrations in China during a heavily polluted event in february 2014. *J. Geophys. Res.*, 122(11), 5955–5975.

Rada, N., Liefert, W., & Liefert, O. (2017). *Productivity Growth and the Revival of Russian Agriculture*. Technical Report ERR-228, U.S. Department of Agriculture, Economic Research Service.

Ramanathan, V., Chung, C., Kim, D., Bettge, T., Buja, L., Kiehl, J. T., Washington, W. M., Fu, Q., Sikka, D. R., & Wild, M. (2005). Atmospheric brown clouds: Impacts on South Asian climate and hydrological cycle. *Proc. Natl. Acad. Sci.*, 102(15), 5326–5333.

Randerson, J. T., Chen, Y., van der Werf, G. R., Rogers, B. M., & Morton, D. C. (2012). Global burned area and biomass burning emissions from small fires. *J. Geophys. Res. Biogeosciences*, 117, G04012.

Reddy, D. N., Reddy, A. A., & Bantilan, M. C. S. (2014). The impact of Mahatma Gandhi National Rural Employment Guarantee Act (MGNREGA) on rural labor markets and agriculture. *India Rev.*, 13(3), 251–273.

Rein, G., Cleaver, N., Ashton, C., Pironi, P., & Torero, J. L. (2008). The severity of smouldering peat fires and damage to the forest soil. *Catena*, 74(3), 304–309.

Riley, K. L., Williams, A. P., Urbanski, S. P., Calkin, D. E., Short, K. C., & O'Connor, C. D. (2019). Will Landscape Fire Increase in the Future? A Systems Approach to Climate, Fire, Fuel, and Human Drivers. *Curr. Pollut. Reports*, 5, 9–24.

Rodell, M., Famiglietti, J. S., Wiese, D. N., Reager, J. T., Beaudoing, H. K., Landerer, F. W., & Lo, M. H. (2018). Emerging trends in global freshwater availability. *Nature*, 557(7707), 651–659.

Rogers, B. M., Soja, A. J., Goulden, M. L., & Randerson, J. T. (2015). Influence of tree species on continental differences in boreal fires and climate feedbacks. *Nat. Geosci.*, 8(3), 228–234.

ROSSTAT (2020a). *Socio-Economic Situation in Russia (In Russian: Социально-экономическое положение России)*. Technical report.

ROSSTAT (2020b). Unified Interdepartmental Statistical Information System (UniSIS) [In Russian: Единая межведомственная информационно-статистическая система (ЕМИСС)].

Roteta, E., Bastarrika, A., Padilla, M., Storm, T., & Chuvieco, E. (2019). Development of a Sentinel-2 burned area algorithm: Generation of a small fire database for sub-Saharan Africa. *Remote Sens. Environ.*, 222, 1–17.

Roy, D. P., Giglio, L., Kendall, J. D., & Justice, C. O. (1999). Multi-temporal active-fire based burn scar detection algorithm. *Int. J. Remote Sens.*, 20(5), 1031–1038.

Russell-Smith, J., Edwards, A. C., Sangha, K. K., Yates, C. P., & Gardener, M. R. (2019). Challenges for prescribed fire management in Australia's fire-prone rangelands-the example of the Northern Territory. *Int. J. Wildl. Fire*, 29(5), 339–353.

Sakamoto, T., Yokozawa, M., Toritani, H., Shibayama, M., Ishitsuka, N., & Ohno, H. (2005). A crop phenology detection method using time-series MODIS data. *Remote Sens. Environ.*, 96(3-4), 366–374.

Saraf, A., Bora, A., Das, J., Rawat, V., Sharma, K., & Jain, S. K. (2010). Winter fog over the Indo-Gangetic Plains: Mapping and modelling using remote sensing and GIS. *Nat. Hazards*, 52(1), 199–220.

Sarkar, S., Singh, R. P., & Chauhan, A. (2018). Crop Residue Burning in Northern India: Increasing Threat to Greater India. *J. Geophys. Res. Atmos.*, 123(13), 6920–6934.

Sayer, A. M., Hsu, N. C., Bettenhausen, C., & Jeong, M. J. (2013). Validation and uncertainty estimates for MODIS Collection 6 "Deep Blue" aerosol data. *J. Geophys. Res. Atmos.*, 118, 7864–7872.

Schierhorn, F., Faramarzi, M., Prishchepov, A. V., Koch, F. J., & Müller, D. (2014). Quantifying yield gaps in wheat production in Russia. *Environ. Res. Lett.*, 9, 084017.

Schroeder, W. & Giglio, L. (2018). *NASA VIIRS Land Science Investigator Processing System (SIPS) Visible Infrared Imaging Radiometer Suite (VIIRS) 375 m & 750 m Active Fire Products, Product User's Guide Version 1.4*. Technical report.

Schroeder, W., Oliva, P., Giglio, L., & Csiszar, I. A. (2014). The New VIIRS 375m active fire detection data product: Algorithm description and initial assessment. *Remote Sens. Environ.*, 143, 85–96.

Seager, R., Hooks, A., Williams, A. P., Cook, B., Nakamura, J., & Henderson, N. (2015). Climatology, variability, and trends in the U.S. vapor pressure deficit, an important fire-related meteorological quantity. *J. Appl. Meteorol. Climatol.*, 54(6), 1121–1141.

Sembhi, H., Wooster, M., Zhang, T., Sharma, S., Singh, N., Agarwal, S., Boesch, H., Gupta, S., Misra, A., Tripathi, S. N., Mor, S., & Khaiwal, R. (2020). Post-monsoon air quality degradation across Northern India: Assessing the impact of policy-related shifts in timing and amount of crop residue burnt. *Environ. Res. Lett.*, 15, 104067.

Shi, Y., Matsunaga, T., Saito, M., Yamaguchi, Y., & Chen, X. (2015). Comparison of global inventories of CO2 emissions from biomass burning during 2002-2011 derived from multiple satellite products. *Environ. Pollut.*, 206, 479–487.

Shyamsundar, P., Springer, N. P., Tallis, H., Polasky, S., Jat, M. L., Sidhu, H. S., Krishnapriya, P. P., Skiba, N., Ginn, W., Ahuja, V., Cummins, J., Datta, I., Dholakia, H. H., Dixon, J., Gerard, B., Gupta, R., Hellmann, J., Jadhav, A., Jat, H. S., Keil, A., Ladha, J. K., Lopez-Ridaura, S., Nandrajog, S. P., Paul, S., Ritter, A., Sharma, P. C., Singh, R., Singh, D., & Somanathan, R. (2019). Fields on fire: Alternatives to crop residue burning in India. *Science.*, 365, 536–538.

Sidhu, H. S., Singh, M., Yadvinder, S., Blackwell, J., Lohan, S. K., Humphreys, E., Jat, M. L., Singh, V., & Singh, S. (2015). Development and evaluation of the Turbo Happy Seeder for sowing wheat into heavy rice residues in NW India. *F. Crop. Res.*, 184, 201–212.

Sidorenko, S., Trubilin, E., Kolesnikova, E., & Hasegawa, H. (2017). Current Situation, Issues and Trends of Mechanization for Grain Harvesting in the Russian Federation. *Agric. Mech. Asia, Africa, Lat. Am.*, 48, 31–35.

Singh, K. (2009). Act to Save Groundwater in Punjab: Its Impact on Water Table, Electricity Subsidy and Environment. *Agric. Econ. Res. Rev.*, 22, 365–386.

Singh, N. & Ranade, A. (2010). *Determination of onset and withdrawal dates of summer monsoon across India using NCEP / NCAR re-analysis*.

Singh, N. J., Kudrat, M., Jain, K., & Pandey, K. (2011). Cropping pattern of Uttar Pradesh using IRS-P6 (AWiFS) data. *Int. J. Remote Sens.*, 32(16), 4511–4526.

Singh, R. P. & Kaskaoutis, D. G. (2014). Crop residue burning: A threat to South Asian air quality. *Eos (Washington. DC).*, 95(37), 333–334.

Sinha, B., Singh Sangwan, K., Maurya, Y., Kumar, V., Sarkar, C., Chandra, B. P., & Sinha, V. (2015). Assessment of crop yield losses in Punjab and Haryana using 2 years of continuous in situ ozone measurements. *Atmos. Chem. Phys.*, 15(16), 9555–9576.

Stein, A. F., Draxler, R. R., Rolph, G. D., Stunder, B. J., Cohen, M. D., & Ngan, F. (2015). NOAA's HYSPLIT Atmospheric Transport and Dispersion Modeling System. *Bull. Am. Meteorol. Soc.*, 96(12), 2059–2077.

Stockwell, C. E., Jayarathne, T., Cochrane, M. A., Ryan, K. C., Putra, E. I., Saharjo, B. H., Nurhayati, A. D., Albar, I., Blake, D. R., Simpson, I. J., Stone, E. A., & Yokelson, R. J. (2016). Field measurements of trace gases and aerosols emitted by peat fires in Central Kalimantan, Indonesia, during the 2015 El Niño. *Atmos. Chem. Phys.*, 16(18), 11711–11732.

Sulla-Menashe, D., Gray, J. M., Abercrombie, S. P., & Friedl, M. A. (2019). Hierarchical mapping of annual global land cover 2001 to present: The MODIS Collection 6 Land Cover product. *Remote Sens. Environ.*, 222, 183–194.

Tallis, H., Polasky, S., Shyamsundar, P., Springer, N., Ahuja, V., Cummins, J., Datta, I., Dixon, J., Gerard, B., Ginn, W., Gupta, R., Jadhav, A., Jat, M., Keil, A., Krishnapriya, P., Ladha, J., Nandrajog, S., Paul, S., Lopez Ridaura, S., Ritter, A., Sidhu, H., Skiba, N., & Somanathan, R. (2017). *The Evergreen Revolution: Six Ways to empower India's no-burn agricultural future*. Technical report.

The Guardian (2017). Delhi doctors declare pollution emergency as smog chokes city.

The Indian Express (2019). How advancing paddy sowing by a week helps Punjab farmers, and Congress.

The Times of India (2017). Air pollution: NGT bans construction, waste burning in Delhi.

The Tribune India (2019). Crumbling canal system takes toll on groundwater.

Thumaty, K. C., Rodda, S. R., Singhal, J., Gopalakrishnan, R., Jha, C. S., Parsi, G. D., & Dadhwal, V. K. (2015). Spatio-temporal characterization of agriculture residue burning in Punjab and Haryana, India, using MODIS and Suomi NPP VIIRS data. *Curr. Sci.*, 109(10), 1850–1855.

Torres, O., Tanskanen, A., Veihelmann, B., Ahn, C., Braak, R., Bhartia, P. K., Veefkind, P., & Levelt, P. (2007). Aerosols and surface UV products from Ozone Monitoring Instrument observations: An overview. *J. Geophys. Res. Atmos.*, 112, D24S47.

Tosca, M. G., Randerson, J. T., & Zender, C. S. (2013). Global impact of smoke aerosols from landscape fires on climate and the Hadley circulation. *Atmos. Chem. Phys.*, 13(10), 5227–5241.

Trauernicht, C., Brook, B. W., Murphy, B. P., Williamson, G. J., & Bowman, D. M. (2015). Local and global pyrogeographic evidence that indigenous fire management creates pyrodiversity. *Ecol. Evol.*, 5(9), 1908–1918.

Tripathi, A., Mishra, A. K., & Verma, G. (2016). Impact of Preservation of Subsoil Water Act on Groundwater Depletion: The Case of Punjab, India. *Environ. Manage.*, 58(1), 48–59.

Turpin, B. J. & Lim, H. J. (2001). Species contributions to PM2.5 mass concentrations: Revisiting common assumptions for estimating organic mass. *Aerosol Sci. Technol.*, 35, 602–610.

USDA (2020). Crop Explorer - Commodity Intelligence Reports - Russian Federation.

Vadrevu, K. & Lasko, K. (2018). Intercomparison of MODIS AQUA and VIIRS I-band fires and emissions in an agricultural landscape-implications for air pollution research. *Remote Sens.*, 10(7), 978.

Vadrevu, K. P., Csiszar, I., Ellicott, E., Giglio, L., Badarinath, K. V., Vermote, E., & Justice, C. (2013). Hotspot analysis of vegetation fires and intensity in the Indian region. *IEEE J. Sel. Top. Appl. Earth Obs. Remote Sens.*, 6(1), 224–238.

Vadrevu, K. P., Ellicott, E., Badarinath, K. V. S., & Vermote, E. (2011). MODIS derived fire characteristics and aerosol optical depth variations during the agricultural residue burning season, north India. *Environ. Pollut.*, 159(6), 1560–1569.

Vadrevu, K. P., Lasko, K., Giglio, L., & Justice, C. (2015). Vegetation fires, absorbing aerosols and smoke plume characteristics in diverse biomass burning regions of Asia. *Environ. Res. Lett.*, 10, 105003.

van der Werf, G. R., Dempewolf, J., Trigg, S. N., Randerson, J. T., Kasibhatla, P. S., Giglio, L., Murdiyarso, D., Peters, W., Morton, D. C., Collatz, G. J., Dolman, A. J., & DeFries, R. S. (2008). Climate regulation of fire emissions and deforestation in equatorial Asia. *Proc. Natl. Acad. Sci.*, 105(51), 20350–20355.

van der Werf, G. R., Randerson, J. T., Giglio, L., Collatz, G. J., Mu, M., Kasibhatla, P. S., Morton, D. C., DeFries, R. S., Jin, Y., & Van Leeuwen, T. T. (2010). Global fire emissions and the contribution of deforestation, savanna, forest, agricultural, and peat fires (1997-2009). *Atmos. Chem. Phys.*, 10(23), 11707–11735.

van der Werf, G. R., Randerson, J. T., Giglio, L., van Leeuwen, T. T., Chen, Y., Rogers, B. M., Mu, M., van Marle, M. J. E., Morton, D. C., Collatz, G. J., Yokelson, R. J., & Kasibhatla, P. S. (2017). Global fire emissions estimates during 1997–2016. *Earth Syst. Sci. Data*, 9(2), 697–720.

van Wagtendonk, J. W., Root, R. R., & Key, C. H. (2004). Comparison of AVIRIS and Landsat ETM+ detection capabilities for burn severity. *Remote Sens. Environ.*, 92(3), 397–408.

Vermote, E., Roger, J. C., & Ray, J. P. (2015). *MODIS Surface Reflectance User's Guide: Collection 6*. Technical report.

Wang, H., Peng, Y., Zhang, X., Liu, H., Zhang, M., Che, H., Cheng, Y., & Zheng, Y. (2018a). Contributions to the explosive growth of PM2.5 mass due to aerosol-radiation feedback and decrease in turbulent diffusion during a red alert heavy haze in Beijing-Tianjin-Hebei, China. *Atmos. Chem. Phys.*, 18(23), 17717–17733.

Wang, X., He, X., Miao, S., & Dou, Y. (2018b). Numerical simulation of the influence of aerosol radiation effect on urban boundary layer. *Sci. China Earth Sci.*, 61(12), 1844–1858.

Wang, Y. X., McElroy, M. B., Jacob, D. J., & Yantosca, R. M. (2004). A nested grid formulation for chemical transport over Asia: Applications to CO. *J. Geophys. Res. Atmos.*, 109(22), D22307.

Wegren, S. (2011). Food security and Russia's 2010 drought. *Eurasian Geogr. Econ.*, 52(1), 140–156.

Weiss, D. J., Nelson, A., Gibson, H. S., Temperley, W., Peedell, S., Lieber, A., Hancher, M., Poyart, E., Belchior, S., Fullman, N., Mappin, B., Dalrymple, U., Rozier, J., Lucas, T. C., Howes, R. E., Tusting, L. S., Kang, S. Y., Cameron, E., Bisanzio, D., Battle, K. E., Bhatt, S., & Gething, P. W. (2018). A global map of travel time to cities to assess inequalities in accessibility in 2015. *Nature*, 553(7688), 333–336.

Whitehead, P. J., Bowman, D. M., Preece, N., Fraser, F., & Cooke, P. (2003). Customary use of fire by indigenous peoples in northern Australia: Its contemporary role in savanna management. *Int. J. Wildl. Fire*, 12(3-4), 415–425.

Wiedinmyer, C., Akagi, S. K., Yokelson, R. J., Emmons, L. K., Orlando, J. J., & Soja, A. J. (2011). The Fire INventory from NCAR (FINN): a high resolution global model to estimate the emissions from open burning. *Geosci. Model Dev.*, 4, 625–641.

Wilson, A. M. & Jetz, W. (2016). Remotely Sensed High-Resolution Global Cloud Dynamics for Predicting Ecosystem and Biodiversity Distributions. *PLoS Biol.*, 14(3), 1–20.

Wooster, M. J., Roberts, G., Perry, G. L., & Kaufman, Y. J. (2005). Retrieval of biomass combustion rates and totals from fire radiative power observations: FRP derivation and calibration relationships between biomass consumption and fire radiative energy release. *J. Geophys. Res. Atmos.*, 110, D24311.

Worden, J. R., Bloom, A. A., Pandey, S., Jiang, Z., Worden, H. M., Walker, T. W., Houweling, S., & Röckmann, T. (2017). Reduced biomass burning emissions reconcile conflicting estimates of the post-2006 atmospheric methane budget. *Nat. Commun.*, 8(1), 2227.

Xiang, H.-b., Liu, J.-s., Cao, C.-x., & Xu, M. (2013). Algorithms for Moderate Resolution Imaging Spectroradiometer cloud-free image compositing. *J. Appl. Remote Sens.*, 7, 073486.

Xu, J., Morris, P. J., Liu, J., & Holden, J. (2018). PEATMAP: Refining estimates of global peatland distribution based on a meta-analysis. *Catena*, 160, 134–140.

Yengoh, G. T., Dent, D., Olsson, L., Tengberg, A. E., & Tucker, C. J. (2015). *Use of the Normalized Difference Vegetation Index (NDVI) to Assess Land Degradation at Multiple Scales: Current Status, Future Trends, and Practical Considerations*. SpringerBriefs in Environmental Science. Springer International Publishing.

Yi, Y., Kimball, J. S., & Reichle, R. H. (2014). Spring hydrology determines summer net carbon uptake in northern ecosystems. *Environ. Res. Lett.*, 9(6), 064003.

Yibarbuk, D., Whitehead, P. J., Russell-Smith, J., Jackson, D., Godjuwa, C., Fisher, A., Cooke, P., Choquenot, D., & Bowman, D. M. (2001). Fire ecology and Aboriginal land management in central Arnhem Land, northern australia: A tradition of ecosystem management. *J. Biogeogr.*, 28(3), 325–343.

Zhang, F., Wang, J., Ichoku, C., Hyer, E. J., Yang, Z., Ge, C., Su, S., Zhang, X., Kondragunta, S., Kaiser, J. W., Wiedinmyer, C., & da Silva, A. (2014a). Sensitivity of mesoscale modeling of smoke direct radiative effect to the emission inventory: A case study in northern sub-Saharan African region. *Environ. Res. Lett.*, 9(7), 075002.

Zhang, T., Wooster, M. J., de Jong, M. C., & Xu, W. (2018). How Well Does the 'Small Fire Boost' Methodology Used within the GFED4.1s Fire Emissions Database Represent the Timing, Location and Magnitude of Agricultural Burning? *Remote Sens.*, 10, 823.

Zhang, T., Wooster, M. J., Green, D. C., & Main, B. (2015). New field-based agricultural biomass burning trace gas, PM2.5, and black carbon emission ratios and factors measured in situ at crop residue fires in Eastern China. *Atmos. Environ.*, 121, 22–34.

Zhang, X., Kondragunta, S., & Roy, D. P. (2014b). Interannual variation in biomass burning and fire seasonality derived from geostationary satellite data across the contiguous United States from 1995 to 2011. *J. Geophys. Res. Biogeosciences*, 119, 1147–1162.

Zhang, Y., Shao, M., Lin, Y., Luan, S., Mao, N., Chen, W., & Wang, M. (2013). Emission inventory of carbonaceous pollutants from biomass burning in the Pearl River Delta Region, China. *Atmos. Environ.*, 76, 189–199.

Zhao, H., Yang, Z., Di, L., Li, L., & Zhu, H. (2009). Crop phenology date estimation based on NDVI derived from the reconstructed MODIS daily surface reflectance data. In *2009 17th Int. Conf. Geoinformatics* (pp. 1–6). Fairfax, VA.